

Experimental characterisation of laminar and turbulent simulated biogas/syngas flames

Aadil Dowlut

Submitted in partial fulfilment of the requirements for the degree of
Doctor of Philosophy



Department of Mechanical Engineering

University College London

12th February 2016

Declaration of authorship

I, Aadil Dowlut confirm that the work presented in this thesis is my own. Where information has been derived from other sources, I confirm that this has been indicated in the thesis.

Abstract

The need to diversify the fuels used in gas turbine power generation has driven forward the development of fuel – flexible combustion systems. However, the change in chemical, thermal and transport properties of fuels due to the variation of the constituents can have a significant effect on the performance of the combustor. It is known that the fuel properties have a strong influence on the dynamic response of flames. One of the key parameters required to enable detailed understanding of the flame response is heat release rate. To date there are no measurements that can directly provide this quantity. Simultaneous OH/H₂CO PLIF (HRX – pixel by pixel product of LIF signals) can provide planar local heat release rate and it has shown to work on premixed hydrocarbon flames (methane, propane and ethylene air flames) and ethanol. For the first time this method was extended to biogas/syngas type flame application. Here H₂/CO/CH₄/CO₂ flames are investigated and the heat release response was measured under high curvature and rates of strain. In the case of laminar flames the results suggest that simultaneous OH/H₂CO PLIF can be used to provide information about the heat release rate in methane and methane/carbon-dioxide (biogas) flames. The trend in spatial distribution of HRX agrees well with the one-dimensional flame calculations. The spatial distribution of the HRX is of great interest for studying combustion modelling and instabilities. Therefore the measurement technique was extended to turbulent flames on a laboratory scale gas turbine combustor to study the flame response of multi-component fuels. The HRX technique was found to be suitable to study biogas flames subjected to flow perturbations. The measurements allowed to spatially resolve the heat release region under different perturbation conditions, especially in the region where the vortex is formed. These measurements were also carried out for methane/carbon-monoxide/hydrogen (syngas) flames. For the first time experimentally, spatially resolved heat release regions of biogas and syngas were measured and compared to a conventional natural gas (methane). Also part of the study was to investigate the flame response while the flame speed of the different fuels were matched. In the case of biogas and methane flames, provided the flame speed and the overall bulk velocity were similar, the same flame responses were observed at all forcing frequencies. In the case of syngas and methane flames, a similar response was observed at higher forcing frequency but not for low frequency.

Acknowledgements

I would never have been able to finish my dissertation without the guidance of my committee members, help from friends, and support from my family and partner. I would like to express my deepest gratitude to my advisor, Dr. Rama Balachandran, for his excellent guidance, caring, patience, and providing me with an excellent atmosphere for doing research. I would also like to thank Professor Nicos Ladomatos for giving constructive comments and suggestions on the experiments and data.

I must also acknowledge Richard, Neil and Barry for helping in the construction of the laser diagnostic lab and a special thanks to Phil for the patience and helpful advice on the complex design on the laminar flame burner. A special thanks to my lab colleagues Taaha, Mart, Baptiste, Midhat, Elina and Aaron for the great support throughout the PhD.

I take this opportunity to express gratitude to all of the faculty members for their help and support. I also thank my parents for the unceasing encouragement, support and attention. I am also grateful to my partner who supported me through this venture.

I also place on record, my sense of gratitude to one and all, who directly or indirectly, have helped me in this venture.

Table of contents

Chapter 1	1
1. Introduction	1
1.1. Literature review	5
1.2. Flames characterisation	5
1.2.1. Laminar flame speed measurement technique.....	7
1.3. Turbulent Flames.....	14
1.3.1. Turbulent flame characterisation	15
1.4. Challenges of Biogas combustion.....	20
1.5. Motivation and scope	23
1.5.1. Objectives	27
Chapter 2.....	30
2. Experimental Methods.....	30
2.1. Burner development	31
2.1.1. Development of a Impinged Jet Combustor	31
2.1.2. Development of Bluff Body Combustor	33
2.2. Measurement methods.....	35
2.2.1. Flow rate measurements	35
2.2.2. Acoustic measurements	35
2.3. Optical measurement technique	35
2.3.1. Chemiluminescence measurements	36
2.3.2. Planar laser induced fluorescence (PLIF).....	44
2.3.2.1. Heat release imaging measurements.....	46
2.3.3. Simultaneous PLIF measurements for heat release imaging.....	47
2.3.4. Particle image velocimetry	51
2.4. Data processing	53
2.4.1. Determination of the flame response based on OH* chemiluminescence	53
2.4.2. Image analysis	53
2.4.2.1. Background noise correction	54
2.4.2.2. Flame surface calculation	54
2.4.2.3. Simultaneous PLIF of OH and H ₂ CO.....	55
2.4.2.4. Flame curvature	56
2.5. Chapter 2 Summary.....	58
Chapter 3.....	66
3. Laminar flame characterisation	66

3.1.	Characterisation of the burner	66
3.1.1.	Flow field visualisation – cold/hot flow	66
3.1.2.	PIV measuring conditions	67
3.1.3.	PIV accuracy and uncertainty	68
3.1.4.	Laminar flame speed determination	69
3.2.	Results and Discussions	71
3.2.1.	Methane/carbon-dioxide/air.....	71
3.2.2.	Methane/carbon-monoxide/hydrogen air mixture	74
3.3.	Heat release measurements for methane and biogas	77
3.4.	Chapter 3 Summary.....	81
Chapter 4.....		93
4.	Turbulent flame characterisation	93
4.1.	Cold Flow Characterisation.....	93
4.1.1.	Acoustic characteristics	93
4.1.2.	Cold Flow visualisation	95
4.2.	Reacting Unforced Flow	100
4.2.1.	Behaviour of different premixed flames using OH* chemiluminescence.....	100
4.2.2.	OH and H ₂ CO PLIF measurements of premixed methane/carbon-dioxide/air flames without swirl	103
4.2.3.	OH and H ₂ CO PLIF measurements of premixed methane close to blow-off	108
4.3.	Chapter 4 Summary.....	110
Chapter 5.....		128
5.	Forced Response of turbulent Bluff-body CH ₄ /CO ₂ /H ₂ flames	128
5.1.	Periodic heat release rate response and experimental conditions	128
5.1.1.	Heat release rate response of methane air flames.....	129
5.2.	Heat release response of methane flames.....	132
5.2.1.	Frequency and amplitude dependence of the flame response	132
5.2.2.	Effect of equivalence ratio.....	136
5.3.	Biogas Combustion	137
5.3.1.	State of the art related to biogas combustion.....	139
5.4.	Syngas Combustion.....	142
5.4.1.	Flame response of syngas flames	142
5.5.	Chapter 5 Summary.....	145
Chapter 6.....		170
6.	Conclusions & Suggestions for Further Research	170

6.1. Summary of various conclusions	170
6.1.1. Development of the impinged jet burner, laminar flame speed and heat release rate measurements.....	170
6.1.2. Development of the bluff-body combustor and Heat Release Measurement in turbulent unforced flames	172
6.1.3. Heat Release measurements for methane, biogas and syngas flames subjected to velocity perturbations.....	173
6.2. Future work	174
List of publications:	I
Reference:	II

List of Figures

Figure 1-1: Laminar Bunsen Flame (left) a typical laminar flame (middle) flame front detection depending of measuring technique (right) cone angle (Natarajan et al. 2007).....	28
Figure 1-2: Left: Schematic of a typical thermal structure of a premixed flame (Kuo, 1986) & Right: S R Turns (2000).....	28
Figure 1-3: Stagnation flame stabilisation (Law et al. 1984).....	29
Figure 1-4: Premixed combustion regime diagram (Borghi diagram). Loglog graph of the relative intensity of turbulence (u'/S_L) vs. the relative large-eddy size of turbulence. The bold lines separate the combustion regimes (Borghi , 1985).....	29
Figure 2-1: Schematic of the stagnation burner	59
Figure 2-2: Model Gas turbine.....	59
Figure 2-3: Typical OH PLIF image of Bluff-Body stabilised flame.....	60
Figure 2-4: (left) Open & (right) Enclosed instantaneous OH PLIF image	60
Figure 2-5: (left) Unforced and (right) forced pure methane flame OH PLIF images	60
Figure 2-6: Frequency response due to acoustic forcing	61
Figure 2-7: Intensity of different chemiluminescence species (Lee & Santavicca, 2003)	61
Figure 2-8 : Fuel intensity with Equivalence ratio variation (Lee & Santavicca, 2003)	62
Figure 2-9: Reaction path of H_2CO (Haber, 2000)	62
Figure 2-10: Chemiluminescence spectra of premixed pure methane (Haber, 2000)	63
Figure 2-11: Spatial distribution of OH, H_2CO , Heat Release and Heat Release Rate (HRX) based on $[OH] \times [H_2CO]$	63
Figure 2-12: Numerical Chemkin of Methane and Biogas at equivalence ratio 0.6.....	64
Figure 2-13: Theoretical Heat Release versus Heat Release Rate (HRX) based on $[OH] \times [H_2CO]$ correlation	64
Figure 2-14: (left) Shows an instantaneous OH PLIF image, (middle) Its corresponding flame surface contour, and (right) the average of the flame surface.....	65
Figure 3-1: Strain rate calculation using different seeding particles and velocity field (Bottom right).....	82
Figure 3-2: (Top left) Effect of co-flow on the velocity profile (Bottom) with the same bulk velocity, Pure Methane air, equivalence ratio 0.825.....	83
Figure 3-3: Flame speed measurement of Pure Methane flame at equivalence ratio 0.75, Difference between numerical and experimental of 0.88%	84
Figure 3-4: Flame speed measurement of biogas (60% CH_4 & 40% CO_2) flame at equivalence ratio = 0.95, Difference between numerical and experimental of 5.6%	85
Figure 3-5: Laminar Flame Speed measurement of syngas with composition 50/25/25, equivalence ratio = 0.67, Flame speed = 26.89 cm/s	86
Figure 3-6: Laminar Flame Speed measurement of syngas with composition 50/35/15, Equivalence ratio = 0.7, Laminar flame speed = 32.5 cm/s.....	87
Figure 3-7: Laminar Flame Speed measurement of syngas with composition 25/50/25, Equivalence ratio = 0.58, Laminar flame speed = 29.54 cm/s.....	88
Figure 3-8: Strain rate of different syngas composition	89
Figure 3-9: Laminar flame speed of multi component fuels based on measurement with respect to equivalence ratio	90
Figure 3-10: FWHM H_2CO variation with change in bulk velocity.....	91

Figure 3-11: (left) FWHM H ₂ CO variation and (right) HRX with equivalence ratio	91
Figure 3-12: Effect of CO ₂ Dilution on HRX.....	92
Figure 3-13: Spatial distribution of HRX based on numerical model (left) and experimental results (right).....	92
Figure 4-1: Resonance frequency of the bluff-body combustor	112
Figure 4-2: Velocity field of the bluff-body combustor at 250 lpm	112
Figure 4-3: Phased locked vortex evolution – vorticity plot.....	113
Figure 4-4: Velocity field of unforced flow for different swirler	114
Figure 4-5: Velocity plot at 5 mm above the bluff-body for an unforced flow with different swirler	115
Figure 4-6: Comparison of the velocity magnitude 5 mm above the bluff-body for different swirler	116
Figure 4-7: Phased lock forced flow for different swirler Phase Angle 0 -60 -120 -180 -240 -330.....	117
Figure 4-8: Numerical laminar flame speed measurements	118
Figure 4-9: OH* chemiluminescence variation for different biogas composition with respect to bulk velocity.....	118
Figure 4-10: OH* chemiluminescence variation with respect to change in equivalence ratio	119
Figure 4-11: Instantaneous OH PLIF and FS (left) & Average OH PLIF and FS (right)	119
Figure 4-12: FS Variation with bulk velocity	120
Figure 4-13: Turbulence intensity variation at various flow rates	120
Figure 4-14: Curvature of Pure Methane Flames at different Bulk Velocity	121
Figure 4-15: FS of Pure Methane Flame at various bulk velocities with increasing bulk velocity from left to right – FS calculation of Pure Methane flames showing the effect of wrinkling along the flame front due to an increasing bulk velocity (increasing bulk velocity from left to right, 120 lpm, 250 lpm & 330 lpm).....	121
Figure 4-16: Cold flow visualisation of length scales at 250 lpm with a 20 mm interrogation window above the bluff-body	122
Figure 4-17: Length scales at 250 lpm (top left), 300 lpm (top right) & 350 lpm (bottom middle)	123
Figure 4-18: Curvature comparison of Methane and Biogas flames at various bulk velocities	124
Figure 4-19: OH* & HRX variation with equivalence ratio.....	125
Figure 4-20: OH* chemiluminescence with corresponding HRX at different equivalence ratio 0.7 – 0.85, overall bulk velocity 250 lpm	125
Figure 4-21: Analysis of HRX at top location of the bluff-body.....	126
Figure 4-22: Analysis of HRX at bottom location of the bluff-body	126
Figure 4-23: Biogas OH* and HRX measurements for varying equivalence ratio 0.7 -0.85, overall bulk velocity of 250lpm.....	127
Figure 4-24: OH* & HRX for biogas at different equivalence ratio	127
Figure 5-1: HRX measurement for Phased Average of Pure Methane, f = 315 Hz & A = 0.5, equivalence ratio of 0.75	147
Figure 5-2: HRX measurement for Phased Average of Pure Methane, f = 315 Hz & A = 0.9, equivalence ratio of 0.75	148

Figure 5-3: Phased Average of Pure Methane at 30 degrees Phase Angle – Representing the formation of a new vortex as the previous one collapses – $f = 315$ Hz & $A = 50\%$	149
Figure 5-4: Typical FS of an unforced Pure Methane flame, equivalence ratio of 0.75	149
Figure 5-5: Phased Average FS calculation for $f = 315$ Hz and $A = 0.9$, equivalence ratio of 0.75.....	150
Figure 5-6: Normalised Phased average over one complete cycle of HRX & FS Pure Methane, $f = 315$ Hz, $A = 50\%$	150
Figure 5-7 : (Left) Flame response (Right) Flame transfer function showing the amplitude dependence of pure methane at $f = 315$ Hz at equivalence ratio = 0.75	151
Figure 5-8: Flame response from chemiluminescence measurements and FS calculations at $f = 255$ Hz (figure on the left), 315 Hz (figure on the right) and varying A	152
Figure 5-9: HRX images at $A = 0.1, 0.2, 0.5$ & 0.9 , $f = 315$ Hz, equivalence ratio of 0.75..	153
Figure 5-10: Cyclic FS calculation for $f = 255$ Hz and varying A , equivalence ratio of 0.75	154
Figure 5-11: FS calculation of Pure Methane at highest amplitude of forcing $f = 255$ Hz (figure on the left) & $f = 315$ Hz (figure on the right), equivalence ratio of 0.75	154
Figure 5-12: Pure Methane flame response $f = 30$ Hz (Top Left), 255 Hz (Top Right) & 315 Hz (Bottom Left) at varying equivalence ratio and A	155
Figure 5-13: Pure Methane flame response with varying equivalence ratio at $f = 30$ Hz (Top Left), 255 Hz (Top Right) & 315 Hz (Bottom Left) for overall bulk velocity = 250 lpm, & 300 lpm	156
Figure 5-14: HRX & FS for $f = 315$ Hz and $A = 90\%$, equivalence ratio of 0.75.....	157
Figure 5-15: Phase angle variation in regions, equivalence ratio of 0.75.....	157
Figure 5-16: Pure Methane $f = 30$ Hz (Top Left), 255 Hz (Top Right) & 315 Hz (Bottom Left) at equivalence ratio = 0.8 – Air bulk velocity = 250 lpm, 300 lpm & 350 lpm.....	158
Figure 5-17: Comparison of Natural gas and Biogas.....	159
Figure 5-18: Biogas flames $f = 30$ Hz (Top Left), 255 Hz (Top Right) & 315 Hz (Bottom Left) at varying equivalence ratio	160
Figure 5-19: Flame response of Pure Methane and Biogas Flames at laminar flame speed of 19 cm/s.....	161
Figure 5-20: Flame response of Pure Methane and Biogas Flames at laminar flame speed of 23 cm/s.....	162
Figure 5-21 Flame response of Pure Methane and Biogas Flames at laminar flame speed of 19 cm/s, air bulk velocity of 300 lpm	163
Figure 5-22: Phased Resolved HRX Pure Methane & Biogas Flames at the same laminar flame speed and A	164
Figure 5-23: Comparison between Pure Methane swirl and no Swirl at the same forcing amplitude and phase angle, at equivalence ratio of 0.7	164
Figure 5-24: Flame Response of Swirl Methane and Syngases (methane/carbon-monoxide/hydrogen) of varying composition, at the same equivalence ratio of 0.7.....	165
Figure 5-25: Comparison between Pure methane swirl and no swirl at the same forcing amplitude.....	166
Figure 5-26: HRX Methane and Syngas (methane/carbon-monoxide/hydrogen) at Phased angle 90 & 135 degrees at the same forcing amplitude equivalence ratio of 0.7	166
Figure 5-27: HRX Phased resolved swirl Pure Methane flames at 45 degrees phase intervals, at equivalence ratio of 0.7	167

Figure 5-28: HRX Phased resolved Syngas 25:50:25 (methane/carbon-monoxide/hydrogen) at 45 degrees phase angle, at equivalence ratio of 0.7 168

Figure 5-29: Normalised Syngas (methane/carbon-monoxide/hydrogen) mixtures with their respective laminar flame speed and the unforced vertical velocity fluctuation..... 169

Table of Tables

Table 3-1: Flame height and overall bulk velocity with respect to change in equivalence ratio for pure methane	77
Table 3-2: Flame height and overall bulk velocity at constant equivalence ratio for pure methane	78
Table 3-3: Overall bulk velocity at different carbon-dioxide dilution.....	78
Table 4-1: Summary of experimental conditions.....	108

Nomenclature:

Variables:

S_1 – Laminar flame speed

HRX – Heat Release Rate

FS – Flame surface

ϕ - Equivalence ratio

$w/\langle U \rangle$ – Normalised velocity fluctuation

OH – Hydroxyl

H₂CO – Formaldehyde H₂ – Hydrogen

CH₄ – Methane

N₂ – Nitrogen

NO_x – Nitrogen oxides

CO₂ – Carbon dioxide

CO – Carbon Monoxide

Units:

slpm – Standard litres per minute

mm – millimetres

μm – micrometres

nm – nanometres

Hz – Hertz

W – Watts

Pa – Pascals

V – Volts

s – seconds

Chapter 1

1. Introduction

The potential of renewable energy sources is enormous as in principle it can meet many times the world's energy demand. A transition towards renewable based energy is looking increasingly likely due to the greater demand for energy as well as financial cost of producing fossil based fuels. It is becoming clear that the future growth in the energy sector will be primarily in the new regime of renewable sustainable energy. Because of these new developments, opportunities now exist in the usage of existing gas turbine technologies or the design of new gas turbine systems to accommodate for the sustainable fuels. It is also important that low emissions are achieved to comply with increasingly strict governmental regulations. The use of renewable energy source and its implementation can enhance diversity in energy supply markets, contribute to securing long term sustainable energy supplies, help reduce local and global atmospheric emissions, and provide commercially attractive options to meet specific energy needs, particularly in developing countries and rural areas helping to create new employments technologies there.

Biogas, syngas and oxyfuels are example of fuels which are considered as viable sustainable fuels that could power modern low emission gas burning combustion systems. But, due to the complexity of the interactions between flame chemistry and turbulent flow fields in gas turbines, an important question is whether reliable operation with those sustainable fuels will be possible. Therefore the optimal operation of such combustion devices relies heavily on trial and error experiments, and increasingly on computational fluid dynamic (CFD) tools using turbulent flame models to predict the behaviour (Armitage et al. 2006). Such CFD models are based on the combustion mechanisms with the aerodynamics of the flow field in order to estimate the structure and response of the flame operating in different turbulent regimes. However, the developments of the detailed chemistry modelling of the industrial gas turbines with complex geometries are computationally expensive and demanding, therefore, these flame models rely on experimental information from small-scale combustors with simple geometries for their developments and validations. Laboratory scale combustors have shown

to have idealised geometrical configurations while retaining features that are relevant to industrial systems (Balachandran 2011; Kutne et al. 2011).

One critical problem however still remains, which is the lack of available data that describes the combustion properties of different sustainable fuels. The diverse composition of all the different fuels leads to significant variations in the combustion properties. Therefore, it is key to have information about fundamental properties like the flame speed, reactivity and flammability as these will influence the key combustion characteristics such as flame spatial distributions, generally referred as flame shape, flashback and blowoff. Other important criterias are the point of flame anchoring, flammability range, flame propagation and sensitivity to perturbations. Without the adequate information in the form of experimental and numerical databases it will be hard to predict all of the aforementioned criteria in order to maximise the fuel efficiency or even to prevent failure of the plant.

The substantial variations in composition from fuel to fuel primarily due to differences in production methods and sources are among the largest barriers towards introducing fuel flexibility in combustion systems. Different research groups have made attempts in understanding those fundamental combustion properties for different laminar and turbulent combustion flames. Scholte et al. (1959), Gunther et al. (1972) Vagelopoulous et al. (1994), Hassan et al. (1997), Ren et al. (2001), Natarajan et al. (2007), Das et al. (2011) and Wu et al. (2012) are among those who studied the effect of temperature, pressure and presence of different inert or reactive components on the laminar flame speed of syngas (H₂/CO) mixtures. As laminar flame speed is an important parameter of a combustible mixture as it contains fundamental information on reactivity, diffusivity, and exothermicity. Knowledge about the laminar flame speed is very beneficial in order to predict the burning rate in turbulent combustion modelling and engine design. Because of the significance of laminar flame speed information, substantial experimental work has been devoted over the years to develop methodologies for accurate determination of laminar flame speeds. One of the difficulties in determining the laminar flames speed is to achieve a planar, stationary, and adiabatic flame and the determination of the flame front. Therefore several methods of determining the flame speed has been devised and although there are no general consensus on the best approach used to measure the laminar flame speed, spherical bombs and stagnation flames are currently considered to be the most systematic and accurate approaches (Zhao et al. 2004). Other studies by Gibbs & Calcote, (1959), Daly et al. (2001). Zhao et al. (2004) and Cheng et al. (2011) used the same aforementioned approach to measure the laminar flame speed of dimethyl ether air

mixtures. The experimental data obtained by the different research groups were mainly used as a method to validate computational models so that it could be used to predict more accurately the laminar flame speed for a range of equivalence ratio. Although the laminar flame speed provides an insight on the fundamental combustion properties, it doesn't provide an answer to whether or not that sustainable fuels will be a suitable substitute to the current fuel used in gas turbine combustion, particularly without reduction in power output/throughput.

In order to meet the stringent pollutant control measures, lean burning has been adopted in gas turbine combustion. Lean combustion system has many advantages which are mainly fuel economy and lower pollutant emissions. However, lean systems are often susceptible to acoustic combustion oscillations (Dowling 1995; Balachandran et al. 2005). Combustion oscillations are a consequence of the sensitivity of combustion processes due to the pressure and velocity fluctuations. Often during lean burn mode of operation, these systems experience complex resonant feedback interaction between the heat release rate perturbation in flames and the different acoustic modes which can cause pressure and flow oscillations. Experimental observations from Poinso et al. (1987), Schadow & Gutmark, (1992), Wu et al. (2003) and Balachandran et al. (2005) examined the role the various phenomena plays in this complex process. During the combustion process the presence of mixture and flow inhomogeneities produce unsteady heat release. The unsteady heat release produces sound and in an enclosed region (i.e. the combustor) the sound can reflect back from the wall of the combustor therefore interacting with the combustion process. The interaction between the acoustic modes of the combustor and the heat release fluctuations can add or remove energy from the acoustic mode. The condition under which heat release fluctuations could amplify the pressure oscillations was first stated by Rayleigh, 1945. Rayleigh stated that the amplification or attenuation of the pressure oscillations by heat release fluctuations would occur if the periodic heat release occurs in or out of phase with the pressure oscillations respectively.

Among the various mechanisms that can trigger interactions between acoustic oscillations and heat release, the following mechanisms are notable: flame-acoustic wave interactions, flame vortex interactions, flame-wall interactions and the effect of unsteady stretch rate (Dowling & Hubbard 2000; Lieuwen & Zinn 1998; Balachandran et al. 2005). Instabilities can also be driven by the unmixed nature of a fuel-oxidiser mixture (Balachandran et al. 2005). The pressure oscillations in the combustor can interact with the supply line, leading to oscillations in the fuel flow rate. The fuel flow oscillations may also influence air flow oscillations. The combined oscillations in the fuel and air can then lead to equivalence ratio fluctuations. These

fluctuations of equivalence ratio will result in heat release fluctuations, sustained by feedback of pressure/velocity fluctuations. These pressure and flow oscillations may often lead to excessive vibrations which can eventually result in structural damage. Therefore it is key to understand the sensitivity of the fuel and its behaviour in a turbulent enclosed environment. Part of the study was to observe the effects of combustion oscillations of different fuel mixtures to velocity perturbations on a turbulent flame stabilised on a laboratory scale model gas turbine. Fuel mixtures with similar laminar flame speed at a given equivalence ratio to conventional fuel were investigated. From which a relationship between the laminar flame speed and the dynamic response of flames of different fuel were studied.

As part of this study, a burner capable of measuring the laminar flame speed of multi components sustainable fuels was developed. The laminar flame speed measurements were used as a ground for comparison between commonly used natural gases. The impact of different components present in the fuel mixture on laminar flame speed will further help the understanding of the combustion chemistry. The work carried out here hope to further the understanding of the dynamic behaviour of multi-components fuels which in turn can provide an insight as to whether those fuels can be interchanged for the purpose of gas turbine combustion.

A detailed analysis of the instantaneous reaction zone of a turbulent flame reveals thin flame fronts which can be likened to that of laminar flames and are often referred to as ‘flamelets’. Therefore the following sections will discuss the structure and chemical mechanisms of laminar premixed flames. Also the importance of flame speed and different techniques for laminar flame speed measurements are discussed. Along with the laminar flame speed, the concept of flame thickness are introduced and employed to describe the different regimes encountered in turbulent combustion. A literature review of non – intrusive measurement technique is described, emphasising on the different methods of experimentally measuring the heat release rate. This will be followed by a review on the challenges encountered during combustion of different fuel mixtures such as biogas. The last part of this chapter will review the type of fuels used experimentally and also identify the gap within the research with regards to specific fuel composition.

1.1. Literature review

1.2. Flames characterisation

Flames can be classified essentially in two different ways, which is dependent on how the reactants are brought together. In the one case, the fuel and oxidiser are supplied separately and the flame is formed at the location where they meet. The combustion processes is highly dependent on the rate of the diffusion of the fuel and the oxidiser. These types of flames are generally referred to as diffusion flames or non-premixed flames. Flames can also be produced with the reactants mixing well before the combustion happens and such flames are called premixed flames. Premixed flames have altogether different characteristics from non-premixed flames. Lewis & Holbe, (1931) described those flames as combustion waves, as they propagate in the direction normal to themselves at a constant flame speed. Both diffusion and premixed modes are used in many combustion systems such as power generation, aero-propulsion, the automotive industries, water and space heating and have a variety of industrial applications. While it remains relatively simpler to design combustion systems to use diffusion flames, there are issues in regards to pollution and those flames are not easily controlled. Therefore combustion systems that use premixed flames have been commonly favoured.

Flames can be further classified as laminar or turbulent. Laminar flames studies do not only provide a deeper understanding of the behaviour of laminar flames but also turbulent ones. Provided the level of turbulence isn't too high, such turbulent flames often behave like perturbed laminar ones. It follows that a detailed study of the chemistry of laminar flames will provide useful information which is applicable to a variety of premixed flames. Laminar premixed flames can be characterised by a narrow reaction zone measuring a few millimetres in thickness at atmospheric condition. They propagate or stabilise by the combining effects of the heat flux and species diffusivity across the reaction zone; both as a result of a large temperature gradient due to the exothermic nature of combustion chemistry. In laminar premixed combustion, the most important property is the laminar flame speed, S_L . The laminar flame speed can be defined as the velocity that a planar flame front travels relative to the unburned gas in a direction normal to the flame surface. When an unburned fuel-oxidiser mixture travels with velocity U_g , the flame front propagates with velocity S_L in the unburned mixture. The flame is said to be stable when the fuel oxidizer velocity U_g is equal to S_L . Figure 1-2 shows the trend in the profiles of the reactants and products temperature across the flame

front of a laminar premixed flame. From the picture it can be seen that the flame front is divided into two regions, which are the preheat zone and the reaction zone.

In the preheat zone the temperature is relatively low, consequently the reaction rate is low and as a result the convection is balanced by diffusion. In this region low temperature reaction takes place which involves the production and the consumption of species such as formaldehyde. On the other hand, in the reaction zone the temperatures are high and can be further subdivided into a thin region of fast chemistry, followed of a much wider region of slow chemistry. The destruction and the formation of many intermediate species occur in the fast chemistry region which is dominated by bimolecular reactions.

The major exothermic chemical reactions only occur in the reaction zone releasing heat which is convected to the reactants through the preheat zone. Therefore it can be said that the laminar flame speed not only provides an insight on the stability of the flame but also on other parameters such as the reactivity, diffusivity and exothermicity.

1.2.1. Laminar flame speed measurement technique

The commonly adopted method of studying flame chemistry is through the simulations of laminar, one dimensional flames. Complex chemical kinetic reaction schemes are designed for the use in simulations, and the results are then validated against experimental laminar flame speed data. Therefore accurate measurements are needed in order to acquire such experimental data as it plays a key role in understanding a large range of flames.

As mentioned above, one distinguishing feature of laminar premixed flames is that they have a characteristic propagation rate and the accurate measurement of this characteristics is essential. To date there are no satisfactory or unified computational model to predict this property for multi components fuels based on chemical kinetic data alone. The continuing effort to accurately measure the flame burning rate has been an area of interest to many scientists for decades and it can be dated back to 1815 in the work carried out by Sir Humphrey Davy.

The first systematic measurements can be attributed to the work by Bunsen in Germany in 1866. A gas mixture was made to flow through a tube and out of an orifice. A flame was stabilised at the orifice and the flame speed was defined as the flow in the tube which was low enough so that the downward velocity of the flame front just exceeded the upward velocity of the gas mixture at the point of flashback. The flame speed was determined from the volumetric flow rate by assuming a constant velocity at the exit of the tube. Experimental flame speed values of 34 ms^{-1} for pure hydrogen at stoichiometry were obtained.

Bunsen method of measuring laminar flame speed was adopted by Gouy in 1879 where he used the shape and size of the flame to measure the flame speed. In his paper, Gouy provided the equation $V = v \sin\alpha$ where V is the burning velocity, v is the gas velocity and α is the angle between the flow direction and the flame surface. Gouy estimated the area of several Bunsen flames on burners of different diameters by projecting the image onto a screen. His main objective was to show that the burning velocity was constant over the flame surface. The flame speed can be estimated by dividing the flame surface area by the volumetric flow. One of the main challenges that Gouy encountered was measuring the flow rate accurately. Further experimental work using the same principle was reported by Mallard & Le Chatelier, (1883) and Michelson, (1889) which said that the burning velocity was dependent on flame curvature. However he found that any dependence on curvature was less than the experimental error.

Therefore, in order to obtain accurate measurements of flame speed using the Bunsen method there are several factors that need to be considered. The flame shape is influenced by the velocity profile at the exit of the burner tube and heat loss to the tube wall. In order to maintain the uniform velocity profile, higher tube lengths must be used to ensure a fully developed flow at the exit. For a stationary Bunsen flame a mass balance across the flame can provide an expression for the burning velocity.

$$S_L = U_g \frac{A_t}{A_F} \quad \text{Equation 1-1}$$

Where U_g is the average flow velocity in the tube, A_t is the tube cross sectional area and A_F is the conical surface area of the flame which can be determined using different flame visualisation techniques. Although a simple method to apply, the challenge still remains of accurately determining the flame surface area. Depending on the optical technique used the conical area calculated can have a variation of up to 10%. The three methods that are widely used to visualise the flame front are:

- Luminous photography
- Shadowgraph photography
- Schlieren photography

In luminous photography, the luminous part of the flame is observed which occurs towards the burnt side of the flame. Therefore this method does not provide a very accurate burning velocity representation as the fundamental burning velocity is defined as the speed of the flame front with respect to unburned gas. On the other hand shadowgraph and schlieren are two special flame photographic methods which use basic physical phenomena. In shadowgraph, the flame is located corresponding to the second derivative of the density which attains a highest value closer to the inflexion point of the temperature profile. Therefore, the shadowgraph measures the variation of flame front but does not specify a surface precisely. However Schlieren's method the flame surface corresponds to the maximum gradient density which is closest to the unburnt mixture. That is the reason why Schlieren's method is the preferred technique for locating the flame surface. Also in the flame tip stretch effect occurs, which can in turn influence the laminar burning velocity. At the base of the flame heat loss of the exit rim of the burner has an effect on the laminar burning velocity.

Another way to determine the laminar burning velocity is to use the flame angle method as mentioned by Gouy, (1879). In this method, the angle suspended by the flame edge to the unburned incoming flow velocity in the shoulder region of the conical flame is measured and the flame speed is calculated by:

$$S_L = U_g \sin \alpha \quad \text{Equation 1-2}$$

Where U_g is the unburnt gas velocity and α is the half cone angle as shown in Figure 1-1. The conical stabilised flame configuration is preferred over a straight cylindrical tube burner for the following reasons:

- The exit velocity profile of a long cylindrical tube is parabolic and hence the flame angle to the incoming flow varies along the flame height
- On the other hand a contoured nozzle produces a nearly uniform exit velocity profile which gives a fairly straight edge along the shoulder of the flame to determine the half angle more accurately.

The main drawback apart from the stretch mentioned previously is that the measurements are highly sensitive even to the small divergence in the streamline approaching the flame.

In 1883, while experimenting with Gouy's method, Mallard and Le Chatelier came up with a new tube method. In this method a tube was filled with a fuel/air mixture and then ignited at an open end. The uniform speed at which the flame propagates towards the close ends was taken as to be the burning velocity. The results were very close to those obtained by Bunsen and they also proposed an improved theory. From this point onwards subsequent experimental work was divided into two groups. Measurements on stationary flames using Gouy's method or a derivative of it or measurements of a propagating flame using the tube method (Wheeler et al. 1914; Coward & Hartwell 1932), and later in spherical vessels proposed by Stevens (1926). Stevens enclosed the air/fuel mixture in a spherical soap film which acted as a constant pressure bomb and found that the speed of the expanding spherical flame was constant. Later, Steven's work was revised by Lewis and von Elbe in 1928, in which they pointed out the simplicity and directness of the method and that it eliminated some of the disadvantages of flame speed in a tube. But on the other hand it had a major limitation whereby it could not be used for gases that are affected by the soap film.

Law et al. (1984) revisited the concept of flame stretch and gave a good description of the fundamental concepts. They also introduced a methodology for subtracting both the flame stretch and flow divergence effects in order to obtain the true, one dimensional burning velocity. They proposed the use of the stagnation flame method as a method by which the flame stretch can be subtracted. The stagnation flame approach is a method by which a steady one dimensional laminar flame is stabilised in a well-defined stagnation flow field. The stagnation flow field is achieved either by impinging two identical nozzle-generated nozzle flows or impinging a generated flow with a solid wall. The stretch imposed is due to the non-uniformity of the upstream flow or hydrodynamic strain. The flame speed and the imposed strain rate on the flame are determined from the axial velocity profiles across the flame (Law et al. 1985).

Typically the axial velocity decreases from the nozzle exit due to the presence of the stagnation plane and it reaches a minimum before flame (Figure 1-3). As the flow enters the flame, due to preheating and thereby thermal expansion, the axial velocity increases and reaches a maximum after the peak of the heat release. After the heat release region the axial velocity is reduced to zero at the stagnation plane. The unburned strain flame speed S_u is generally referred to as the minimum velocity before the preheat zone and the maximum gradient of the axial velocity ahead of the minimum velocity location is taken as the imposed strain rate (k). The influence of strain on the flame speed S_u is subtracted by evaluating the flame speeds at various strain rates and taking advantage of the linear relationship between the flame speed and the imposed strain.

$$S_L = S_u^o - L_m k \quad \text{Equation 1-3}$$

S_u^o = Unstrained flame speed which is obtained from linearly or non-linearly extrapolating the strained flame speed to zero strain rate

L_m = Markstein length or strain sensitivity

Like the spherically expanding flame this method measures the stretch corrected unburned flame speed and also the strain sensitivity of the fuel mixtures. But in cases where the effect of high preheat temperature on stretch flames are investigated the stagnation flame approach is the preferred method of measurement. This is mainly is due to the fact that the inflowing premixed gases in the stagnation flame can easily be set to desired uniform temperature. Whereas in the case of the spherical expanding flame, it is difficult to maintain a stationary

combustion region with a uniform reactant temperature profile. Heat transferred to and from the wall of the combustion bomb will tend to produce a non-uniform profile.

The downside of using this approach to measure the laminar flame speeds are:

- The complexity and practicality for measurements under adverse conditions such as high pressure and temperature
- The time factor associated with each measurement compared to the Bunsen burner method. It is a lot simpler and faster to measure the flame speed for wide range of operating conditions

The stagnation wall method was also employed by Zhao et al. (2004) in an attempt to determine the laminar flame speed in nitrogen diluted propane/air. The flow velocity was obtained from particle image velocimetry. As it was previously mentioned the laminar flame speed was obtained by using linear or non-linear extrapolation to zero stretch. They reported in their findings that the stagnation wall method allows the determination of the flame speed at considerably lower strain rates than are typical of data obtained using opposed-jet configuration. Lower strain rates are critical to obtaining a reliable extrapolation since the strain rate and flow velocity determination each have statistical experimental uncertainties. Their results show that the laminar flame speeds for propane/air mixtures agree well with modelling based on the detailed mechanism of propane oxidation. Both the data and model predictions have revealed linear relationship between the laminar flame speed and the dilution ratio.

Natarajan et al. (2007) used the stagnation approach to measure the laminar flame speed of strain sensitive mixtures of hydrogen/oxygen/nitrogen mixture at high preheat temperature (700K). The burner is formed from a smoothly contoured nozzle with high contraction ratio (the ratio of the cross-sectional area at the nozzle inlet to that of the plenum), in order to create a uniform velocity profile at the burner exit and a uniform flame stretch throughout the flame area. The advantage of having a high contraction ratio is that a laminar flow is maintained even at high Reynolds number based on the burner exit diameter. The flame speed obtained from the measurements were in reasonable agreement with the computation models. The reason this method was used was because of the strain sensitivity of the reactants and its effect on the resulting laminar flame speed. Furthermore this method is advantageous for the following reasons (Natarajan et al. 2007):

1. The use of a solid wall leads to more stable flames

2. Problems related to heating of the upper burner are eliminated
3. The use of a single jet greatly simplifies the burner operation

Law et al. (1985) also investigated the effect of the stagnation surface on the data recorded. The apparatus they used consisted of a uniform flow nozzle and a stagnation plate positioned about one nozzle diameter above the exit. The plenum chamber was 100 mm diameter and reduced to a nozzle with interchangeable exit diameters of 40, 30, 20, 10, 7 and 5 mm. The flow velocity was measured using a TSI LDV system with 1 μm MgO particle seeding and measuring a volume of 0.1 mm diameter x 0.9 mm length. In the presence of the stagnation plate the pressure field and velocity profile are modified, producing a slightly dish-shaped flame when it is not close to the stagnation plate. The centre portion of the flame can however be considered to be planar and perpendicular to the central streamtube. To ensure that the experimental results were not affected by the specific nature of the stagnation surface, the cooled brass plate was replaced with either a counterflow of cold air, cold nitrogen, or an opposed flame.

As in the case of the wall stagnation configuration, the counterflow burner achieves a stable flat flame due to flame stretch (the presence of an axial velocity gradient). First after leaving the nozzle the cold jet decelerates but after reaching the preheat zone thermal expansion of gas creates acceleration of the stream which is followed again by deceleration again after the reaction zone. Finally the axial velocity reaches zero at the stagnation plane. Due to the conservation of mass the radial velocity is constantly growing downstream. However, in the reaction zone the radial velocity component is still small therefore the counterflow flame configuration is often considered as one-dimensional.

In all of the cases the minimum velocity was observed at the flame and that the burnt gas temperature immediately after the flame remained unchanged. Also it was noted that the boundary layer effect was negligible as long as the flame is not too close to the stagnation surface.

All the techniques described for laminar flame speed measurement have its advantages as well as its disadvantages. The two acceptable methods of flame measurement as seen through the literature survey are the spherical expanding method and the impinged jet configuration. For the purpose of the study the impinged jet configuration is employed. As previously mentioned the spherically expanding flame is suitable for high temperature and pressure flame speed measurements but it has heat loss from the electrodes and suffers from gravity distortion

(Cheng et al. 2011). Also it is difficult to produce a stationary combustion bomb with a uniform reactant temperature profile, and while using the stirring methods to solve this problem will inevitably impart motion to the reactants voiding the important requirement for the bomb method. While on the other hand, the inflowing premixed gas in the stagnation flame can more easily be set to the desired uniform temperature. Also if the fuel mixture contain a significant amount of hydrogen, the flame is likely to develop spontaneous wrinkles due to the nonequidiffusive nature of the fuel mixtures (Natarajan et al. 2007). In the case of the stagnation flame approach these wrinkles can be suppressed by applying a sufficiently strong positive stretch. For these reasons the impinged jet configuration is utilised in this work to determine flame speeds across a wide range of conditions.

All of these fundamental flame properties, developed from the analysis of laminar flames can now be extrapolated so it can be used in the characterisation of the flame response to turbulent flows.

1.3. Turbulent Flames

Turbulent combustion involves a complex coupling of fluid dynamics and chemical kinetics over a wide range of spatial and temporal scales. Each instantaneous realisation is different from the next and none is identical to the average (Vagelopoulos et al. 1994). Therefore there is a need to have a deeper understanding of each of those quantities individually or simultaneously, as turbulent premixed combustion has a vast number of applications. They are encountered in many practical applications such as spark ignition engines, gas turbines found in both in the aerospace industry and stationary power systems. Due to the continuing efforts of many research groups especially the work by Peters and Williams (1987), resulted in the theory of turbulent premixed flames being accepted as an important topic of research within the combustion community. Experimental observations has shown that in general the structure of a turbulent premixed flame is to be seen as superimposed instantaneous contours of convoluted reaction zones. The position of the reaction zones move rapidly in space producing a time-averages view that gives appearance of a thick reaction zone, referred to as the flame brush. The appearance of the reaction zone depends heavily on the governing turbulent structures and chemical of the flow. The structure of the turbulent premixed flame depends can be described of various time, length and velocity scales. In order to classify the flame a combustion regime diagram is used, which is also known as the Borghi diagram (Figure 1-4). Factors differentiating the different regime will be discussed in the following section.

1.3.1. Turbulent flame characterisation

The turbulent flame does not only depend on the thermal and chemical properties (which are the case for laminar flame speed) but also on propagation velocity which in turn also depends on the characteristic of the flow and on the mixture properties. The effect of turbulence can be seen as distortion or wrinkling of the laminar flame front. This flame front locally propagates with a velocity S_L consistent with a plane laminar flame. On the other hand the turbulent flame speed S_t can be described as the velocity at which reactants enter the flame zone in a direction normal to the flame. In this definition, the flame surface is represented as some time-mean quantity \bar{A} recognising that the instantaneous flame front (with surface area A_{fl}) may be fluctuating wildly. Due to the difficulty in measuring the unburned gas velocities at any given point with the turbulent flame, the flame velocity is usually determined from the measurements of reactant flow rates. Therefore the turbulent flame speed can be expressed as

$$\dot{m} = \rho_u \bar{A} S_t = \rho_u A_{fl} S_L \quad \text{Equation 1-4}$$

Consequently the ratio of the turbulent flame speed to the laminar flame speed is equal to the ratio of the wrinkled area A_{fl} to the time-mean flame area \bar{A}

$$\frac{S_t}{S_L} = \frac{A_{fl}}{\bar{A}} \quad \text{Equation 1-5}$$

Due to the curvature of turbulent flame, the turbulent flame is quite complicated to be determined experimentally. Therefore the resulting measurement will have a considerable degree of uncertainty. A model was introduced by Damkohler and is expressed as:

$$\frac{S_t}{S_L} = 1 + \frac{u'}{S_L} \quad \text{Equation 1-6}$$

Further models were proposed however experimental measurements are required to verify their accuracy.

In turbulent flows there are a various length scales that exist ranging from the largest characteristics length scale down to the smallest Kolmogorov scale. There are also two intermediate length scales that are present and the significance of each of the length scales will be discussed individually. In decreasing order, the different scales are as follows:

L Characteristic width of flow or macroscale

l_0 Integral length scale

l_λ Taylor length scale

l_k Kolmogorov length scale

The macroscale L is the largest scale in the system and is the upper bound for the largest possible eddies, those of low frequencies. For example in a pipe flow the largest eddy would be equal to the pipe diameter and for a jet flow, L would be the local width of the jet at any axial location.

The integral length scale, l_0 physically represents the mean size of the large eddies in a turbulent flow. The integral scale is always smaller but of the same order of magnitude as L , and contributes to the greater part of the turbulent kinetic energy. The integral length scale is defined by means of the spatial correlation function, but the autocorrelation function is incorrect if the domain is insufficiently large. In practice, the spatial domain in an experimental or numerical investigation is limited by either restrictions in the experimental equipment or computational resources. Using the available spatial domain, an autocorrelation function is obtained from which the integral length is determined. The accuracy of the integral length is usually evaluated by comparing it to the spatial domain.

The Taylor length scale, l_λ is an additional length scale, intermediate in size between integral length scale and the Kolmogorov length scale but is weighted more towards the smaller scales. This length is representative for the dimension at which strain occurs in a particular viscous medium. This length scale is traditionally applied to turbulent flow which can be characterised by a Kolmogorov spectrum of velocity fluctuations. In such flows length scales larger than the Taylor length scales are greatly not affected by viscosity.

The Kolmogorov length scale, l_k represents the smallest eddies in the flow. These eddies rotate rapidly, have high vorticity, and exist only for a very short time before they vanish due to viscous dissipation. The large eddies break up in smaller ones; until the smallest Kolmogorov

eddies dissipate their kinetic energy into heat in the flow.

The flame thickness is a length scale associated with laminar flame structures in reacting flows. The laminar flame thickness characterises the thickness of a reaction zone controlled by molecular, not turbulent, transport of heat and mass. More detailed analysis have shown that the zone with high chemical reaction rates which includes the heat release, is confined to a narrow luminous zone at the high temperature side of the flame.

The basic structure of a turbulent flame is governed by the relationships of the turbulent length scales l_k and l_0 to the laminar flame thickness δ_L , displaced along the abscis of the graph. The relative intensity of turbulence (u' / S_L where u' – fluctuation velocity, S_L – laminar flame speed) is plotted on the ordinate. In the Figure 1-4, the regimes are separated by means of the bold lines. More explicitly, besides the laminar flames regime, four turbulent combustion regimes are defined by:

$\delta_L < l_k$ Wrinkled flames

$l_k < \delta_L \approx l_\lambda$ Thin reaction sheets

$l_\lambda < \delta_L < l_0$ Flamelets in eddies

$l_0 < \delta_L$ Distributed reactions

The aim of such a representation is to estimate the flame regime that might occur in practical combustion devices, provided that sufficient information is available characterising the turbulent flow field.

When the flame thickness is much thinner than the smallest scale of turbulence the turbulent motion can only wrinkle or distort the thin laminar flame zone. The criterion for the existence of a wrinkled laminar flame is sometimes referred to as the Williams-Klimov criterion. This regime is characterised by fast chemistry in comparison with the fluid mixing and the combustion occurs in thin wrinkled flame fronts. The turbulence intensity is of the same order of magnitude as the laminar flame speed. The bold line formed by setting $u' = S_L = 1$ defines roughly a boundary between a smooth and a corrugated flame surface. This regime lies in the wedge-shaped region between the strongly wrinkled (corrugated) flames and the flamelets in eddies regimes. As the intensity of turbulence goes up, and the thickness of a laminar flamelet exceeds the size of the smallest eddies in the flow the structure of the flame front changes in

that the corrugated flames form small tongues that move large distances and may eventually split off.

Thin reaction sheets

As such, a set of multiple, instantaneous burning thin reaction sheets are created in a zone where products and reactants co-exist, and the ensemble creates a wider time averaged flame brush. The condition that Karlovitz number greater than 1 (Ka is defined as the ratio of the characteristics fluid and chemical time scales) means that the smallest eddies can enter into the flame structure.

Many large-scale combustion applications such as fires, industrial furnaces and boilers, and marine diesel engines are expected to operate in the thin reaction sheets regime, depending on the specific operating conditions.

Flamelet in eddies:

This region is typified by moderate high turbulence intensities and Damkohler numbers (Da) which are dimensionless numbers used to relate the chemical reaction timescales with the transport phenomena rate. Also this region is of particular interest in that it is likely that some practical combustion devices operate in this regime. For example, a portion of the estimated region of spark-ignition engine combustion lies in the flamelets in eddies regime. In addition, the experiments of Ballal & Lefebvre, 1975 utilising premixed propane flames in a confined flow provide much of the experimental data related to this regime.

The reaction zone consists of short-lived parcels of reactants that are embedded in almost fully burned gas. The intrinsic idea behind the eddy-breakup models that the rate of combustion is determined by the rate at which parcels of unburned gas are broken down into smaller ones, such that there is sufficient interfacial area between the unburned mixture and hot gases to permit reaction.

The implication of this is that chemical reaction rates play no dominant role anymore in determining the burning rates, but, rather, turbulent mixing rates completely control combustion, i.e. $Da < 1$.

Application examples in this regime are to be found in rather compact applications with a high degree of turbulence, creating premixed flames that are to some extent dispersed in the confinement, a structure that is very likely to occur for $Da \leq 1$. Up to present, very little is

known with respect to this type of combustion and there is a lack of good theoretical models in this regime (Turns 2000).

Distributed reaction:

In order to enter this regime it is required that the integral scale length ($l_0/\delta_l < 1$) and the Damkohler are small ($Da < 1$). This will be difficult to achieve as it implies that l_0 must be small while on the other hand v'_{rms} is large, i.e, small flow passages at extremely high velocities. These conditions will be very hard to achieve in practical devices and also the inevitable pressure losses will render such a configuration impractical. Also, it is not clear that a flame can be sustained under these conditions (Turns 2000). Nevertheless by studying how the chemical reactions and turbulence might react in this regime may provide useful information since many pollutants formation reactions are slow and hence occur in the distribution regions.

It is clear that in order to have a better understanding of the behaviour of turbulent flames, the study of the length scales due to the flow process is very important. In addition to the length scales the importance individual components of the multi components fuels must not be overlooked. A lot of work has been carried out on methane flames under laminar and turbulent conditions but there is lack of information on the response of diluted methane combustion with carbon-dioxide (commonly referred to as simulated biogas) under force oscillations. The next section describes the reason behind the selection of biogas and the reason why a fundamental understanding of the flame response is required for gas turbines.

1.4. Challenges of Biogas combustion

Biogas is one of the sustainable fuels that could be utilised in natural gas burning combustion systems with minimum modifications. The growing popularity of biogas utilisation is due to ease of availability, but biogas composition can vary widely due to the large array of sources. These variations in composition can affect flame properties such as flame speed, heating value, adiabatic flame temperature, which in turn affect the flame dynamics. Flame dynamics in this work is described as the response in heat release rate to acoustic perturbations and can be represented as the flame transfer function (Hendricks & Vandsburger 2007). The variation in fuel compositions is also known to have a direct implication on the emission levels of pollutants. One commonly used strategy to combat pollutions levels, increasing efficiency and lowering fuel consumption is through lean premixed combustion. The major drawback of lean premixed combustion system is in its susceptibility to thermoacoustic instability. Thermoacoustic instabilities can be described as a closed loop between the heat release rate and the acoustic of the system.

Often during lean burn mode of operation, these systems experience complex resonant feedback interaction between the heat release rate perturbation in flames and the different acoustic modes which can cause pressure and flow oscillations. These pressure and flow oscillations may often lead to excessive vibrations which can eventually result in structural damage. Therefore a detailed understanding of the underlying physical mechanism is required in order to predict these instabilities so that mitigations or control method can be devised. Obtaining detailed knowledge of these instabilities have been an area of great interest in which intensive experimental (Veynante et al. 1994; Lee et al. 2000) and computational (Armitage et al. 2006) work has been carried out over the last two decades. And continuous advancement in diagnostics and computational methods, have helped achieved a greater understanding of these mechanisms.

As previously mentioned, among the various mechanisms that can trigger interactions between acoustic oscillations and heat release, the following mechanisms are notable: flame-acoustic wave interactions, flame vortex interactions, equivalence ratio oscillations, flame-wall interactions and the effect of unsteady stretch rate (Altay et al. 2009). Experimental observations from Poinot et al. (1987), Schadow & Gutmark. (1992), Wu et al. (2001) and Balachandran et al. (2005) explained the role of that these various phenomena played in this complex process. During the combustion process the presence of

mixture and flow inhomogeneities produce unsteady heat release. The unsteady heat release produces sound which would normally radiate away in an open field. But in an enclosed region (i.e. the combustor) the sound could reflect back from the combustor wall allowing the reflected waves to interact with the combustion process (Balachandran et al. 2005). This triggers what is referred to as the Kelvin – Helmholtz instability waves in the flame shear layer which usually stabilises the flame (Balachandran et al. 2005). These waves amplify and roll up on the shear layer and finally break down into small scale motions, which in turn affect the flame surface and hence the heat release. The fluctuation in heat release in turn affects the acoustics in the chamber, thus making the whole process a closed cycle (Balachandran et al. 2005). Balachandran et al. (2005) have shown that in fully premixed turbulent flame whereby the temporal or spatial variation in equivalence ratio remains unchanged, the heat release modulation was primarily due to the fluctuation in the flame area. From the study it was also reported that the response remains linear as long as the imposed velocity oscillations remain below 15% of the mean flow. Also the flame response saturation observed was primarily due to the flame-vortex interaction. The flame area fluctuation was shown to correspond to events whereby the flame rollup will increase the flame area and flame annihilation will decrease the flame area (Balachandran et al. 2005).

Due to the breadth of research carried out in the field thermoacoustic instabilities a variety of methods to tackle the problem exists. The flame transfer function (H) has been one of the preferred approaches to model these instabilities (Dowling et al. 2000; Candel 2002, 2003). The transfer function can be explained as follows, if the instantaneous flow velocity at the burner exit is U , then $U(t) = \langle U \rangle + u'(t)$, where $\langle \rangle$ and prime denotes the mean and fluctuating component respectively. Similarly, if Q is the heat release $Q(t) = \langle Q \rangle + q'(t)$ (Balachandran et al. 2005). For completely premixed mixtures the non-linear flame transfer function can be defined as $H(f, A)$:

$$H(f, A) = \frac{Q'(f)/\langle Q \rangle}{u'(f)/\langle U \rangle} \quad \text{Equation 1-7}$$

Where $\langle Q \rangle$ is the time average heat release rate, $\langle U \rangle$ is the bulk velocity of the entering the combustor, $Q'(f)$ and $u'(f)$ are their corresponding amplitude at the forcing frequency, f .

In the study carried out by Liewen et al. (2006) and Balachandran et al. (2005), the global heat release was measured using OH* chemiluminescence in the flame transfer calculation. It was reported that the captured chemiluminescence signal, scales linearly with the rate of fuel consumption and has thus been assumed that to correlate with the global heat release rate. Later discussed in section 2.3 are different chemiluminescence techniques for heat release measurement and the one which is most suitable for the study carried out.

1.5. Motivation and scope

The change in the fuel type and composition usually leads to significant changes in the characteristics time scale of chemical reactions in the combustion system which consequently has a major impact on combustion operability which includes flashback, auto-ignition, lean blowout and combustion dynamics. Consequently this provided the motivation for the development of fuel flexible combustion systems capable of burning a variety of fuels without significantly altering the combustor operability and performance. Richards et al. (2001), Janus et al. (1998), Lieuwen et al. (2006), Ferguson et al. (2008) and Figura et al. (2007) have all studied the influence of fuel type and fuel composition on turbulent combustion.

Lieuwen et al. (2006) investigated the effect of fuel composition on the operability of lean-premixed combustion system. They first studied the combustion properties such as laminar and turbulent flame speed, auto-ignition and chemical kinetic time scale. One of the key observations was that the combustion behaviour such as, turbulent flames speed and ignition delay of the fuel can be markedly be different from that of the individual constituents. Also they exhibit highly non-linear dependency with respect to the fuel composition. The work presented by Kido et al. (2002) have shown that different fuels with the same laminar flame speed have a substantial variation in the turbulent burning velocity due to different diffusion properties of the reactions. Because of those complex fuel variability effects it is apparent that combustor operability is strongly affected by fuel composition. Further studies by Lieuwen et al. (2006) and Figura et al. (2007) explored the effect of fuel composition on the flame structure and combustion dynamics in lean-premixed combustor. In the work they carried out, a spatially distributed flame was approximated as a point-source which was referred to as the centre of heat release in the flame. Variation in fuel composition produces changes in the location of the centre of heat release due to the changing flame speed. As a result the convective time scale from the inflection point to the flame was changed, which resulted in the modification of the heat release and pressure oscillations. From these studies there is evidence that fuel composition exert a significant impact on the stability characteristics of the system (Huang et al. 2009).

Ferguson et al. (2008) studied the influence of fuel composition and heat content on combustion instabilities in laboratory scale and atmospheric – pressure combustors. The effect of fuel Wobbe index (a parameter characterising fuel interchangeability in terms of heating value) was examined by blending natural gas with various amount of ethane, propane and nitrogen. The

results show that a constant Wobbe index would not necessarily produce a constant dynamic response. It was also noticeable that a moderate variation in fuel composition did not significantly change the dynamic properties of the system. The different dynamic responses of the flames were observed in fuels with high concentration of heavy hydrocarbons such as propane. Together with the fuel composition, the geometry of the combustor also plays an important role on the combustion characteristics. The geometry of a combustor consists of the chamber dimensions (length and diameter), inlet and exit configurations, fuel injector arrangement, and flame stabilisation setup which are among other factors.

Therefore the combustor geometry is of crucial importance to the stability characteristics, because it not only determines the acoustic properties, but also exerts considerable influence on the flow and flame structures in the system Huang et al. (2009). Using a bluff-body stabilised premixed combustor Katsuki and Whitehall, (1986) studied the influence of several duct configurations on the flame response. Several ducts of different sizes and shape were used. Ducts of different configurations were used and among those are a straight pipe with a baffle, a sudden contraction, a smooth contraction and a sudden expansion with or without a central baffle. Apart from the smooth contraction configuration, all of the other geometries gave rise to combustion oscillations in a certain range of equivalence ratio. They reported that the dominant instability oscillations were associated with quarter wave of the upstream cold-gas duct. Straub and Richards, (1999) investigated the effect of fuel nozzle configurations on combustion dynamics in a lean-premixed combustor fuelled by natural gas. They modified the fuel nozzle geometry in order to alter the axial location of the point of fuel injection in the premixer. They also employed a two injections point along the axial direction. In the case of the first injection mechanism they observed a significant change in the root-mean square (rms) of the pressure amplitude and the dominant oscillations frequencies in the combustor. However reduced root-mean square pressure could be obtained with the dual-port fuel injection at most operating conditions. Venkataraman et al. (1999) examined the effect of a centrebody recess on combustion stability in a coaxial, bluff-body stabilized dump combustor. It was observed that the buff body with no recess was more susceptible to combustion instabilities. But with the recessed centrebody (different diameters were used) the instability oscillations is gradually attenuated and the flame is more stable over a wider range of equivalence ratios. The authors explained the reduction combustion oscillations were due to the fact that recessing the centrebody alters the flame-vortex interaction and causes the flame to stabilise.

Therefore in order to understand the behaviour and response of different fuel mixtures in modern combustion system, the fundamental combustion properties must first be investigated on a combustor with a relative simple geometry. The study can then be extended to a combustor with a more complex geometry to simulate certain characteristics of real combustion system. As previously mentioned the laminar flame speed is one of the combustion properties that have been thoroughly investigated by Law et al. (1985), Vagelopoulous et al. (1994), Natarajan et al. (2007) and many others using the stagnation flame approach with a linear or nonlinear extrapolation approach to obtain the laminar flame speed at zero strain. While the laminar flame speed might be sufficient to explain some combustion properties such as reactivity, diffusivity and exothermicity, it doesn't provide a detail understanding of the combustion chemistry of different fuel mixtures. By examining the natural emission from different intermediates such as OH*, CH*, C₂* and CO₂* that occurs during the combustion process, the preferred reaction of the different fuel mixtures can be deduced. As mentioned previously chemiluminescence measurement can also be used as an indicator of heat release. Most heat release measurements have been based on a narrow-band OH*, CH*, C₂* and broadband CO₂* chemiluminescence emission (Ayoola et al. 2006; Haber 2001; Samaniego et al. 1999). Chemiluminescence measurement for heat release measurement wasn't restricted to laminar flames but also used in turbulent combustion studies (Bernier et al. 2003; Bloxside et al. 1995; Lawn 2000; Lawn & Polifke, 2004; Lieuwen & Neumeier, 2002; Pun et al. 2003). The studies used chemiluminescence to measure the transfer function to understand the combustion dynamic of turbulent flames. In most of the studies the chemiluminescence measurement have been seen to scale linearly with fuel consumption rates and thus assumed to correlate with global heat release. But careful interpretation of the different intermediate radicals as a measurement of heat release needs to be carried out. In the study by Hardalupas et al. 2004, on opposed jet flames they found that as OH*, CH*, and CO₂* chemiluminescence are better correlation with heat release as C₂* chemiluminescence fail at high strain rate conditions. CH* chemiluminescence has been reported to disappear at high curvature and strain rates (Nguyen et al. 1998). Ayoola et al. (2006) also reported that OH* chemiluminescence was very sensitive to strain and turbulence and strong chemiluminescence signals were recorded from region with relatively low heat release.

Najm et al. (1998) have shown that a direct way of measuring heat release can be achieved using simultaneous OH and H₂CO PLIF on pure hydrocarbon flames. Pixel to pixel multiplication of the resulting PLIF images have shown to correlate well with the local heat release (Najm et al. 1998; Ayoola et al. 2006). Najm et al. (1998) have shown this technique

is well suited for flames that has the presence of a strong vortex. Ayoola et al. (2006) have shown that the technique can be reliable to for high strain and curvature flames. However, this measurement method has been proved to work only for completely premixed flames. Although some previous work employed this technique, there is still a lack of understanding of its applicability on multi-component fuels in highly turbulent premixed flames.

It is clear that in order to have a better understanding of the behaviour of different fuel mixtures knowledge of how each of the individual components of the fuel affects properties such as laminar flame speed is required. Therefore in order to be able to probe for the different radicals formed during the reaction non-intrusive measurement techniques such as chemiluminescence were employed. The laminar flame speed was also experimentally measured using an impinged jet configuration. Furthermore OH and H₂CO PLIF were used to spatially resolve the concentration of OH and H₂CO and their product to obtain a correlation of heat release for different fuel mixtures. Also this enabled evaluation of the applicability to OH and H₂CO PLIF heat release measurement technique to a variety of hydrocarbon fuels blend. The study was then extended to investigate to fuel flexible model gas turbines. By varying the overall bulk velocity, the strain and the shear induced turbulence effects on the flame response such as the flame shape, heat release rate and curvature were investigated using the aforementioned diagnostic mentioned. Also the dynamic flame response due to small and large scales acoustic perturbations to mimic similar combustion oscillations in gas turbines were analysed for multicomponent fuels.

1.5.1. Objectives

To summarise, the objective of the work to is to understand the effect of different fuels on the flame shape, heat release rate, sensitivity to perturbations, emissions and laminar flame speed. The first part of the work was set-up the facilities in order to observe the flame shape, position and heat release rate using OH and H₂CO PLIF. Along with the PLIF measurement OH* chemiluminescence and pressure oscillations (for the specific experiments) were also carried out. The second part of the work consisted of the development and manufacturing of an impinged jet burner for measurement of the laminar flame speed of different fuels such as methane, biogas, syngas and enriched biogas. The laminar flame speed measurements were carried out using particle image velocimetry (PIV) will be carried.

Specific objectives:

1. Modify the current experimental set - up in order to operate with different fuels
2. Implement a heat release measurement technique on a strain and turbulent flames from which the flame shape, position and structure can be obtained
3. Implement a laminar flame speed measurement technique for a range of fuels and conditions
4. Understand fuel sensitivity to flow perturbations

Therefore this work extends the current method employed in measuring heat release rate to methane and biogas flames. The effect equivalence ratio and CO₂ dilution in biogas was investigated on a laminar flame and the trend obtained were compared with computational simulation. Also the key mechanisms of periodic oscillation were investigated using simultaneous OH and H₂CO PLIF bluff-body stabilised turbulent flame.

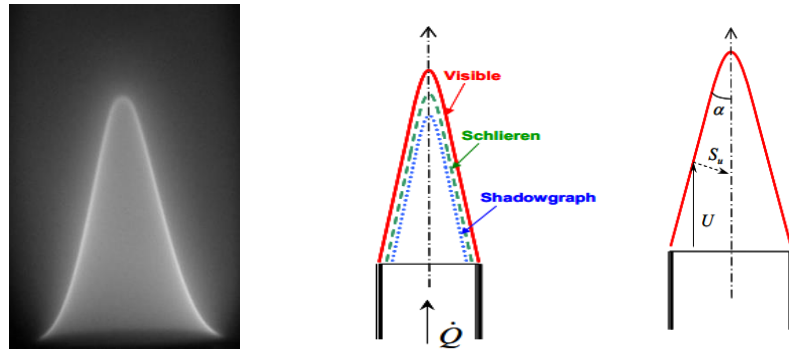


Figure 1-1: Laminar Bunsen Flame (left) a typical laminar flame (middle) flame front detection depending of measuring technique (right) cone angle (Natarajan et al. 2007)

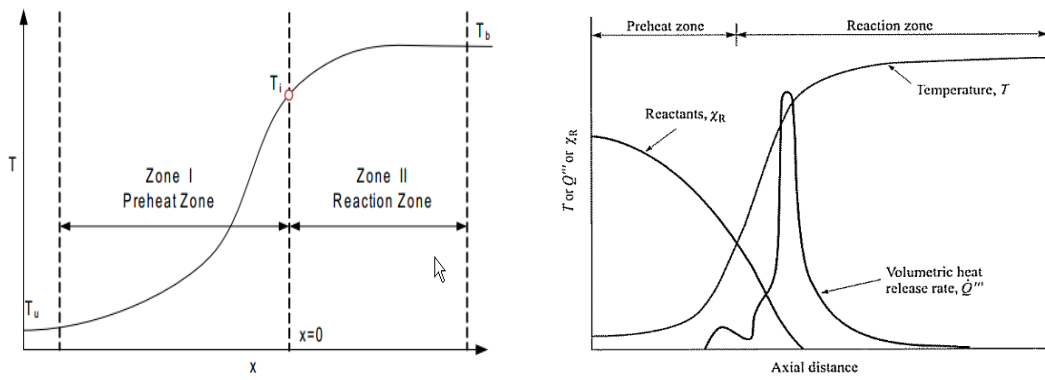


Figure 1-2: Left: Schematic of a typical thermal structure of a premixed flame (Kuo, 1986) & Right: S R Turns (2000)

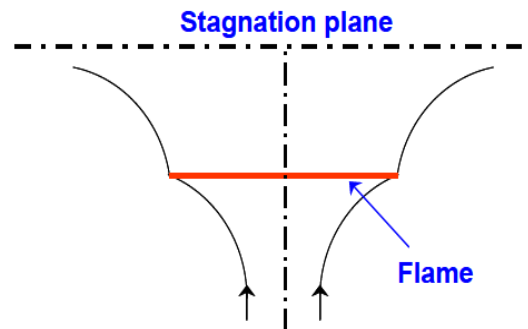


Figure 1-3: Stagnation flame stabilisation (Law et al. 1984)

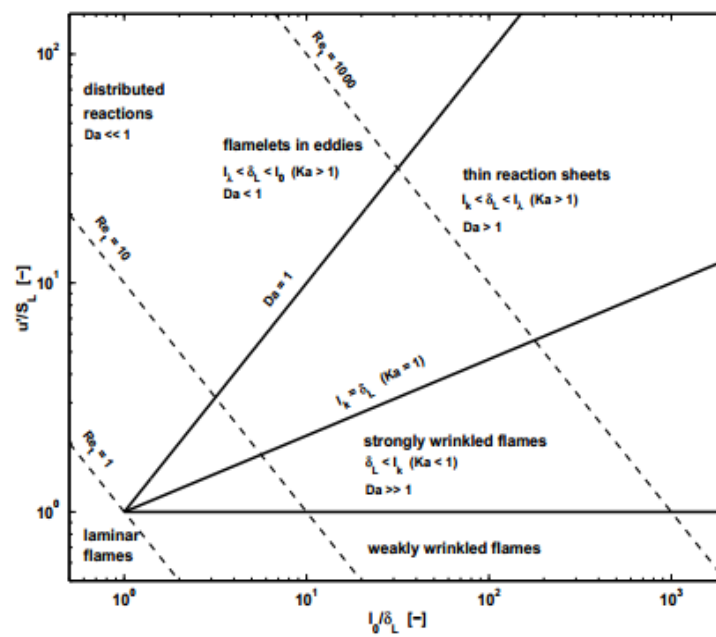


Figure 1-4: Premixed combustion regime diagram (Borghi diagram). Loglog graph of the relative intensity of turbulence (u'/S_L) vs. the relative large-eddy size of turbulence. The bold lines separate the combustion regimes (Borghi, 1985)

Chapter 2

2. Experimental Methods

This chapter describes the experimental apparatus, flow configurations and the experimental techniques employed during the present work. The chapter is divided into 3 main sections, the experimental set-up, measuring techniques and image analysis. The experimental set-up section describes the design of the laminar stagnation and the turbulent burner. The measuring technique section describes the laser system, the flow controllers and also the different experimental technique also with its applicability are discussed. Lastly the data processing and image analysis section details the procedures and methods employed to extract the data measured.

2.1. Burner development

2.1.1. Development of a Impinged Jet Combustor

A general schematic of the stagnation burner is shown in Figure 2-1. The stagnation burner has 4 sections which are as follows: (1) inner nozzle, (2) outer nozzle, (3) inner plenum, and (4) cooling plug.

Therefore using this set-up a stagnation flow field could be achieved by a combination of the contoured nozzles and the solid surface (cooling plug) situated above the exit of the nozzle. This configuration has certain advantages compared to the more commonly used opposed jet configuration for the following reasons: (1) the use of a solid surface leads to a more stable flame, (2) problems related to heating of the upper part of the burner are eliminated, and (3) the operation is simplified by having to deal with a single jet (Natarajan et al. 2007). The fuel and air mixture enter the inner plenum at a distance of 0.95 m above the nozzle in order to allow the flow to be fully developed prior to exiting the burner. In an effort to obtain a steady flame the inner and outer profile were designed to smoothly join the outer surface of the inner plenum and the tip of the nozzle and provide vertical outflow in the annular jet. The profiles of the inner and outer nozzle were calculated in order to minimise the exit boundary – layer displacement thickness and formation of vortices in concave section. These features ensured that a uniform velocity profile is maintained at the burner exit which in turn helps to sustain a uniform flame stretch throughout the flame area. The inner and outer nozzles had diameters of, D_1 22 mm and D_2 26 mm respectively. During operation the fuel/air mixture was shrouded by a small nitrogen co-flow, which helps reduce shear layer development along the periphery of the jet. The use of an inert co-flow also reduced the tendency of the flames to attach to the nozzles (Ishizuka et al. 1982).

Flow stagnation was achieved with a rounded plug at a distance L above the contoured nozzle. The plug was manufactured from stainless steel with a flat surface of 80 mm and rounded corners. The rounded corner compared to a flat plate, provides a more steady stagnation flow field due to its aerodynamics natures (the flow follows the contour of the rounded plug with more ease, helping in the improve flame stability). The plug was also maintained at a very specific temperature while performing the measurements while having water flow through. The water flowed radially outwards along the top portion of the plug and out through two outlets

ports radially distributed around the plate. The outlet ports were also fitted with thermocouples for continuous monitoring of the exiting water temperature.

The distance L of the plug above the nozzle was adjusted depending on the mixture used so that the ratio of L/D_1 ranges from 0.5 to 1 (a ratio 1 – 2 is commonly used for counter flow flames). These L/D_1 values are sufficiently large that the effect of the finite domain on the measured flame speed can be considered small (Vagelopoulos et al. 1994). The wall effect of the unburned flame speed measurement can be considered to be insignificant, provided that the flame is stabilised sufficiently away from the stagnation plane (Natarajan et al. 2007).

2.1.2. Development of Bluff Body Combustor

A laboratory scale bluff-body stabilised combustor was used to carry out the study on turbulent premixed flames. Figure 2-2 and Figure 2-3 shows the schematics of the burner assemble. The burner can be divided into three main sections which are the plenum, the concentric circular ducts and the bluff-body. In order to facilitate for different excitation modes inside the combustor, four speakers were mounted orthogonally along the circumference of the plenum. The plenum had an inner diameter (ID) of 100 mm and a length of 200 mm and was designed in such that it had divergent and convergent cross-sections at the inlet and the exit, which minimises the risk of flow separation during the expansion and contraction. From the plenum leading to the bluff-body were three concentric circular ducts of length 90 mm, 150 mm and 160 mm and with each of them with an inner diameter of 35 mm. The concentric circular ducts were also fitted with pressure taps from which the acoustic pressure measurements were recorded. As seen from Figure 2-2 one end was connected to the plenum whereas the other end had a conical bluff-body of diameter 25 mm, giving a blockage factor of 50%. The bluff-body was used to stabilise the flame, which was in turn enclosed in a circular silica fused quartz tube to prevent entrainment of air which can result in local variation in the equivalence ratio. The quartz tube has an inner diameter (ID) of 70 mm, outer diameter of (OD) of 90 mm and height of 100 mm. The combustor was designed in such a way to accommodate for premixed, imperfectly premixed and non-premixed combustion modes. In the work carried out, the premixed combustion mode was used.

For the present work a premixed mixture of fuel and air was used. Therefore, in order to achieve a completely premixed combustion at the bluff-body, the fuel-air mixture was mixed further upstream (~ 8.5 m) of the combustor. The premixed fuel then entered the plenum travelling downstream along the concentric ducts and finally exiting at the bluff-body (where combustion takes place). Propulsion systems such as ramjets and afterburners have similar bluff-body configuration fitted to stabilise the combustion process in those fast flowing environment (Schimmer et al. 1977). The physical processes that anchors a premixed flame behind a bluff-body flame holder involves the combustible mixture being in contact with the hot combustion products residing in the recirculation zone and continuous ignition of the incoming mixture in shear layers bounding the recirculation zone (Balanchandran et al. 2005). When the flame is enclosed there is a secondary outer recirculation zone and two flame fronts are present, one in the inner shear layer and the second present in the outer recirculation shear layer. Figure 2-4

shows a typical OH fluorescence of a premixed flame without and with the enclosure respectively at equivalence ratio of 0.77 and a bulk velocity of 9.9 m/s. The OH fluorescence was obtained from laser excitation sheet across the flame which will be described in greater details in the subsequent sections. It can be seen that the open flame has a single flame front where the flame stabilise at the inner shear layer whereas in the enclosed flame, two flame fronts can be seen. The first flame front is caused by the re-circulation due to the bluff-body while the second flame front is caused by the side re-circulation in the dump plane. This will be discussed in greater details in chapter 4. As previously mentioned an important feature of the burner are the four loudspeakers mounted orthogonally which can be used to study the flame response to impose oscillations.

From the work of Schimmer & Vortmeyer, (1977) there are several ways in which perturbation of the flame will result in heat release oscillations:

1. Oscillation of the input mass flow rate of the reactants
2. Oscillation of the equivalence ratio
3. Oscillation of the turbulence generation or by vortex shedding
4. Oscillation of the heat transfer to the burner
5. Oscillation of the change of reaction rate by adiabatic compression

The experiments were divided into two configurations, where the first one was done without any acoustic perturbations and the second sets of experiments were performed with acoustic perturbations. The acoustic perturbations were introduced by the four acoustic drivers (loudspeakers) located at the circumference of the plenum. A sinusoidal signal from a waveform generator (TTi 20MHz function generator) was first amplified and then supplied to the speakers. The modulation of the speakers in turn introduces a mass flow oscillation which causes heat release fluctuations (Balachandran et al. 2005). The input amplitude to the speakers (peak-to-peak voltage to the speakers) and the frequency of forcing were varied independently to understand the dependence of the flame response on the amplitude and the frequency of forcing.

Figure 2-5 shows OH fluorescence of an unforced and forced premixed flame of equivalence ratio of 0.77 and a bulk velocity of 9.9 m/s. The OH fluorescence was obtained from laser excitation sheet across the flame which will be described in greater details in the subsequent sections.

2.2. Measurement methods

2.2.1. Flow rate measurements

The air input to the combustor was supplied by a reservoir at a constant pressure of 8×10^5 Pa. The fuel was supplied from commercial cylinders with appropriate gas regulators, from which the gas was supplied at a pressure of 3×10^5 Pa. The air and fuel mass flow rates were monitored using Red-Y smart mass flow controllers with measurement ranging from 40 – 450 litres per minute (lpm) for air, 0 – 60 lpm for methane, 1 – 50 lpm for carbon – dioxide, 1 – 20 lpm for carbon – monoxide and 1 – 200 lpm for hydrogen, all of which have an accuracy of 1.5% of the Full Scale Deflection and 0.5% of the reading.

2.2.2. Acoustic measurements

In order to characterise the acoustic response on the burner, the two microphone methods were used. This was achieved by recording the pressure fluctuations in the flow upstream to the combustion region. As seen from Figure 2-2 there are pressure tapings which was fitted with, two Kulites high sensitivity pressure transducers (Model XCS-093 with sensitivities of 4.2857×10^{-3} mV/Pa). The signal from the pressure transducers were recorded by means of a data acquisition system (National Instruments PCI 6010) which had a visual interface programmed using the commercial labview software. All pressure fluctuations measurements were recorded at a sample rate of 10,000 Hz over a period of 2 seconds. From the acoustic measurements it was found that the peak frequencies occur at 30, 255 and 315 Hz (Figure 2-6).

2.3. Optical measurement technique

From the beginning of fire research, visible flame emission, spectroscopic flame signatures and high-speed photography have proven useful to understand the combustion phenomena (Katharina et al. 2005). These early optical techniques have been made more effective by the use of modern laser technology. The use of laser based techniques offer researchers visualisation and measurements of important combustion parameters such as concentration, temperature, velocity, rate of heat release and pollutant emissions. Laser based techniques offer many advantages over the conventional physical probe measurement technique.

1. The insertion of physical probes within the combustion region can affect the physical mechanism such as the flow field, or act as a thermal source. It can also act a catalyst which subsequently affects the combustion on a chemical level.
2. Spatial and temporal resolution is hard to achieve, especially in severe environment of high temperature and pressure. Concerns about the survivability and reliability of the probes make them very expensive and specific to the application.

On the other hand laser based techniques are of considerable interest due to their remote, non-intrusive and in-situ character and having both spatial and temporal resolution. Laser diagnostic measurements make use of a large number of sophisticated instruments, providing continuous or high-speed measurements with high spatial resolution, flow stopping interrogation times and, advanced strategies for quantitative calibration (Katharina et al .2005). Modern laser-based diagnostic techniques permit the study of combustion, even in the interior of engines, gas turbines and large-scale combustors. Laser based techniques are not without any disadvantages. Optical access to the combustion region can sometimes be difficult due to high pressure and temperature and the smallest turbulence length scales cannot be resolved.

2.3.1. Chemiluminescence measurements

Chemiluminescence measurements are widely used in estimating the global heat release rate in hydrocarbon flames. Its simplicity to implement in experimentation combined with the flexibility of species selectivity make chemiluminescence a very useful diagnostic technique in modern combustion research. Chemiluminescence is the radiation emitted from electronically excited molecules when these return to a lower energy state. The wavelength of radiation which is emitted is characteristic to an individual molecule and the particular transition the molecule undergoes. This will depend on the complexity of the molecule, for example a simple diatomic molecule will show one major peak and relatively weaker secondary peaks whereas for more complicated molecules, the radiation spectrum can be seen to be continuous. OH and CH are examples of molecules that show major peaks at 308 nm and 431 nm respectively whereas CO₂ is an example of a molecule that has a continuous radiation spectrum (Gaydon, 1974). Figure 2-7 shows the chemiluminescence emission from a turbulent lean premixed natural gas flame at an equivalence ratio of 0.8 shown by the work of Lee & Santavicca, (2003).

Flame chemiluminescence is generally referred to as the chemiluminescence emitted in flames during combustion. The work carried out Haber, 2000 provided a good insight on flame chemiluminescence and from which he deduced that the several excited molecules are not only produced by thermal excitation but also are produced as the products of the reactions (the concentrations of excited molecules seen in flames exceed the equilibrium concentrations expected at the same temperature without chemical reactions by several orders of magnitude). As the amount of radiation emitted at a given wavelength is proportional to the concentration for that specific molecule a measurement of radiation can be directly related to the concentration of the excited molecule.

One key aspect of chemiluminescence that is important to understand is that the energy of the excited molecule (denoted by *) is not always removed by radiation. There are three possible scenarios that can take place, firstly the excited molecule can react with another molecule, and secondly, there could be loss of energy in a non-reactive collision. Such collisions occurs without the emission of light and therefore is called quenching collision (Haber, 2000). It should be noted that quenching is strongly dependent on the colliding molecules and the quenching efficiency of a given unexcited molecule is a measure of how likely the molecule will remove the excess energy from a given excited molecule in a collision. Quenching efficiency varies greatly from molecule to molecule and is very often a strong function of temperature (Garland and Crosley, 1986). Thirdly, as mentioned previously the energy is emitted in the form of radiation.

As early as the 1950s researchers had measured chemiluminescence in an attempt to correlate the chemiluminescent light with the integral heat release. Clarke, (1958) studied the radiations from propane - air and ethylene - air in laminar and weakly turbulent flames. They reported that there is a linear dependency of the chemiluminescence on fuel flow rate at constant equivalence ratios, and a decrease in intensity as a result of a decrease in equivalence ratio. Four types of chemiluminescence were measured which are: OH*, CO₂*, CH* and C₂*, which are still today the four most commonly measured chemiluminescent species. From the chemiluminescence measurement of these four different types of radicals they found that the slope of the linear dependence can be interpreted as a function of the equivalence ratio and the type of chemiluminescent. It can be said that the behaviour of the chemiluminescent species with equivalence ratio is species specific. OH and CO₂* were observed to both have peaks near the maximum laminar flame speed, with CO₂* decreasing at a slower rate to OH* once the maximum turning point was reached (on the rich side of the reaction). Also it was found that

in both flames the intensities of CH^* and C_2^* were very sensitive to small changes in equivalence ratio.

The observations of Clarke, (1958) were further strengthened by the work of Price et al. (1968) and Hurlle et al, 1968 who observed a correlation between the mean emission intensities of C_2^* and CH^* and the total flow rate of the combustible mixture in both laminar and turbulent flames and in their transition region. For Reynolds numbers up to 10,000 there is a linear dependency of chemiluminescence intensity on fuel flow rate and heat release rate respectively which was a function of the equivalence ratio. But for Reynolds number up to 17,000 a decrease in intensity with increasing fuel flow rate was observed. Also the work carried out by Price at al. 1968, related the noise from turbulent flames to the oscillations in the strength of the chemiluminescence signal. The experiments were carried out in an ethylene-air, turbulent, premixed and flames where they observed an excellent correlation between the time derivative of the C_2^* and CH^* chemiluminescence strength and the root mean square pressure, which was measured by the means of a microphone at some distance from the flame. The relation that was derived in their work relied on the chemiluminescence strength been proportional to the heat release rate.

Further studies in chemiluminescence were carried out by Samaniego et al. (1999) who looked at the emission of CO_2^* in laminar and turbulent premixed methane – air and propane – air flames numerically. They used CO_2^* as heat release indicator. They found that CO_2^* chemiluminescence to be good indicator for fuel consumption in flames with varying dilution, strain rate and equivalence ratio. Unfortunately, their approach was limited to numerical modelling with no validation of the findings with experimental investigations. The authors concluded from their study that CO_2^* chemiluminescence can be used as indicator of heat release and also as a measure of H-atom concentration in steady and unsteady combustion under moderate strain rate.

Najm et al. (1998) performed extensive experimental studies to identify indicators of heat release. The study shows how heat release can be predicted for the case of the unsteady interaction between the flame sheet and a counter rotating vortex pair. Najm et al. (1998) used planar laser induced fluorescence of CH and HCO . They concluded that HCO was a good indicator of heat release everywhere whereas on the other hand CH shows to be a poor indicator in region of the flames of high strain rate and curvature immediately prior to extinction.

Further, Najm et al. (1998) showed a detailed analysis of the reaction mechanism of methane oxidation.

The study of Najm et al. (1998) also points out an important limitation of the assumption that chemiluminescence is proportional to heat release rate. This proportionality breaks down in regimes of very high strain and curvature, near extinction. This can be explained by considering the flame fronts in laminar and weakly turbulent flames that exhibit sheet-like structures; therefore the local flame chemiluminescence per unit area is constant along the flame front. However, in highly turbulent flames, the flamelets are strained and subjected to curvature. Therefore, chemiluminescence emission from the flame front of highly turbulent flames is dependent on the local flamelet properties and cannot be considered constant along the flame front. Furthermore high strain and curvature can lead to local extinction and flame quenching. In the work presented by Price et al. (1968) and Hurlle et al. (1968) the unsteadiness in the flow was performed by perforated plate yielding a very low level compared to the unsteadiness of counter-rotating vortex pair. This can be one of the reasons why Price et al. (1968) and Hurlle et al. (1968) didn't notice any significant change in chemiluminescence intensity at high Reynolds number.

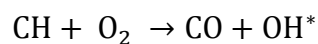
Lee & Santavicca, (2003) investigated chemiluminescence emission from a turbulent swirled flame. They reported similar findings as previous work aforementioned whereby the overall CO_2^* chemiluminescence emission as a function of fuel flow rate for a fixed equivalence ratio and inlet temperature. Their results also show that the overall chemiluminescence emission increases exponentially with equivalence ratio, which can be attributed to the exponential temperature dependence of the reaction rate for the formation of CO_2^* (Samaniego et al. 1999). Figure 2-8 shows the overall CO_2 chemiluminescence emission divided by fuel flow rate vs. the equivalence ratio. The other factor affecting the overall chemiluminescence emission and the overall heat release is the area of the flame. Any factors causing the flame area to change, for example, flame-vortex interaction will result in a change in the overall chemiluminescence emission and the overall rate of heat release. Changes in the flame area will not alter the relationship between the overall chemiluminescence emission and the overall heat release as long as the flame temperature and the effects of strain and curvature are constant (Najm et al. 1998). If, however, the effects of stretch and/or curvature change over the flame surface as the flame area changes, as might be expected during flame-vortex interaction, then the relationship between the overall chemiluminescence emission and the overall rate of heat

release is likely to change as the flame changes (Najm et al. 1998). Moreover, they reported a strong influence of premix level, curvature and stretch on the chemiluminescence signal.

Ayoola et al. (2006) used OH and H₂CO PLIF and OH* chemiluminescence imaging to measure the heat release rate. They employed a pixel by pixel product of OH and H₂CO PLIF signal heat release imaging technique to characterize the OH* chemiluminescence as a measure for spatially resolve heat release rate. The heat release imaging shows a good correlation with the local heat release rate. Two different types of flames were used, during the study, the counter flow flame and the bluff-body stabilized flames. It was found that OH* chemiluminescence was very sensitive to strain and turbulence and that strong OH* chemiluminescence signals emerged from region within the flame with relatively low heat release rate. It was also observed that in bluff-body stabilised flames the equivalence ratio dependency of the OH* chemiluminescence was different for different positions in the flame brush. Ayoola et al. (2006) conclude that OH* chemiluminescence is not a reliable indicator for heat release.

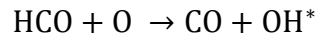
The chemical reaction that leads to the formation of radicals holds the key to fully understanding the signal collected. Experimental determination of all the reaction rate constants involved to a precision necessary to achieve such an understanding is very difficult. Most methods deduce rate constants of one or a set of reactions by measuring the concentrations of molecules involved in the reactions in time (Gunther et al. 1979).

The current accepted reaction for OH* production is given by the following proposed by Krishnamagari & Brioda, (1961).



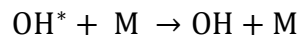
Several studies have found supporting evidence for the reaction given above. Becker et al. (1996) reported OH* chemiluminescence in hydrocarbon atom flames. They found that the proposed reaction adequately explained the observations made in their two-hydrocarbon atom flames. The other proposed reaction path which involves the reaction of CH with O and HCO with O₂ were rejected as formation paths OH* because of lack of energy release in these reactions paths to produce the excited OH radical.

In the work carried out by Haber, he proposed an alternate reaction path for the formation of OH*.

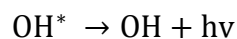


The reason why it was suggested is due to the fact that the reaction of CH and with molecular oxygen, (which produces carbon-monoxide and a hydroxyl radical as products) is a simplification of the true chemical kinematics path from CH to CO (via the formyl radical (HCO) reaction with atomic oxygen). The formyl radical, precursor of OH*, is an important intermediate species in methane combustion because HCO – consuming reactions are generally very exothermic and contribute significantly to flame heat release (Gunther et al. 1979). HCO is formed primarily from formaldehyde CH₂O. HCO – forming reactions generally have no or very low activation energies which can be seen from Figure 2-9. The role of HCO in the measurement of heat release will be discussed in greater details in section 2.3.3 (simultaneous PLIF measurements for heat release imaging). HCO consumption reactions however exhibit a variety of activation energies.

Another aspect of chemiluminescence chemistry is the destruction of chemiluminescent species (Gunther et al. 1979). As mentioned above there are three possible paths by which energy can be removed from the excited molecule. The most common path is quenching through collision with another molecule. A typical quenching reaction is given by (Gunther et al. 1979):



The other path is the energy loss whereby the excited radical loses energy by spontaneous emission, which can be observed through the natural luminescence (combination of different radicals). The reaction which involves only the excited molecule can be represented as follows:



As mentioned before '*' denotes the excited state OH radical and ν is the frequency of the chemiluminescence. Figure 2-10 shows the chemiluminescence emission spectrum for a lean premixed turbulent flame. It can be seen that OH* exhibits a peak of 310 ± 10 nm at $A^2\Sigma^+$ emission. Also from the figure it can be noted that within this region there is a contribution from CH*, C₂* and CO₂* with the latter having a broadband emission spectrum ranging from 350 nm to 600 nm. During measurement the effects of the aforementioned signal can be significantly reduced by using a narrow – band collection of OH* chemiluminescence which will be discussed in further details in the experimental methodology section.

In the experimental data on CH* chemiluminescence by Najm et al. (1998) acquired under vortex V - shape condition similar to the one used by Nguyen & Paul, (1996), shows that CH* was only observed in the primary flame zone and the CH* surface around the vortex pair disappear early into the interaction. Devriendt et al. (1997) have shown that the primary source of flame CH* is the reaction of $C_2H + O^3P \rightarrow CH A^2\Delta + CO$ which might also provide a measure of the final step of C₂ reaction chain. Therefore for vortex dominated flames CH* might be a poor measure of heat release.

Samaniego et al. (1999) have suggested that CO₂* chemiluminescence can be used as a measure of heat release. The region which the CO₂* is in its excited state surface is not well characterised (Najm et al. 1998). As such the spectral signature of CO₂* and the signal quantum yield are poorly known function of total density and the composition of the collisional path. Najm et al. (1998) represented the production rate of CO₂* with peak theoretical heat release rate and despite the scatter a useful correlation is evident. Here again the details of CO₂* production and consumption will govern its actual concentration and details of its chemiluminescence will govern the eventual utility of its chemiluminescence signal. Therefore careful interpretation of the signal is required when using CO₂* chemiluminescence as a measure of heat release.

C₂* chemiluminescence has been widely applied in diagnostic for study of premixed flames. It is generally accepted that the C₂* production goes through the reaction of CH with C atom or OH (Najm et al. 1998). Currently there a limited amount of work present to explain the reported signal levels and spectral signatures. With C₂* exhibiting a maximum in signal even at richer condition (lower heat release) than CH* signal suggests a complicated relation with heat release as a function of local stoichiometry (Najm et al. 1998).

From the review of the different chemiluminescence techniques we can conclude that C₂*, CH*, OH* and CO₂* are not reliable flame markers for the turbulent flame under investigations, in that their presence in the flame says nothing about the chemical path followed by most of the carbon down to CH₂O, HCO and CO. Rather, they are useful indicators of the minor carbon flow rates in their associated chemical paths (Najm et al, 1998). Also CO₂* chemiluminescence may have complicated dependence on curvature, which may lead to an ambiguous correlations with heat release rate. Among the different chemiluminescence species OH* will be a better indicator, as opposed to CH* and CO₂* as it persists in regions of high curvature and being capture in the UV spectrum eliminates background noise from the visible

spectrum. Also there are extensive research carried out on the different wavelengths at which OH* emits and careful choice of optics again eliminate background noise. On the other hand Najm et al. (1998), has found HCO to be an excellent marker for heat release rate over a wide range of unsteady curvature and strain-rate. The spectroscopy of HCO has revealed that PLIF measurements of OH was possible but with certain limitations. The next section will review those limitations and the use of alternative dual PLIF measuring technique to find a correlation for heat release measurement via the HCO reaction path.

2.3.2. Planar laser induced fluorescence (PLIF)

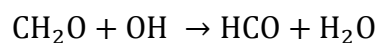
The flexibility of laser-based technique includes the capability of spreading the laser beam into a sheet. Planar laser-induced fluorescence can be performed yielding species information as a 2-D planar image. Laser induced fluorescence works on the principle of selectively exciting atomic or molecular species with at specific wavelengths to a higher energy state. The excitation of the species is followed by a spontaneous emission of a photon when the excited atom or molecule decays back to its ground state. This spontaneous emission is referred to as fluorescence that is captured on an ICCD camera. The ICCD camera is ideally suited for the application because of its high quantum efficiency in the lower-wavelength region (200 to 500 nm). The intensity of the fluorescence can be correlated to the concentration of the species in the integration area. A careful interpretation need to be carried out between the concentration of the species and intensity of the fluorescence. As there are losses due to quenching, vibrational and rotational energy transfer (Taylor, 1993). Collisional redistribution will lead to different spectral signatures and also quenching decreases the signal over time. Thus, information on the quenching and energy transfer rate coefficients as a function of collider species, temperature, and probed quantum level is necessary to assess the influence of collision processes on the measured signal. A technique to avoid errors that are introduced by unknown quenching rates is to perform saturated LIF. To achieve the quenching state a high intensity laser is required so that the quenching rate is small compared to the absorption and the emission rates. In the saturation regime, the fluorescence signal is independent of both the laser irradiance and the quenching, therefore obviating the need to measure or evaluate either (Eckberth, 1998). One major drawback of saturated LIF is the need for a high powered, tuneable laser with a relatively good beam quality. Further difficulties include the finite time required to achieve saturation and subsequent relaxation of the probed species, especially when temporal accuracy is necessary (Eckberth, 1998).

In terms of selecting the transition state for PLIF imaging in combustion system, a temperature-independent strategy is employed. A quantum state is selected which minimizes the overall temperature dependence in the temperature range of the experiment, and the measured signal is directly proportional to the species mole fraction. If only the relative mole fraction is of interest, then the fluorescence intensity data can be used directly after corrections for background signal and non-uniform sheet illumination. If absolute mole fraction are sought an in-situ calibration with a known mixture, for example using a flat-flame burner or static sample,

can be used to provide the missing proportionality factor. The bulk of all PLIF imaging during the combustion process has been aimed at species measurement such as OH, CH and H₂CO. Due to the difficulties, as mentioned above of converting fluorescence signals to values for absolute concentration or number densities, measurements are qualitative rather than quantitative. Thus, qualitative species imaging, usually in the form of false-colour PLIF intensity maps, can be used as an effective tool for locating flame fronts, region of burned or unburned gases, recirculation zones, shock waves and so on.

2.3.2.1. Heat release imaging measurements

As opposed to chemiluminescence, which suffers from been a line-of-sight technique and which lack spatial resolution, planar laser induced fluorescence (PLIF) can be used to capture small scales structures that occurs during turbulent combustion. As previously mentioned, this technique is species selective with signal levels proportional to the relative concentrations of the excited species (Lee et al. 2000). Najm et al. (1998) found a temporal and spatial correlation between the concentration of formyl radical (HCO) and heat release rate (Lee et al. 2000). They suggested that this occurs because: firstly, reaction of HCO (to form H and CO) occurs rapidly compared to its formation rate, thus HCO concentration appears as directly proportional to HCO production rate. Secondly, for lean to slightly rich flames, a substantial fraction of the carbon flows through HCO making HCO a good point for the flow of carbon from fuels to products. Thirdly HCO production is directly dependent on the concentration of H₂CO that in turn is directly dependent on the reaction $\text{CH}_3 + \text{O} \rightarrow \text{H}_2\text{CO} + \text{H}$ which shows the largest fractional influence on changes in heat release. But HCO PLIF has one major drawback as it has a low signal-to-noise ratio. In their experiments Najm et al. (1998) were forced to average 100 frames of data to achieve a reasonable signal-to-noise ratio of 2:1. They concluded that there is insufficient signal available to apply HCO PLIF as single-pulse imaging diagnostic as would be required for studies of turbulent reacting flows. An alternative approach uses the simultaneous OH and H₂CO PLIF measurements to obtain a signal that correlates with HCO production rate.



The forward rate of reaction can be written as $K(T)[\text{CH}_2\text{O}][\text{OH}]$, where K is the rate constant, T is temperature and '[]' denotes the number density. Since the LIF signals are related to species densities, this provides a method to measure the reaction rate through the concentrations of CH₂O and OH. However as reported by Najm et al. (1998) LIF signals are highly dependent on temperature through the collisional quenching and the Boltzmann population fraction. Therefore the product of simultaneous LIF measurement of OH and CH₂O can be expressed as:

$$(\text{CH}_2\text{O LIF})(\text{OH LIF}) \propto f(T)(\text{CH}_2\text{O})(\text{OH})$$

Over a limited range of temperatures it is possible to select transition lines such that $f(T)$ closely mimic the forward reaction rate $K(T)$ (Paul et al. 1998).

2.3.3. Simultaneous PLIF measurements for heat release imaging

OH and H₂CO PLIF were described in great detail by the work of Najm et al. (1998). Their measurements of heat release rate were based on taking pixel-by-pixel product of OH and H₂CO PLIF images to yield an image closely related to a reaction rate. The types of flames they investigated were laminar premixed flames subject to an interaction with an isolated line-vortex pair. The burner used during the experimental testing was similar to the one described by Nguyen & Paul, (2000). The burner (63.5 mm square) packed with glass beads followed by honeycomb and wire screen flow straighteners. The V-flame was stabilized on a slightly heated nichrome wire suspended above the burner. A laminar vortex pair was generated by impulsively driving through a slot nozzle mounted on one side of the test section. The burner conditions were carefully selected in order to achieve a highly reproducible flow that allowed the time evolution of the flame-vortex interactions to be mapped by adjusting the time between the lasers firing and the image being captured. They also discussed the spectroscopic and collisional process affecting the measured signal. Through a judicious choice of excitation and detection wavelengths, it is possible to cancel out much of the temperature dependence and obtain PLIF images of OH that essentially represent mole fraction. However with CH₂O molecules, there is strong temperature dependence from the Boltzmann fraction. This temperature dependence was modelled by Najm et al. (1998) and the formaldehyde LIF signal was represented by $(\text{CH}_2\text{O LIF}) \propto X_{\text{CH}_2\text{O}} T^{-\beta}$, where X denotes the mole fraction, with $2.2 < \beta < 3$ over a range the temperature range of 800 – 1800 K, with the functional dependence for $f(T)$ between $T^{-0.2}$ and T^{-1} . In the work by Paul et al. (1998) it was shown that in the range of temperatures expected in the region of overlap of the OH and CH₂O, the primary dependence in the product of LIF signals is through the product of number densities. Thus, the product of the two LIF signals provided a measure of a quantity that correlated with local heat release rate (Balachandran et al. 2005, Ayoola et al. 2006, Bockle et al. 2000).

Vagelopoulos et al. (1994) investigated the correlation between heat release rate and CH both experimentally and numerically. Experimental heat release rate was measured by OH and CH₂O LIF. During the study two types of flames were investigated; firstly a V-flame configuration for assessing the effect of reactant composition transients during flame–vortex interactions. Secondly, an axisymmetric configuration was used, to assess the adequacy of CH as a flame-front marker. For that purpose, the response of CH LIF to flow transients and reactant composition variations were compared against results from reaction-rate imaging for

$\text{OH} + \text{CH}_2\text{O} \rightarrow \text{HCO} + \text{H}_2\text{O}$. Their results shows that CH mole fraction doesn't track the heat release rate well when the flame composition varies from rich to lean conditions regardless of the dilution level and equivalence ratio. Caution needs to be exercised when interpreting CH front discontinuities as an indication of local extinction during flow–flame interactions in environments where variations in reactant composition may exist (Najm et al. 1998).

CH is relatively short lived compared to OH and only exist within the flame structure. It was reported by Najm et al. (1998) that CH PLIF in the excitation to the A or B state in an atmospheric hydrocarbon is highly dependent on temperature. But on the other hand due to the narrow region in which CH exists, temperature across the profile isn't very large therefore CH images can be interpreted as mole fraction.

From the work by Najm et al. (1998) it was shown that the CH signal decays much faster than HCO in N_2 - diluted flames. Also the CH signal disappears early in a vortex pair flames interaction. So in the context of the work being carried out CH PLIF will not be an adequate marker for the flame or a good measure of heat release due to the nature of the flame analysed.

The concentration of $[\text{OH}][\text{CO}]$, which is related to the production rate of CO_2 by the reaction of $\text{OH} + \text{CO} \rightleftharpoons \text{H} + \text{CO}_2$, has been suggested in the work by Najm et al. (1998). While the data of the $[\text{OH}][\text{CO}]$ signal exhibit a significant scatter when compared to the theoretical heat release rate, there was an overall trend that was observed in their study. They proposed that $[\text{OH}][\text{CO}]$ should be used as a measure of heat release, allowing the observed degree of uncertainty due to the effects of flow disturbances.

But the disadvantage of using $[\text{OH}][\text{CO}]$ concentration for measurement of heat release is difficult implementation of CO PLIF. Najm et al. (1998) used a two photon excitation PLIF on CO – air flames. They reported that accurate interpretation of the CO signal requires characterization of quenching dependence on temperature and collisional bath composition.

After the review different heat release rate measurements techniques, the work presented here makes use of dual PLIF measurement of OH and H_2CO PLIF (HRX) to estimate the heat release rate. The next section will detail the instruments used for the excitation and capture of OH and H_2CO PLIF. Recent work carried out by Nikolaou et al. (2013), re-examined $[\text{OH}]_x[\text{CH}_2\text{O}]$ based HRX correlation. They found that HRX correlations were strongly dependent on the stoichiometry. For methane-air flames alternative markers were suggested, on the other hand for multi-component fuel a two-scalar based marker is found to be inadequate. It is reported that the product of atomic hydrogen and formaldehyde concentration $[\text{OH}]_x[\text{CH}_2\text{O}]$ correlates

better with HRX, over a broad range of equivalence ratios of practical interest, than $[\text{OH}]_x[\text{CH}_2\text{O}]$ for methane-air mixture that is undiluted and diluted with combustion products as in mild combustion scenario. In the light of these recent observations, the objective here is to investigate the feasibility of $[\text{OH}]_x[\text{CH}_2\text{O}]$ technique for multi component fuels in a laminar and turbulent configuration.

As mentioned previously, OH and H_2CO PLIF measurements is used to measure the heat release rate due to the nature of the flames under examination and the applicability of the technique. The OH PLIF system used consists of an Nd:YAG laser (Litron) and a tuneable dye laser (Fine Adjustments Pulsare-S) with a Rhodamine 6G dye with a frequency doubler which allowed for the wavelength of the outputted beam to be around 283 nm. This wavelength corresponds to the Q1 (6.5) transition of the $\text{A}1 \Sigma\text{-X}2 \Pi (1, 0)$ band of OH. This wavelength was chosen due to its low dependency on temperature. The laser beam was formed into a laser sheet by a combination of a plano-concave and bi-convex lens. The OH fluorescence at a wavelength of approximately 310 nm was then captured using a CCD camera (TSI camera) fitted with a UV intensifier which in turn had a Cerco 100 f/2.8 UV lens fitted with a filter combination of UG 11 and WG 305 Scot glass filters.

For the excitation of the H_2CO PLIF the wavelength of 1064 nm of a Nd:YAG laser (Litron) was tripled to 355 nm to excite the $\tilde{\text{A}}^1\text{A}_2 - \tilde{\text{X}}^1\text{A}_1 4_0^1$ absorption band of formaldehyde (Harrington et al. 1993). Using the same technique as for the OH PLIF the beam was formed into a sheet and the fluorescence was captured by a combination of a visible intensifier and CCD camera (TSI camera) fitted with a Nikon 50 f/1.2 lens and a combination of GG 395 and BG 39 filters.

So far most of the simultaneous OH and CH_2O PLIF measurements for heat release rate measurement was mainly carried out on hydrocarbon flames (Paul et al. 1998, Vagelopoulos et al. 1994, Fayoux et al., 2005, Balachandran et al. 2005, Ayoola et al. 2006), and the technique can also be extended to biogas (primarily methane and carbon-dioxide mixture) and syngas (methane, carbon-monoxide and hydrogen mixture) flames. From computational data obtained (Swaminathan, 2012) for OH and CH_2O concentration for laminar flames of methane and biogas (60% methane and 40% carbon-dioxide), a plot of the product of different radicals against the theoretical heat release is shown below in Figure 2-11.

When biogas is compared to pure methane in Figure 2-12, it can be seen that the point – to – point correlation of the concentration OH and CH_2O ($[\text{OH}]_x[\text{H}_2\text{CO}]$) matches well for both

cases and a close to linear relationship exists with the theoretical heat release. Looking at Figure 2-13, at higher equivalence ratio the linearity with respect with theoretical heat releases start to deviate. But from Figure 2-11, while examining the spatial distribution of the theoretical heat release with $[\text{OH}]\times[\text{H}_2\text{CO}]$ correlation a good spatial correlation seems to exist. A more detailed experimental analysis will be shown in chapter 3.

2.3.4. Particle image velocimetry

Particle Image Velocimetry (PIV) is a laser base technique used to accurately determine the instantaneous flow field across a planar cross-section of a flow field. The flow is generally seeded with tiny and neutrally buoyant tracer particles such as olive oil and aerosols for non-reactive flows and solid particles (Aluminium oxide, titanium dioxide) for combustion processes. Using the same principle explained in the PLIF section, a double pulse laser beam is formed into a sheet and passed through a section of the seeded flow. With the double pulse laser the particles in the flow will be illuminated twice with a small time separation between the pulses.

The displacement of the illuminated particles between the lasers pulses are recorded as either a single image exposed twice or as a pair of two single exposures. Using the captured images the particle displacement field can be measured locally across the whole field of view of the images, scaled by the magnification and then divided by the known pulse separation to obtain flow velocity at each point. Using image-processing technique the displacement can be measured to better than 0.01 pixels on CCD cameras (Willert & Gharib. 1991). Depending on the velocity field and the factor of magnification of the camera lenses the delay of the two pulses have be chosen such that there are enough displacement of the particle images on the CCD images. Enough displacement by the particles is required to increase the accuracy of the velocity calculated. The PIV recording is divided in small sub-areas, so called the interrogation windows. Using statistical correlation techniques one local displacement vector is determined for each interrogation window. For this reason the size of this interrogation window is selected that all the particles within the area have moved homogeneously in the same direction and by the similar distances. Furthermore, it determines the number of independent velocity vector and therefore the maximum spatial resolution of the velocity map which can be obtained at a given spatial resolution of the sensor employed for recording.

The evaluation of the particle images depends on the way these images have been recorded by the camera. One possibility is to record the scattered light of both illuminations in one frame what is called a 'single frame/double exposure'. The other possibility is to record the scattered light from the illuminating particles on two separate frames. This is generally referred to as double frame/double-exposure. So depending on the way the images have been captured, different evaluation technique can be employed. The first method the vector evaluation is

carried by the use of auto-correlation technique whereas the latter employed the cross-correlation technique. For the purpose of the study carried out the double exposure technique was employed during the PIV experimental investigations.

In the case of auto-correlation the scattered light from the tracer particle from the first and second exposure is recorded on the same image. The image is then as mentioned above divided into small interrogation window and the movement of the particle is evaluated using auto-correlation. The auto-correlation works on the underlying principle by two identical correlation peaks rotationally symmetrical about the highest peak indicating zero displacement. This has certain drawbacks as it is not always possible to detect the sign of the displacement as it is not known which particle is illuminated by the first and second laser pulse. So the information obtained from the auto-correlation can often be ambiguous and inconclusive with prior knowledge about the flow. Another problem that can arise using the auto-correlation is the detection of small displacements as the correlation peaks are very close to the central peak.

In the case of cross correlation the scattered light from the particles are collected on two different frames. As with the auto-correlation the image pair are divide into small interrogation windows and each frame is evaluated by cross-correlation. Generally for cross-correlation a fast double shuttered CCD camera is used to record the images. The smallest delay between the two lasers pulses illuminating the particles is limited by the time required for the frame transfer of the camera. Compared to auto-correlation, the cross-correlation method has higher correlation peaks therefore has less unambiguous vectors.

In PIV full information about the flow velocity field (except the magnification of the image) is stored at the recording time. This results in the interesting feature that PIV recordings can be easily exchanged for evaluation and post-processing with different techniques. The information about the flow field can be used in a different ways from that it which was originally intended to obtain other useful information without the need to repeat the experiments.

2.4. Data processing

This section details the data and image analysis technique used to study (1) the flame response based on OH* chemiluminescence, (2) the image analysis for flame surface calculation for forced and unforced flames, (3) HRX measurements and (4) the curvature.

2.4.1. Determination of the flame response based on OH* chemiluminescence

The measurement when subjected to acoustic forcing showed that the pressure, p , and OH* chemiluminescence signal had a cyclic response under acoustic forcing. Using a Fast Fourier Transform (FFT) technique the spectral time traces of OH* were analysed to evaluate the complex amplitude of the quantity, OH*', at the forcing frequency, f . This value was normalised with the time averaged mean $\langle \text{OH}^* \rangle$ to obtain $\text{OH}^{*'}(f)/\langle \text{OH}^* \rangle$. As mentioned earlier, these normalised values were used to represent the heat release fluctuation, $Q(f)/\langle Q \rangle$. Using this quantity with the velocity perturbations, $u'/\langle U \rangle$, determined from simultaneous pressure oscillation measurements it was possible to determine the non-linear transfer function (NLTF) or flame transfer function, H , defined by:

$$H(Q, U) = \frac{Q'(f)/\langle Q \rangle}{u'/\langle U \rangle} \quad \text{Equation 2-1}$$

2.4.2. Image analysis

This next section describes the image analysis performed on the PLIF images. Firstly the method by which the background noise was removed by image subtraction and filtering is shown. Secondly, the flame surface calculation is explained, by first presenting the methodology behind the flame front extraction and then the flame surface calculation. Lastly, the geometrical transformation used for the dual PLIF measurements is presented along with the curvature calculation.

2.4.2.1. Background noise correction

Background noise recorded in the fluorescence contributes to unwanted signals to the pixels on the ICCD chips. The background can be due to reflection of the quartz enclosure that encloses the combustion region or due to elastic scattering of small particles present in the air. In order to correct for these unwanted signal the test area was illuminated with the laser sheet and a set of images were recorded. These images were then averaged and stored and subtracted from every fluorescence image recorded by each camera.

Background noise is not the sole contributor to unwanted noise in the fluorescence image. Other sources of random noise on the fluorescence image can come from several sources such as the thermal charge produced in the intensifier of the CCD chip (dark noise), variation of the detector sensitivity, read out of the CCD chip in regions of low light, electrical power fluctuations and stray radiation from electrical nearby equipment. The presence of such noise affects the accurate extraction of information such as the flame contour or the curvature. Different type of smoothing filters can be used to remove random noise from the images such as low-pass, high-pass or band-pass filter. Although smoothing filters are great at removing random noises, it has a major disadvantage of sometimes blurring the edges and other sharp details. Hence, for the purpose of this work these filters are not appropriate as the preservation of the flame front (sharp contour) is essential. The most suitable type of filter was found to be a median filter as this filtering process works on the principle of comparing each pixel within its neighbouring pixels with a certain kernel size. Using this filter, there was a sharper contrast between the signal and the background noise.

2.4.2.2. Flame surface calculation

The raw OH PLIF images were postprocessed before calculating the flame surface (FS). Firstly, a background image which was measured in the absence of the flame was subtracted from the raw fluorescence images. To reduce the noise a median filter was first applied, which was followed by filtering in order to smooth the image while preserving the flame-front edges. The resulting images were then converted into binary images by means of an intensity thresholding procedure. The pixel value of 1 corresponds to progress variable equal to 1 (burnt gases) and pixel valued of zero indicate a progress variable of zero (unburnt gases). The instantaneous

flame contour of unit pixel width was obtained from the map of progress variable. The revolution of the average flame front data about its symmetrical axis was used to compute the flame surface area. This quantity (FS) can be used to evaluate heat release modulation in forced premixed flames (Figure 2-14).

As well as acquiring OH PLIF, H₂CO PLIF was also measured during some of the experiments. Before the spatial distribution of OH and H₂CO PLIF can be compared or pixel by pixel multiplication can be carried out, both set images had to be geometrically transformed into the same co-ordinate system. The geometrical transformation plays a critical role in calculating HRX accurately. The following section illustrates the steps taken to achieve the geometrical calculation.

2.4.2.3. Simultaneous PLIF of OH and H₂CO

The measurement of the product of OH and H₂CO PLIF requires the multiplication of two PLIF images that were simultaneously recorded by the ICCD cameras that were arranged in such a way that they were facing each other. The images from both cameras are misaligned with each other. Both cameras were imaging the same area of the flame but due to misalignment of the cameras in the experimental set-up there was a displacement of several pixels between the images. Also in order to increase the accuracy of the overlap of the OH and H₂CO PLIF only one part of the flame was imaged. In order to correct for the shift, one PLIF image (in this case OH PLIF image) was transformed using a geometric mapping algorithms to match the corresponding reference PLIF image on a pixel-by-pixel basis. Due to the relatively small flame thickness of hydrocarbon flames (100µm) a precision in the sub pixel is required to accurately resolve the flame fronts. Therefore an accurate geometrical transformation is critical for successful product of OH and H₂CO PLIF.

Also the precision if the geometrical transformation enables the capture of small variations in the flame structure. This alignment process was carried out in several stages. Firstly, a target image was taken using both the cameras. The target was a grid pattern with several reference points positioned in the same alignment of the measuring plane defined by the laser sheets. Secondly, the H₂CO image was mirrored and the corresponding coordinates of the same reference point were identified. Thirdly, a transformation matrix relating the two sets of coordinates was computed and then used to map the OH images onto the coordinates system

of the H₂CO images. The geometric transformation ψ relating to the pixel movement between a reference points from the reference image to the target image is given by:

$$x' = \psi_x(x, y) = \sum_{i=0}^N \sum_{j=0}^N a_{i,j} x_{\text{ref}}^i y_{\text{ref}}^j \quad \text{Equation 2-2}$$

$$y' = \psi_y(x, y) = \sum_{i=0}^N \sum_{j=0}^N b_{i,j} x_{\text{ref}}^i y_{\text{ref}}^j \quad \text{Equation 2-3}$$

The geometric transformation can be modelled as a quadratic polynomial and express as follows:

$$x' = a_0 + a_1 x_{\text{ref}} + a_2 y_{\text{ref}} + a_3 x_{\text{ref}} y_{\text{ref}} + a_4 x_{\text{ref}}^2 + a_5 y_{\text{ref}}^2 \quad \text{Equation 2-4}$$

$$y' = b_0 + b_1 x_{\text{ref}} + b_2 y_{\text{ref}} + b_3 x_{\text{ref}} y_{\text{ref}} + b_4 x_{\text{ref}}^2 + b_5 y_{\text{ref}}^2 \quad \text{Equation 2-5}$$

2.4.2.4. Flame curvature

In order to compute the flame curvature, firstly the flame contour was defined in the same way as in the case of the flame surface area. Secondly the flame curvature H , can be calculated using the flame edger co-ordinates (x, y) of the OH PLIF image as:

$$H = \frac{\frac{d^2 y}{dx^2}}{\left(1 + \left(\frac{dy}{dx}\right)^2\right)} \quad \text{Equation 2-6}$$

However, the use of an independent variable, s , has been reported to provide improvement over the curvature measurement as it can analyse the curvature regardless of the slope and complexities of the flame. The coordinates (x,y) of each point along the OH PLIF contour was evaluated with respect to an origin s taken to be the point along the contour at which $x=0$. With (x, y, s) , the curvature H at every point on the flame front is calculated using the following equation:

$$H = \left[\left(\frac{d^2x}{ds^2} \right)^2 + \left(\frac{d^2y}{ds^2} \right)^2 \right]^{1/2} \quad \text{Equation 2-7}$$

Here the positive curvature is defined as being convex to the reactant gases and negative curvature is defined as being concave to the reactant gases. The choice of ds in the above equation is crucial as it needs to capture both the small scales and large scale wrinkles. In the study by Ayoola et al. (2006) the value of ds was obtained from the average crossing length of the instantaneous flame front with the OH PLIF progress variable contour, \bar{c} of 0.5. In the study by Haq et al. (2002), they observed that the size of the window has a strong influence on the accuracy on the calculation of the curvature. If a small window was used high curvatures could accurately be fitted however there was a large scatter in the measurements of low curvature. It should be noted that the type of flames used in the work by Haq et al. (2002) were spherically expanding flames. Therefore for the purpose of this study, the same approach used by Ayoola et al. (2006) was employed. The contour was obtained by making a contour plot of an average binary image of OH PLIF images. The crossing lengths are then obtained by superimposing instantaneous flame contours $\bar{c} = 0.5$ and calculating the distance along the flame front of which \bar{c} is crossed by the instantaneous flame contour. A probability density function of all the crossing lengths analysed for all the instantaneous images was then plotted. The crossing length which was chosen to represent adequately both the large and small scales curvatures were taken to be the length corresponding to the minimum between the major peaks of the probability function. Ayoola et al. (2006) found that a crossing length of 4 mm was sufficient to capture both the large and small scales wrinkling for bluff-body stabilised turbulent premixed flames.

2.5. Chapter 2 Summary

In this chapter firstly, the design and development of a laminar and turbulent burner is shown. The laminar burner was developed so that the laminar flame speed of multi components fuels could be measured. The burner was designed in such a way that a fully developed laminar flow will be achieved at the exit. Also a large enough nozzle to stagnation plane separation allows for accurate implementation of different laser diagnostic technique. The development of the turbulent burner allow for the study of the flame response of premixed multi-components fuels. Also described in this chapter are different experimental techniques for heat release rate measurements and the methods chosen for this experimental study. Finally, the last part of the chapter provided details of the different data analysis techniques used, particularly highlighting its applicability for the study of forced turbulent premixed flames.

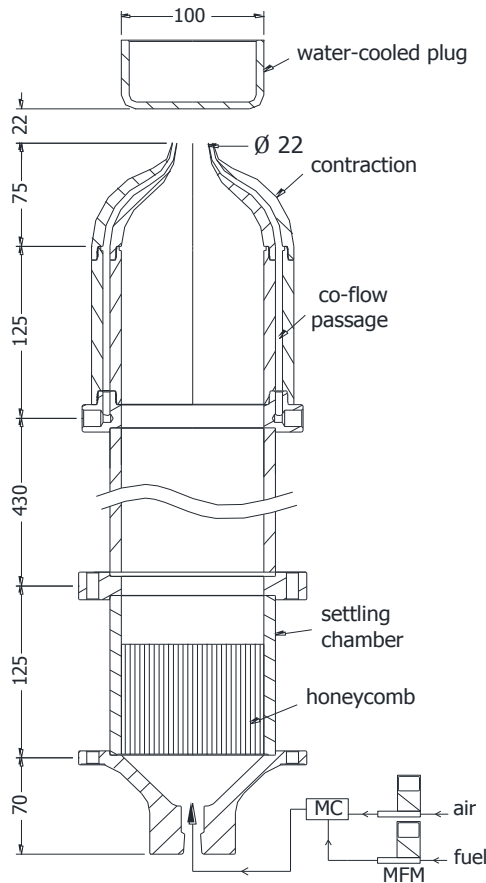


Figure 2-1: Schematic of the stagnation burner

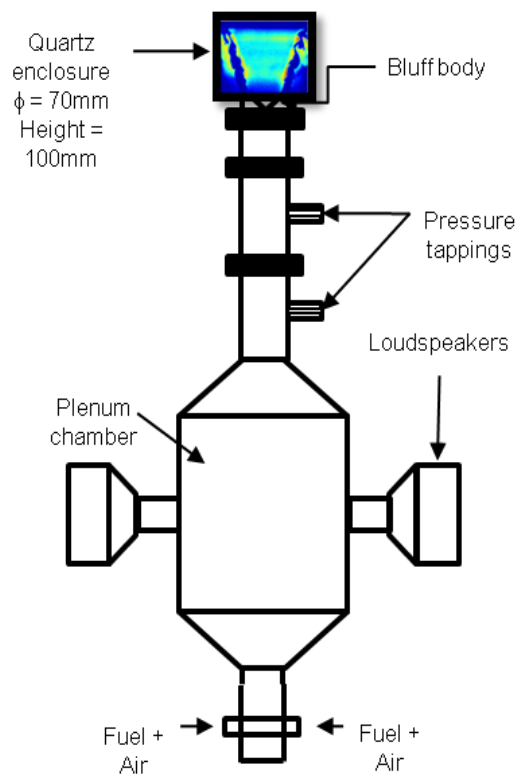


Figure 2-2: Model Gas turbine

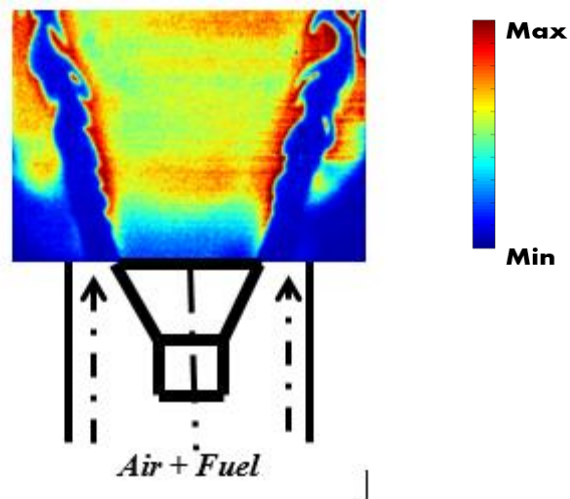


Figure 2-3: Typical OH PLIF image of Bluff-Body stabilised flame

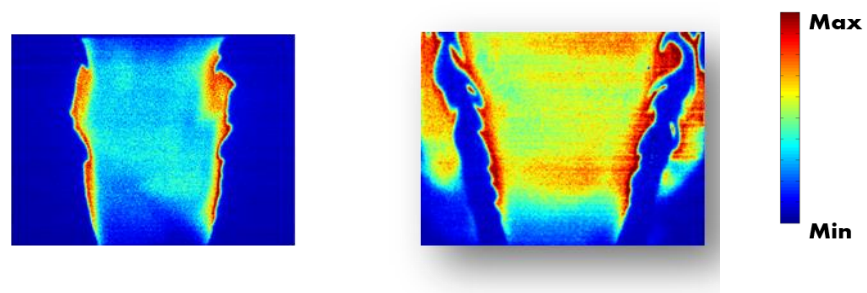


Figure 2-4: (left) Open & (right) Enclosed instantaneous OH PLIF image

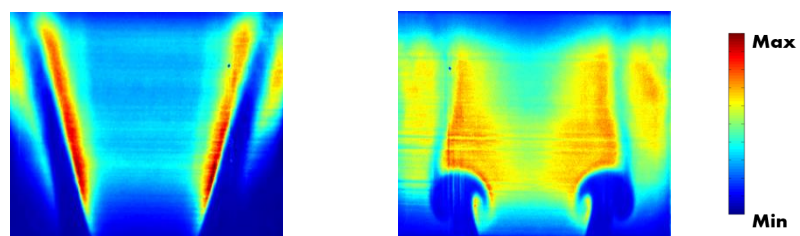


Figure 2-5: (left) Unforced and (right) forced pure methane flame OH PLIF images

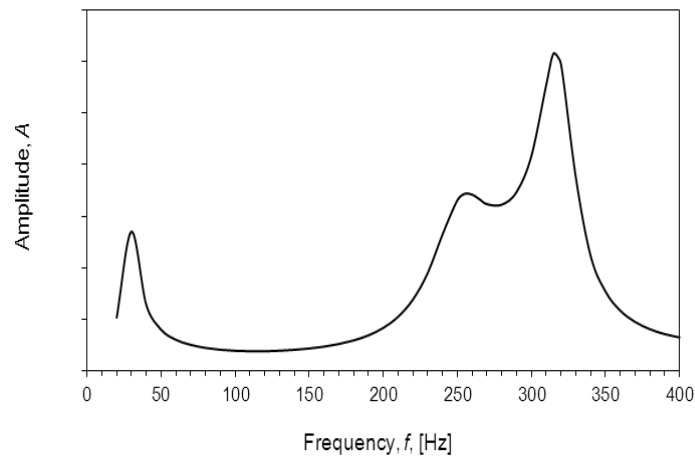


Figure 2-6: Frequency response due to acoustic forcing

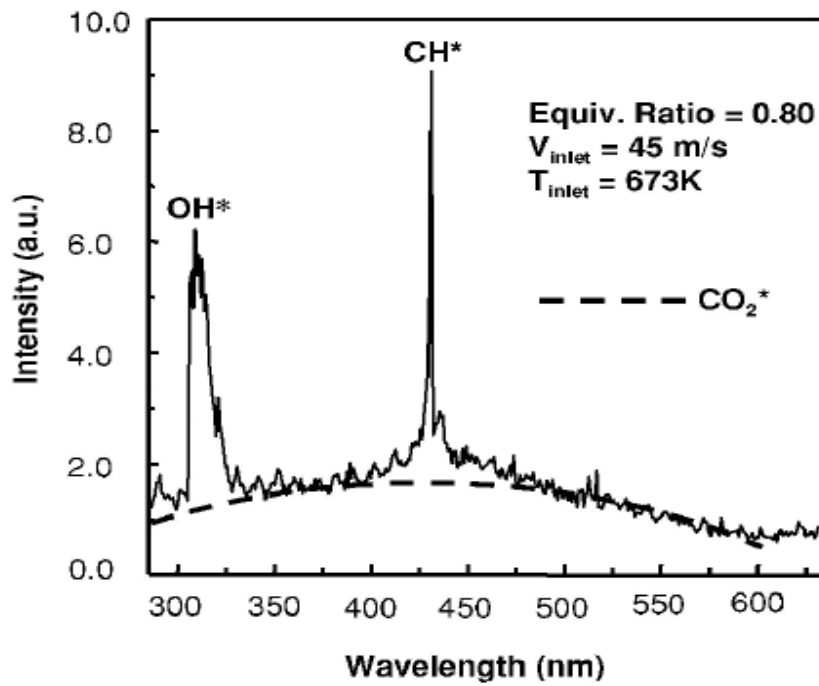


Figure 2-7: Intensity of different chemiluminescence species (Lee & Santavicca, 2003)

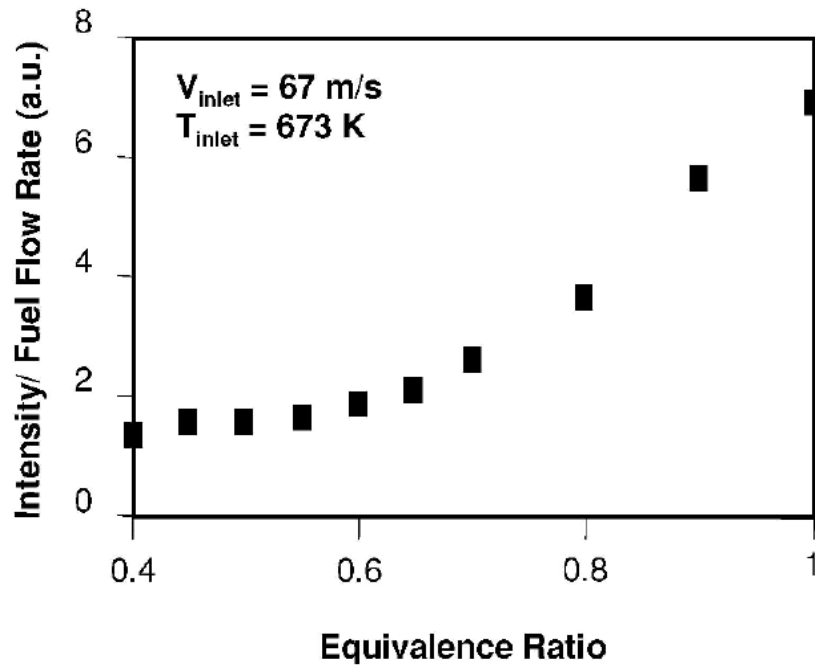


Figure 2-8 : Fuel intensity with Equivalence ratio variation (Lee & Santavicca, 2003)

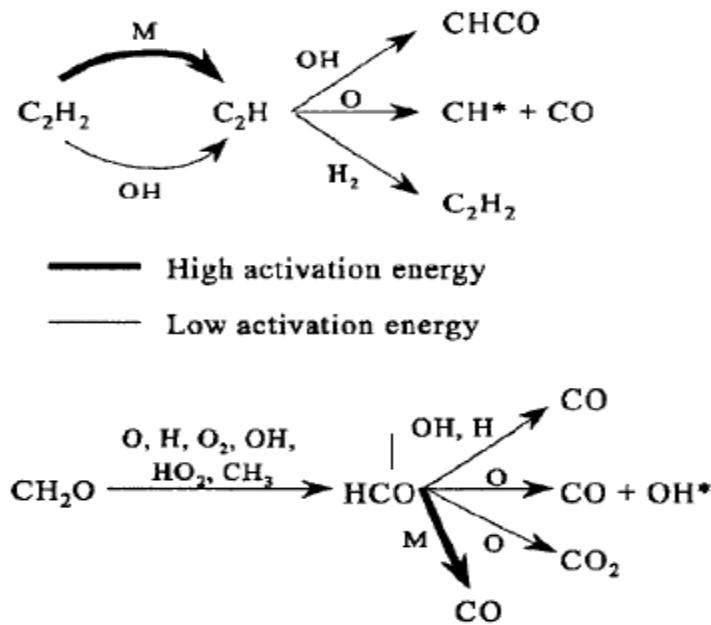


Figure 2-9: Reaction path of H_2CO (Haber, 2000)

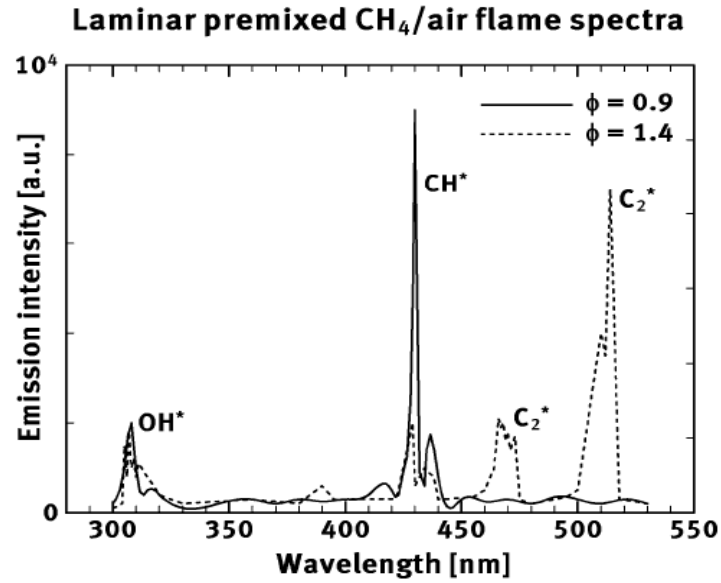


Figure 2-10: Chemiluminescence spectra of premixed pure methane (Haber, 2000)

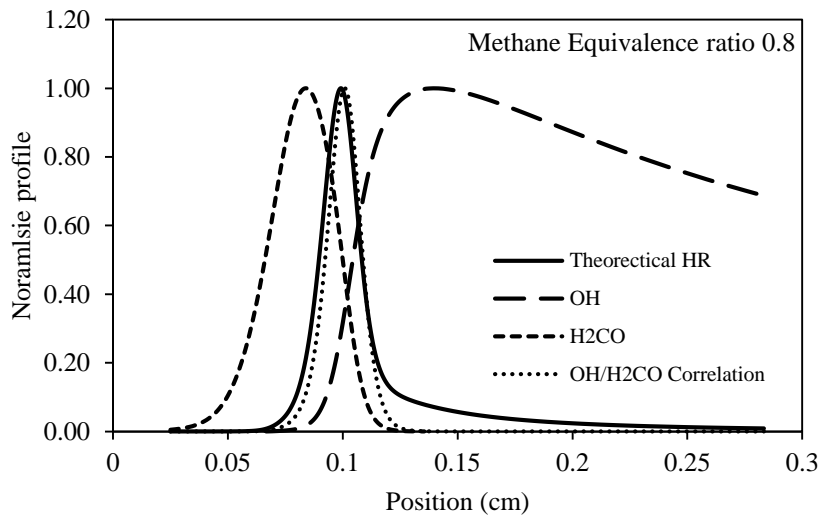


Figure 2-11: Spatial distribution of OH, H₂CO, Heat Release and Heat Release Rate (HRX) based on [OH]x[H₂CO]

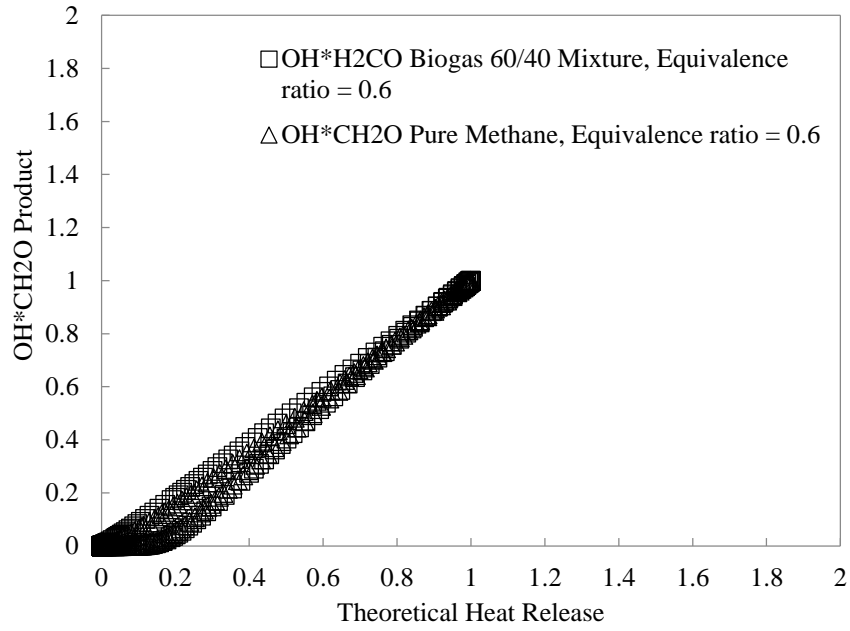


Figure 2-12: Numerical Chemkin of Methane and Biogas at equivalence ratio 0.6

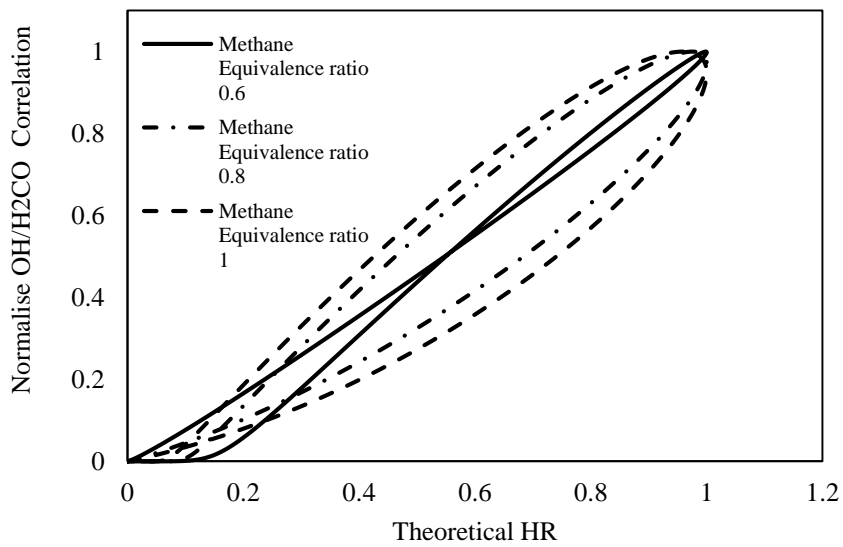


Figure 2-13: Theoretical Heat Release versus Heat Release Rate (HRX) based on [OH]_x[H₂CO] correlation

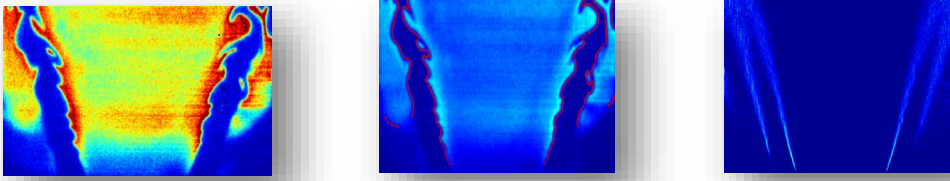


Figure 2-14: (left) Shows an instantaneous OH PLIF image, (middle) Its corresponding flame surface contour, and (right) the average of the flame surface.

Chapter 3

3. Laminar flame characterisation

One of the prime objectives of this chapter's work is to measure the laminar flame speed of multi components fuel such as biogas and syngas. Then, using simultaneous OH and H₂CO PLIF to measure the heat release rate of methane and biogas flames. As discussed in chapters 1 and 2, the stagnation flame approach for stretch corrected measurements was employed to measure the laminar flame speed. The first part of the chapter describes the cold flow characterisation of the burner. Using known laminar flame speed of different hydrocarbon/air fuel mixtures the suitability of the method is discussed. Laminar flame speed computed using Chemkin kinetic simulation (Nikolaou et al. 2013), was used to validate the experimental laminar flame speed for methane and methane/carbon-dioxide mixture. Then syngas at various compositions (varying methane, carbon-monoxide and hydrogen concentration) measurements were performed and the influence of the constituents on the results were discussed, leading on to the heat release rate measurements of methane and biogas on the same burner configuration. The result obtained from the heat release measurements was again compared with some computational results (Chemkin Model). The last part of the chapter assesses the feasibility of the laminar flame speed and heat release measurements (currently the literature lacks information about the laminar flame speed of the mixture under investigation which motivated the development of the system to measure the desired flame speed and HRX).

3.1. Characterisation of the burner

3.1.1. Flow field visualisation – cold/hot flow

As discussed previously the corrected flame stretch method can be used to measure the laminar flame speed. Since the measurement are susceptible to any changes in the flow field, understanding the flow field was important in order to accurately account for and systematically correct for the flame stretch to obtain upstretched flame speed values. It is well known that stagnated stabilised flames are subjected to some type of aerodynamic stretch. This can manifest itself through flow non-uniformity, flame curvature or flame unsteadiness (Chung

et al. 1984, Goey et al. 1997). Flame stretch can be defined as the fractional rate of change of a flame surface area (Law et al. 2000), $K = 1/A \cdot dA/dt$, which can be attributed due to the contribution from aerodynamic strain, flame curvature and flame motion (Law et al. 1994). The stretch effect on the laminar flame speed is dependent on the Lewis number (Le). For mixtures with $Le = 1$, the heat and mass transfer are in balance and its resulting effect on the flame speed is close to zero. For $Le < 1$, the flame speed tends to increase with strain rate due to the local flame acceleration. This can be explained by examining the shape of the flame which takes a convex orientation to the reactants. In doing so the flame tends to accumulate heat in the products adjacent to the flame front. On the other hand, a $Le > 1$, will result in a decrease in flame speed with strain rates as the thermal diffusivity through conduction is greater than molecular diffusivity. This is due to the fact that as flame front curves towards the reactants, it slows down due to thermal influence on the reactant mixture. This in turn causes the flame front to straighten itself and become stabilised (Law et al. 1984). The relation of the strain effect of the flame to the thermal-diffusivity of the mixture is manifested in the slope of the unstrained flame speed S_u against stretch rate K . Under the condition of one-dimensional stagnation flame, Kumar et al. (2008) showed that the flame response to stretch rate variation differs according to fuel mixture. Further on in this chapter the method by which the upstretched laminar flame speed is obtained from different strain rates will be shown.

3.1.2. PIV measuring conditions

The impinged jet velocity was obtained using one dimensional PIV. The flow was seeded with titanium dioxide (TiO_2) particles. The nominal size of these particles was chosen to be 1 – 2 μm to minimise the effect of thermophoretic effects (Natarajan et al. 2007). Due to the range of flow rates used during experimentation, care has to be taken to make sure the selected particles seeded the flow correctly and were not affected by the co-flow or the plug position. Therefore cold flow measurements of the same flow rate with different tracer particles were measured and then compared. Two different types of seeding particles were used, oil droplets and titanium dioxide particles. From these experiments the radial profile axial velocity and the centreline axial velocity gradient were measured close to the nozzle exit. The measurements show less than a 12% variation of the axial velocity in the radial direction and moving towards the centreline the axial velocity gradient tend to zero reaching a minimum at the nozzle exit. Figure 3-1 shows the centreline velocity profile obtained for cold flow measurements close to

the exit of the nozzle up to the stagnation point. The measurements show that strain rate for the same flow rate with different tracer particle has less than a 1% deviation. Furthermore, Figure 3-2 shows that flow rate of the co-flow does not have a significant effect on the centreline velocity profile provided the flow rate doesn't exceed 19.5 lpm. As described in chapter 2 the laser sheet was obtained through a combination of a Plano – concave and Bi - convex lens arrangement. A laser sheet of 300 mm was produced, with the Nd:YAG laser operating at 50mJ/pulse at 532nm. The scattered light was captured on a CCD camera with 1024x1264 pixels, fitted with a band pass filter centred at 532 nm to remove any flame luminosity and the correct capture of the particles movement across the flame front. The commercial software Insight3G was used for the image acquisition and subsequent image processing. The field of view was fixed at 25 x 25 mm area with a magnification factor M equal to 0.4.

3.1.3. PIV accuracy and uncertainty

The timing between the two laser pulses was kept at a Δt ($\sim 200 - 225 \mu s$) such that the particle movement in the region of the flame was within $\frac{1}{4}$ of the interrogation window. Uncertainties in velocity measurement using any optical method that tracks particle motion is highly dependent on statistical information gathered from the optical interrogation cell window within which the sampling occurs. In the case of PIV, there is a trade-off between seeding density and interrogation window size on the number of statically significant particle displacement measurements. While increasing the size of the interrogation window improves the statistics, it may also limit the spatial resolution, since the average particle within the window may be skewed (Zhao et al. 2004). A Study by Zhao et al. (2004) have shown that as the window size is decreased, the seeding must be increased to maintain a sufficient number of particles within the window required to obtain an appropriate level of statistical sampling. While further decreasing the window size and increasing the number of particles, the statistics will decay due to overlapping of particle images. Therefore, a comprise between the window size and the particle density needs to be achieved. For the purpose of the work carried out the number of seeding particles was kept between 8 – 10 particles per sub-region to obtain a high quality for the PIV correlations. For the image analysis the cross-correlation technique with an adaptive multi-pass method was employed for the image analysis. Initially an interrogation

window of 64 x 64 was used before the final window size is spatially reduced to a 32 x 32 with a 50% region overlap to optimise for the spatial resolution of the velocity field.

Other sources of uncertainties in the measurements could be due to the timing error of the laser but it was found that this was small enough that it had an insignificant contribution towards the velocity measurements. Another common source of error in the experimental method can be attributed to peak locking, which occurs when the particle image size drops, resulting in a loss of sub pixel precision. The full scale PIV measurement error can be determined by the ratio of the nominal correlation peak value to the maximum displacement permitted, namely $\frac{1}{4}$ of the final interrogation window (Westerweel et al. 2006). For the purpose of this work the final window was chosen to be 32 x 32, the accuracy full scale is approximately $\pm 1.5\%$.

3.1.4. Laminar flame speed determination

Using the planar 2-D velocity vector field the reference stretched flame and the imposed strain rate can be determined. Figure 3-2 shows an axial velocity field and the corresponding flat flame shape. It can be seen that axial velocity decreases from the exit of the nozzle and reaches a local minimum and then through the flame there is a sharp increase in the axial velocity due to thermal expansion. Then the lowest velocity was found to be at the stagnation plane.

Therefore, from the data extracted (from the PIV measurements), the laminar flame speed can be computed based on a similar principle as proposed in the study by Law et al. (1984). There was a standard approach which was employed whereby the minimum velocity before the preheat zone is considered as the reference strained unburned flame speed and, the maximum gradient of the axial velocity before the minimum velocity location is taken as the imposed strain rate (K). The imposed strain rate could be controlled by changing the nozzle exit velocity. It was observed with an increase the nozzle exit velocities in turn increases the strain rate which also pushes the flame closer to the stagnation plane. During the experiment, the strained unburned flame speed was measured across a range of strain rates with the upper and lower limit restricted by flashback or flame stability. Once a range of strain rates with their respective strain unburned flame speed were obtained, a linear correlation was found to exist between them. This relationship was also reported in previous work by Law et al. (1984).

Previous work has shown that the unstretched flame speed can be obtained by using the methodology of either linear or nonlinear extrapolation to zero stretch rate. The linear

extrapolation is the most commonly employed method but work has been carried out whereby the nonlinear approach was used. Vagelopoulous et al. (1994) have shown that if the Karlovitz is lower than 0.1, the laminar flame speed obtained from the linear extrapolation method yield sufficiently accurate results. A typical strain rates ranges from $\sim 100 - 250 \text{ s}^{-1}$ was used Vagelopoulous et al. (1994) which yielded a Karlovitz value less than 0.1. Generally the flame speed measurement obtained from linear extrapolation yields a lightly higher upstretched flame speed compared to nonlinear extrapolation method (Vagelopoulous et al. 1994). Chao et al. (1994) reported that the accuracy of the linear extrapolation method can be increased using a larger separation between the nozzle and the stagnation plane. As mentioned by Vagelopoulous et al. (1994), Chao et al. (1994) also observed that a low Karlovitz yielded a more accurate laminar flame speed measurement when the linear interpolation was used. The nozzle diameter used in this investigation was 22 mm, which allows sufficient nozzle-stagnation plane separation making the linear extrapolation method suitable.

3.2. Results and Discussions

3.2.1. Methane/carbon-dioxide/air

Flame speed measurements for equivalence ratio 0.75 methane/air mixture at room temperature and pressure as shown in Figure 3-3 was used to validate the system. Results are shown for a large set of data, from 200- 250 image pairs for each strain rate measurement. The precision for the averaged results is ± 0.1 cm/s based on a 95% confidence level. These results show good agreement when compared with simulation from Chemkin. The accuracy of the measurements was better than the one expected from counter flow twin flame system which has a deviation of 5% as shown by Law et al. (1986). Throughout the experimental procedure some of the strain rates were selectively performed as control test to demonstrate good repeatability. The experiments were conducted for various nozzle exits' velocities and ratio of L/D (this ratio was altered by changing L) to modify the strain rates. For a fixed nozzle diameter the flame shape was primarily dependent on the exit velocity and L (the position of the stagnation plane). At a ratio of $L/D \sim 1$, the flame was observed to be planar for large exit velocities. As the exit velocities decrease the flame starts to approach the nozzle with a non-uniform shape. By further lowering the exit velocity the flame non-uniformity intensifies especially around the centreline. Eventually the flame becomes very unstable and flashback of the flame occurs. Lower strain rates could also be achieved by increasing the distance of the stagnation plane from the nozzle exit. By keeping the exit velocity constant and increasing L , the flame moves away from the burner and lower strain rates could be obtained. This approach has been shown by Vagelopoulous et al. (1994) to result in low-strain rate flames, which are both stable and planar. As noted by Vagelopoulos et al. (1994) it was found that stable flames of large values of L can only be achieved under certain conditions, given that various instabilities started to develop; these instabilities can be thermo diffusional and hydrodynamic nature. It is also worth mentioning that for large value of nozzle to stagnation plane separation the flame is more sensitive to external perturbation and seeding particles.

Vagelopoulous et al. (1994) recorded that as L increases, the local preflame strain does not change notably beyond a certain values of L/D . Experimental and numerical results have shown that if L/D is very large, the axial velocity profile is a hybrid between a free-jet close to the nozzle and a stagnation type flow, close to the stagnation plane (as the flow exits the nozzle, the axial velocity reduces gradually and at a higher rate as it approaches the flame).

Furthermore it was observed that a planar flame can become a Bunsen like flame by reducing the exit velocity and by further increasing L . If L is sufficiently large the exiting jet behaves as a free-jet whereby the Bunsen flame stabilisation mechanism prevails. The present experimental study supported by previous studies seems to indicate that nozzle separation ratio of $0.7 - 1$ of L/D is a good compromise for most hydrocarbon/air flames with burning characteristics similar to that of methane/air flames such as the rate of reaction, exothermicity and laminar flame speed. For the methane/air mixture at an equivalence ratio of 0.75, the laminar flame speed obtained was 22.1 cm/s which have a deviation of less than 1% compared to values found in literature.

The next step consisted of measuring the laminar flame speed of a methane/carbon-dioxide/air at ratio of 0.6:0.4 methane/carbon-dioxide mixture (Figure 3-4). Having very similar burning characteristics as methane/air mixture, the same nozzle and stagnation plane separation was used. The experimental studies with the addition of carbon dioxide have revealed that the presence of CO_2 in the fuel mixture has a significant effect on the flame propagation, extinction and detailed thermal and compositional structures (Ju et al. 2005, Shy et al. 2005, Ruan et al. 2001). Such effects of CO_2 can be kinetic and/or thermal nature. Qin et al. (2005) have shown through detailed numerical simulations that carbon-dioxide can be considered as a relatively stable species that can be treated as being inert. Furthermore its production in hydrocarbon flames is mainly attributed to the oxidation of carbon-monoxide, of $\text{CO} + \text{OH} \rightarrow \text{CO}_2 + \text{H}$. Qin et al (2005), have also shown that compared to the production rate the destruction rate of carbon-dioxide appears to be lower but not negligible. In order to further understand the destruction paths of carbon-dioxide Qin et al. (2005) and Liu et al. (2003) performed a species path analysis. Based on their findings they concluded the kinetic effect of carbon-dioxide could be considered as minor for small concentrations of carbon-dioxide in the fuel/air mixture.

The presence of carbon-dioxide could also thermally affect the combustion intensity primarily through two mechanisms. The first mechanism is the reduction of the flame temperature as the carbon-dioxide is inert and acts as a heat sink. The second mechanism is the radiative heat loss enhancement as carbon-dioxide efficiently radiates. Studies by Ruan et al. (2001) showed that when re-absorption is neglected the radiation losses due to carbon-dioxide have a strong influence on the combustion intensity: the higher the radiation losses, the lower the combustion

intensity. As expected, the results indicate for the same equivalence ratio, the addition of carbon-dioxide to the fuel decreases the laminar flame speed.

At equivalence ratio of 0.75 of methane/air mixture and an equivalence ratio of 0.95 methane/carbon-dioxide/air mixture both have very similar laminar flame speed measurement of 22.1 and 22.8 cm/s respectively. Diluting the fuel mixture with carbon-dioxide as expected reduces the laminar flame speed and as shown from the measurement more methane is required to equalise the laminar flame speed.

3.2.2. Methane/carbon-monoxide/hydrogen air mixture

The next set of experimental investigations focused on measuring the laminar flame speed of methane /carbon-monoxide/hydrogen/air mixture. These tests gave an insight on the effect on hydrogen and carbon-monoxide for different CH₄:CO:H₂ ratio: 50:25:25, 50:35:15 and 25:50:25. These compositions were chosen as the same overall power output can be achieved without affecting the Reynolds number when it was later used on the bluff-body stabilised turbulent flames. Although the Wobbe index changes by altering the fuel compositions the flame response was observed not to be affected provided the laminar flame speed remains the same for the bluff-body stabilised flames. This has been one of the main objectives in measuring the laminar flame speed of those fuels of varying compositions. The implications of how the response is unaffected will be further discussed in the next chapter. Measuring the laminar flame speed of methane/carbon-monoxide/hydrogen air mixture was a greater challenge due to the faster fundamental flame velocities of these mixtures due to large percentage of hydrogen.

Most flames for the methane/carbon-monoxide/hydrogen mixture were perfectly stable, however for certain experimental parameters and configurations, such as the equivalence ratio, the $\frac{L}{D}$ ratio, the bulk exit velocity of the mixture and co-flow flow rates. The flame was observed to be perturbed which gave rise to flapping of the flame edges and would on occasion be coupled with noise. The flapping characteristics has been previously been mentioned by Berghorson et al. (2011) and Bouvet et al. (2011) but only the latter characterised this phenomenon in his work. As in the case of Natatrajan et al. (2007), Berghorson et al. (2011) and Bouvet et al. (2011) the flapping of the flame edges were observed at higher strain rates. These can be associated with by a vortex roll-up structures moving from the burner rim towards the flame edge. For certain experimental configurations a symmetrical vortex pair was observed on both sides of the flame, which was generally accompanied by noise. Whereas on the other hand for a few cases asymmetrical vortices were observed on either side of the flame. The vortex would appear at different height and sometimes would even vary in size.

The effect of the vortices were observed to have a minimal effect on the axial velocity. Since higher flow rates were chosen for the methane/carbon-monoxide/hydrogen mixture efforts were made to suppress the flapping of the flame edges. Higher velocities were also chosen to

prevent any flashback from occurring during the experiments. One way in which the suppression of flapping was achieved, was by matching the co-flow velocities with the velocity of the central jet. As shown previously the co-flow has minimal effect on the axial velocity provided it was kept below 19.5 lpm. Due to the dimension of the nozzle it wasn't always possible to match both set of velocities but care was taken to ensure that no vortices were present on the flame edges. Bouvet et al. 2011 proposed an explanation for those oscillations as the burner system behaving like a Helmholtz resonator. These induced bulk oscillations could be characterised by a resonant frequency which is dependent on the fuel composition as well as the geometry on the burner, which are primarily the nozzle diameter and the size and length of the plenum. They also observed that the oscillations would disappear by changing the nitrogen co-flow with helium.

The mixtures investigated were selected based on the overall power output due to the practical implications which will be later discuss in further details. The individual components of the fuel, methane/carbon-monoxide/hydrogen were adjusted so that the theoretical power output would match. For the various fuel compositions of 50:25:25 (Figure 3-5), 50:35:15 (Figure 3-6) and 25:50:25 (Figure 3-7), the measured laminar flame speed was 26.89 cm/s, 32.51 cm/s and 29.54 cm/s respectively. From the measurement it was observed that increasing the hydrogen and carbon-monoxide content by volume of the fuel resulted in a higher flame speed. This behaviour can be explained by: (1) the overall reactivity of the fuel mixture increases with the amount of hydrogen present, and (2) the low molecular weight of hydrogen acts to increase the diffusivity of the reactant mixture. The equivalence ratios for those mixtures investigated with the same order as above were 0.67, 0.7 and 0.58. From Figure 3-5 and Figure 3-7 it can be seen that the slope of the mixture 50/25/25 is nearly twice the one measured from the 25/50/25 mixture. In order to fully quantify the effects of hydrogen and carbon-monoxide, a wider range of flames and equivalence ratio need to be tested to gain an in-depth understanding of role the different components plays in the reaction. Yu et al. (1986) noted that an increase in the hydrogen content in the fuel decreases the overall flame thickness as it would have been expected that an increase in the hydrogen would increase the flame thickness due to the high thermal diffusivity of the mixture. The explanation proposed was that the overall heat release rate with high hydrogen content is dominant which causes the overall decrease in flame thickness. Therefore the addition of inhibitors to the fuel and measuring the flame speed might provide a further insight on the reaction path. Figure 3-8 and Figure 3-9 shows a summary of

the measurements of the strain rates different syngas mixtures and the laminar flame speed for the syngas mixtures, methane and biogas respectively.

Following from the characterisation of the laminar burner and laminar flame speed measurements the heat release rate was measured. The next section of this chapter presents the results for heat release measurement of methane and biogas flames. The results were also compared with a Chemkin model.

3.3. Heat release measurements for methane and biogas

The heat release rate measurements were performed on laminar flames stabilised in the same impinging jet configuration. The equivalence ratio of 0.8 is used as the base case. Three sets of experiments were performed: 1) Effect of varying equivalence ratio in pure methane-air flames, 2) Effect of bulk strain rate in a pure methane-air flame, 3) Effect of varying CO₂ addition on a methane air flame.

The profiles of OH and H₂CO were extracted from instantaneous realisation and averaged in flame-fixed co-ordinates. For laminar flames if the profiles are not averaged in a flame-fixed co-ordinates, mild variation (~ 0.2 mm rms) in the flame position will introduce an artificial thickening of the flame. Therefore to avoid such uncertainty the flame was corrected to be in a flame fixed co-ordinate system. Hence from the corrected images the profiles for OH and H₂CO could be extracted and subsequently compared. Furthermore the HRX profile could be also spatially extracted to assess effect of CO₂ dilution.

Table below shows the equivalence ratio, the inlet bulk velocity and the flame height (distance above the nozzle).

Φ	<i>Height mm</i>	<i>Bulk Velocity (m/s)</i>
0.7	0.7	15.41
0.8	0.8	12.54
0.9	0.8	8.00
1	0.95	9.51
1.1	1	10.16
1.2	0.95	8.81

Table 3-1: Flame height and overall bulk velocity with respect to change in equivalence ratio for pure methane

Φ	<i>Height mm</i>	<i>Bulk Velocity (m/s)</i>
0.8	0.6	8.54
0.8	0.7	10.81
0.8	0.8	12.54
0.8	0.9	13.73
0.8	1	14.92

Table 3-2: Flame height and overall bulkk velocity at constant equivalence ratio for pure methane

Φ	<i>% CO₂</i>	<i>Bulk Velocity (m/s)</i>
0.8	0	12.54
0.8	10	13.19
0.8	15	13.35
0.8	25	13.89
0.8	40	14.59

Table 3-3: Overall bulk velocity at different carbon-dioxide dilution

As inferred from Table 3-1, Table 3-1 and Table 3-3, the flames are stabilised at different heights depending on the imposed bulk velocity and the corresponding flame speed. The calculated global strain rate ($2V/h$) varies from 63 – 100 1/s. From literature related to impinge flames, the strain variations were commonly between 150 and 300 1/s (Natarajan et al. 2007). In this work, the strain was varied from 63 – 100 1/s. This variation in strain rate does not appear to affect the thickness of CH₂O as shown in Figure 3-10. Any change in strain rate was not high enough to show any significant change in the integrated HRX estimation.

The thickness of H₂CO profile is evaluated as a full width at half maximum (FWHM). The variation in the H₂CO profile thickness with the equivalence ratio is plotted in Figure 3-11. As the equivalence ratio is increased from 0.7 the H₂CO thickness decreases to a minimum at equivalence ratio 1.1 and subsequently increases with equivalence ratio (Figure 3-11). This trend is similar to that of the variation in flame thickness with the equivalence ratio (Andrews

& Bradely, 1972). On the other hand the HRX profile showed an inverse trend. This trend is comparable to that of the variation in flame speed with equivalence ratio (Andrews & Bradely, 1972). These trends are as expected and in accordance with 1-D flame simulations with small discrepancy in the width of the H₂CO width profile. This difference between experimental and calculated profiles can be attributed to the limited spatial resolution present in the experimental system. The projected pixel resolution in the experimental configuration is 55 μm , however true spatial resolution is governed by the thickness of laser sheet or diameter of laser beam, which are 0.3 mm. The present measurements are uncertain to this extent and observed discrepancies are within this resolution.

The trend in the results was as expected; the HRX increased with equivalence ratio to reach a maxima at 1.1 and then start to decrease. Careful interpretation of the HRX signal needs to be carried out in the region in rich flames (Najm et al. 1998).

Next, the effect of CO₂ addition on the flame characteristics is discussed. The CH₂O thickness shows a mild increase as the CO₂ addition was increased from 0 to 40% of the methane flow rate. The heat release rate decreases mildly with increase in CO₂ concentration. While the proportion of CO₂ was increased, changes in flame structure were observed. While the HRX measurement showed a slight decrease, the formaldehyde thickness showed proportionally increasing trend. The decrease in heat release rate with CO₂ addition can be explained by following the work of Halter et al. 2009 (Figure 3-12). This work investigates effect of CO₂ dilution on methane-air flames. The flame speed reduces as the CO₂ dilution is increased. This behavior is attributed to carbon dissociation and the associated heat capacity of carbon dioxide.

The spatial profile of heat release rate obtained from simulation and experiments are compared for methane and biogas in Figure 3-13. A good agreement is observed on the reactant side, whereas mild difference in the profile can be noted on the product side. This mild disparity can be explained by looking at the respective flame position for methane and biogas. As mentioned earlier flame stabilises at different locations above the nozzle. . In the case of methane the corresponding flame height was measured to be 12.5 mm and 14.6 mm for methane and biogas respectively. Due to the fact that biogas flames were stabilised closer to the stagnation plane a higher convective heat loss to the stagnation plug will be expected, potentially contributing to the difference in the profile.

It was evident from the measurement that the flame position changed for every change in equivalence ratio (Table 3-1). Due to this, the local strain rate experienced by the (either on unburnt and burnt side) flame is different for different equivalence ratio, even if the inlet velocity was kept nearly the same (i.e. the constant inlet bulk strain rate value). The comparison of profiles from the experiments and the simulation has to be taken with caution. In particular, post flame region is not only affected by varying local strain rate but also heat loss to the stagnation plate as suggested earlier. Looking back, it can be seen from Figure 2-12 and Figure 2-13 that the numerical model did not fully capture the global heat release if the product of $[\text{OH}]_x[\text{H}_2\text{CO}]$ was used, because the total heat release rate depends on combination of certain important elementary reaction rates (Nikolaou et al. 2013). However, as in the case for pure methane flames, the trend in variation in the heat release rate with equivalence ratio agrees well with the HRX technique. Also the variation in heat release for lean biogas flames was seen to agree with the HRX technique when compared to the numerical simulation. This would suggest that even for biogas flames the chemical pathways for the global heat release is captured well by the HRX technique.

3.4. Chapter 3 Summary

Laminar flame speed of lean methane/carbon-dioxide, methane/carbon-monoxide/hydrogen fuel mixtures at a few selected equivalence ratios at atmospheric condition were carried out. The stagnation flame approach was the method used to determine the laminar flame speed measurements. The first step was to perform a set of controlled experiments using a methane/air mixture, which shows good agreement with literature and data obtained from the Chemkin model. Then, the laminar flame speed measurements for methane/carbon-dioxide air mixture with the same theoretical laminar flame speed were performed. The addition of carbon-dioxide acts as an inhibitor and greatly reduces the laminar flame speed measurement. From the methane/carbon-monoxide/hydrogen fuel mixtures one key observation was that the flame was more sensitive to periodic oscillations at higher strain rates compared to methane/carbon-dioxide air flames. Although oscillations were observed on the outer end of the flames, its effect on the strain rate were minimal but as explained above the condition whereby no oscillations were present were preferred for the actual measurements. One of the primary objectives of measuring laminar flame speed of certain methane, carbon-monoxide and hydrogen blend was due to the limited information available in literature. The experimental results obtained for premixed methane and biogas flames agree well with the computational model. The measurement of the HRX for methane was also performed for varying equivalence ratio and strain, and also for different level of CO₂ dilution at a fixed equivalence ratio. A good agreement with the Chemkin model was observed. The HRX measurements provided added confidence in the use of dual OH and H₂CO PLIF for heat release measurements. The results suggest that during the combustion of premixed methane and biogas, a substantial fraction of the carbon flows through HCO which in turn makes HCO a good point for the flow of carbon from fuels to products. Also from the work carried out by Najm et al. (1998), it is known that HCO production is directly dependent on H₂CO concentration and from its forward reaction of $\text{CH}_3 + \text{O} \rightarrow \text{H}_2\text{CO} + \text{H}$ shows the largest fractional influence on changes in heat release.

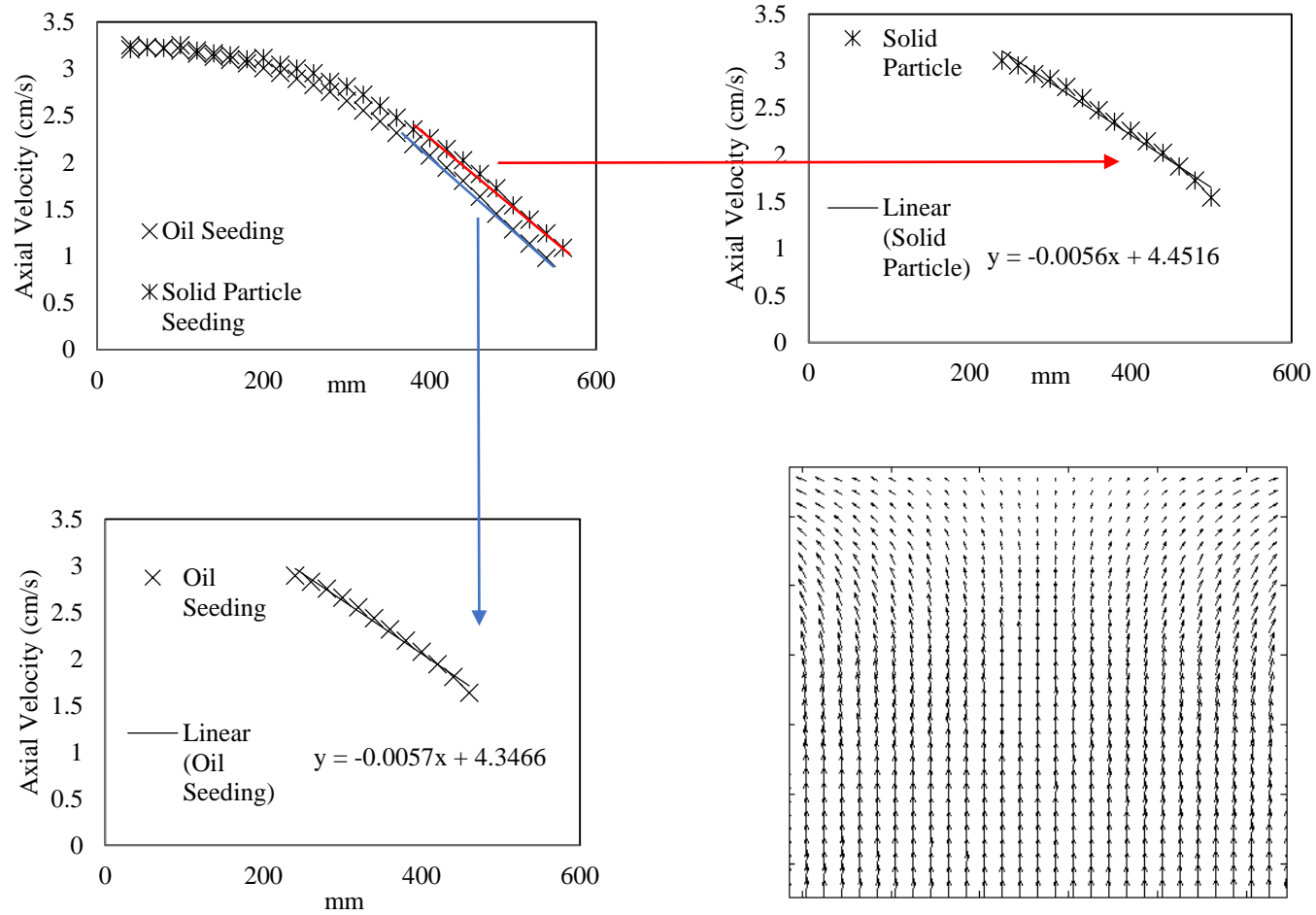


Figure 3-1: Strain rate calculation using different seeding particles and velocity field (Bottom right)

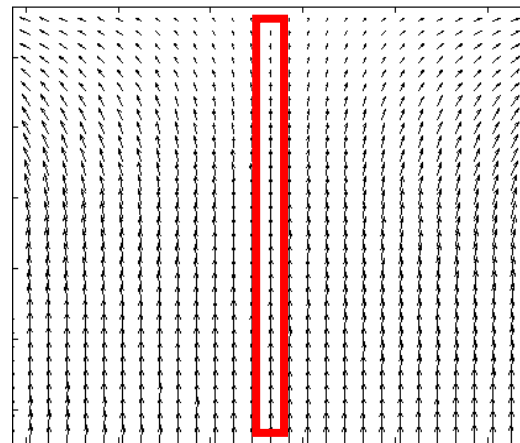
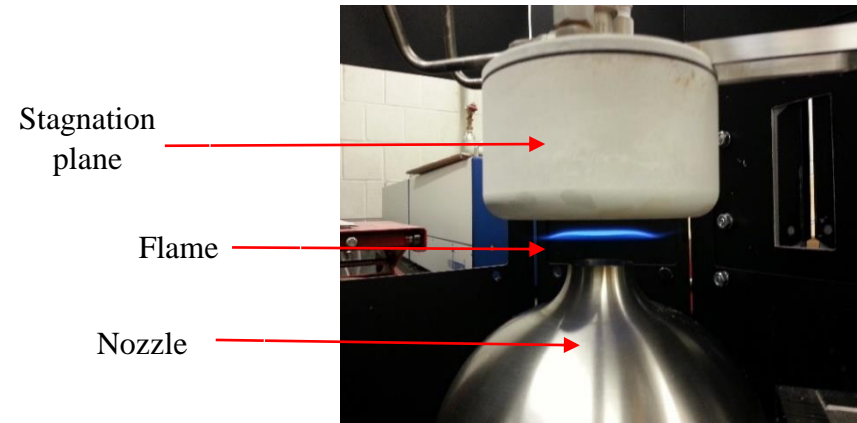
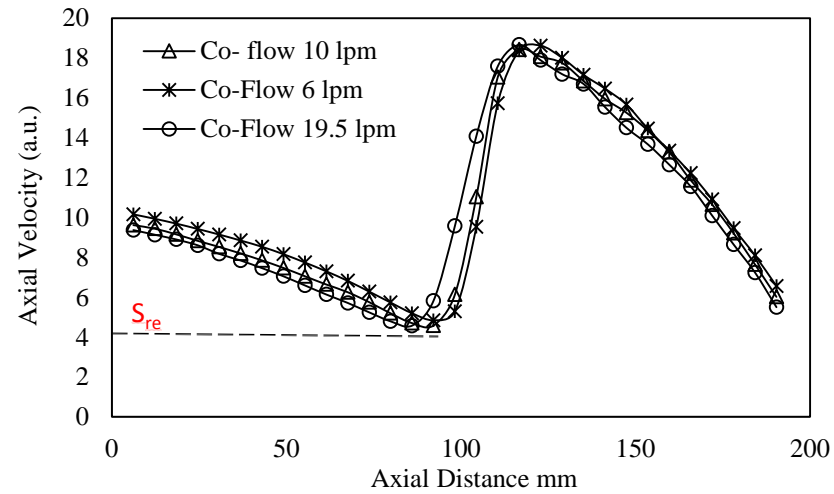


Figure 3-2: (Top left) Effect of co-flow on the velocity profile (Bottom) with the same bulk velocity, Pure Methane air, equivalence ratio 0.825

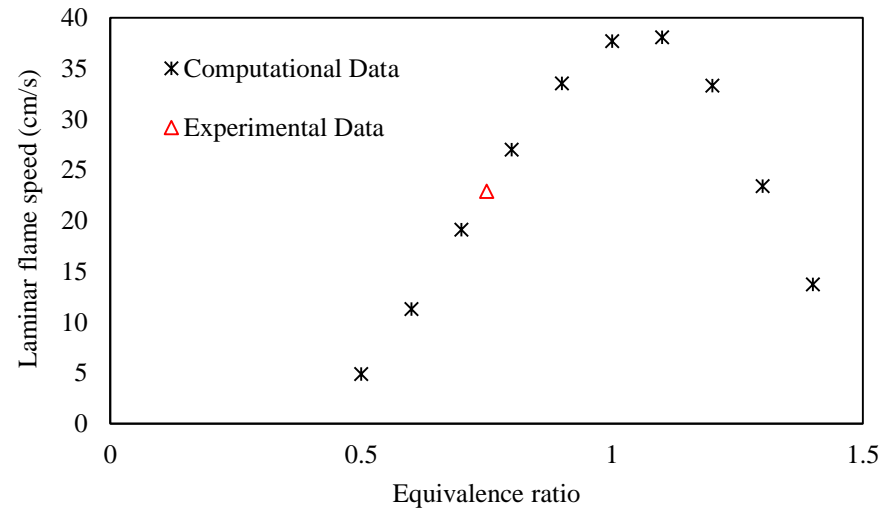
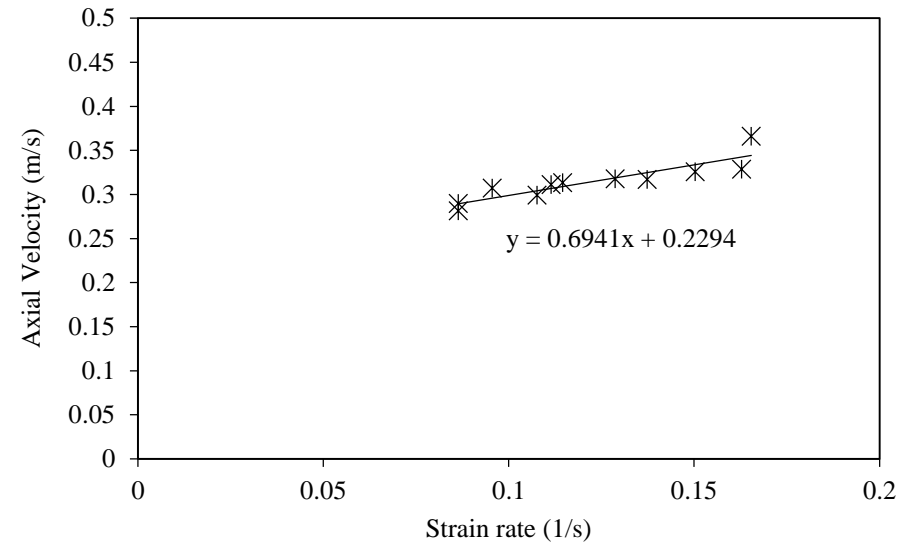
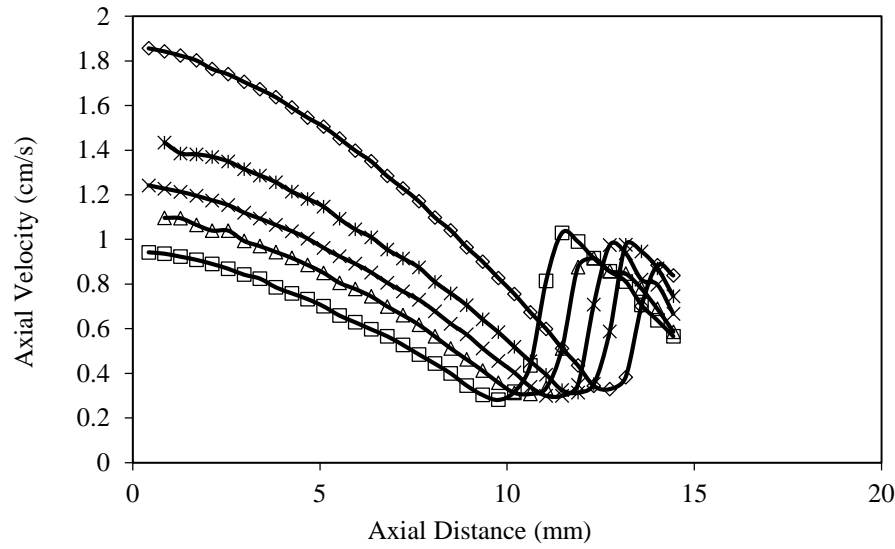


Figure 3-3: Flame speed measurement of Pure Methane flame at equivalence ratio 0.75, Difference between numerical and experimental of 0.88%

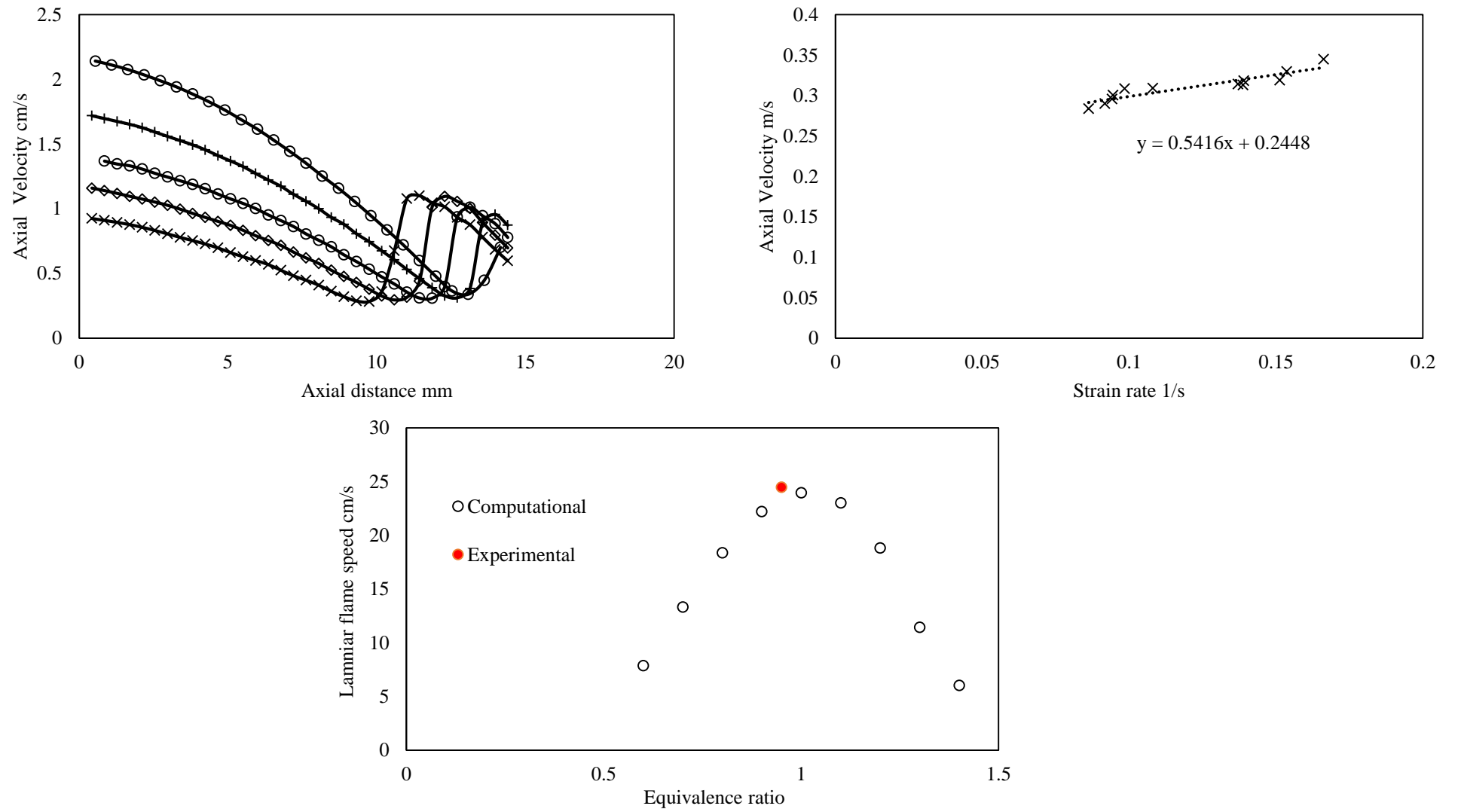


Figure 3-4: Flame speed measurement of biogas (60% CH₄ & 40% CO₂) flame at equivalence ratio = 0.95, Difference between numerical and experimental of 5.6%

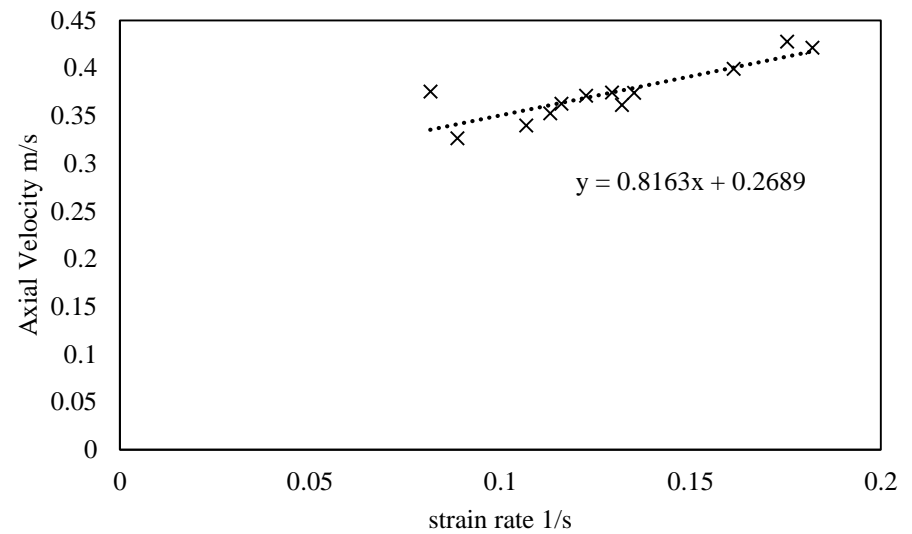
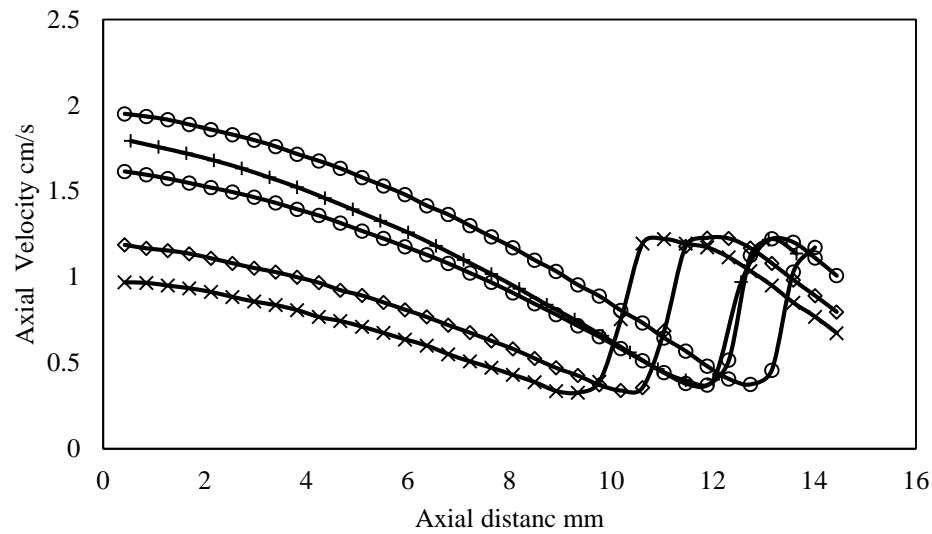


Figure 3-5: Laminar Flame Speed measurement of syngas with composition 50/25/25, equivalence ratio = 0.67, Flame speed = 26.89 cm/s

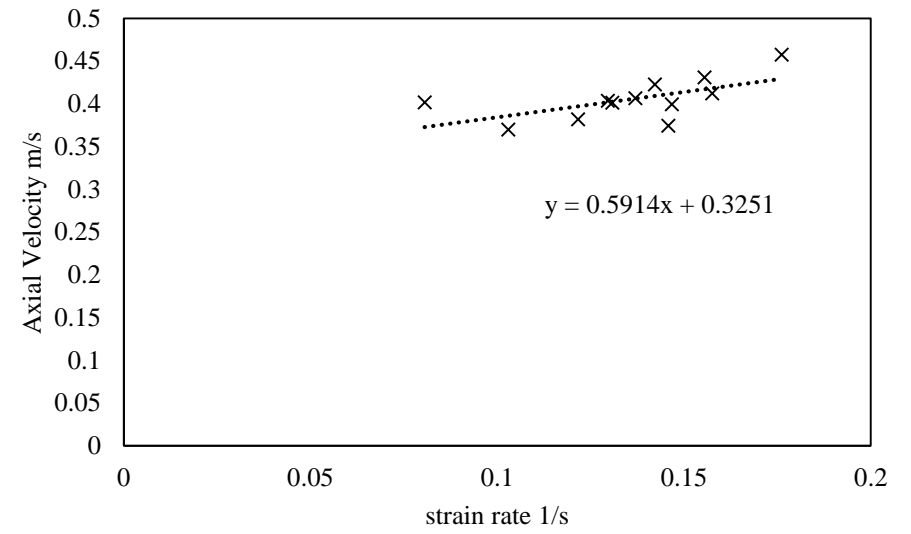
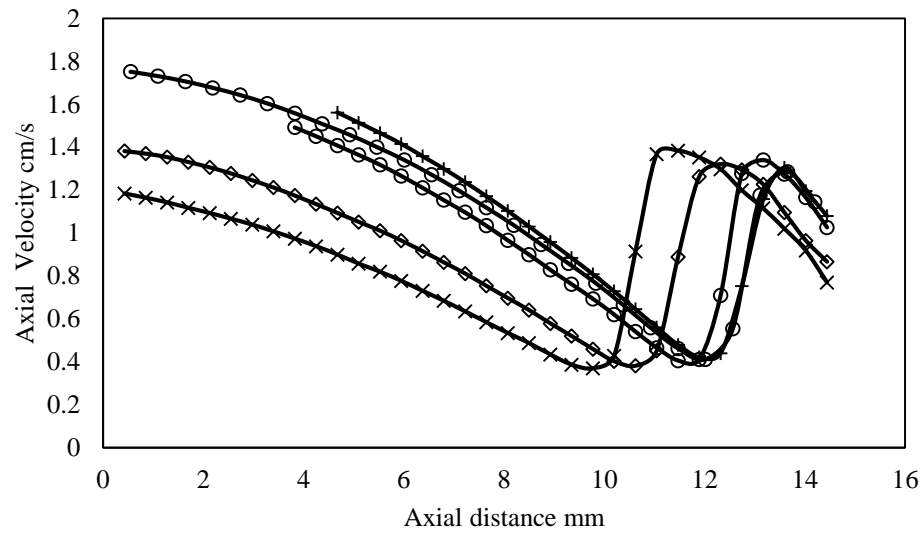


Figure 3-6: Laminar Flame Speed measurement of syngas with composition 50/35/15, Equivalence ratio = 0.7, Laminar flame speed = 32.51 cm/s

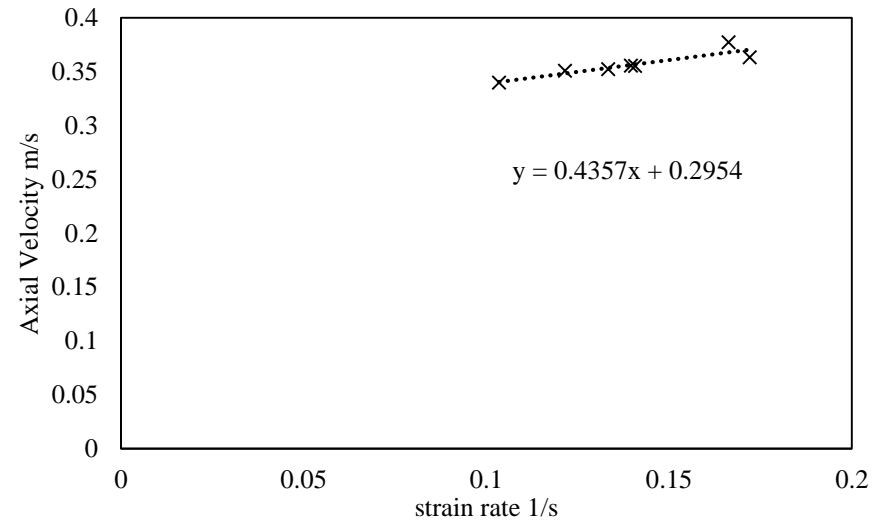
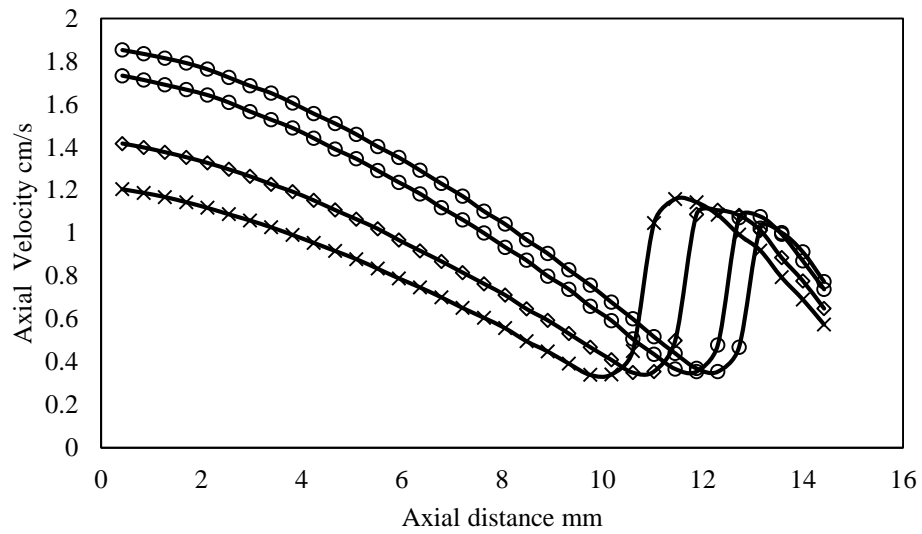


Figure 3-7: Laminar Flame Speed measurement of syngas with composition 25/50/25, Equivalence ratio = 0.58, Laminar flame speed = 29.54 cm/s

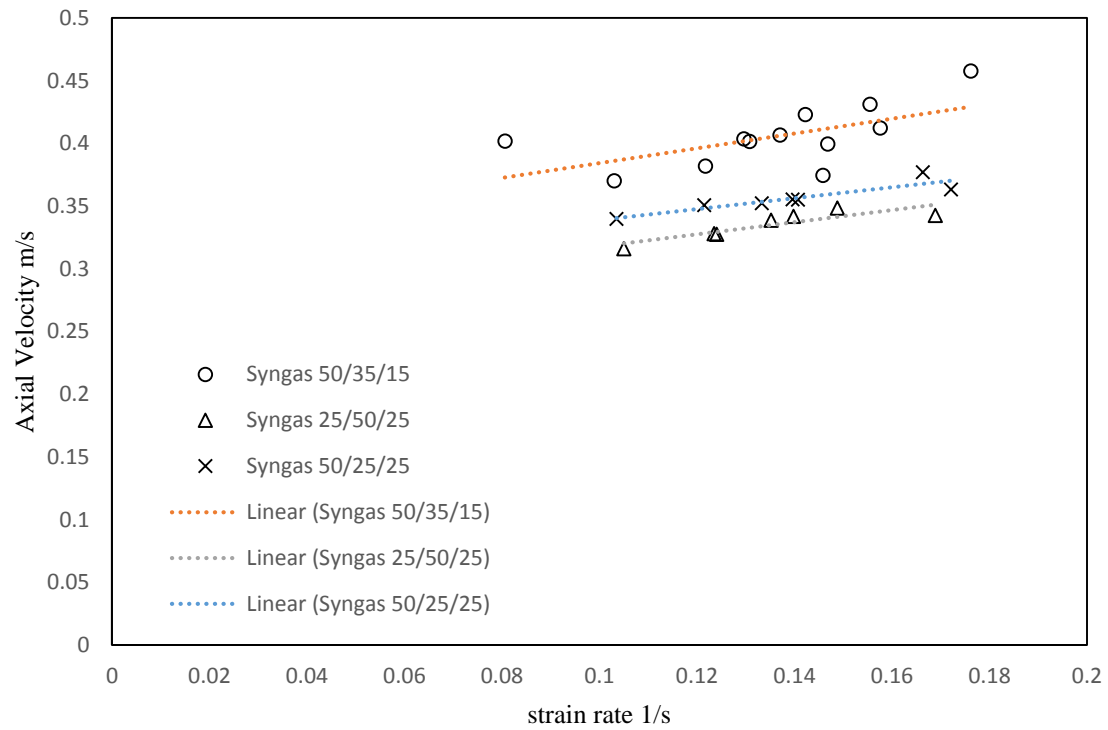


Figure 3-8: Strain rate of different syngas composition

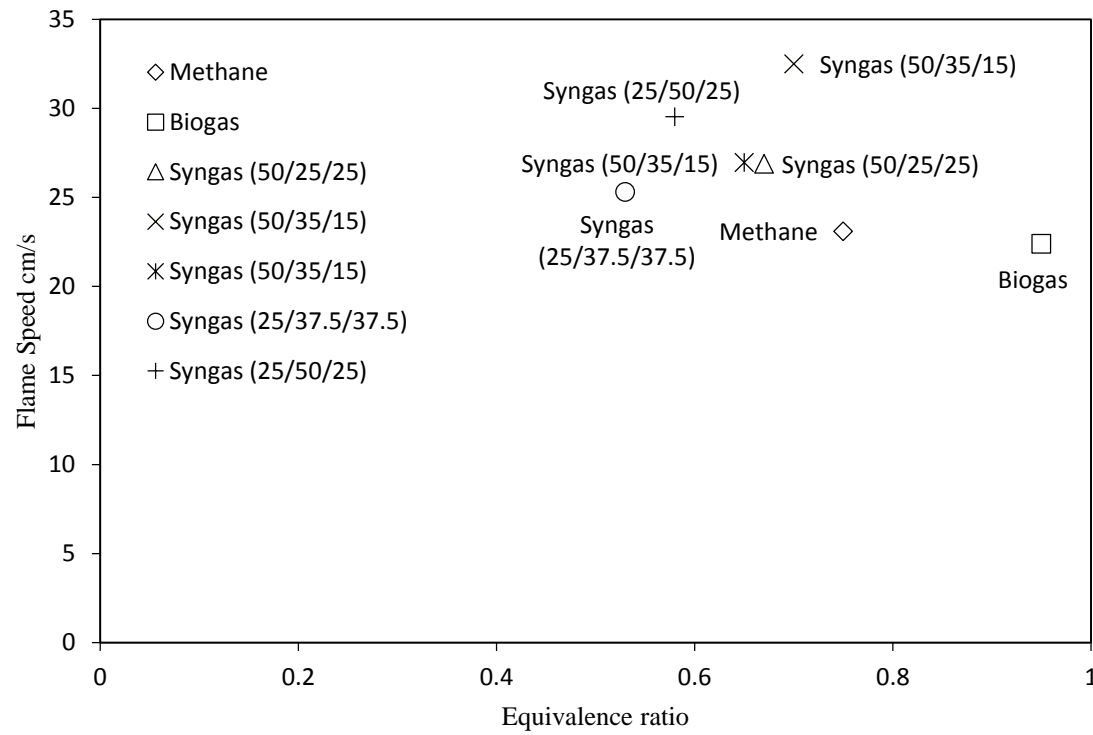


Figure 3-9: Laminar flame speed of multi component fuels based on measurement with respect to equivalence ratio

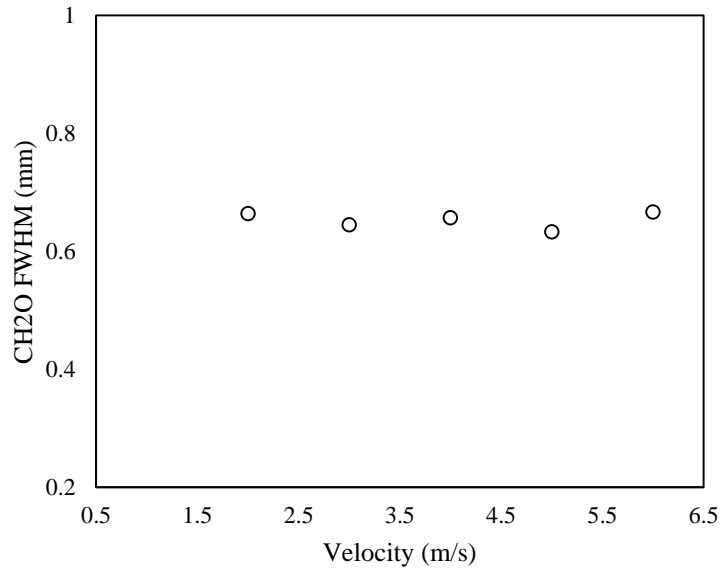


Figure 3-10: FWHM H₂CO variation with change in bulk velocity

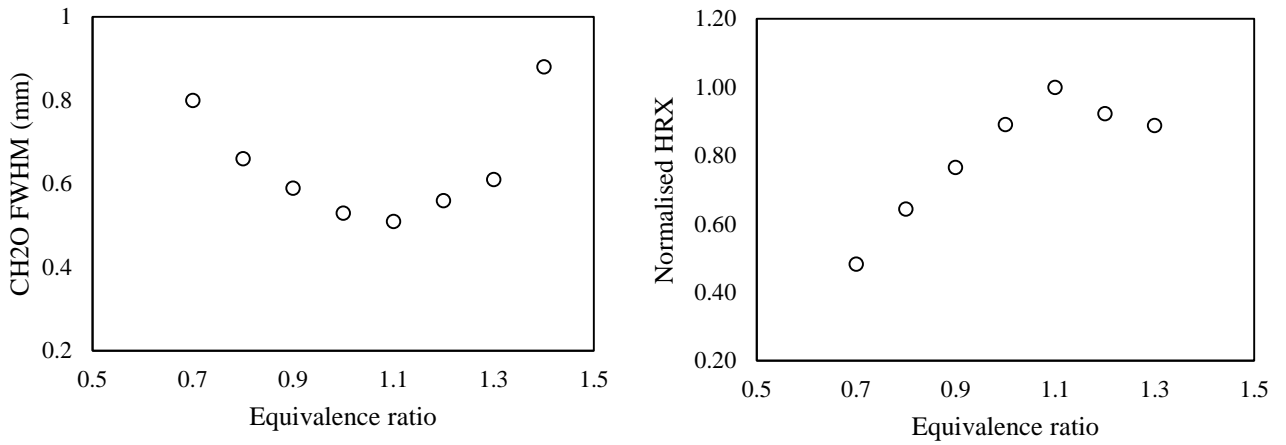


Figure 3-11: (left) FWHM H₂CO variation and (right) HRX with equivalence ratio

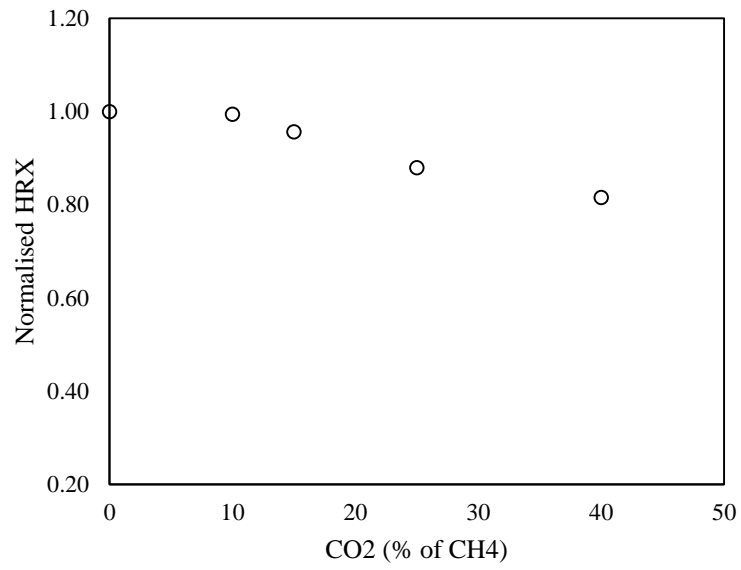


Figure 3-12: Effect of CO₂ Dilution on HRX

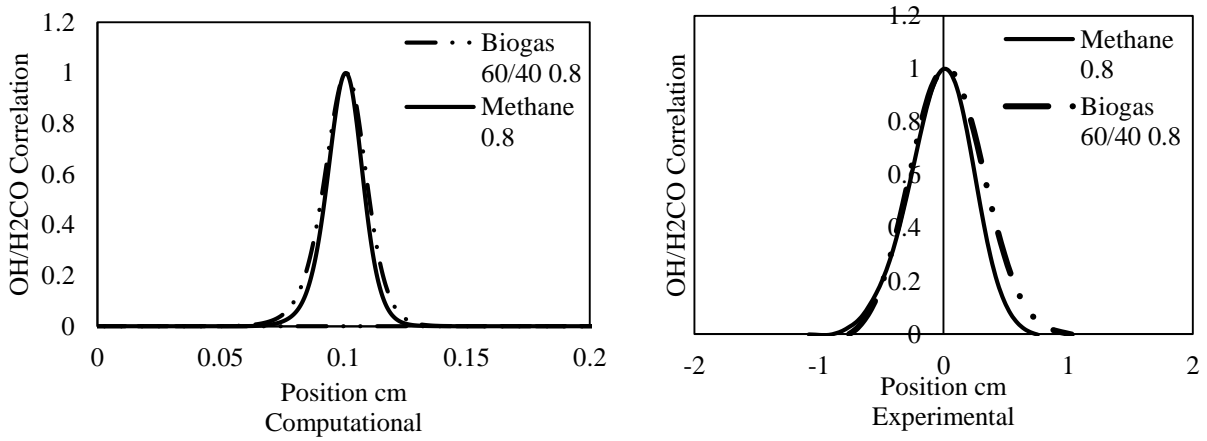


Figure 3-13: Spatial distribution of HRX based on numerical model (left) and experimental results (right)

Chapter 4

4. Turbulent flame characterisation

This section summarises the acoustic and flow characteristics of the turbulent flame burner under isothermal conditions. A similar PIV arrangement as employed in the previous chapter is used to visualise the flow at different bulk velocities and with 60 degrees swirl. Also discussed in this chapter is the effect of bulk velocity on chemiluminescence, flame surface and heat release rate of premixed methane and simulated biogas (methane/carbon-dioxide) flames

4.1. Cold Flow Characterisation

4.1.1. Acoustic characteristics

Having a clear understanding of the acoustic characteristics of the combustor under isothermal for non-reacting flow is of great importance in forced flames studies. Several studies such as Balachandran et al. (2005), Lieuwen et al. (2002) and Hardalupas et al. (2004) work have shown that in the study of forced flames, one of the requirements is high amplitude this is generally obtained by having the forcing frequency coinciding with the resonant frequency of the burner.

In this work, the acoustic response was investigated at a fixed air flow rate of 250 lpm which equates to 9.5 m/s at the exit of the combustor inlets. The air flow was perturbed by four loudspeakers mounted orthogonally on the plenum's circumference. Using an amplified signal from a waveform generator a frequency sweep was carried out from 20 to 400 Hz in steps of 5 Hz. As described, in chapter 2 the acoustic response was determined from acoustic pressure measurements. With the data from the acoustic pressure measurements, the velocity fluctuations were determined using the two-microphone method (Seybert et al. 1978). The two-microphone methods have been previously employed in the work by Dowling et al. (2003), Balachandran et al. (2005) and Hussain et al. (2012) and have shown to provide an accurate

method of measuring the velocity fluctuations. Along with the acoustic pressure measurements, Balachandran et al. (2005) also recorded the velocity fluctuations using a Dantec Dynamic hotwire. Their results show that the two-microphone slightly overestimates the magnitude of the velocity fluctuations but the trend of the variation is well captured. The discrepancy was mainly due to the fact that an area average-velocity was used in the two-microphone calculations.

In this study a quartz enclosure was used to confine the flame. The purpose of the quartz enclosure was mainly to prevent any entrainment of air. A quartz enclosure of the same length was used for all of the measurements so that the acoustic response would remain unaffected. It is well known that altering the length of the enclosure affects the response of the combustor. Since the resonant peaks were mainly due to longitudinal acoustic modes, any change in the enclosure length would affect the acoustic characteristics of the combustor by altering the acoustic boundary conditions and hence the resonant responses. During a similar study carried out by Balachandran et al. (2005) three resonant frequencies were identified. It was also shown that there were no major shifts in the first two resonant frequencies with only a shift present at the third peak when altering the length of the enclosure. An additional smaller peak was observed between the second and third dominant frequencies when varying the enclosure length. The most notable change was observed with respect to the decrease in resonant amplitude of the third dominant frequency peak whereas the amplitude of the first two peaks remains nearly unaffected.

Figure 4-1 shows the acoustic response of the combustor across the frequency sweep. It can be clearly seen from this figure that there are three distinct resonant peaks at 30 Hz, 255 Hz and 315 Hz. These results indicate that the combustor plenum chamber along with the air supply line act in a similar manner to a resonator with peaks as aforementioned. The first peak corresponded to the Eigen mode of combustor assembly including the supply line.

4.1.2. Cold Flow visualisation

Under isothermal (at atmospheric) forced and unforced conditions, experiments were performed to understand qualitatively the flow-field. The flow field plays a key part in the flame stabilisation as well as the mechanism responsible for the flame response. As explained in chapter 3, PIV was employed to visualise the 2D velocity field of un-swirled flow and stereo PIV was used to investigate 3D velocity map of the swirled flow.

The velocity field for the un-swirled and unforced non-reacting flow can be seen in Figure 4-2. The recirculation zone formed by the wake of the bluff-body will be referred as the inner recirculation zone. Although not seen clearly in the Figure 4-2 there was also another outer recirculation zone formed by the rearward facing step (dump plane). The shear layers as shown by Correa & Pope, (1992) and Ma & Harn, (1994) have shown to play important for flame stabilisation. Prasad & Williamson, 1997 have shown that the flow field of a bluff-body is a superposition of three flow regions: the boundary layer along the bluff-body, the separated free shear layer and the wake. In the work by Shanbhogue et al. (2008) the boundary layer is referred to as the region starting from the bluff-body leading edge until the point of separation. The separated free shear layer refers to the portion of the flow that starts where the boundary layer ends and terminates at the closure point of the inner recirculation zone. The wake begins where the shear layers merge. Therefore the flow field of a bluff-body can be described as a complex superposition of a boundary layer, a shear layer and a wake (Prasad & Williamson, 1997). The flow accelerates due to the obstruction caused by the bluff-body and further downstream undergoes a sudden expansion at the trailing edge. The presence of the inner recirculation zone can be attributed to the sharp trailing edge that causes the flow to separate thus creating the recirculation zone. In the far field, away from the bluff-body, both the recirculation zone and the accelerated region surrounding it disappear and the flow velocity tends towards a uniform velocity as the viscous momentum transfer diminishes the velocity gradient (Porumbel et al. 2006). Below a Reynolds number of 200,000 the dynamics of the flow field can be connected to the physics of the shear layer and wake alone, without any major contributions from the boundary layer (Shanbhogue et al. 2008). In the present work only the region encompassing the end of the inner recirculation zone was under investigation. The average axial velocity field in the region above the bluff-body provide insightful information about the inner recirculation region both in its intensity and shape as well as useful information about the free stream in the near and far field. The axial velocity difference between the axial velocity directly behind the

bluff-body and the free stream surrounding it decreases with an increase in the axial distance due to the viscous forces that ensure momentum transfers along the velocity gradient. The free stream velocity, accelerated in the convergent section created by the bluff-body, also decreases in such a manner that further downstream the inflow velocity tends to be recovered in the entire domain. This reflects the overall energy conservation as shown by Porumbel et al. (2006). With an increase in the bulk velocity a decrease in the length of the inner recirculation zone is observed.

The next section investigates the effect of acoustic perturbations on the shear layer at a given bulk flow rate. Earlier studies by Cala et al. (2002), Cho et al. (1988) and Zhou et al. (2001) and Balachandran et al. (2005) have shown that when the shear layer is subjected to pulsation it may roll-up to form a coherent vortex ring. In the present study for certain sinusoidal forcing frequencies and amplitudes, a pair of counter rotating vortices were observed (cross sectional view). The shape and size of the counter rotating vortices were frequency and amplitude dependent. The dependency on both amplitude and frequency will be discussed later in more detail. As described earlier in this section the highest amplitude of oscillations were observed for frequencies of 30 Hz, 255 Hz and 315 Hz. The experiments were performed at 255 Hz and at an amplitude of forcing where a pair of counter rotating vortices can be clearly seen. The Figure 4-3 shows the evolution of the vortex ring during the pulsation of the flow for a forcing frequency of 255 Hz at an amplitude $A = 0.8$. It can be seen that the shape of the inner recirculation zone changes and there is a small deformation formed at the base of the recirculation which finally evolves into an inward rolling vortex ring. Also it can be noted that the height of the inner recirculation zone was reduced at some point during the cyclic variation however at other points on the cycle the inner recirculation zone were found to be taller but smaller in width. While the inner shear layers of the inner recirculation zone showed an inward rolling vortex, the outer shear layer at the outer recirculation zone also rolled up outwardly from the bluff-body. The synchronised motion of the inner and outer vortex thus form a pair of counter rotating vortices – a counter rotating toroidal pair in a three dimensional context. The pair of counter rotating vortices grew in size and moved downstream with the speed of the local flow velocity. Subsequently this vortex ring moved far downstream from the combustor inlet after which a new vortex pair formed at the base of the recirculation zones. This process repeated itself for every forcing cycle. As a consequence, during the hot flow experiments these vortices not only generate flame surface area where the flame is wrapped around them, but also

caused cusps and large-scale flame annihilation events as shown by Balachandran et al. (2005). This will be discussed in more detail in section 5.2, when the flame dynamics due to inlet velocity fluctuations is examined.

The introduction of swirl was found to greatly affect the structure of both the inner and outer recirculation zone greatly. The primary role of the swirl is to create internal recirculation zones. These zones create low velocity regions where the flame can be anchored. The recirculation zones also increases the turbulence level which has been shown by Dricoll et al. (2011) to increase the flame speed. Batchelor et al. (1963) explains the mechanism responsible for the formation of the internal recirculation zones. The swirling flow that enters has a vorticity vector that points in the axial direction. A recirculation zone also contains velocity vectors that point in the azimuthal direction. There is no additional source of vorticity, so the only way to create a recirculation zone is to convert some of the axial vorticity into azimuthal vorticity. Each fluid element follows the helical path, and as the radius of this helical path increases the direction of the vorticity vector is altered such that its axial component is decreased and its azimuthal component increases (Batchelor et al. 1967 and Zukoski et al. 1954). In order to have a better understanding of the swirl flow behind the conical bluff-body, stereo-PIV was employed in this study.

The method of using two cameras to obtain out of depth-per-deception has been practiced in various engineering applications. In fact, such twin camera system mimics the binocular vision that enables human beings to distinguish between near and far objects (Prasad et al. 2000). Essentially with a single view alone, the out-of-plane dimension of the object cannot be resolved. Therefore the stereo-PIV configuration allows for recording of two simultaneous, but different views of the same object. There have been different approaches proposed for the stereo PIV computation. In all the cases the 2D vector fields are firstly computed for each camera. These are then used to stereoscopically reconstruct the 3D vector field (Prasad et al. 2000). There have been numerous suggestions proposed to achieve a stereoscopic reconstruction and for the purpose of this work, the method employed was the dewarping of the image prior to the computation of the vectors by Insight 3G software.

As described by Prasad et al. (2000), Ganapathisubramani et al. (2002) and Soloff et al. (1997), a stereo PIV system can be calibrated with a target containing markings spaced in an orderly manner in all three spatial directions. In the present work, a target similar to the one provided

by TSI, Inc. was used. This way dual-plane target at a 1 mm depth separation made of a matrix with white dots spaced at 5 mm intervals over a region of 5 cm x 8 cm. The target was positioned in such a way that it was coincident with the plane defined by the laser sheet. Once in position, images of this target were acquired by both cameras and a mapping function was constructed that relates positions in the image plane to the corresponding locations in the object plane as demonstrated by Wu et al. (2009). A third-order polynomial was used for the in-plane (x and z) co-ordinates, while a first-order polynomial was employed for the out-of-plane (y) coordinate. To reduce registrations errors generated by inherent misalignment between laser sheet and calibration target, a self-calibration scheme proposed by Wieneke et al. (2005) was used to optimise the mapping function. The final mapping function was then employed to reconstruct the three-dimensional velocity vectors. As mentioned in chapter 2 all of the image acquisition, calibration and reconstruction were performed within the Insight 3G software. The procedures for the calibration of the stereo PIV measurements are described in details in the Insight 3G manual and were strictly followed for the current work.

The pair of PIV images for each camera was interrogated in a manner similar to that employed in the aforementioned 2D PIV experiments. The size of the interrogation windows were initially chosen as 64 x 64 before the final window size was spatially shifted to a 32 x 32 with a 50% region overlap to maximise the spatial resolution of the velocity field. For an angular PIV configuration with perfect registration the in-plane errors for u and w velocity components are reduced by a factor of $1/\sqrt{2}$ compared to the uncertainty of approximately 0.1 pixels for a single camera arrangement (Prasad et al. 2000). However, the error for the out-of-plane velocity component is $\frac{1}{\tan\theta}$ times the in-plane error (Zang & Prasad 1997, Lawson & Wu 1997, Prasad et al. 2000). Soloff et al. (1997) have shown that the error associated to the out-of plane velocity component can be of several orders of magnitude higher than the error of the in-plane velocity components, but the use of the self-calibration scheme to correct the registration errors, can greatly reduce the uncertainty in the measurements (Wu et al. 2009). Wu et al. (2009) suggested that this method could yield final displacements with uncertainties which were less than those introduced by a basic PIV correlation algorithm. Therefore for the current work it could be estimated that the errors with the stereo PIV measurements would be similar to the 2D uncertainties of 1% of the full scale deflection.

In the next section, a swirl flow with no forcing is presented first, which will then be followed by a forced swirl scenario at a given frequency of 255 Hz and $A = 80\%$ (0.8). From Figure 4-4 it can be seen that with an increase in the swirl angle, the jet stream diverges away from the bluff body. It can be also noted that with the addition of a swirl to the incoming flow there were no variation in the axial velocity profile taken 5 mm above the bluff-body plane but on the other hand there was an increase in the radial and tangential velocity components (Figure 4-5). Thus an overall increase in velocity magnitude would be expected as it can clearly be seen in Figure 4-6. While using smoke visualisation in the study carried out by Balachandran et al. (2005) it was noted that with the introduction of a swirl the flow starts to impinge on the sidewall of the quartz enclosure at a distance equal to approximately 1 to 1.5 the bluff-body diameter. The strength of the swirl would dictate how fast the main flow moves towards the wall. A strong swirl would make the main flow move faster towards the wall. As a result the size of the outer recirculation could also be reduced considerably (Huang & Yang, 2005). In a non-swirl flow the tangential component was found to have negligible effect on the flow compared to the axial component. While on the other hand adding a swirl to the flow the tangential component started to play an important role which would explain the observation by Balachandran et al. (2005).

Figure 4-7 shows the dynamics of an oscillated flow with a moderate and high swirl intensity with a forcing frequency and amplitude of 255 Hz and $A = 80\%$ respectively. The figures suggest that the oscillation has changed the structure of the recirculation zones, however the vortex evolution and the dynamics are very similar to that of the non-swirl scenario. These results suggest that the flow field is greatly affected by the acoustic forcing. As seen in the previous work by Kulsheimer & Buchner, (2002) and Balachandraan et al. (2005) the effect of forcing was frequency and amplitude dependent. While the introduction of a swirl changed the flow structure, the recirculation shape and introduced some form of impingement at the wall of the quartz, there were no observable effect on the vortex evolution. Any notable change can be observed when the vortex is about to collapse at phase angle 300 (Figure 4-7). Under the no swirl condition the vortex is clearly distinguishable but for a 60 degrees swirl the vortex is not prominent.

4.2. Reacting Unforced Flow

The static stability of the combustor, operated with completely premixed reactants, pertains to the physical flame attachment and its response to small flow fluctuations. However for the combustors with spatial and temporal variation in equivalence ratios the mixing of the fuel and air stream dictates the stability. The main objective of Section 4.2 is to investigate the characteristics of fully premixed turbulent flames of different fuel compositions. The change in the fuel type and composition can lead to changes in the characteristics time scale of reactions which can have an impact on the performance and efficiency. This can lead to flashback, auto-ignition, lean blowout and combustion dynamics. Therefore this section will investigate the effect of varying fuel composition, change in bulk velocities and equivalence ratio values on the flame statistics.

4.2.1. Behaviour of different premixed flames using OH* chemiluminescence

In premixed combustion systems, fuel and air are premixed upstream of the point of stabilisation and the recirculation generated by the flame holder (bluff-body) helps to trap the hot products. This in turn serves as an ignition source for the incoming combustible mixture. Premixed combustion systems are very often prone to flash back, which occurs if the mixture velocity is less than the turbulent flame speed. Conversely if the mixture velocity is too high at the point of flame stabilisation, the flame may blow off. Both flashback and blow-off are undesirable in premixed systems. In the case of flashback, flame stabilisation can occur at locations inside the combustor which can be catastrophic, whilst blow-off is especially not desirable at high altitude flight conditions, since re-ignition can be very difficult to achieve. In these fully premixed combustors, the flame surface will appear at the point where the local mixture matches the local flame speed as shown by Balachandran et al. (2005).

The investigation of the flame position, its shape and curvature is described in this section. Different fuel compositions, with the same laminar flame speed value at various bulk velocities (in order to introduce variation in shear produced turbulence intensity levels) were studied using the aforementioned experimental methods aforementioned. The influence of the change in turbulence intensity levels on different fuel compositions can offer a better understanding of the flame stability and provide an insight into the interchangeability of fuel. The investigation

was carried out for the same theoretical laminar flame speed while the overall mixture bulk velocity and the fuel flow rate were both varied. As mentioned previously, one of the aims of the study was to investigate the forced flame response of multi components fuels with the same laminar flame speed. Therefore, a good understanding of the different flames under unforced conditions is needed.

During these experiments the global OH* chemiluminescence of pure methane and different biogas mixtures were measured in a turbulent premixed bluff-body stabilised flame configuration. The theoretical laminar flame speed, S_L , was kept at 22 cm/s while the Reynolds number (Re) of the flame was varied. The Reynolds number, Re , of the flame was changed by adjusting the air and fuel flow rate accordingly, thereby introducing variation in shear produced turbulence intensity levels.

The values of the theoretical laminar flame speed were computed numerically using Chemkin by Swaminathan, for details of chemical mechanisms used please refer to Nikolaou et al. (2013). Figure 4-8 shows the computed laminar flame speed of different biogas mixtures and pure methane. It can be seen that an increase in the content of carbon-dioxide results in a decrease in the laminar flame speed for the same equivalence ratio which was also observed by Ju et al. (1998). At a laminar flame speed of 22 cm/s pure methane has an equivalence ratio of 0.73 and at compositions of 5, 25 and 40% CO₂; the biogas mixture has an equivalence ratio of 0.75, 0.79 and 0.89 respectively. Therefore as the carbon-dioxide content increases in the biogas mixture higher equivalence ratios were required in order to achieve the same laminar flame speed.

From Figure 4-9 it can be seen that turbulent premixed CH₄/CO₂ flames with the same laminar flame speed have the same global OH* fluctuation irrespective of the dilution level of carbon – dioxide. There is only an increase in the global OH* fluctuation with an increase in the bulk velocity. This can be attributed to the increase in wrinkling effect at higher bulk velocity due to an increase in the shear produced turbulence, which will be examined in the following section. Measurements with a change of equivalence ratio followed the investigation of constant laminar flame speed at varying bulk velocities. Figure 4-10 shows the global OH* chemiluminescence variation at different equivalence ratio values. Measurements were performed at a bulk velocity of 9.5 m/s with equivalence ratio ranging from 0.7 to 0.95. The maximum equivalence ratio investigated was 0.95 because at these values, the flame speeds become much greater than what can be supported by the axial velocity; thus, the flame can

propagate into the burner causing flashback. OH* chemiluminescence is expected to increase with increasing equivalence ratio because of an increase heat release or flame speeds, see Figure 4-8. As the flame speed increases, more reactants are consumed per unit time and results in more OH*. Once the global OH* measurement were carried out, the next step was to further understand the flame shape and position under the influence of varying turbulence intensity levels.

4.2.2. OH and H₂CO PLIF measurements of premixed methane/carbon-dioxide/air flames without swirl

OH PLIF measurements give a spatial distribution of the OH radicals in the post-flame gases. As previously mentioned, OH PLIF can be used to capture the flame front as well as the small and large scales wrinkling structures of different flames. From Figure 4-11, high OH concentrations of OH radicals are observed in the region immediately following the flame front and after which OH concentration decreases. The high OH concentration can be attributed to the high reaction rates and temperatures present in the reaction zones of the flame front. A typical instantaneous OH PLIF image can be seen in Figure 4-11 for lean premixed methane/air flame stabilised on the bluff-body. It can be seen from the figure that the flame is primarily anchored at the shear layer, which is formed as a consequence of the inner recirculation zone created by the bluff-body. Due to the outer recirculation formed by the dump plane occasionally flame elements would be seen to stabilise on the resulting shear layer. From the simultaneous OH and H₂CO PLIF a weak signal of heat release was measured in this region, indicating that the majority of the OH radicals present on the outer shear layer are due to the recirculation of the post combustion, which will be discussed in further details later on.

OH PLIF measurements were extended to different biogas flames with the same theoretical laminar flame speed, but at different bulk velocities. From the instantaneous OH PLIF images of each biogas composition, the captured flame front was computed. During each set of experiments 100 – 150 images were recorded for each given condition; then the flame surface calculations were performed on each image and averaged from which a time averaged flame surface was obtained. At lower equivalence ratio values and the addition of carbon-dioxide resulted in a decrease in OH PLIF signal and for this reason a dynamic thresholding technique was employed whereby each individual image would have its own threshold value depending on the signal noise ratio.

The increase of turbulence significantly wrinkles the flame front and a direct resultant effect of the wrinkling is an increase in the surface area. This can be observed in Figure 4-12; with an increase in the bulk velocity an increase in the flame surface (FS) is also observed. The findings from the experiments indicates that a positive correlation exists between an increase OH* chemiluminescence and the wrinkling effect. From Figure 4-12, it can also be deduced that the variation in the FS is predominately due to the shear produced turbulence as a direct result of increased bulk velocity.

From the data presented so far, it can be said that the variation in the CO₂ dilution did not have a significant impact on the FS and OH*. It was also noted that the flame shape did not change significantly with the variation of CO₂ dilution. Figure 4-13 shows the variation of the turbulence intensity estimations with respect to the change in air flow rates. The turbulence intensity estimations were carried under cold condition using the aforementioned PIV technique. A trend of increase in turbulence intensity levels with an increase in flow rates is evident from the results. Therefore it can be expected that the flame front will experience a large degree of wrinkling at higher turbulence intensity i.e. at higher bulk velocities. The next section shows the result obtained from the analysis for the wrinkling at various turbulence intensities.

The influence of turbulent wrinkling on flame surfaces can be quantified in a variety of ways; however, it is particularly problematic if only a small portion of the flame is imaged or modelled. When information on the detailed flame structure is desired, high resolution is required; limiting the total imaging area. But even for relatively short flame lengths meaningful information about the curvature can be easily derived. The curvature can reveal both the effect of the turbulence flow field on the flame which is dependent on the shape the flame has adopted due to the turbulent structures encountered and gives insight to the influence of the flame shape on flamelet burning (Woolley et al. 2002). The Lewis number, Le is a one dimensional parameter defined as the ratio of thermal diffusivity to mass diffusivity, is often used to describe the flow field where there is a simultaneous heat and mass transfer by convection.

For all of the different biogas flames the Lewis number was calculated to be approximately one. Figure 4-14 shows the probability density function (PDF) of curvature for pure premixed methane flames. It can be seen that all of the PDF's are symmetrical about the 0 mm⁻¹. The distribution of the curvature (H) widens with an increase in bulk velocity. The maximum and minimum curvatures measured were +1.5 and -1.5 mm⁻¹ respectively. The observations made in Figure 4-14 seem to be in agreement with Woolley et al. (2002) Flames with $Le = 1$ having generally been found to be nearly symmetrical with a mean of approximately zero. As can be seen from Figure 4-15, the wrinkling on the surface of the flame also increases with an increase in bulk velocity.

Curvature convex to the reactants is generally defined as positive and curvature concave to the reactants is defined as negative. Haworth & Poinot, (1992) and Rutland & Trouve, (1993) have observed flames with $Le = 1$ have weak bias towards negative curvature, but Bradley &

Cant, (1991) observed a positive bias. The weak biases were explained on the basis of cusp formation or Huygen propagation. Heavily cusped flames should exhibit slightly positive curvature over most of their length as shown by Bradley & Cant, (1991). However small lengths of very negative curvature also exist as observed in the PDF's of Haworth & Poinso, (1992), and Rutland & Trouve, (1993). The negative cusp may not have had time to develop fully in turbulent flame as a result of the diffusive nature of the turbulent flow field (Woolley et al. 2002). Curvature has been shown to have very significant effect on local flame structure; however, it has little effect on global parameters such as the turbulent burning velocity as the PDF of curvature is symmetrical and the positive and negative curvatures cancel each other out. Looking at Figure 4-16 & Figure 4-17 an increase in the overall bulk velocity also resulted in an increase in magnitude of the length scales in the regions closest to the bluff-body. This explains the increase in wrinkling at the lower part of the flames at higher bulk velocities as shown in Figure 4-15. From these experimental observations, it can be noted that the large length scales predominately played a major roles in wrinkling of the flames compared to smaller length scales.

Figure 4-18 shows a combination of the PDF of curvature of biogas of composition 60% CH₄ and 40% CO₂ and pure methane. It can be seen that for the same overall bulk velocity the effect of CO₂ dilution on the wrinkling does not have a major impact. But the increased wrinkling at higher bulk velocity is confirmed with a broad PDF. Also it can be noted that methane at bulk velocity 16 ms⁻¹ has a broader distribution than biogas with 60% CH₄ and 40% CO₂ composition at the same bulk velocity. This indicates that the methane flame has slightly less wrinkling tendency than the biogas flames. This can be explained by the fact that at higher bulk velocity in order to keep the equivalence ratio constant at the same proportion of carbon-dioxide to methane, a lot more carbon-dioxide is required, thus increasing the shear produced turbulence. Along with the curvature statistics the heat release measurement from the combined OH and H₂CO PLIF were also carried out.

Najm et al. (1998) have shown OH and H₂CO PLIF can be used as a correlation for heat release measurement for premixed hydrocarbon flames. A similar experimental technique was applied in the work carried out by Balachandran et al. (2005) and Ayoola et al. (2006) on hydrocarbon flames and the results obtained showed good agreement with the work by Najm et al. (1998). The experiments were carried out on different types of flames ranging from counter-flow flames to premixed flames. As previously mentioned currently there is a lack of information on the applicability of the HRX technique on multi-components fuels. Especially, biogas and

syngas type fuel with significant amount of CO₂ and H₂ and it is not well defined for the HRX technique. Therefore in order to assess the suitability of the method for fuel of varying compositions, methane/carbon-dioxide/air flames were first investigated.

Figure 2-12 shows the laminar premixed flame calculations of species (H₂CO and OH) profile for methane/air and methane/carbon-dioxide/air flames at varying equivalence ratio Figure 3-13 illustrates the spatial HRX difference for methane and biogas both experimentally and numerically. Figure 2-13 shows that at low equivalence ratio the normalised [OH]×[CH₂O] and the theoretical heat release rate have a linear relationship with a deviation that appears at a higher equivalence ratio. It can be noted that both methane and methane/carbon-dioxide showed similar pattern which provided added confidence in the measurement technique. It can be seen that the HRX curve lies over the curve showing the product [OH]×[CH₂O]. Yuan et al. (2014) has shown that at the higher strain rates there is a greater overlap between the [OH]×[CH₂O] and the theoretical heat release rate. Thus, at low strain rate conditions, the HRX is not fully quantitatively represented by the product [OH]×[CH₂O]; the latter could only contribute around 50% in magnitude of the true HRX (heat release rate). In contrast, at high strain rate conditions, the two quantities are quite close. A further observation is that the OH peaks at the lean side of the HRX peak, while for both low and high strain rates the peak [OH]×[CH₂O] coincides with the HRX peak. Unlike the strong variations of CH₂O with strain rate, the OH curve and levels do not vary greatly, although a decrease in the peak OH is evident.

From heat release measurements, it was observed that the flame was mainly stabilised at the inner shear layer with flame elements occasionally found along the outer recirculation zone. With an increase in equivalence ratio it was observed that there was less of the latter up to a point where the stabilisation was achieved by the inner recirculation zone only. In the bluff-body combustor measurements were performed at a bulk velocity of 9.5 m/s at equivalence ratio ranging from 0.7 – 0.95, for methane and methane/carbon-dioxide. There is an increasing trend in HRX with increasing equivalence ratio, normalised with overall mean of heat release rates (Figure 4-19). The increase in heat release rate was expected with increase equivalence ratio due to the increase in flame speed. As the flame speed increases more reactants are consumed per unit time thus resulting in an overall increase in heat release rate.

From Figure 4-19 a thin flame brush was observed close to the bluff-body while further downstream a thicker flame brush was noticeable. This can be attributed to the fact that closer to the bluff-body the length scales are smaller, the flow is highly strained and also due to heat

loss at the bluff-body. Looking at Figure 4-16 under cold flow conditions it was observed that at a bulk velocity of 9.5 m/s that the length scales starts to increase as the flow moves away from the bluff-body. From the same set of PIV measurements it can be observed that the highest strain happens closest to the bluff-body also shown in Figure 4-16. Consequently, to investigate the HRX and OH* response in different parts of the flame, localised spatial averages were computed at two different locations along the flame front as seen in Figure 4-21 and Figure 4-22. The average heat release was calculated for HRX and OH* images obtained at different equivalence ratios at 2.5 mm and 7.5 mm above the bluff-body from a box section of 5 mm. With respect to the HRX measurements both sections show the same increasing trend with varying equivalence ratio. The same procedure was used for the OH* chemiluminescence images; while the trend was similar in both sections there were some differences in the profile. OH* in the bottom section rises less steeply with change of equivalence ratio compared to the top section. These observations could be due to the fact that OH* chemiluminescence is strongly affected by variations in strain rate and curvature as shown by the work of Samaniego et al. (1999). Also Najm et al. (1998) suggested that, under the influence of unsteady strain rates, there are subtle shifts in the reaction path of hydrocarbon combustion. From the profiles obtained from the different sections of both HRX and OH* it can be concluded that HRX measurement is less sensitive to different regions of strain while the latter seemed to be more sensitive to strain and turbulence. This provided added confidence in the use of simultaneous OH and H₂CO PLIF as correlation of heat release measurement for turbulent strained flames.

As previously mentioned in chapter 2, the computational simulation of biogas (60% methane and 40% carbon-dioxide) showed a good correlation of OH and CH₂O and a good relationship exists between the theoretical flame speed and the product of OH and CH₂O (Figure 4-23 and Figure 4-24). This correlation was extended experimentally to the bluff-body turbulent flames and as in the case of methane the product of OH and CH₂O PLIF was compared to the OH* chemiluminescence. While the normalised HRX values vary slightly from the normalised OH* chemiluminescence, similar trends were observed in both cases.

4.2.3. OH and H₂CO PLIF measurements of premixed methane close to blow-off

The heat release rate (HRX) of unconfined lean premixed methane/air stabilised on an axisymmetric bluff-body was measured for conditions increasingly closer to blow-off. The same technique of simultaneous OH and H₂CO PLIF measurements are presented in section 4.2.2 was used to study the HRX at conditions approaching blow-off by slowly reducing the fuel flow rate. Four conditions were investigated starting from a condition far from blow-off, to a condition prior to blow-off (refer to Kariuki et al. (2014) for more details on the experimental conditions e.g. A1, A2, A3 & A4)

Flame	Bulk Velocity (m/s)	Φ
A1	21.6	0.75
A2	21.5	0.70
A3	21.4	0.67
A4	21.4	0.64

Table 4-1: Summary of experimental conditions

At condition A1, the HRX region located along the shear layer of the annular jet is observed to be wrinkled but unbroken with occasional vortex like structures. At the instance when the vortex appears, the width of H₂CO and HRX are seen to increase locally between the flame surfaces. This behaviour was previously reported by Balachandran et al. (2005) and will be discussed in greater detail in the next chapter. Also the HRX region along the shear layer at this condition is mostly continuous, however breaks along this region are observed occasionally. This may indicate the presence of localised extinctions along the flame front, which is not so apparent while observing only OH PLIF signal (Kariuki et al. 2014). These localised extinctions could be due to high aerodynamic stretch that the flame along the shear layer experiences, together with the heat loss effect on the burnt side of the flame locally.

At condition A4 near to blow off the shape of the flame is very different, as the flame is highly fragmented and its shape changes significantly. Dawson et al. (2011) observed that the changes happened both temporally and spatially. The local quenching of the flame downstream at condition A4 intensified and isolated regions of OH were observed inside the inner recirculation zone. This lead to a build-up in H₂CO both downstream and inside the inner

recirculation zone. From the simultaneous measurements of OH and H₂CO the small pockets of OH overlapped with the H₂CO islands, indicating that reaction takes place on the boundaries of these OH pockets. Also on occasion H₂CO was not observed in regions devoid of OH in the inner recirculation zone. This seems to indicate that fresh reactants do penetrate inside the inner recirculation zone. The data provided here from the study can be used qualitatively for the validation of turbulent premixed flame models that include finite-rate chemistry effects (Kariuki et al. 2014).

4.3. Chapter 4 Summary

This chapter described a detailed acoustic characterisation of the bluff-body combustor. The results have shown the peak Eigen frequencies to be around 30, 255 and 315 Hz at which the highest amplitude of forcing could be achieved. PIV measurements on both forced and unforced cases were also carried out. In the unforced scenario an increase in the turbulence intensity was observed while increasing the overall bulk velocity. From these PIV measurements spatial length scales and strain rate measurements were extracted. It was observed in regions close to the bluff-body that the length scales were notably smaller compared to region further downstream and the largest strain rate was recorded in close proximity to the bluff-body. For the forced flow, at low frequency of forcing the recirculation zone was affected the most, while the shear layer seemed to be oscillating without any roll-up in the process. PIV measurements indicated that at higher frequency forcing the degree of shear layer roll-up, was dependent on the strength of the forcing applied.

The unforced combustion experiments in the absence of acoustic forcing helped to identify the lean limit of the bluff-body for different air/fuel mass flow rates. OH* chemiluminescence and HRX measurements were firstly applied to pure methane flames at different equivalence ratio and overall bulk velocities (i.e. variation on turbulent intensities). Secondly, biogas flames were investigated for different equivalence ratio and turbulence intensities. For methane and biogas flames, the chemiluminescence measurements (PMT recordings) showed an increasing trend in OH* with increasing equivalence ratio. Also, when the laminar flame speed was matched and the turbulence intensity was increased, a similar increasing trend in OH* was observed. From OH PLIF measurements the flame surface was calculated which again showed an increasing trend with increasing turbulence intensity. This indicates that the increase in OH* was mainly due to the increase in wrinkling of the flame (i.e. overall flame area increase). These observations were further supported by calculating the curvature. Addition of CO₂ seem to have very little effect on the PDF of curvature at very similar bulk velocity (with the mixtures at the same theoretical laminar flame speed). The only notable change in PDF of the curvature was observed when the turbulence intensity was increased which was as expected.

Also described in this chapter is the application of simultaneous OH and H₂CO PLIF to methane flames and biogas flames. Firstly the simultaneous PLIF measurements were applied to methane and biogas flames at varying equivalence ratios and then compared to OH* chemiluminescence captured using ICCD. The two experimental measurement approaches

seem to agree very well with each other for non-swirl methane and biogas flames. An increasing trend in the integrated HRX values were observed with increasing equivalence ratio and any notable changes were observed for biogas flames at low equivalence ratio (0.6). This could be attributed to the disappearance of the outer recirculation and this possibly result in incomplete combustion on the incoming premixed fuel (i.e. the efficiency is less than 100% while part of the incoming air/fuel mixture remains unburnt). Additionally, the HRX technique was applied to conditions approaching blow-off for premixed methane flames. At conditions near to blow-off, HRX occurs on the boundary of the isolated flame pockets inside the inner recirculation. In some cases, regions were void of both OH and H₂CO indicating the entrainment of cold reactants. The experiments carried out in this chapter helped in establishing the basis for the work in chapter 5 in terms of flow rates and the adequacy of the PLIF measurement techniques.

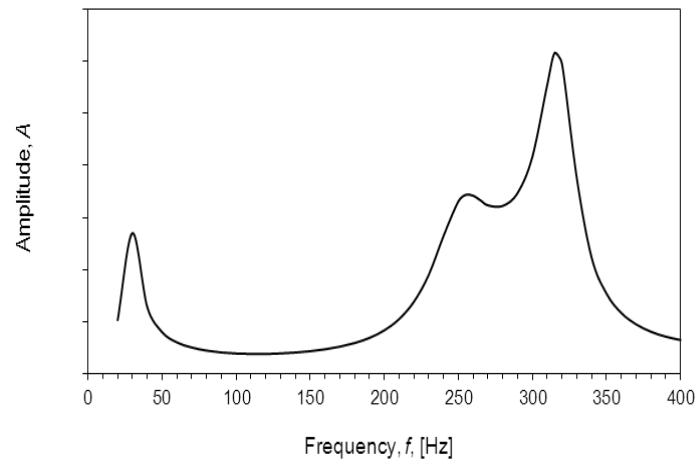


Figure 4-1: Resonance frequency of the bluff-body combustor

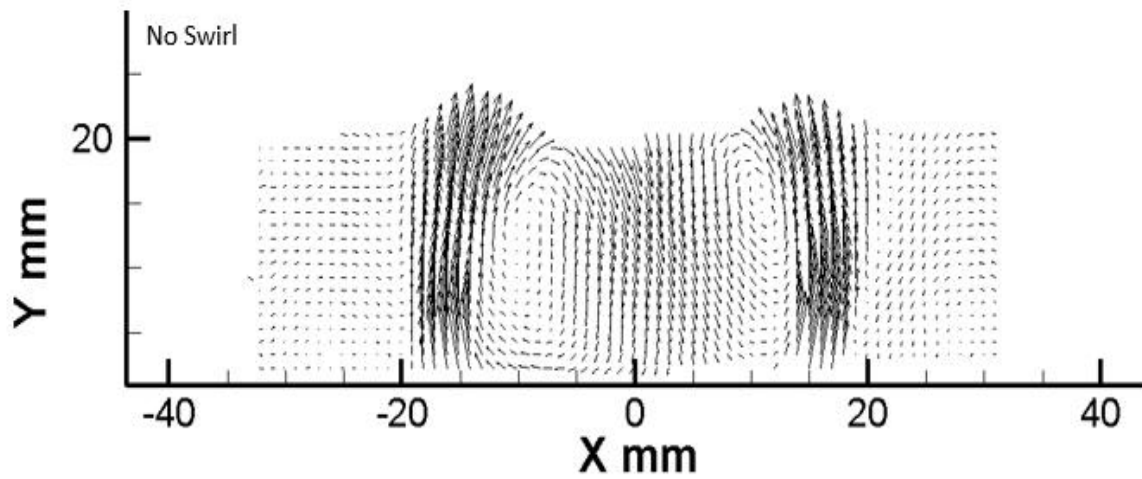


Figure 4-2: Velocity field of the bluff-body combustor at 250 lpm

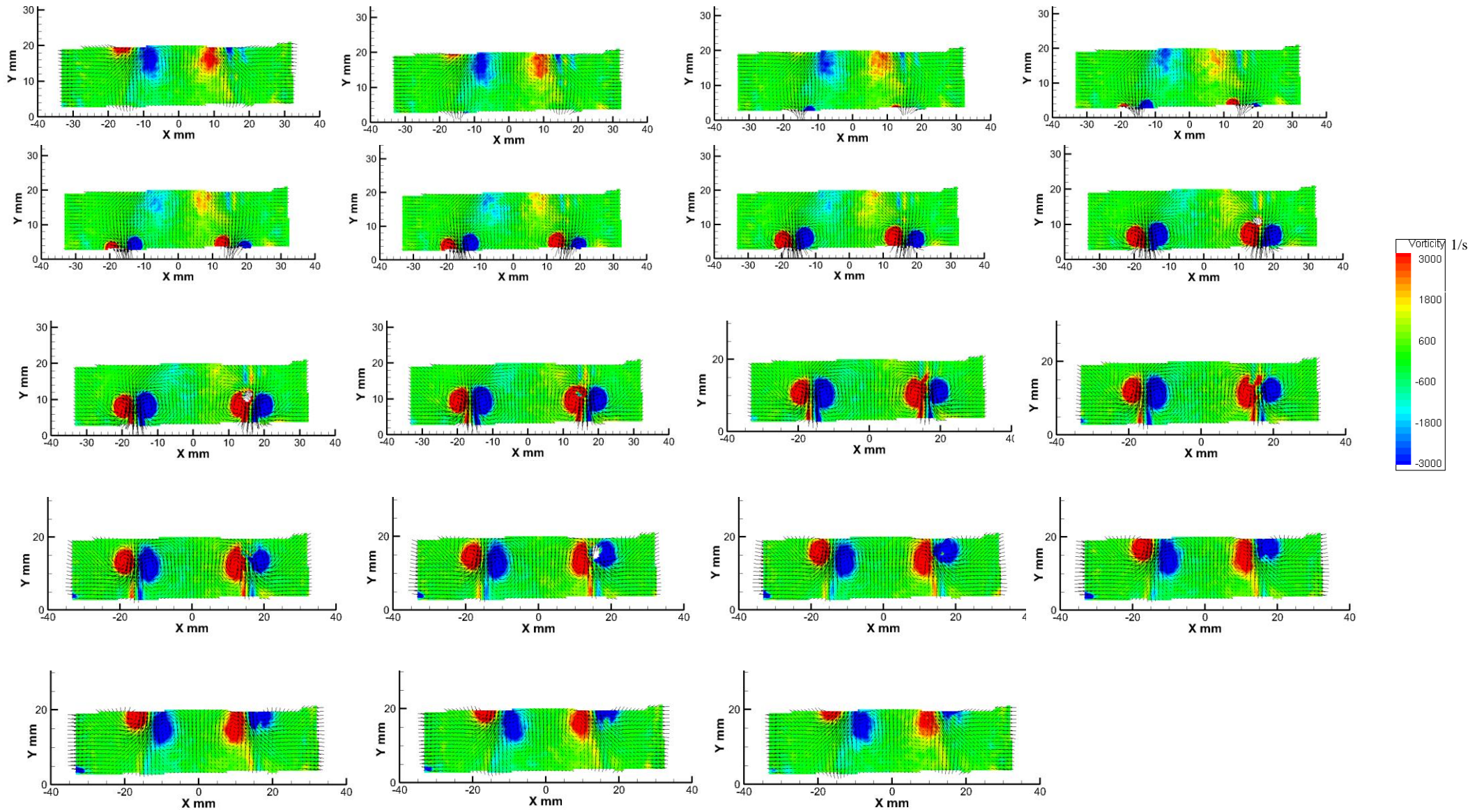


Figure 4-3: Phased locked vortex evolution – vorticity plot

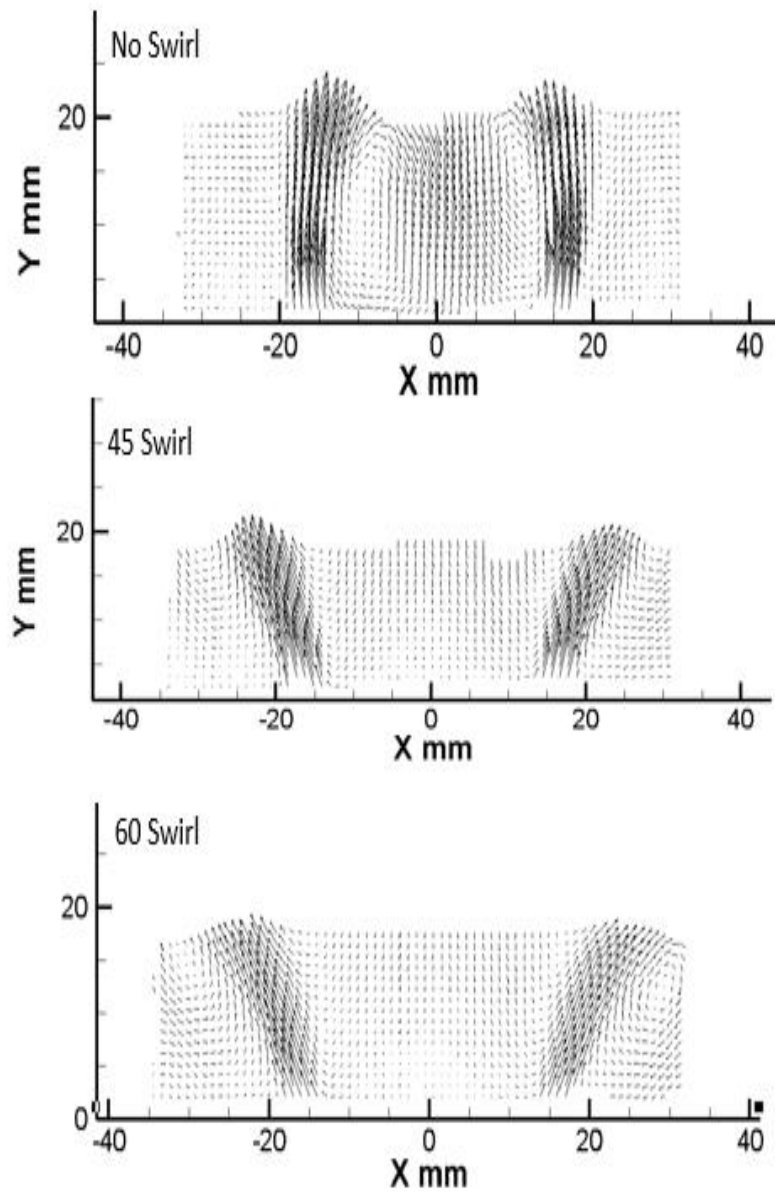


Figure 4-4: Velocity field of unforced flow for different swirler

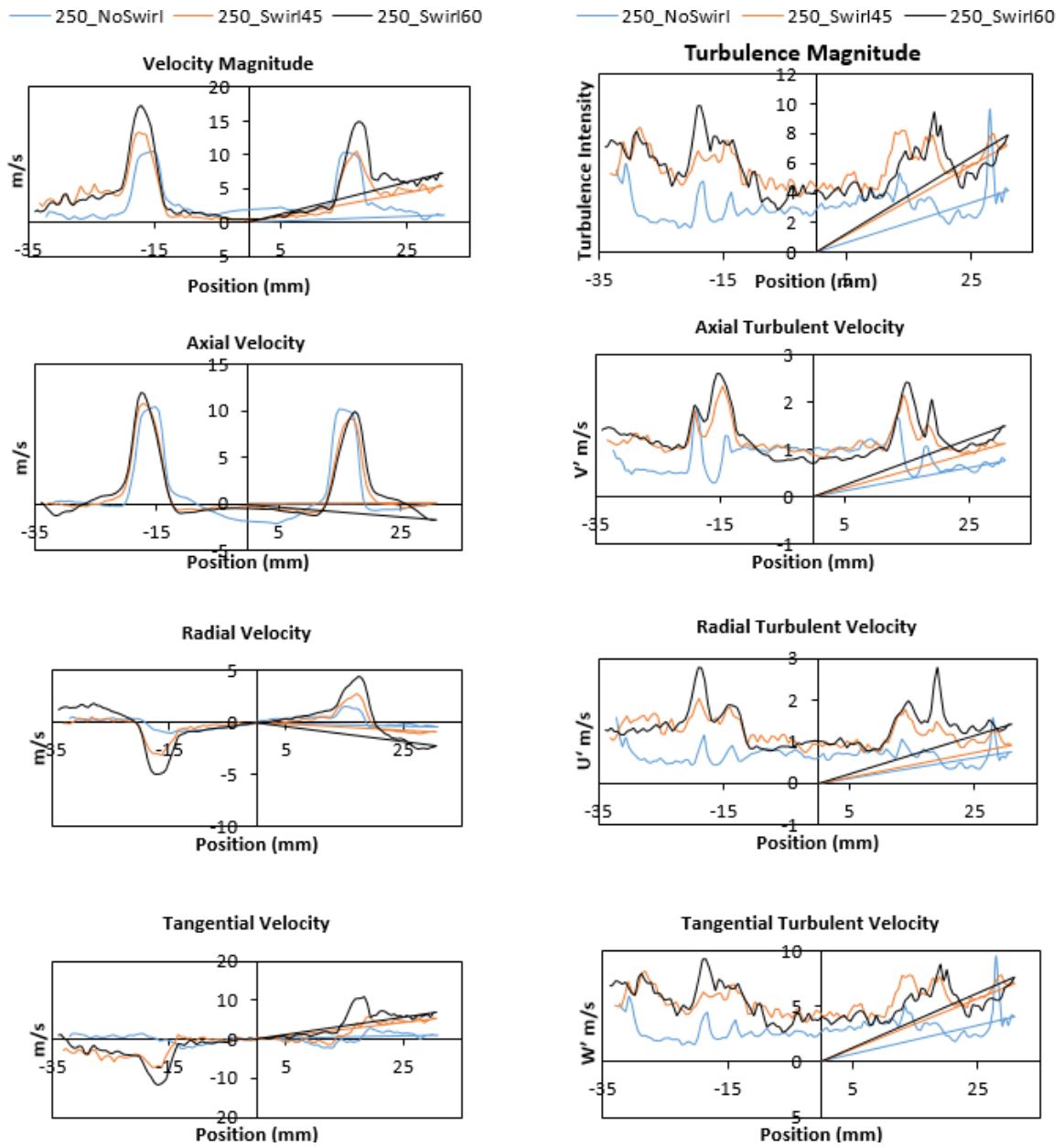


Figure 4-5: Velocity plot at 5 mm above the bluff-body for an unforced flow with different swirler

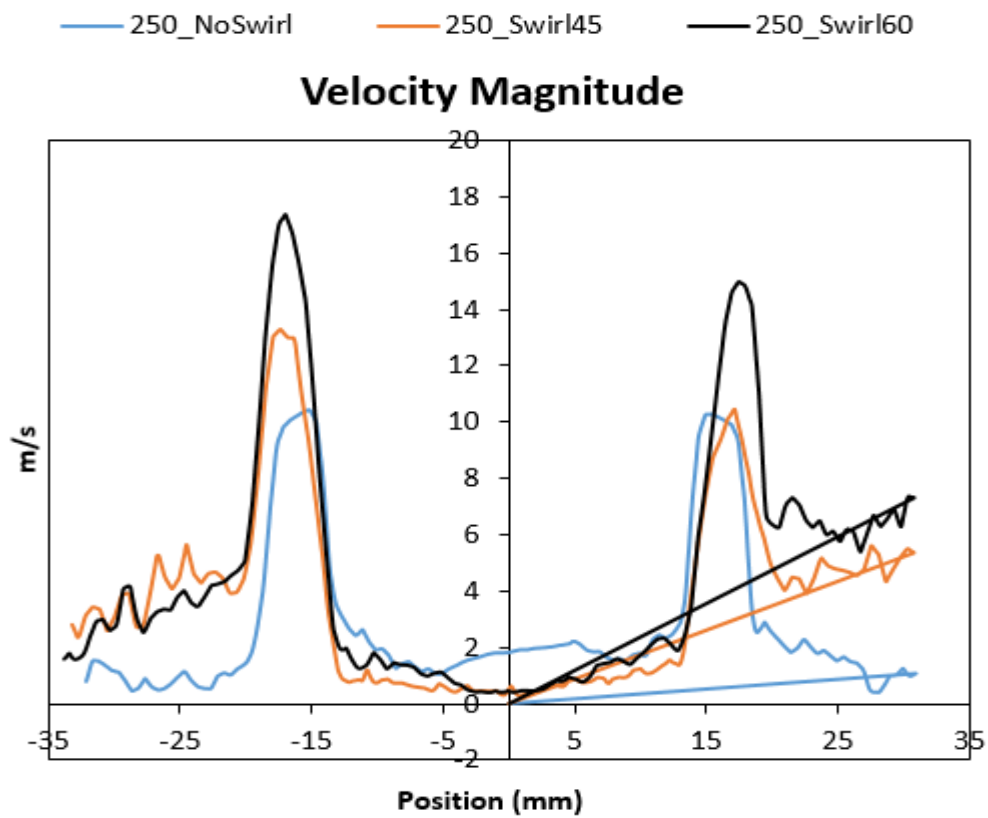


Figure 4-6: Comparison of the velocity magnitude 5 mm above the bluff-body for different swirler

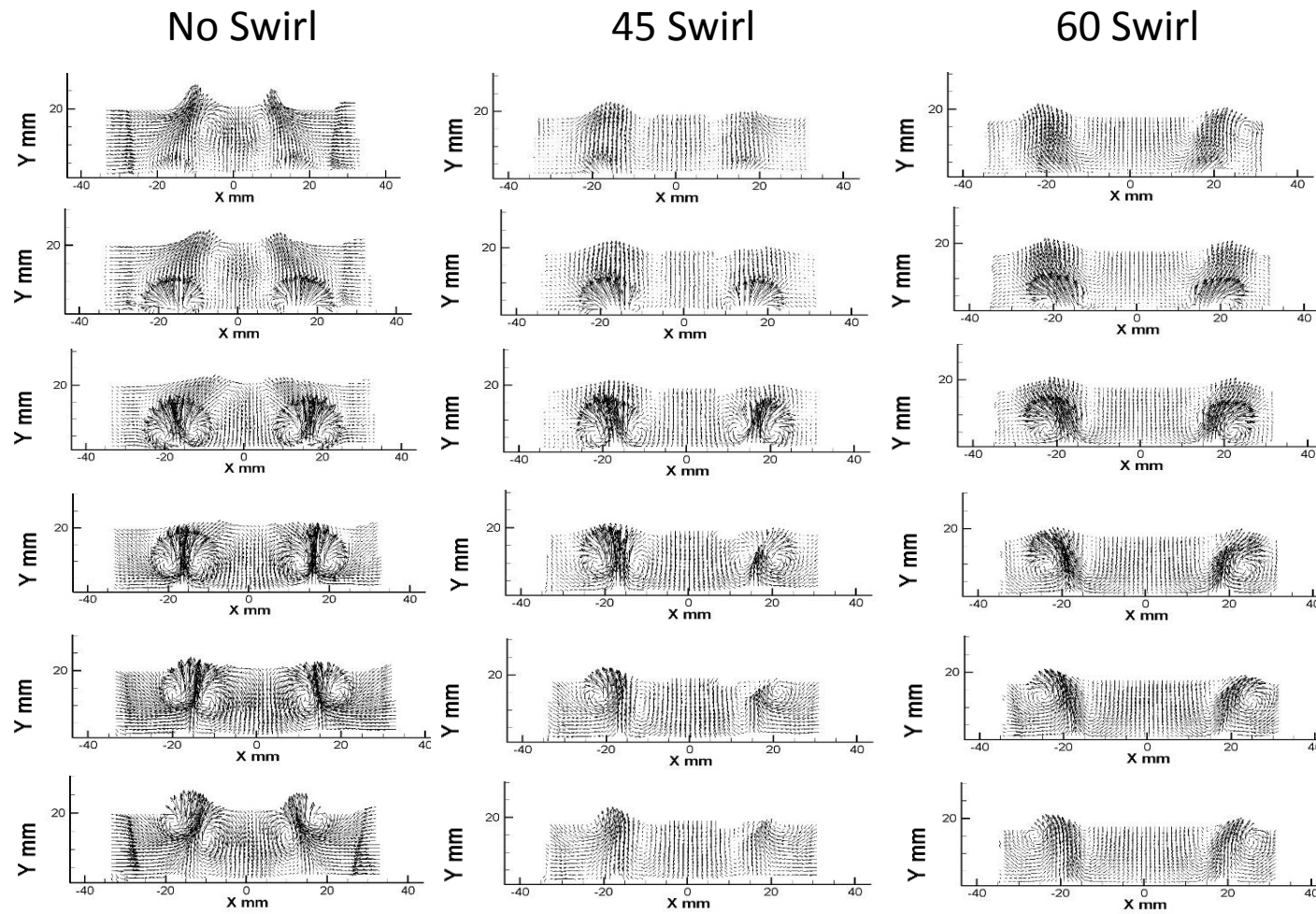


Figure 4-7: Phaselocked forced flow for different swirler Phase Angle 0 -60 -120 -180 -240 -330

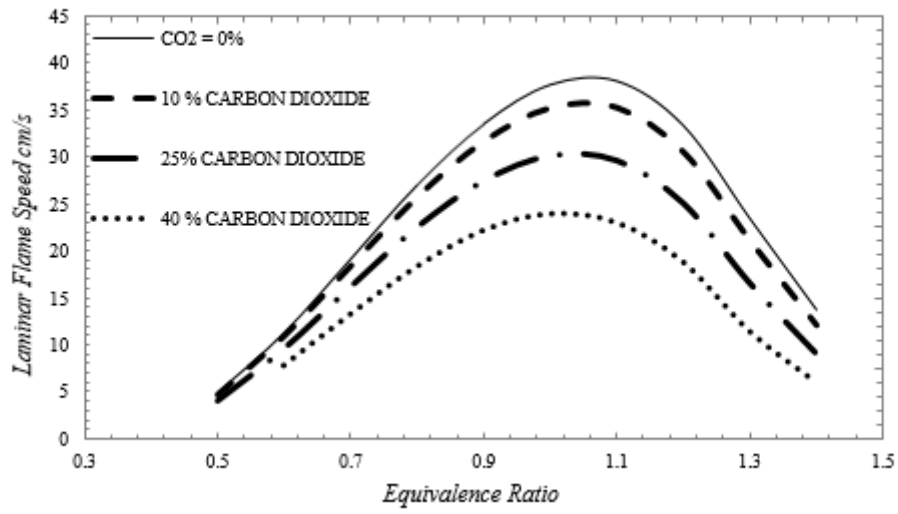


Figure 4-8: Numerical laminar flame speed measurements

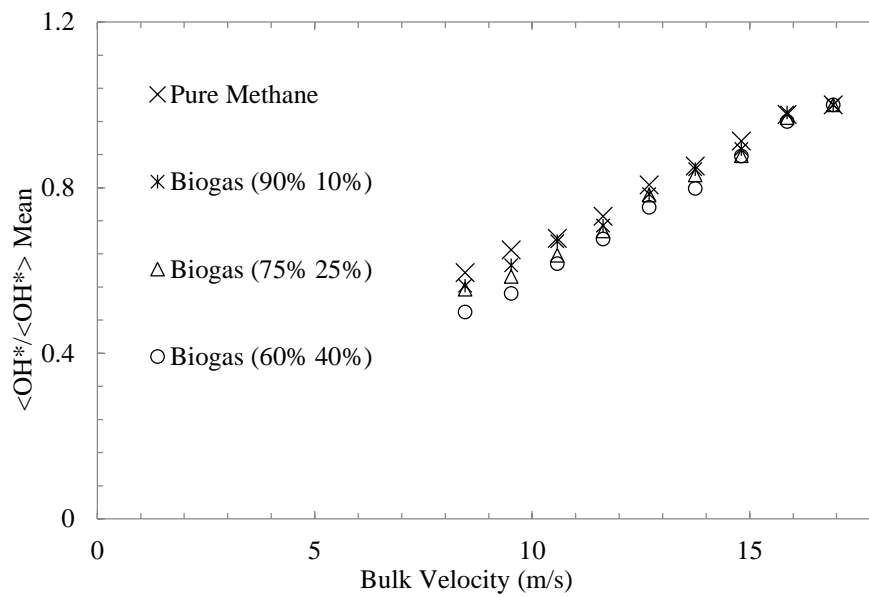


Figure 4-9: OH^* chemiluminescence variation for different biogas composition with respect to bulk velocity

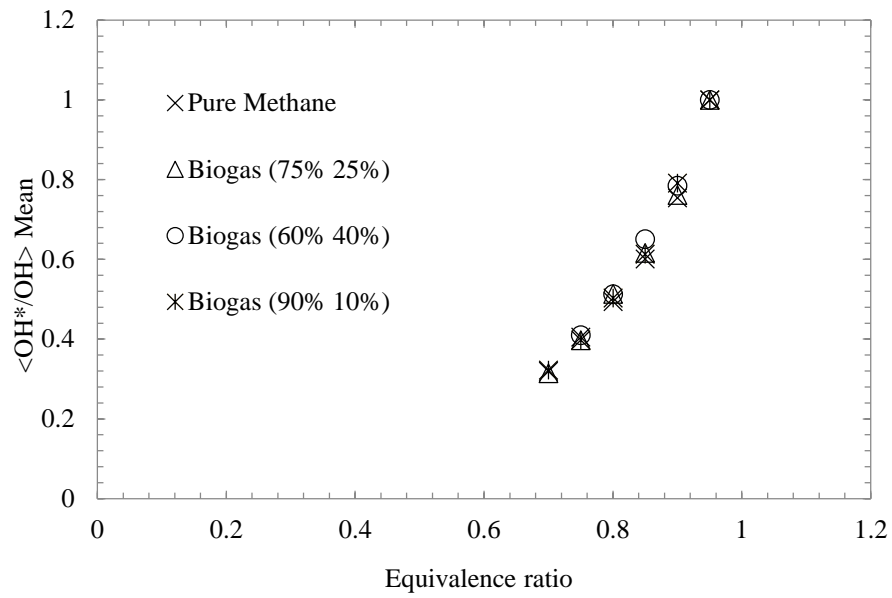


Figure 4-10: OH* chemiluminescence variation with respect to change in equivalence ratio



Figure 4-11: Instantaneous OH PLIF and FS (left) & Average OH PLIF and FS (right)

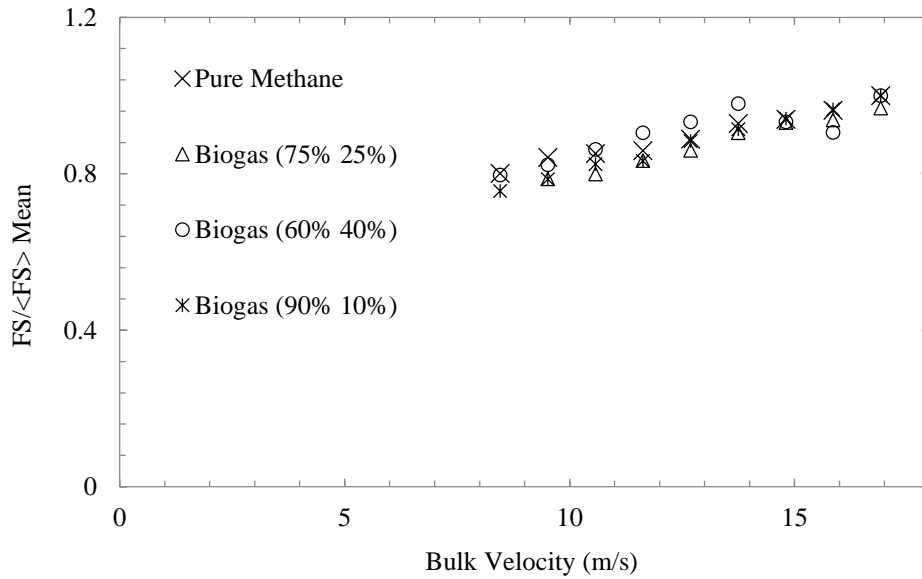


Figure 4-12: FS Variation with bulk velocity

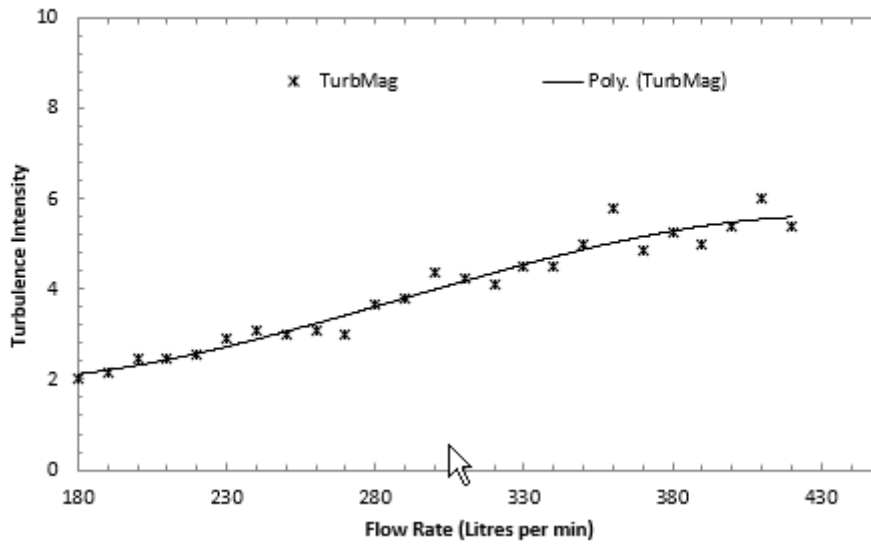


Figure 4-13: Turbulence intensity variation at various flow rates

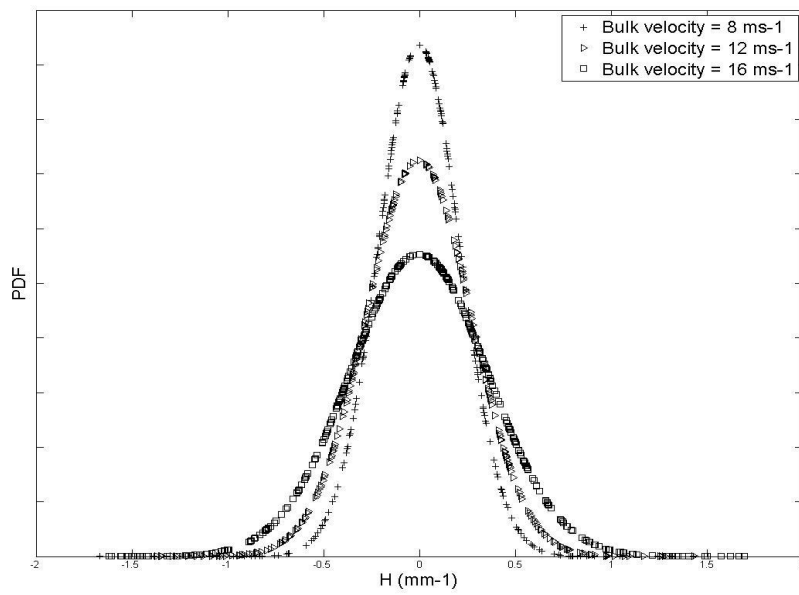


Figure 4-14: Curvature of Pure Methane Flames at different Bulk Velocity

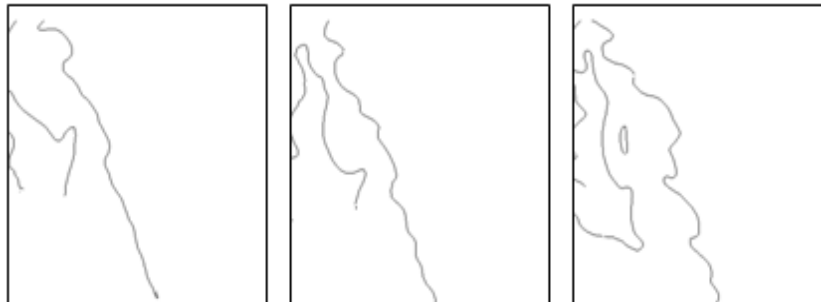


Figure 4-15: FS of Pure Methane Flame at various bulk velocities with increasing bulk velocity from left to right – FS calculation of Pure Methane flames showing the effect of wrinkling along the flame front due to an increasing bulk velocity (increasing bulk velocity from left to right, 120 lpm, 250 lpm & 330 lpm)

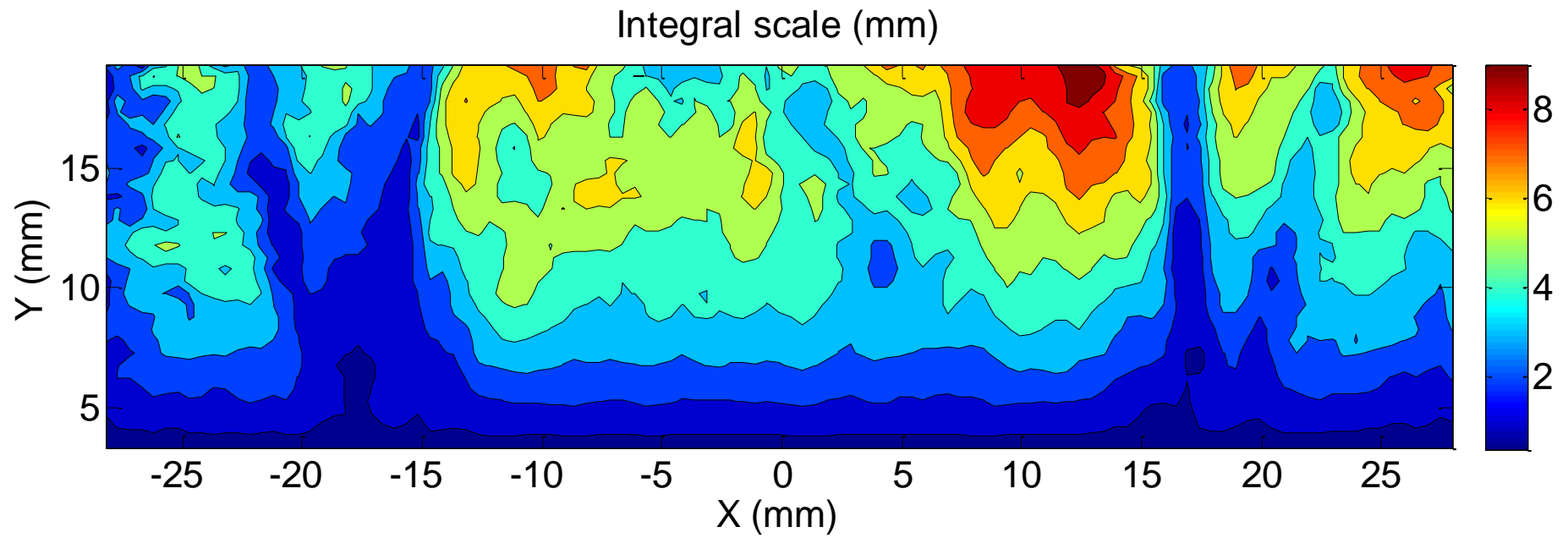


Figure 4-16: Cold flow visualisation of length scales at 250 lpm with a 20 mm interrogation window above the bluff-body

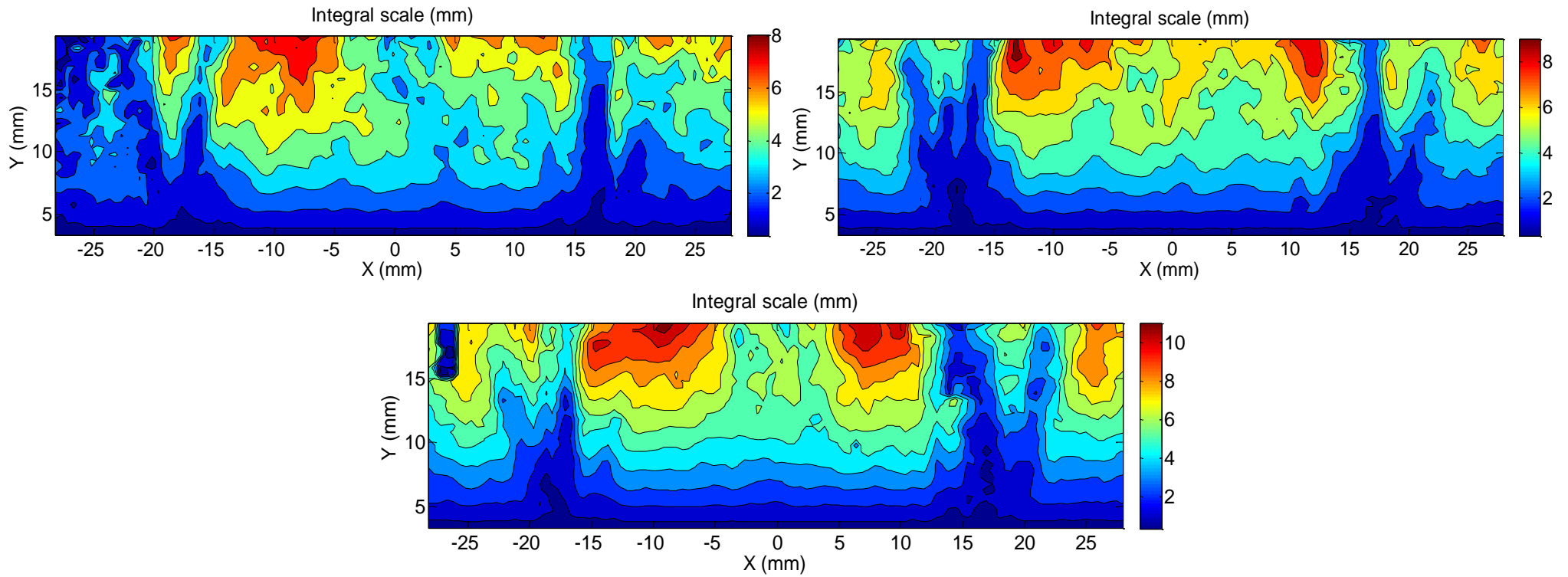


Figure 4-17: Length scales at 250 lpm (top left), 300 lpm (top right) & 350 lpm (bottom middle)

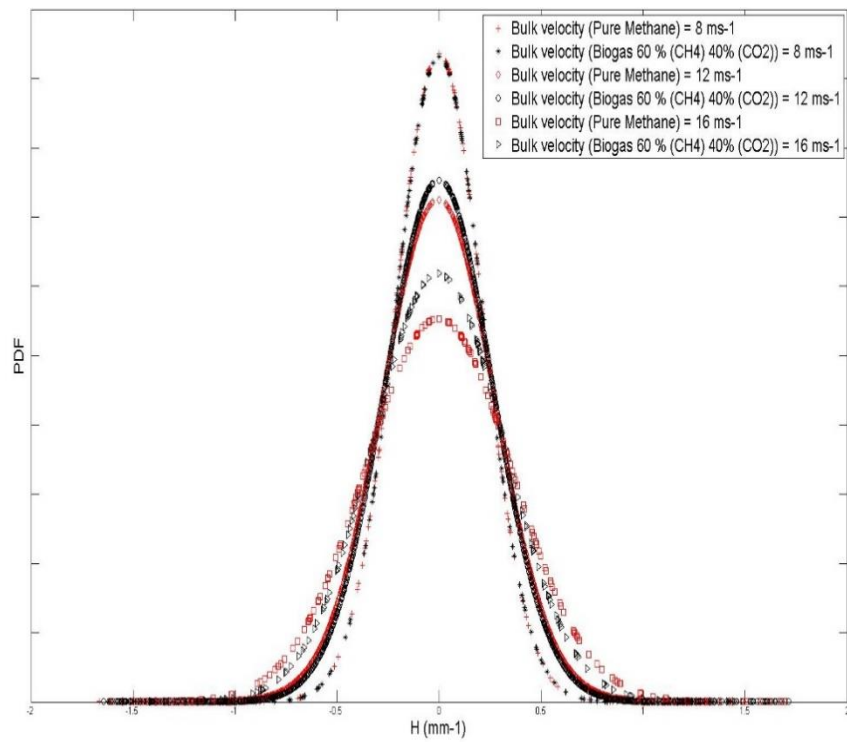


Figure 4-18: Curvature comparison of Methane and Biogas flames at various bulk velocities

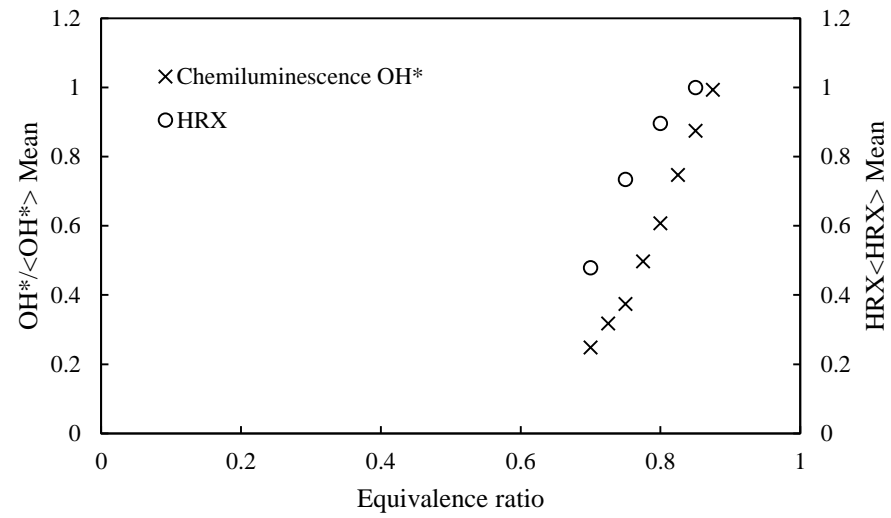


Figure 4-19: OH* & HRX variation with equivalence ratio

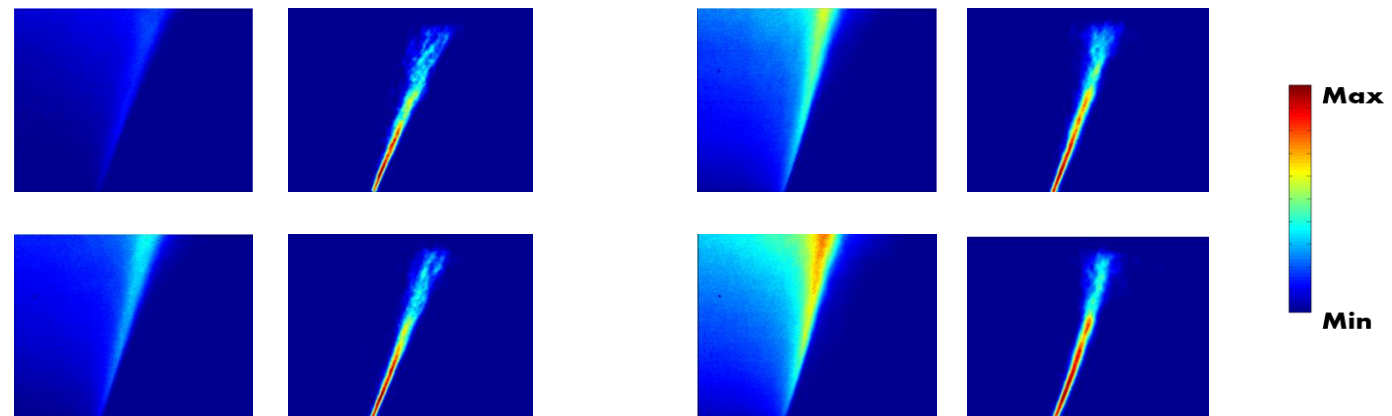


Figure 4-20: OH* chemiluminescence with corresponding HRX at different equivalence ratio 0.7 – 0.85, overall bulk velocity 250 lpm

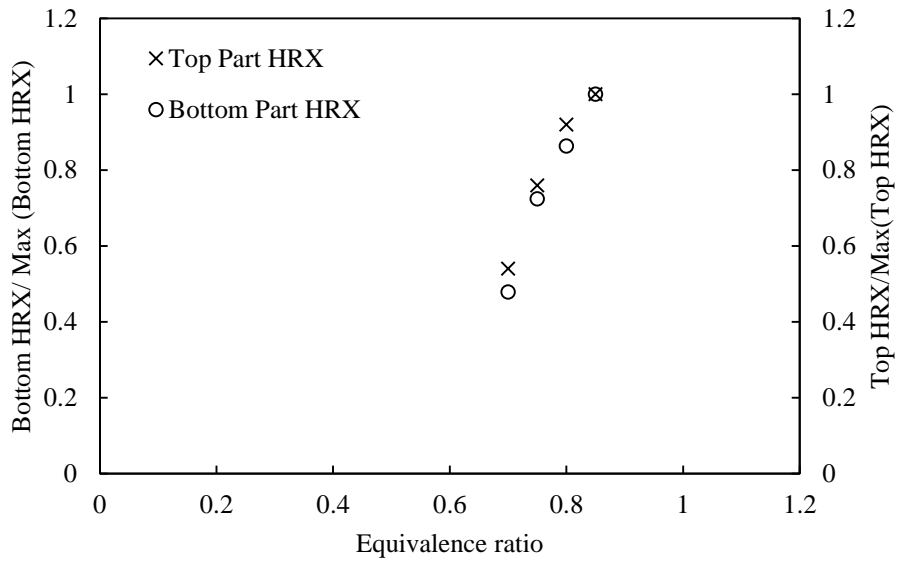


Figure 4-21: Analysis of HRX at top location of the bluff-body

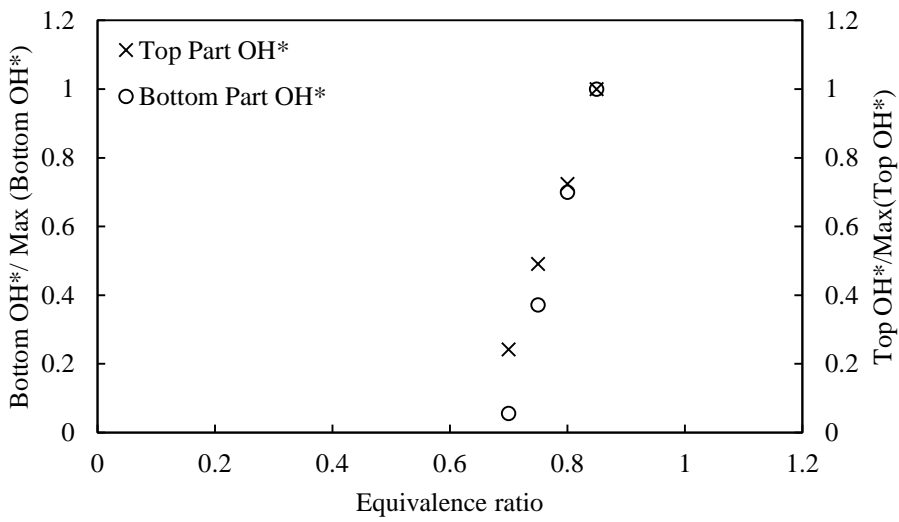


Figure 4-22: Analysis of HRX at bottom location of the bluff-body

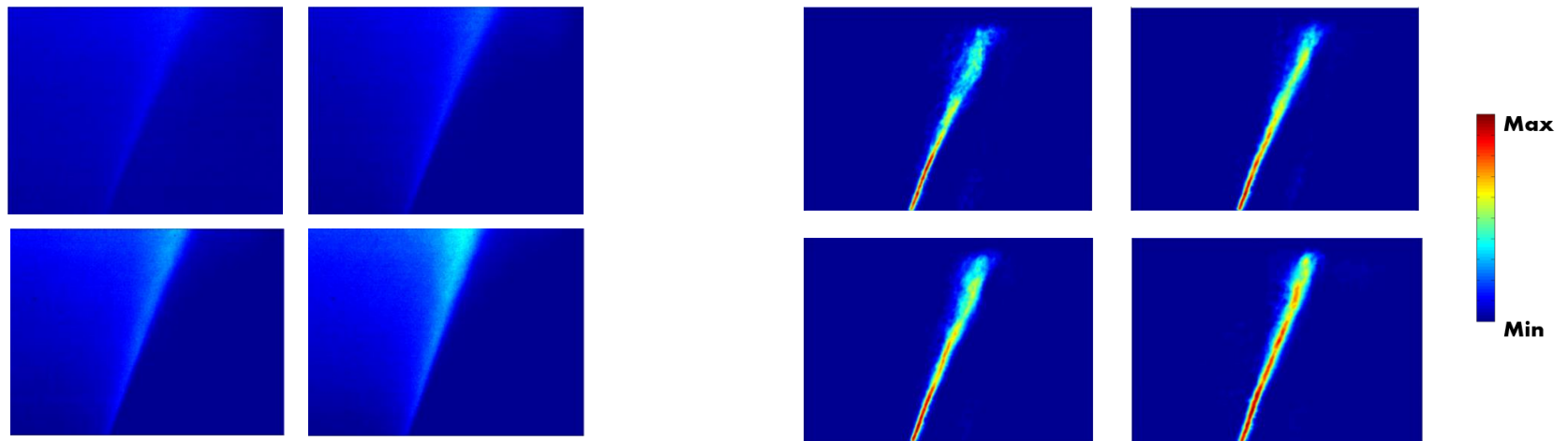


Figure 4-23: Biogas OH* and HRX measurements for varying equivalence ratio 0.7 -0.85, overall bulk velocity of 250lpm

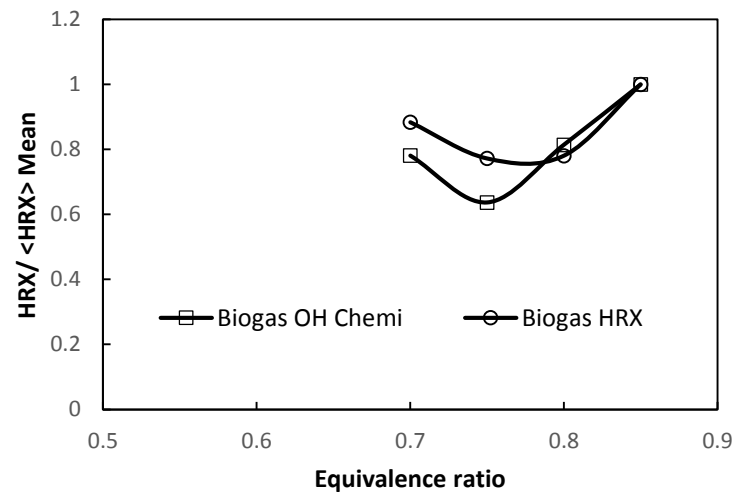


Figure 4-24: OH* & HRX for biogas at different equivalence ratio

Chapter 5

5. Forced Response of turbulent Bluff-body CH₄/CO₂/H₂ flames

This chapter focuses on evaluating the use of simultaneous OH and H₂CO PLIF heat release measurement technique in the study of turbulent premixed flames. The investigation was carried out on bluff-body stabilised flames of varying fuel compositions. The frequencies of forcing were chosen to match the natural/resonant frequency of the system in order to obtain the highest amplitude of forcing. The measurements presented for methane and biogas were performed at the same theoretical laminar flame speed. The acoustic response of simulated syngas was also investigated. This chapter starts with the investigation of the amplitude and frequency dependence of flame response on different fuels at varying equivalence ratio. This is followed by the investigation of flame response using phase locked heat release rates (HRX) at given frequencies and amplitudes of forcing. Finally, a detailed analysis of the results based on the PMT (Photomultiplier tube) and PLIF measurements discussing the flame response of methane, biogas and syngas flames and concluding with a summary.

5.1. Periodic heat release rate response and experimental conditions

The periodic heat release rate (HRX) response to inlet fluctuations were investigated using simultaneous OH and H₂CO PLIF measurements. In this section, phase averaged HRX performed at the 315 Hz for different forcing amplitudes are presented. Hussain, (2014) have shown for similar configuration a self-excited frequency of 338 Hz can be achieved by the addition of an extension over the quartz enclosure. The frequency selected here is close to the above indicated self-excitation frequency. Also presented are the flame surface calculations from OH PLIF images for frequencies of 255 Hz and 315 Hz at varying amplitudes.

5.1.1. Heat release rate response of methane air flames.

For these measurements, the flames were forced at a frequency of 315 Hz at amplitudes corresponding to inlet velocity fluctuations of 20 % - 90% (0.2 – 0.9) of the inlet velocity. As previously mentioned the amplitudes of the inlet velocity fluctuations U'/\bar{U} are denoted by A . Methane at a forcing frequency of 315 Hz and $A = 90\%$, is considered as the base case to which the other methane/carbon-dioxide mixture compositions are compared to. Figure 5-1 (at the onset whereby the counter-rotating vortices are clearly visible), showed the sequence of 12 phase averaged images of HRX at 0.265 ms (30 degrees) apart for a bluff-body stabilised flame. From the HRX images a thin flame brush was observed close to the bluff-body which could be explained by high velocity, high strain and short length scales, with the thicker flame brush observed further downstream where the length scales are correspondingly longer. In previous studies (Ayoola et al. 2006, Balachandran et al. 2005) on forced ethylene flames it was found that at relatively low forcing amplitude corresponding to $A = 12\%$ heat release rate measurements were observed to vary along the length of the flame brush with the higher values recorded downstream of the bluff-body. It is also worth noting that the appearance of the counter rotating vortices happens at $A > 15\%$. Below this threshold the flame structure such as the flame front and position, resembles that of the unforced condition. The alteration of the flame front becomes more noticeable with an increase in forcing amplitude. The amplitude dependence will be further investigated in later parts of this chapter.

Similar to Figure 5-1, Figure 5-2 shows a set of HRX of premixed methane flames forced at the 315 Hz and $A = 90\%$. At the start of the sequence a distortion of the inner shear layer, on which the flame front is stabilised, was observed. In the next set of images along the sequence, the distortion of flame front could be observed clearly as the formation or evolution of an inner vortex as it starts to propagate along the shear layer away from the bluff-body. One noticeable feature was the increase in size of the vortex as it propagates along the shear layer and away from the bluff-body. As the vortex propagates away the inner shear layer inner shear layer returns to its original form and structure which was very similar to the unforced case. This can be seen in the highlighted region of Figure 5-3. After the collapse of the vortex a small distortion of the flame brush close to the bluff-body started to build again. As a new vortex is formed, the flame front becomes distorted (rolled-up) and the process is repeated. In previous studies it was observed that the distortion of the flame surface area has a significant effect on

the HRX distribution. Higher HRX measurements were observed with negatively curved flames than compared to those with a positive curvature. A similar pattern was observed in the premixed methane case, whereby the flame area fluctuated due to the presence of the counter-rotating vortices, which had a significant effect on the distribution of the HRX at the flame front that required further investigations.

In order to further understand the effect of the counter-rotating vortices on heat release modulation, the flame surface area in the region of the vortices were analysed. Figure 5-4 shows a typical time-averaged flame surface (FS) image of an unforced flame. As seen previously the flame was primarily anchored at the shear layer generated by the bluff-body with some flame elements on the side recirculation zone. The reason no flame stabilisation was observed on the side recirculation was mainly due to the lower local temperature (i.e. heat loss). In the case of forced methane flames (Figure 5-5) the FS captured similar flame structures as those observed using HRX images except for one particular case ($A = 90\%$) which is discussed in an upcoming section. The shear layer rolled to form counter-rotating vortex pairs with the inner shear layer rolling inwards while the outer-shear layer has an outward motion. In Figure 5-6, it can be noted that the flame surface area decreases with the beginning of the roll-up and decreases further to reach its lowest value at around 70 – 90 degrees phase angle. This also corresponded to the case where HRX was measured at its lowest value. As the vortex starts to move downstream its size starts to increase resulting in an increase in size of the flame area. Again a similar pattern was observed in the HRX measurements. A maximum value of integrated heat release estimation using this method was attained at a phase angle corresponding to 240 degrees.

For the case shown, $A = 50\%$, the heat release rate estimate (HRX) and the flame surface area showed good agreement with each other with a small difference in magnitude (Figure 5-6). A similar trend was previously observed in the work by Ayoola et al. (2006) and Balachandran et al. (2005), when simultaneous OH and H₂CO PLIF and the flame surface density were compared for ethylene flames. It was also mentioned in these studies that the flame surface density tends to underestimate the heat variation. Therefore, careful interpretation of the result is required and it should be done on a case-by-case basis. Also observed in this study, is that the difference in the measurements was more noticeable at larger amplitude of forcing and the difference of flame surface was no more than 20%.

It has to be noted that the accuracy of the HRX technique is critically dependent on the geometrical transformation. In order to minimise the error in the HRX imaging the largest possible interrogation window was used. The PIV data in chapter 4 shows that the flow had the same profile and pattern on either side of the bluff-body. Therefore, in order to assess and confirm that the flame was completely axis-symmetric during combustion, under the same experimental conditions, two sets of images were captured. Firstly the whole combustion region was captured and secondly, the ICCD camera was adjusted so that only half of the flame was captured. The flame surface was then computed for both set of experiments and compared to each other. The results showed no difference in the flame surface results, which provided confidence that the choice of interrogation window did not affect the accuracy of the global heat release estimate.

The measurements carried out so far on methane flames suggest that the HRX method captured the global heat release rate well for the type of flame under investigation and can therefore be extended to simulated biogas HRX. Before the HRX measurements for biogas are presented, firstly the frequency and amplitude dependence of forced methane flames will be discussed. The flame response was computed from measurements of the pressure fluctuations and OH* chemiluminescence for a range of different frequencies and amplitude of forcing. By employing the two microphone methods the amplitude A was calculated for a given frequency and amplitude of forcing, which is then plotted against its corresponding OH* chemiluminescence measurements.

5.2. Heat release response of methane flames

The spectral analysis of the heat release measured using a chemiluminescence technique along with the acoustic velocity from the two-microphone technique was used to understand the nonlinear heat release - velocity coupling. The effects of various parameters that have an impact on the flame response are presented in this section.

5.2.1. Frequency and amplitude dependence of the flame response

Figure 5-7 illustrates in the OH* chemiluminescence at varying forcing amplitude while the forcing frequency is kept constant at 315 Hz. When the first part of the graph is examined at an amplitude A below 15% ($A = 0.15$), a linear dependency is observed. When the amplitude exceeds 15% a first saturation plateau can be seen. With further increase in amplitude the flame response reaches a second saturation point which occurs at amplitudes above 80%. Figure 5-7 also shows the flame transfer function and the corresponding phase extracted from the data in the same figure. At low amplitudes the flame transfer function has a linear dependence until a forcing amplitude value of $A = 15\%$ is reached. Then a gradual increase in amplitude of the flame transfer function is observed until 45%, and beyond which any further increase in amplitude resulted in little change in the flame transfer function. When examining how the phase is affected by the amplitude it was observed, that below a 15% forcing amplitude, the phase showed no dependency on the amplitude but the higher amplitude resulted in an increase in phase difference. Studies carried out by Balachandran et al. (2005) and Bellows et al. (2007) showed that similar saturation levels and evolution of the flame surface area were found to have a direct implication for the non-linearity observed.

Figure 5-8 shows the flame response evaluated from the flame surface. For these experiments the whole flame region was imaged. A flame at a laminar flame speed of approximately 22 cm/s and bulk velocity of 9.5 cm/s were used at fixed forcing frequencies of 255 Hz and 315 Hz. The measurements were carried out for a range of amplitudes ranging from 10% to 80%. The figure shows that two saturation points were observed which were similar to the OH* measurements. From the image sequence in Figure 5-9 it can be observed that at an amplitude of 20%, the flame surface is increasingly more wrinkled compared to that at 10% and takes on the appearance of the vortex roll-up. The appearance of the vortex roll-up shortened the flame,

which in turn reduced the total flame area non-linearly, despite the fact that the flame area is expected to be increased by flame elements wrapping around the vortex. Balachandran et al. (2005) demonstrated that the fact that the global heat release decreased with the appearance of the vortex suggest that flame destruction or flame annihilation occurs directly above the vortex. Therefore, the balance between the fluctuations in local heat release by the vortex roll-up, the cusp formation and flame destruction events resulted in the global heat release modulation (Balachandran et al. 2005). From both the HRX sequence and flame surface (Figure 5-2 and Figure 5-5) sequence at 80% amplitude it can be observed that the flame elements above the vortex are very sparse. The HRX image also suggests that in the presence of the vortex roll-up, the reaction primarily occurs at the region of the vortex. It can be observed from these images that the intensity of the flame elements above the vortex region decreases with an increase in amplitude of forcing suggesting that the strength of the vortex plays a major role in the flame annihilation. A further increase in the amplitude, increases the flame surface area until 60% whereby the flame response levelled-off. At amplitudes of 70% and 80% there seem to be no difference in the flame structure or in the particular the size of the vortex roll-up.

Figure 5-10 shows the cyclic variation of the flame surface over one complete cycle over a range of amplitudes. It can be seen that with an increase in amplitude there is an increase in peak-to-peak amplitude. The saturation previously observed at amplitude A greater than 60% can also be noticed from the graph. At amplitude $A = 70\%$ & $A = 80\%$, the flame surface variations were nearly identical in magnitude and phase.

The frequency dependency of the flame response was also investigated for different forcing frequencies. Only the three frequencies which produced relatively high amplitude of forcing are presented here. Figure 5-12 shows the frequency and amplitude dependence of heat release response of the flame at 30 Hz, 255 Hz and 315 Hz across a range of amplitudes. At the lowest amplitude of forcing the heat release response was linear at any given amplitude of forcing. The flame surface calculations (30 Hz) have shown that there was no shear layer roll-up and any flame area modulation can only be due to the oscillatory or flapping motion of the flame.

Figure 5-12 shows the amplitude dependence of the heat release response for the flames forced at 255 Hz and 315 Hz. As observed in the case for 255 Hz the appearance of the first saturation point coincides with the appearance of the flame roll-up during the 315 Hz forcing. Presented in Figure 5-11 are the flame surface estimates for methane flames forced at 255 Hz and 315 Hz, at the highest amplitude. It was observed that at the highest amplitude the roll-up in the

case of 255 Hz was less prominent than for 315 Hz. This could be explained by referring back to Figure 2-6 in which the peak occurring at 255 Hz and 315 Hz are compared. At 315 Hz higher amplitude is achieved by excitation of the system, which in turn affected the size of the roll-up. For both cases the occurrence of the saturation point occurs approximately around the same amplitude and as discussed previously, which coincides with the appearance of the counter-rotating vortices. The fact that for the forcing frequency of 30 Hz the heat release response remains linear with varying amplitude compared to 255 Hz and 315 Hz indicates that the heat release response is strongly frequency dependent which is as expected. In an effort to further investigate the frequency and amplitude dependency, the overall bulk velocity was increased and the flame response was measured as aforementioned.

Figure 5-13 shows measurements of the heat response at the same forcing frequencies previously mentioned but at a higher bulk velocity. Comparing the two frequencies that exhibit saturation in the flame response, it can be noted that at 315 Hz the amplitude required to reach the saturation point is much lower. These observations also points to the fact that the amplitude of inlet oscillation required to achieve excitation of the shear layer roll-up into a vortex is highly frequency dependent. The observations corroborated with the work by Balachandran et al. (2005) and Kulsheimer & Buchner, (2002) with the latter showing that the required amplitude needed to excite the shear layer to roll up decreases with increasing frequency. For certain conditions it was observed that before one vortex moves out of the combustion zone a new vortex appears at the base of the flame. The interaction of these two vortices could be a cause for the non-linear dependence of phase on amplitude. A possible explanation could be due to the fact that at this forcing frequency the flame might not be acoustically convectively compact (Lieuwen et al. 2003). The flame Strouhal number, which is defined as the mean length of the flame to the length scale of the imposed fuel/air ratio excitation, determines whether the flame can be regarded as being convectively compact or distributed. Shreekrisha et al. (2010), have shown that at a high Strouhal number the effect of flame stretch and the non-quasi-steady response of the flame structure are mainly because of a time lag due to internal flame processes become more significant.

For premixed flames there are two predominant mechanisms that are responsible for non-linearity in the heat release response. The first is due to nonlinearities in the flame speed and heat of the reaction dependence upon equivalence ratio. The second can be attributed due to the intrinsic nonlinear property of premixed flames in that they propagate normally to themselves at each point (Peters, 2000). Shreekrisha et al. (2010), suggested that the first

mechanism manifests itself in two different ways, but the most likely mechanism is where the instantaneous stoichiometry oscillates between lean and rich stoichiometries. In the current study premixed methane/air mixtures have been used and from Figure 3-3 it can be observed that laminar flame speed has a sharp increase to a maximum at around equivalence ratio 1 and then a similar decrease at higher equivalence ratios. So it would be of interest to investigate the heat release response of other premixed mixtures that have a more progressive or rapid increase in laminar flame speed compared to methane, so that one can utilise this information for analysis of combustion oscillations.

At a forcing frequency of 315 Hz and at an amplitude of $A = 90\%$, a phase difference between the HRX and the flame surface was observed (Figure 5-14). In order to further investigate this phase difference two different sections of the flame were taken as shown in Figure 5-15 and the variation in those regions were analysed. Shown in Figure 5-15 is the HRX variation for the top and bottom section of the flame; with the bottom region represented by a box of 5 by 5 mm at a distance of 2 mm and the top region by a box of 5 mm and 7 mm, 7 mm above the bluff-body. It is clear that the appearance of the vortex coincided with an increase in the HRX signal. As the vortex travels downstream and grows in size, the HRX signal strength increased. As the vortex leaves the bottom window at a phase angle of 210 degrees a sudden drop of the HRX signal is observed. However an opposite trend is observed in the HRX signal when the whole section of the flame is analysed. As mentioned previously the appearance of the vortex at the bottom of the flame coincides with a decrease in HRX signal. This again could be due to the balance between the fluctuations in local heat release caused by vortex rollup, cusp formation and flame annihilation which results in the global heat release modulation observed. In the analysis of the top section of flame (Figure 5-15), downstream of the vortex a low HRX signal was noted at the beginning of the phase and the signal increases as soon as the vortex enters the top region. A drop in HRX signal at a phase angle of 180 degrees was observed which could be attributed to the size of the region as it did not include some of the HRX signal in the recirculation. From the observations in Figure 5-15, it was evident that locally the vortex increases the reaction due to higher integrated HRX signal measured in the region where the vortex is present.

5.2.2. Effect of equivalence ratio

Figure 5-12 also shows the effect of the equivalence ratio for a range of frequencies with different forcing amplitude on pure methane flames. The equivalence ratio was varied from 0.7 to 0.9 and measurements of OH* chemiluminescence and acoustic pressure measurements were taken simultaneously. These were used to obtain the global heat release response of the flame. The mixture under investigation was that of methane/air and the global bulk velocity was kept at 9.5 m/s. At a forcing frequency of 30 Hz, the flame response showed a linear response for all of the equivalence ratio values investigated. At higher frequency of forcing 255 Hz and 315 Hz the heat release response increased with an increase of equivalence ratio and the non-linearity appeared at higher amplitude for higher equivalence ratios. This can be attributed to the fact that at higher equivalence ratio the laminar flame speed increases which shifts the flame position relative to the position of the vortex (Balachandran et al. 2005). At higher amplitude a second saturation point was observed but it was more prominent in the case of higher equivalence ratios. It can be seen that above the 80% amplitude for an equivalence ratio higher than 0.8 there is a decrease in heat release response at forcing frequency of a 315 Hz. However the trend in variation as a function of amplitude was the same for all cases.

In order to better understand this non-linear behaviour the bulk velocity was increased and the equivalence ratio was varied at the aforementioned frequencies and amplitudes. At 30 Hz, the OH* heat release response was seen to be linear irrespective of the change of bulk velocity. At forcing frequency of 255 Hz it can be seen at higher bulk velocity (300 lpm bulk velocity of air) the response was linear up to an amplitude of 20 % and then some degree of non-linearity started to appear. Above an amplitude of 30 % the heat release response seems to behave linearly again. From the Figure 5-16 there are also no indications that a second region of non-linearity will occur at same amplitude of 80 – 90% as previously observed. Additionally at a forcing frequency of 255 Hz the magnitude seems to remain unchanged for different A at bulk velocities of 300 and 350 lpm. At a forcing frequency of 315 Hz as the bulk velocity is increased, the second region of non-linearity was not observed for a bulk velocity of 350 lpm of air. It is interesting to note that while increasing the bulk velocity the first region of non-linearity was less prominent and seems to have a linear behaviour. The results would suggest that at higher bulk velocity the flame does not roll-up as much due to the higher induced strain (due to higher bulk velocity). This seems to indicate that the suppression of the flame rollup appearance could help in the mitigation of the first non-linear region.

5.3. Biogas Combustion

Biogas is produced from the anaerobic digestion of biomass or organic waste or such as industrial waste gases containing hydrogen and carbon-dioxide. Anaerobic digestion is a biological process that happens when bacteria breaks down organic matter in environment with little to no oxygen. Special landfills are developed which capture the gases that are released. If they are not captured and utilised these gases will be released into the environment instead, to the detriment of the ozone layer and the planet. As previously mentioned, biogas have components similar to the natural gas used in combustion turbines. The gas composition, physical properties, and flame response during combustion are key parameters for natural gas and biogas. For both gases the main component is methane, and the main difference is the high content of carbon-dioxide and hydrogen sulphide present in biogas. From a technical point of view the most important difference is that Wobbe index for natural gas is twice of that of biogas (Figure 5-17). The Wobbe index is defined as the heating value divided by the square root of specific gravity. The result is a number that can be used as a basis for comparison between different gases and are often measured in terms of megajoules per standard cubic meter (MJ/Sm³).

The Wobbe index is often used as an indicator of the interchangeability of fuel gases and only gases with a similar Wobbe index can be substituted for each other. The distribution of biogas by natural gas network is also limited by Wobbe index. Adjustment of the Wobbe index by removing carbon-dioxide and the purification (Hydrogen sulphide) can upgrade biogas close to natural gas quality. Once treated, this gas can then be fed into a gas fired combustion turbine where it is used to generate electricity. Opportunities for biogas also exist in the automotive industry.

From a usage standpoint, natural gas has a typical heating value of 39.2 MJ/cm³ and biogas has 23.3 MJ/cm³ (Eriksson, 2014). This means that in order to achieve the same thermal output, a burner must flow 68 % more biogas (by volume). This increase in flow rate brings with it the issue of the flame stability relating to dilution. Over the last 25 years many studies have been carried out on in the field of turbulent and laminar jet flame stabilisation. This area of research is of great importance as it provides an insight into the operation of practical devices such as boilers, combustors and turbines. Issues that are currently investigated in the field of turbulent lifted jet flame stabilisation studies include turbulent burning velocities, large scale structures, scalar dissipation, laminar flamelets, triple flames and streamline divergence. All of these

issues are impacted by the presence of diluents like those present in biogas, hence, an understanding of their relevance is critical in estimating the ability of utilising biogases effectively with the existing hardware. Previous work by Balachandran et al. (2005), Ayoola et al. (2006), and Lieuwen et al. (2012) with ethylene and methane have shown that the study of the flame structure, flame response and heat release rate can be used to provide an insight into the behaviour of such gases. In this section, the flame response and heat release rate of biogas flames will be investigated for mixtures with the laminar flame speed constant.

Usage of biogas is not restricted to gas turbine combustion but can be extended to light duty vehicles. Light duty vehicles can normally run both on natural gas and biogas without any modification whereas heavy duty vehicles without closed loop control may have to be adjusted if they run alternately on biogas and natural gas. Due to the reasons aforementioned the addition of carbon-dioxide into fresh gases has become an important research topic in turbulent premixed combustion especially in studies relating to stationary gas turbines. Firstly, exhaust gas recirculation (EGR) has been primarily used for decreasing NO_x emissions because the dilution of the mixture by EGR decreases the flame temperature. The exhaust gas contains a high content of carbon-dioxide which dilutes the fresh gas mixture when added to it. This will also reduce the heat release rate in the combustion chamber; the stable flame regime can be extended to mixtures with lower equivalence ratios. This turbulent combustion regime is therefore close to the so-called extended or distributed combustion zone regime or in sense to a flameless combustion regime (Kobayashi et al. 2007). Secondly, the addition of carbon-dioxide to the fresh gas mixture is directly related to fuel flexibility (Kobayashi et al. 2007). As mentioned previously in order to diversify fuel resources and move away from fossil fuels, gas turbines can be fed by gaseous fuels containing carbon-dioxide. Such fuels have several origins such as biogas and syngas.

One of the main aims of this work is to compare methane (CH₄) combustion to biogas (CH₄ + CO₂) combustion at the same laminar flame speed and different equivalence ratio. For the purpose of this study flames of simulated biogas (mainly CH₄ and CO₂) are examined. As previously, methane flames with CO₂ dilution with the same theoretical laminar flame speed were studied. The effect of varying equivalence ratio were then analysed. The flame shape and heat release rate of these flames were obtained from OH and H₂CO planar laser induced fluorescence measurements and OH* chemiluminescence. The objective of this work also includes clarification of the effect of CO₂ dilution on the flame response of biogas flames.

5.3.1. State of the art related to biogas combustion

As in the case for methane/air flames, the flame response of biogas (methane/carbon-dioxide) flames with respect to frequency, amplitude and equivalence ratio is investigated. These measurements were necessary in order to fully understand the response of biogas flames to acoustic perturbations. Firstly, the response computed from OH* chemiluminescence and pressure measurements with respect to change in equivalence ratio are presented. Secondly, a comparison of the flame response of the methane and biogas flames with similar laminar flame speed will be discussed. Lastly, simultaneous OH and H₂CO PLIF is used to evaluate the phased locked heat release rate (HRX). The simultaneous OH and H₂CO measurements will also enable the further understanding of its applicability to hydrocarbon flames in the presence of diluents (carbon-dioxide) under high stretch and strain. In previous work by Najm et al. (1998) and Ayoola et al. (2006), it has been shown that the HRX technique is suitable for hydrocarbon flames but there is still a lack of detailed information on its applicability with regards to other hydrocarbon based flames with the presence of diluents.

Figure 5-18 shows the effect of the equivalence ratio over a range of frequencies with different forcing amplitude for biogas flames. The equivalence ratio was varied from 0.75 to 0.95 and measurements of OH* chemiluminescence along with acoustic pressure measurements were taken to obtain the global heat release response of the flame. The mixture under investigation was of biogas/air and the global bulk velocity was kept at 9.5 m/s. At forcing frequency of 30 Hz for all the different equivalence ratio a linear flame response against change in amplitude was noted. At higher frequencies of forcing 255 Hz and 315 Hz the heat release response increased with an increase in equivalence ratio and the non-linearity appeared at higher amplitude for higher equivalence ratio as in the case of methane flames. One key feature that can be observed at a frequency of 315 Hz at $A = 80\% - 100\%$ is that the second region where the non-linearity is normally observed in methane flames does not seem to be present (saturation point). This trend is similar for all the different equivalence ratios investigated at this given frequency. At a frequency of 255 Hz and at an equivalence ratio of 0.75 and 0.8 the second region of non-linearity was as previously observed in methane flames. In the case of a forcing frequency of 315 Hz as the equivalence ratio increases past 0.75 the gradient started to decrease. At A greater than 70% the formation of a saturation point can be observed as at $A = 70\%$ and 80% the flame response seems to be the same. However, due to the lack of data points in this region it would be inaccurate to make any assumptions of this particular trend. Besides

for flame response observed in the region of the second non-linearity, the general trend of biogas flames follow that observed in methane flames.

Presented in Figure 5-19 and Figure 5-20 are the flame response of methane and biogas flames at 30, 255 and 315 Hz with the a laminar flame speed of 19 and 23 cm/s. For these measurements the air bulk velocity was kept constant at 250 lpm and only the fuel flow rates were altered in order to match the laminar flame speed. At the same laminar flame speed, both methane and biogas have the same flame response at all frequencies and amplitudes investigated with a slightly higher response of the biogas flames at A is greater than 40% for 255 Hz and 315 Hz at laminar flame speed of 19 cm/s. In the case of S_l being 23 cm/s, both type of flames (methane and biogas flames), were observed to have the same magnitude in the OH* chemiluminescence response for all frequencies and amplitude under investigation, in the region of $A = 15\% - 20\%$. This region coincides with the first non-linearity (denoted by X in the figure) and, as previously mentioned, with the appearance of the vortex. This change observed could be attributed to the fact that the addition of carbon-dioxide increased the overall flow rate thereby introducing variation in the shear produced turbulence intensity. As suggested earlier higher axial velocity due to the overall increase in flow rate makes it harder for the flame roll-up to occur.

In order to further investigate the effect of the flame response of biogas and methane flames with similar laminar flame speed, the measurements were carried out at a higher bulk velocity of 300 lpm (air bulk velocity). Shown in Figure 5-21 are the flame responses at a laminar flame speed of 19 cm/s. Any notable difference can mainly be observed at frequency of 255 Hz and $A = 15\% - 20\%$ during the first appearance of the vortex. Similar observations can be seen for laminar flame speed of 23 cm/s at the onset of the vortex formation for frequency of 255 Hz and 315 Hz. Also at higher amplitude greater than 65% at 315 Hz, while the methane flames response seems to have reached a saturation plateau, the biogas flames seems to increase gradually with no indication of saturation. Being a line of sight measurement method chemiluminescence lacks the resolution to accurately spatially resolve the flame structures such as the flame surface and the heat release rate. Therefore as in the case of methane flames simultaneous OH and H₂CO PLIF measurements were carried out to obtain the heat release rate as well as the flame surface. Phase locked PLIF measurements were carried out on biogas flames at forcing amplitudes of $A = 20\%$ and 90% at a forcing frequency 315 Hz. As in the case of methane flames the HRX technique captures the cyclic heat release variation in the biogas flames. Figure 5-22 shows a comparison of the HRX for methane and biogas flames at

$A = 80\%$, with a minima and maxima of the normalised HRX at 60 degrees and 240 degrees phase angle respectively. Any notable difference between methane and biogas HRX profile appears in the trough of cycle whereas the crest seems to be in good agreement. Similar to methane flames, at $A = 90\%$ a phase difference between the flame area and HRX measurement was observed. Looking closely at the HRX images that form the trough of the cycle, it can be observed for the methane flames that the end of the lowest point of the vortex in the inner recirculation zones are slightly lower than in the case of biogas flames. This seems to indicate that either there is an increase in reaction rate locally or there is a larger region over which the reaction is occurring and will in turn increased the HRX signal measured. This could be the reason why a higher HRX signal was observed in Figure 5-22 for methane flames. The HRX measurements seem to indicate that the technique is adequate to capture the heat release rate in highly strained and turbulent biogas flames that have been investigated.

5.4. Syngas Combustion

5.4.1. Flame response of syngas flames

The flame response of simulated syngas (methane/carbon-monoxide/hydrogen) will be discussed in this section. Syngas of various compositions of methane/carbon-monoxide/hydrogen. Compositions employed in the study are 50:25:25, 50:35:15 and 25:50:25. As presented previously simultaneous OH* chemiluminescence and pressure measurements were used to characterise the flame response. Also the HRX technique was applied to study the spatial and temporal heat release and flame area variation.

As opposed to the previous studies that have been carried out so far, the syngas measurements were performed using a 60 degrees swirler. As shown in chapter 4, adding swirl to the flow enhances the mixing and therefore stabilises the combustion. Under lean conditions high degrees of swirl have shown to stabilise the combustion process and achieve a high power and good burnout (Benim, 2014). The combustion properties of syngas type fuels are mainly determined by their H₂ and CO content and are generally characterised by high laminar flame speed (as shown in Chapter 3), a wide range of flammability limits and low ignition delay times (Dobbeling et al, 1996) which all contribute to a high probability of flashback. Choudhuri et al. (2011) have shown that even a relatively small amount of hydrogen in fuel blends triggers the onset of flashback by altering the kinetics and thermophysical characteristics of the mixture. Therefore in order to reduce the probability of flashback, the syngas experiments were performed with a configuration that includes a 60 degrees vane swirl. Additionally the presence of hydrogen in the fuel mixture modifies the response of the flame to global effects of stretch and preferential diffusion.

In the study of acoustic behaviour of syngas flames under highly swirled conditions, Allison et al. (2012), have shown that syngas displayed significantly different behaviour than hydrocarbon fuels even when the laminar flame speeds were matched. It was reported by Allison et al. (2012), that the laminar flame speed has a direct impact on both the frequency and amplitude of the acoustic oscillations measured at the onset of instability for partially premixed syngas type flames. As seen previously their work also showed that the air velocity affects the frequencies and amplitudes indicating a convective-acoustic mechanism. Some of the observations can be extended to the current study carried out in this work. Before discussing the flame response of syngas the effect on swirl on the flame response will be presented. In

order to understand the effect of swirl, the flame response of swirl methane flame was compared to the corresponding non-swirled condition.

Shown in Figure 5-23 are the HRX for swirl and no-swirl methane flames with the same bulk velocity of 9.5 m/s and equivalence ratio of 0.7. In the presence of the swirl, the overall flame height is decreased and there is an increase in the flame brush thickness. While comparing the flame response from OH* chemiluminescence measurements, it can be observed for all the frequencies 30 Hz, 255 Hz and 315 Hz a higher flame response was observed for the swirl condition (Figure 5-24). The systematic higher heat release response observed from OH* chemiluminescence can be attributed to the increase in the vortex size during the convection downstream which resulted in the flow becoming more turbulent. Thus, increasing the mixing between the reactants and products as a consequence this increases the heat release. As shown in chapter 4, the addition of a swirl increased the turbulent intensity. The results presented in Figure 5-24 suggest that the flame response at this high swirl condition was nearly linear for most of the forcing frequencies and the non-linearity was mainly present at large amplitudes ($A > 65\%$) for 255 Hz and 315 Hz. As shown in the non-swirl condition, the swirl flame is both dependent on frequency and amplitude. The methane swirl flame is taken as the base case and as a reference point for syngas flames.

All the test conditions for syngas were performed at the same equivalence ratio for practical reasons to avoid both CO poisoning and flashback. At lower equivalence ratio values, the flame was very susceptible to blow-off and not very compact. However, at high equivalence ratio flash-back was observed at very high forcing amplitudes. Therefore in order to keep the flame compact and reduce the risk flashback, an equivalence ratio of 0.7 was found to be a good compromise. These circumstances created the need to measure the laminar flame speed in order to further the understanding of flame response with matching laminar flame speed.

Also shown in Figure 5-24 is the flame response for different syngas mixtures at equivalence ratio of 0.7. At forcing frequency of 30 Hz, all of the different syngas compositions show a linear increasing trend with an increase in amplitude. Any notable difference can only be observed for the case of pure methane flames. A higher flame response was measured for the same amplitude when compared to the other syngas mixture. Conversely for forcing frequencies of 255 Hz and 315 Hz methane flames show a lower magnitude of flame response compared to the other mixtures. At a forcing frequency of 315 Hz and high amplitude of forcing $A > 50\%$, syngas with 25:50:25 composition had a higher flame response when compared to

the other mixtures. This can be associated to the increase of the reaction rate of the mixture when the percentage of hydrogen (by volume) is increased. An increase in reaction rate will most likely increase the heat release rate, which in turn should affect the flame response. While comparing HRX images of swirled methane flames and syngas flames with a mixture composition of 25:50:25 (Figure 5-25), it can be observed that a higher heat release signal is recorded in the outer recirculation in the case of syngas mixture 25:50:25. This could be due to highly diffusive nature of hydrogen gas which can easily penetrate the side recirculation. Another feature of syngas 25:50:25 is that it differs from the swirl methane flame, in the shape and size of the vortex. While in the case of swirl methane, the appearance of the vortex can be clearly seen, in the case syngas 25:50:25 the shape of the vortices are not clearly distinguishable (Figure 5-26, Figure 5-27 & Figure 5-28).

In Figure 5-29, the OH* chemiluminescence flame response was normalised with the laminar flame speed and the unforced velocity fluctuation (v' - from PIV measurements) of the different syngases mixtures. The laminar flame speed measured in chapter 3 was used to perform the calculation. From Figure 5-29, at 30 Hz it was observed that methane had a higher flame response after the normalisation. When compared to Figure 5-24, the difference in the flame response between the different gas mixtures was larger. However, when the normalisation was carried out at frequencies of 255 Hz & 315 Hz, the difference in magnitude between all the different syngas mixture and swirl methane was smaller. Similar observations were noted in the flame response for methane and biogas when the laminar flame speed was matched, for all frequencies. This would suggest that in the case of syngas flames another parameter in addition to flame speed controls the acoustic response at low frequency. The results suggest that a combination of flame speed and fuel densities (low density of hydrogen) control the flame response.

5.5. Chapter 5 Summary

Measurements of heat release rates are presented for bluff-body stabilised flames subjected to inlet velocity fluctuations. Heat release rate response of flames at different amplitude values A for different compositions at forcing a frequency of 315 Hz was studied. Experiments at forcing amplitudes of, $A = 20\%$, 50% and 90% for methane flames, $A = 90\%$ for biogas flames and $A = 20\%$ methane swirl and syngas were carried out while keeping the bulk inlet velocity (overall bulk) at 9.5 m/s. Figure 5-9 shows a sequence of phase averaged heat release images corresponding to $A = 10\% - 50\%$. From the sequence of phase locked images it can be seen that there is little variation in the flame surface through the cycle. When the amplitude is increased from 20% to 50%, distortion of the shear layer and wrinkling of the flame front occurs as the counter rotating vortex pair develops at the bluff-body and propagates along the shear layer. As the vortex propagates away an increase in size can be observed. At the highest amplitude investigated the wrapping of the shear layer and the wrinkling of the flame front by the inner vortex intensifies such that the flame appears to be wrapped upon itself. The high strain region and curvature imposed on the flame front due to the vortex has been seen to influence the heat release rate, with similar observations reported by Ayoola et al. (2006) and Echekeki & Chen, (1996). Additionally in the work by Ayoola et al. (2006) a higher heat release signal was reported in the regions of negative curvature (convex to the reactants) whereas a lower heat release signal was observed for positive curvature (concave to the reactants).

Shown in Figure 5-14 are spatially integrated heat release rate for methane flames at $A = 90\%$ and a forcing frequency of 315 Hz. The profile shows that the lowest heat release rate happens at 60 degrees and while the highest heat release rate signal happens at 240 degrees. While examining the regions around which the vortex is formed, key information about the heat release rate is obtained. The vortex imposes a region of high strain and negative curvature (convex to the reactants) on the flame front and examining the region where the vortex is present reveals a high heat release signal. One possible explanation could be due to the increase of flame area in the region and it could also be due to the diffusion of free radicals in this region thus increasing the local heat release rate.

In the case of biogas flames when the laminar flame speed was matched to that of pure methane, the flame response was observed to be similar for all the different frequencies of forcing and amplitude (Figure 5-19, Figure 5-20 & Figure 5-21). Small changes were observed in the region of forcing amplitude of 15% - 30%, when the vortex starts to appear. As shown in

chapter 3 the HRX measurements capture the spatial distribution of the heat release for the turbulent flames well. When compared to pure methane flames at the same frequency and amplitude, the phased resolved cycle matches well. Any notable difference was found in the trough of the cycle. The HRX technique was extended to syngas, where the HRX measurements provided an insight in the difference observed from the flame response. Also when the flame response was normalised against the laminar flame speed and v' for each syngas mixture it was observed that very small difference in the amplitude of the flame response was observed at 255 Hz & 315 Hz. Any notable difference was observed at forcing frequency of 30 Hz which suggest as well as the flame speed, there could be other parameters that play a role in the acoustic response. One of the parameters could be the density of the mixture as well as the addition of hydrogen which lowers the overall density.

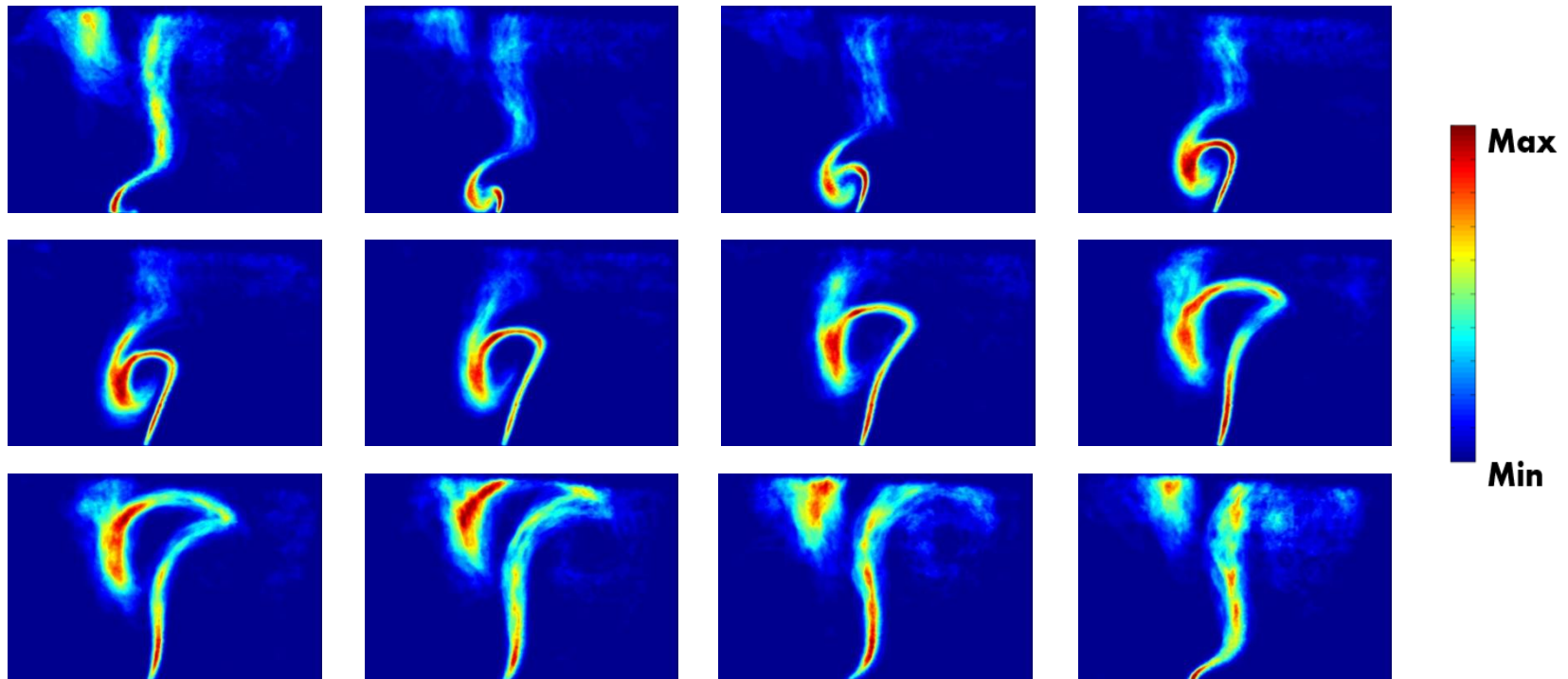


Figure 5-1: HRX measurement for Phased Average of Pure Methane, $f = 315$ Hz & $A = 0.5$, equivalence ratio of 0.75

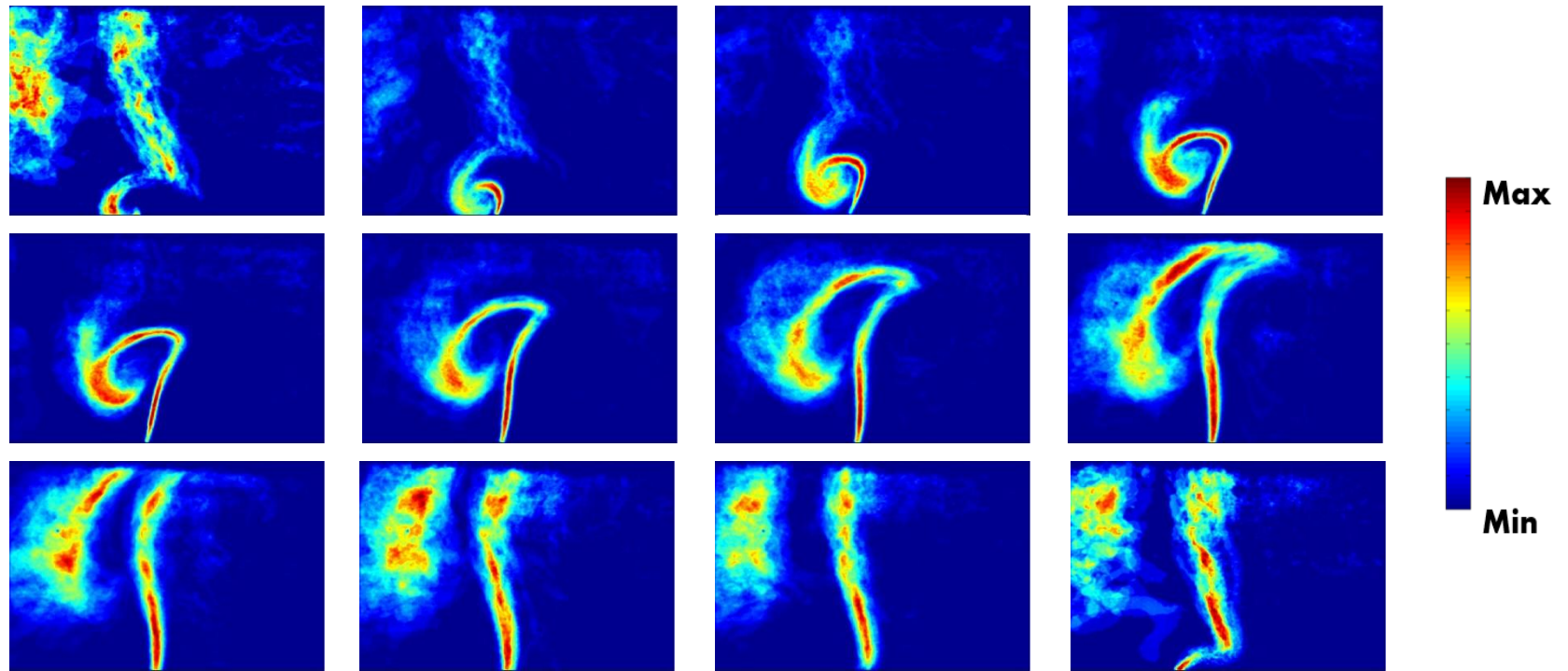


Figure 5-2: HRX measurement for Phased Average of Pure Methane, $f = 315$ Hz & $A = 0.9$, equivalence ratio of 0.75

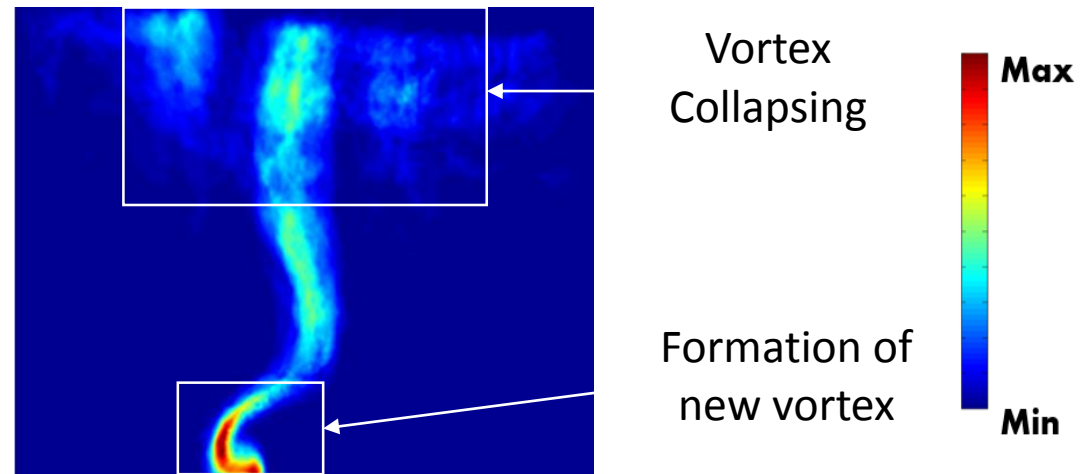


Figure 5-3: Phased Average of Pure Methane at 30 degrees Phase Angle –
Representing the formation of a new vortex as the previous one collapses – $f = 315$ Hz
& $A = 50\%$

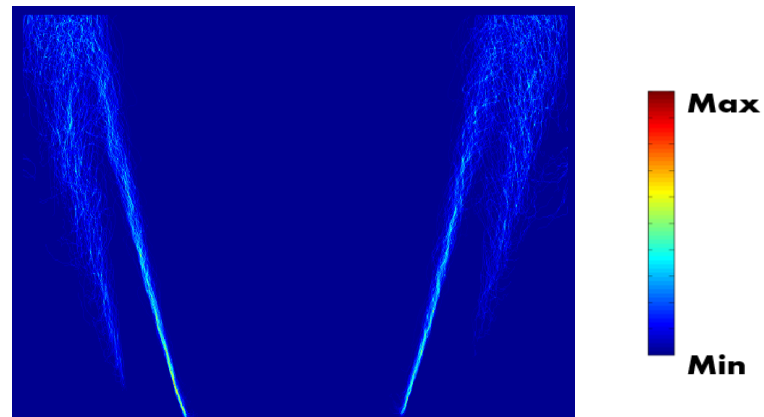


Figure 5-4: Typical FS of an unforced Pure Methane flame, equivalence ratio of 0.75

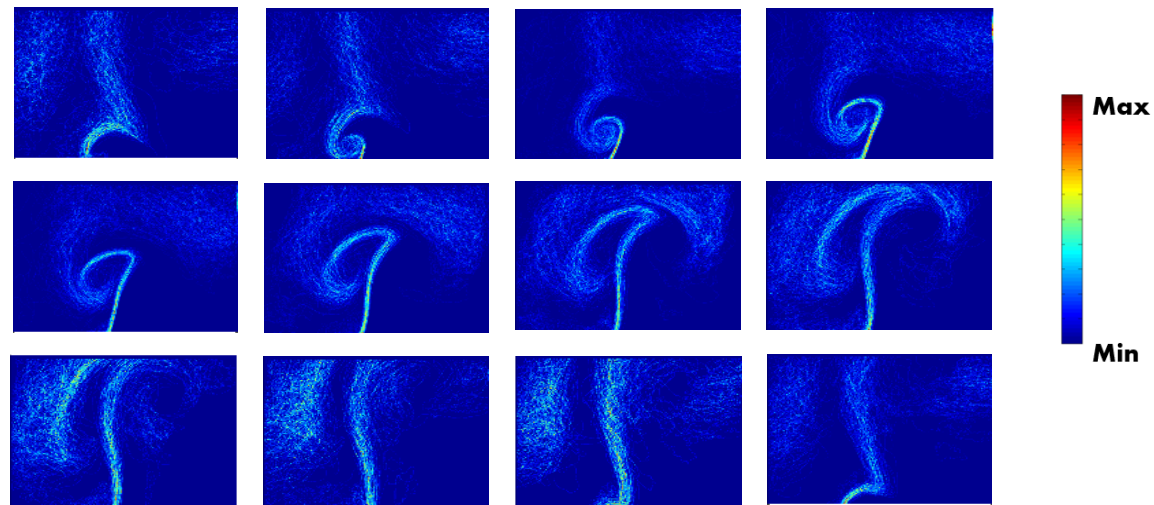


Figure 5-5: Phased Average FS calculation for $f = 315$ Hz and $A = 0.9$, equivalence ratio of 0.75

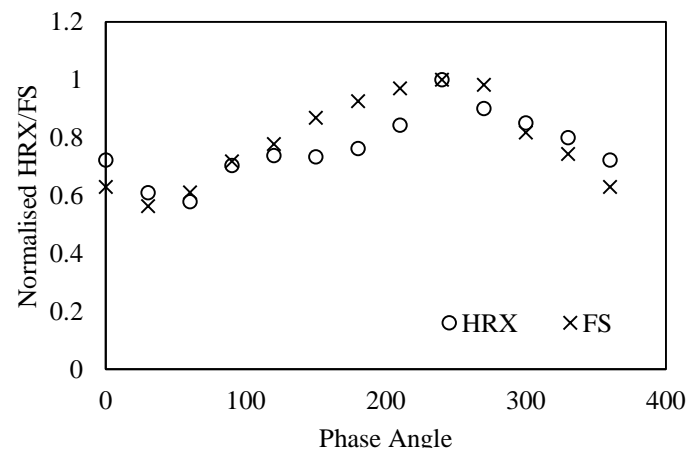


Figure 5-6: Normalised Phased average over one complete cycle of HRX & FS Pure Methane, $f = 315$ Hz, $A = 50\%$

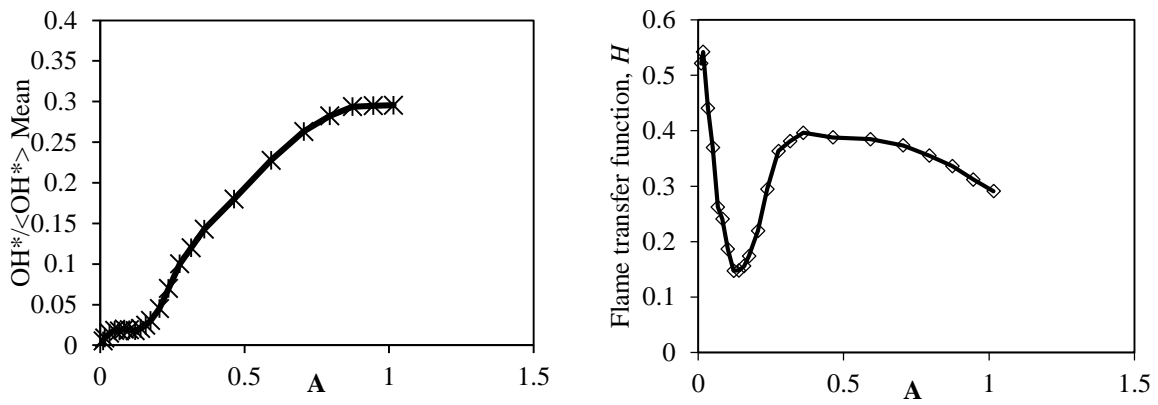


Figure 5-7 : (Left) Flame response (Right) Flame transfer function showing the amplitude dependence of pure methane at $f = 315 \text{ Hz}$ at equivalence ratio = 0.75

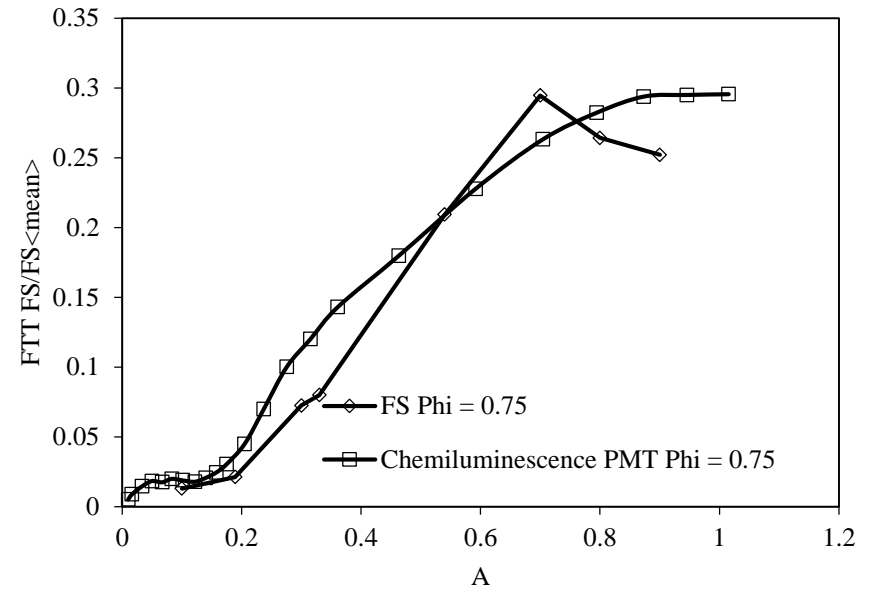
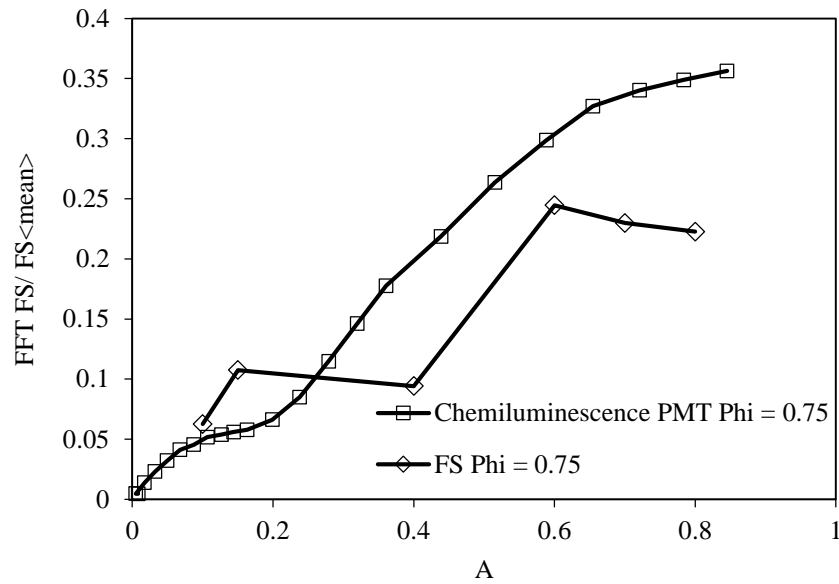


Figure 5-8: Flame response from chemiluminescence measurements and FS calculations at $f = 255$ Hz (figure on the left), 315 Hz (figure on the right) and varying A

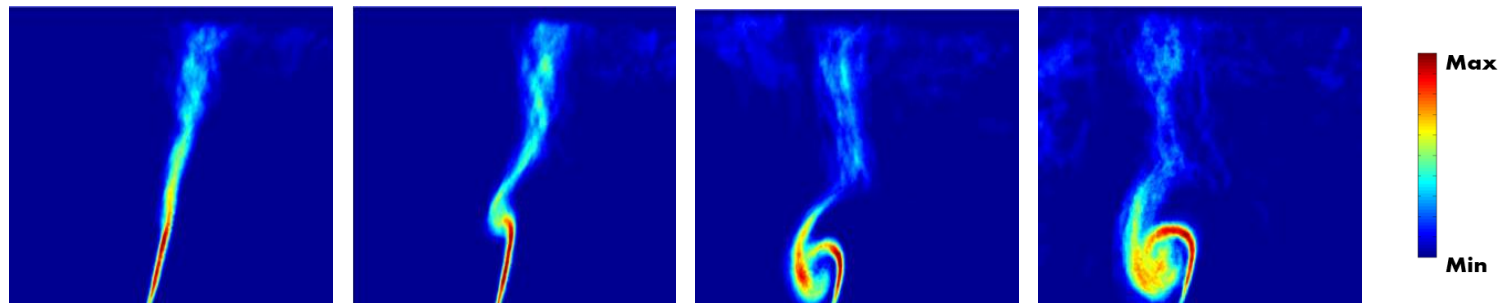


Figure 5-9: HRX images at $A = 0.1, 0.2, 0.5$ & 0.9 , $f = 315$ Hz, equivalence ratio of 0.75

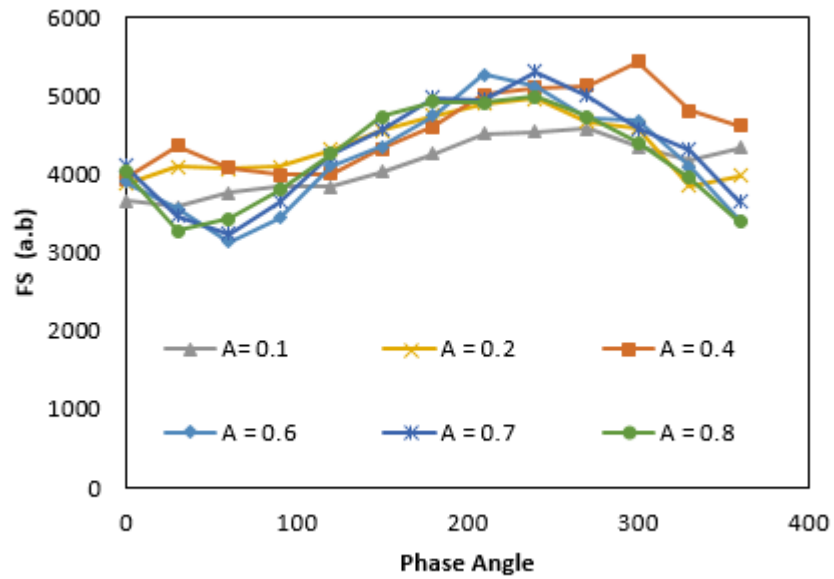


Figure 5-10: Cyclic FS calculation for $f = 255$ Hz and varying A , equivalence ratio of 0.75

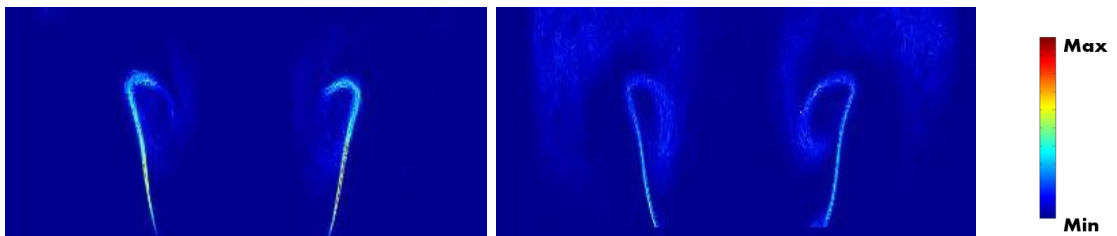


Figure 5-11: FS calculation of Pure Methane at highest amplitude of forcing $f = 255$ Hz (figure on the left) & $f = 315$ Hz (figure on the right), equivalence ratio of 0.75

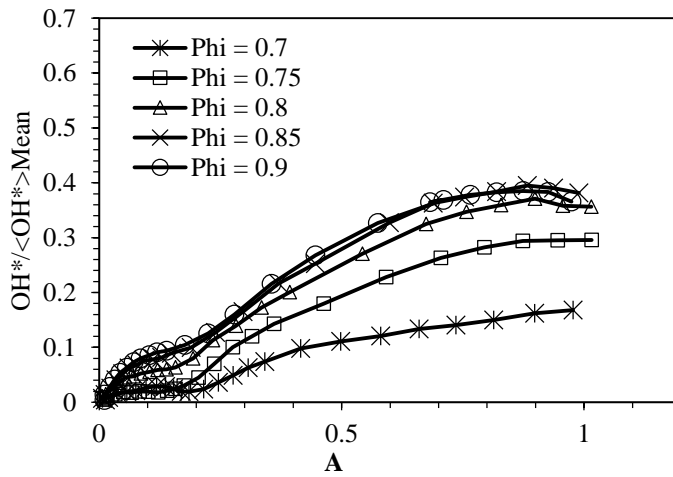
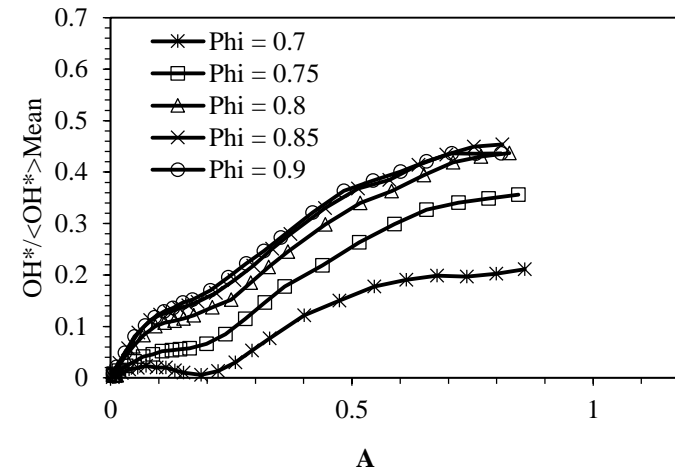
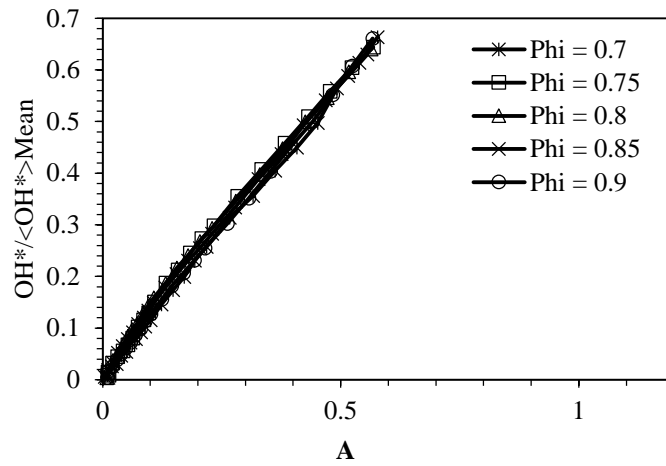


Figure 5-12: Pure Methane flame response $f = 30 \text{ Hz}$ (Top Left), 255 Hz (Top Right) & 315 Hz (Bottom Left) at varying equivalence ratio and A

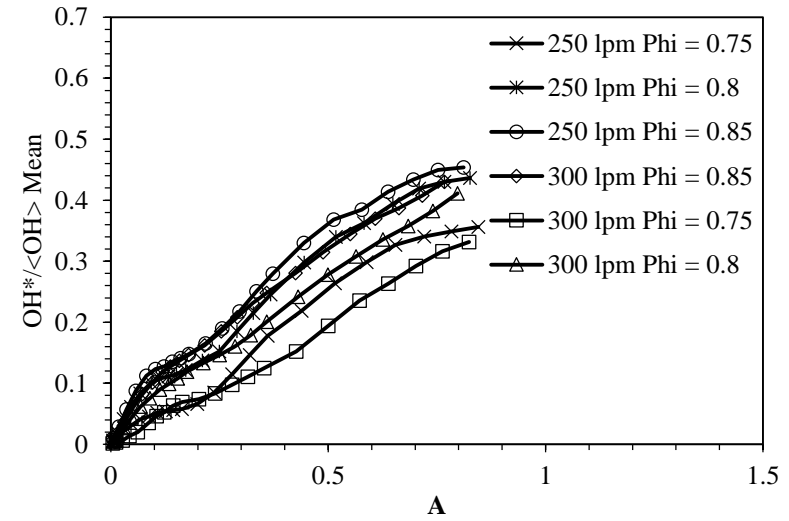
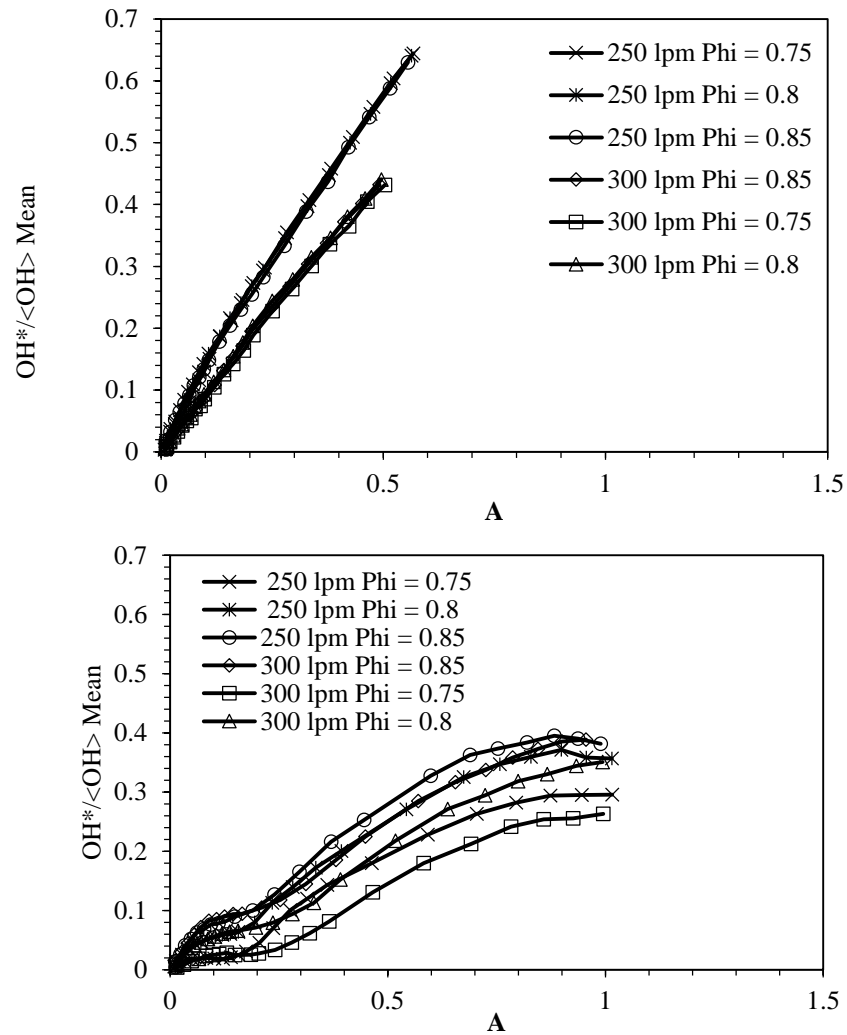


Figure 5-13: Pure Methane flame response with varying equivalence ratio at $f = 30$ Hz (Top Left), 255 Hz (Top Right) & 315 Hz (Bottom Left) for overall bulk velocity = 250 lpm, & 300 lpm

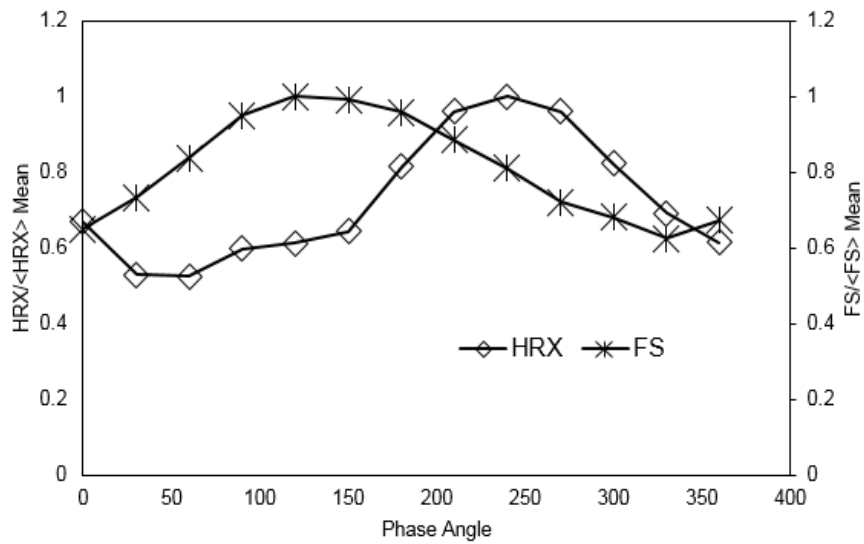


Figure 5-14: HRX & FS for $f = 315$ Hz and $A = 90\%$, equivalence ratio of 0.75

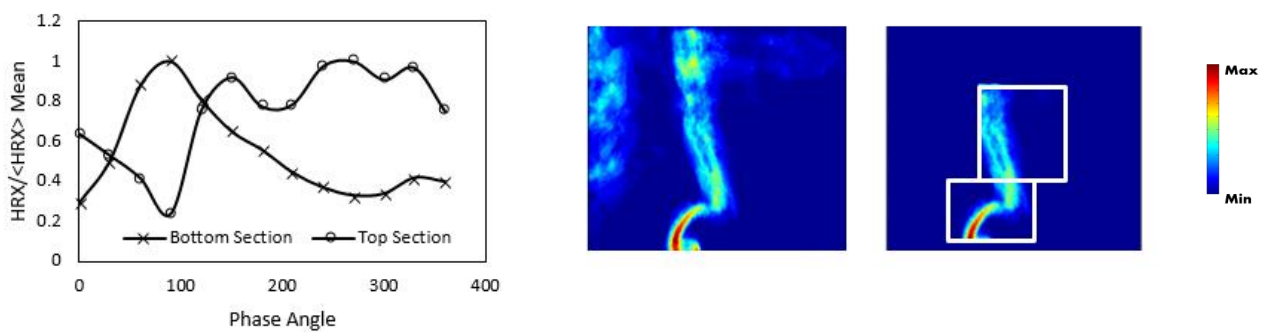


Figure 5-15: Phase angle variation in regions, equivalence ratio of 0.75

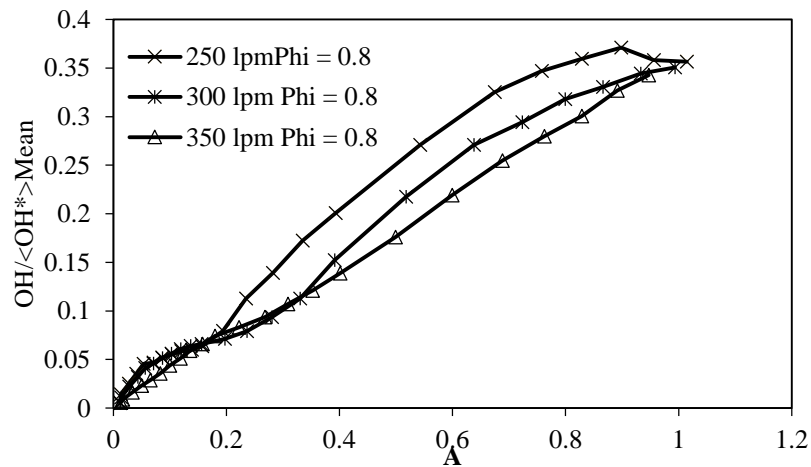
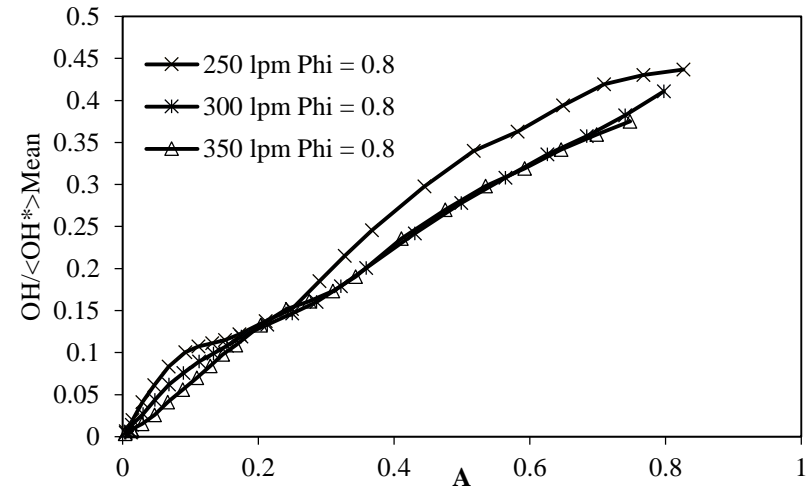
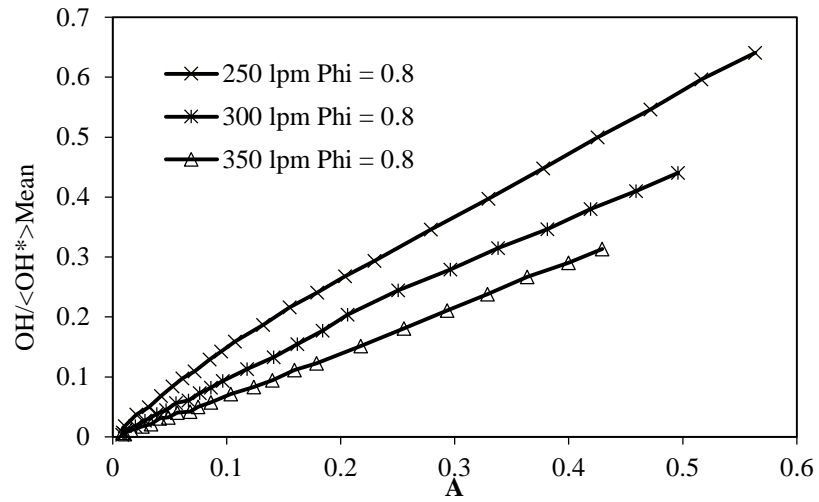


Figure 5-16: Pure Methane $f = 30$ Hz (Top Left), 255 Hz (Top Right) & 315 Hz (Bottom Left) at equivalence ratio = 0.8 – Air bulk velocity = 250 lpm, 300 lpm & 350 lpm

Forced Response of turbulent Bluff-body CH₄/CO₂/H₂ flames

Key numbers		Natural gas	Biogas
CH ₄ (methane)	[vol%]	91.0	55-70
C ₂ H ₆ (ethane)	[vol%]	5.1	0
C ₃ H ₈ (propane)	[vol%]	1.8	0
C ₄ H ₁₀ (butane)	[vol%]	0.9	0
C ₅ + (pentane)	[vol%]	0.3	0
CO ₂ (carbon dioxide)	[vol%]	0.61	30-45
N ₂ (nitrogen)	[vol%]	0.32	0-2
H ₂ S (hydrogen sulphide)	ppm	~1	~500
NH ₃ (ammoniac)	ppm	0	~100
Water dew point	[°C]	<-5	saturated
Net calorific value	[MJ/nm ³]	39.2	23.3
	[kWh/nm ³]	10.89	6.5
	[MJ/kg]	48.4	20.2
Density	[kg/nm ³]	0.809	1.16
Relative density	[-]	0.625	0.863
Wobbe index (W)	[MJ/nm ³]	54.8	27.3
Methane number	[-]	73	~135
Stoichiometric mixtures			
Air requirement	[nm ³ /nm ³ gas]	10.4	6.22
Flame temperature*)	[°C]	2040	1911
Water dew point (flue gas)	[°C]	59.7	59.2
Water vapour (flue gas)	vol%	18.8	19.3

*) Adiabatic flame temperature

Figure 5-17: Comparison of Natural gas and Biogas

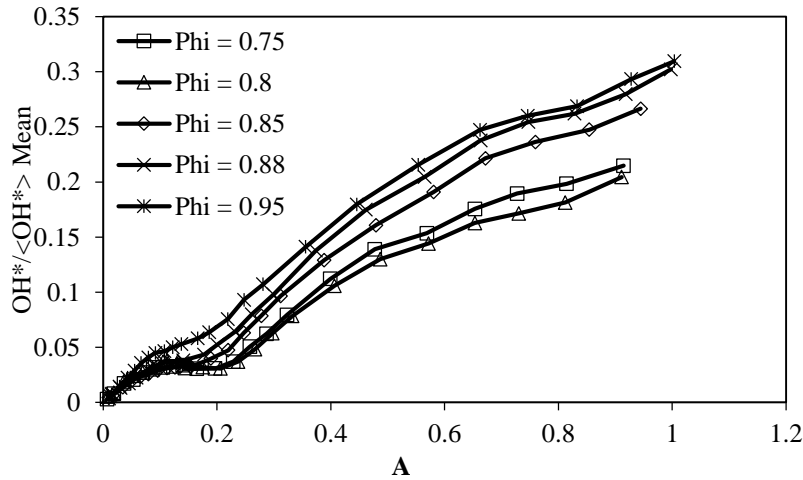
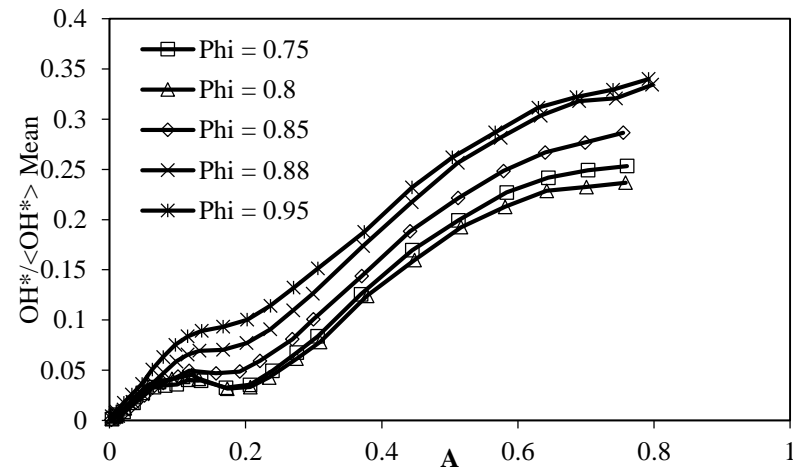
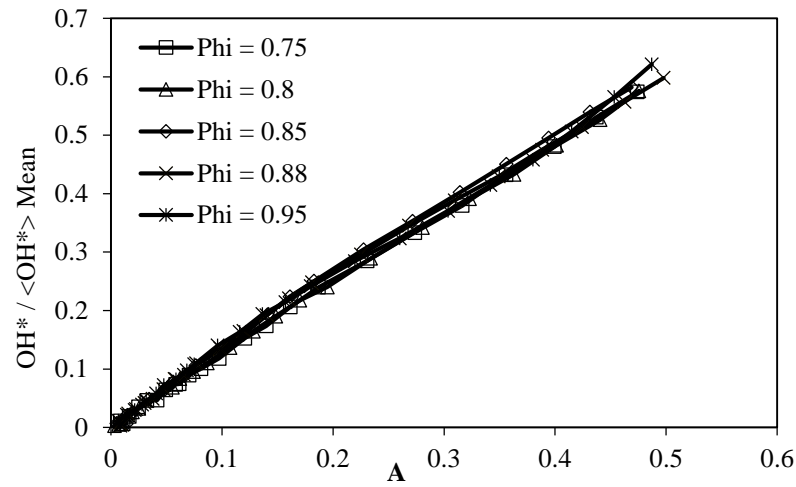


Figure 5-18: Biogas flames $f = 30$ Hz (Top Left), 255 Hz (Top Right) & 315 Hz (Bottom Left) at varying equivalence ratio

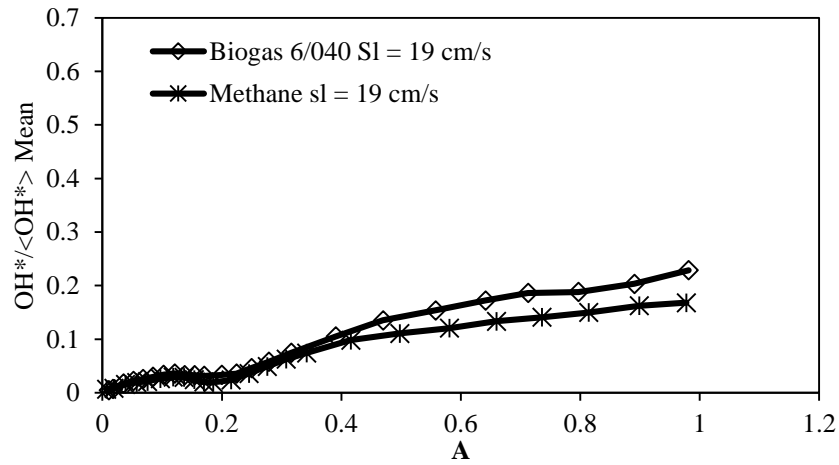
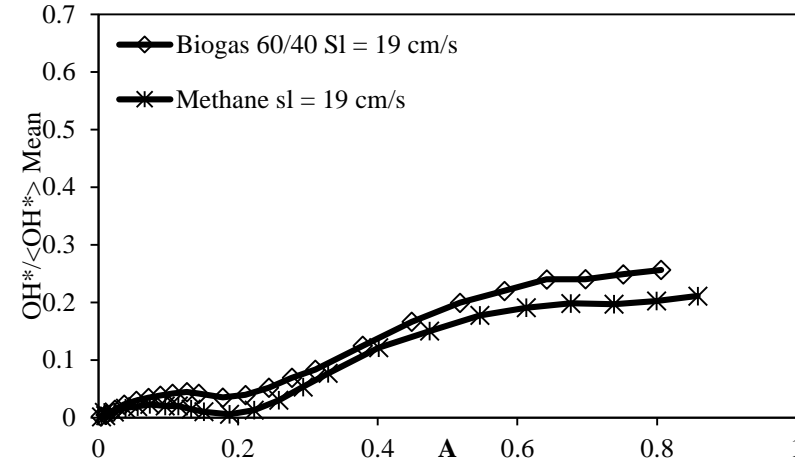
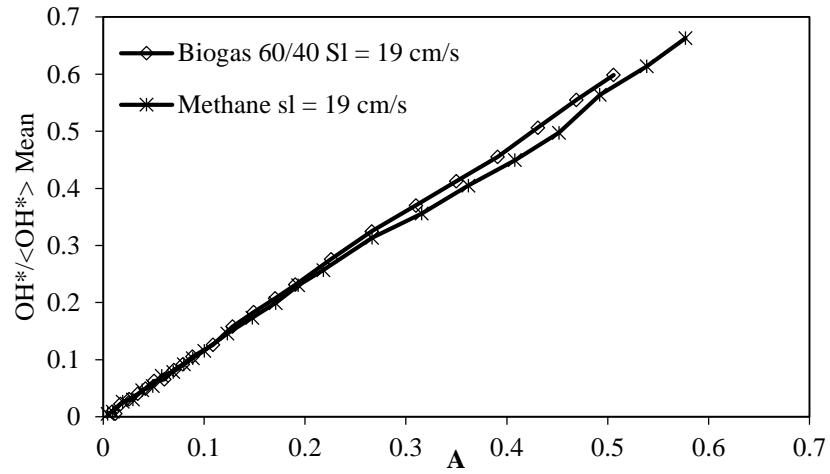


Figure 5-19: Flame response of Pure Methane and Biogas Flames at laminar flame speed of 19 cm/s

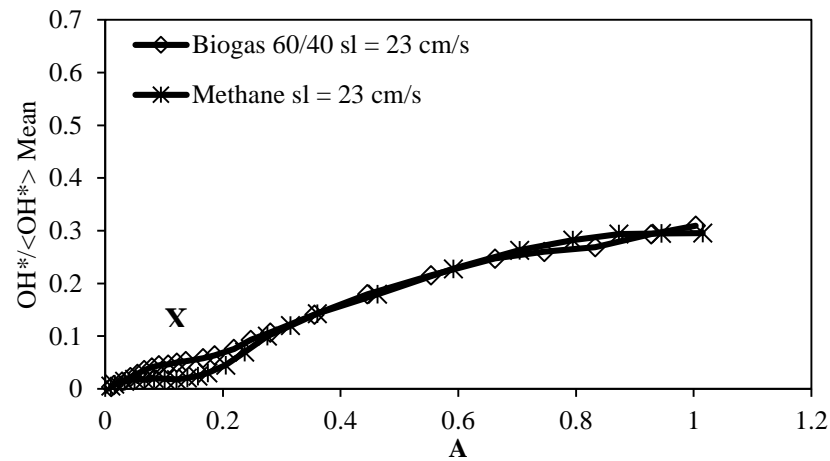
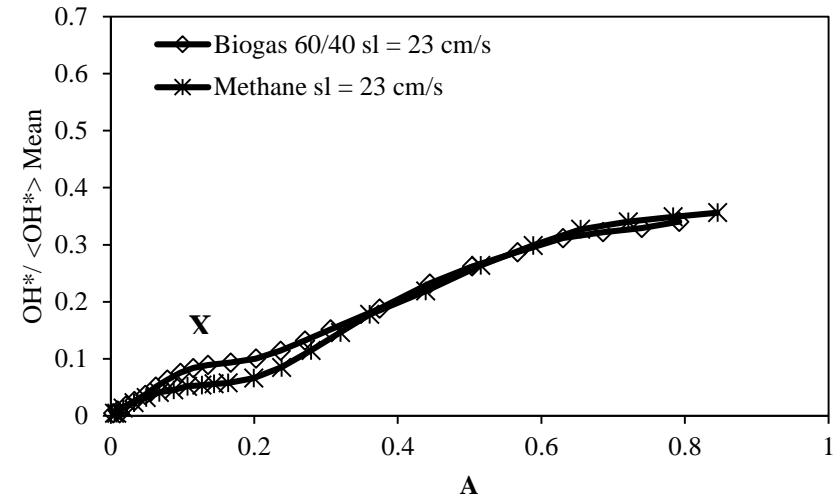
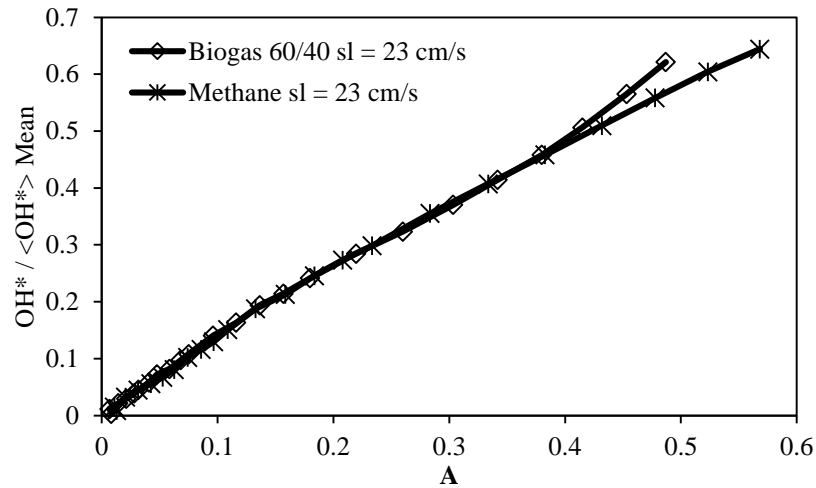


Figure 5-20: Flame response of Pure Methane and Biogas Flames at laminar flame speed of 23 cm/s

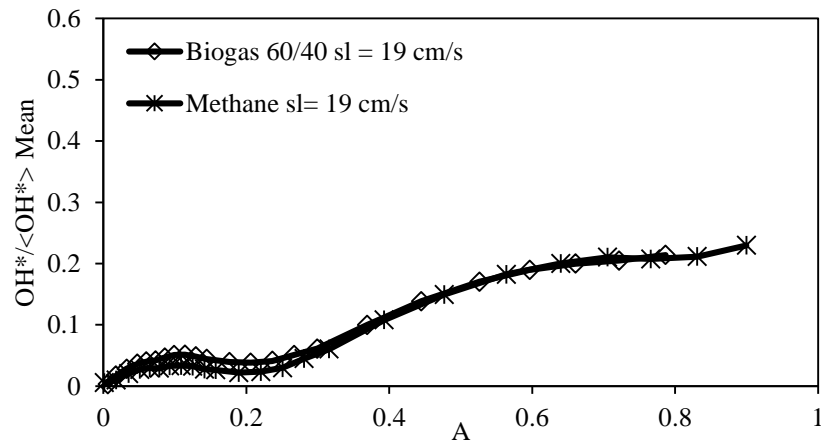
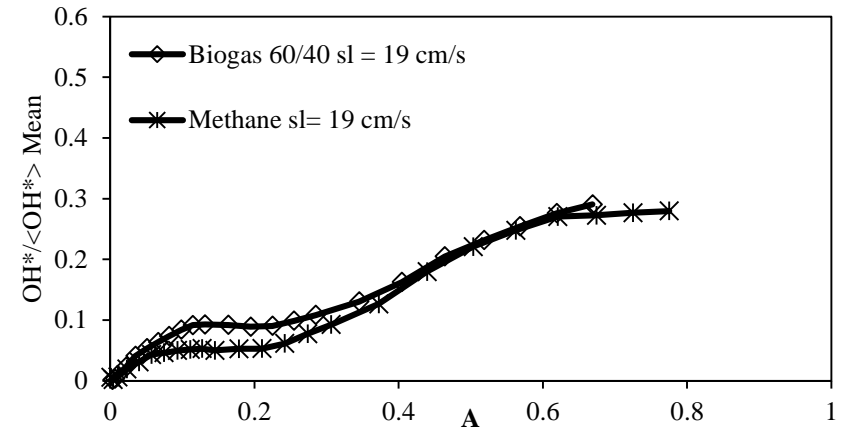
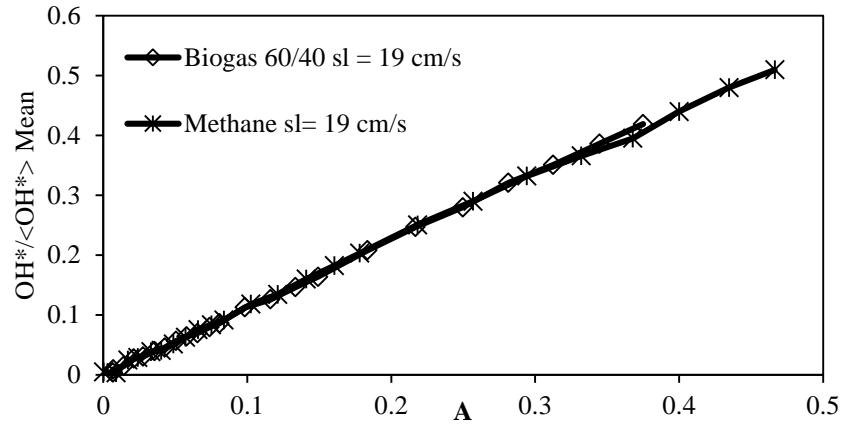


Figure 5-21 Flame response of Pure Methane and Biogas Flames at laminar flame speed of 19 cm/s, air bulk velocity of 300 lpm

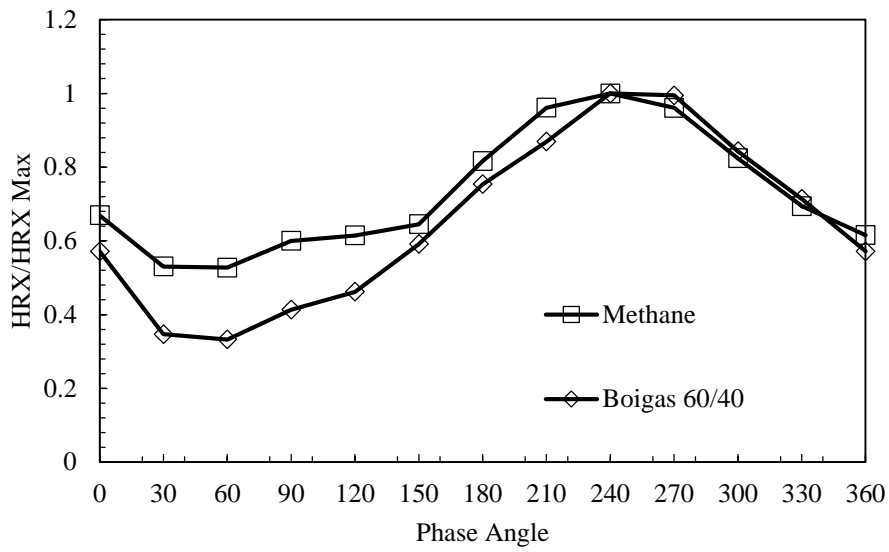


Figure 5-22: Phased Resolved HRX Pure Methane & Biogas Flames at the same laminar flame speed and A

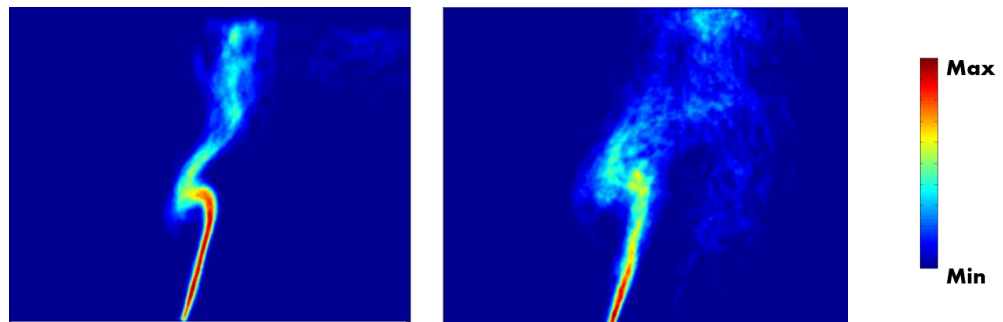


Figure 5-23: Comparison between Pure Methane swirl and no Swirl at the same forcing amplitude and phase angle, at equivalence ratio of 0.7

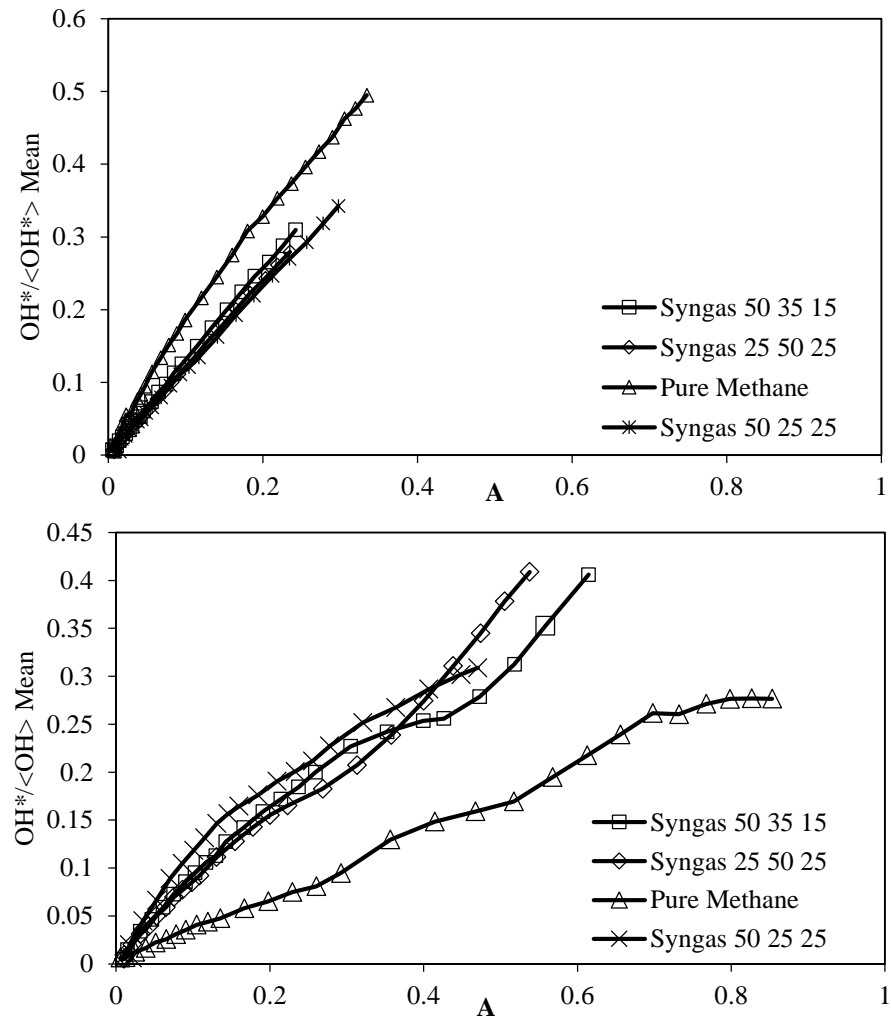


Figure 5-24: Flame Response of Swirl Methane and Syngases (methane/carbon-monoxide/hydrogen) of varying composition, at the same equivalence ratio of 0.7

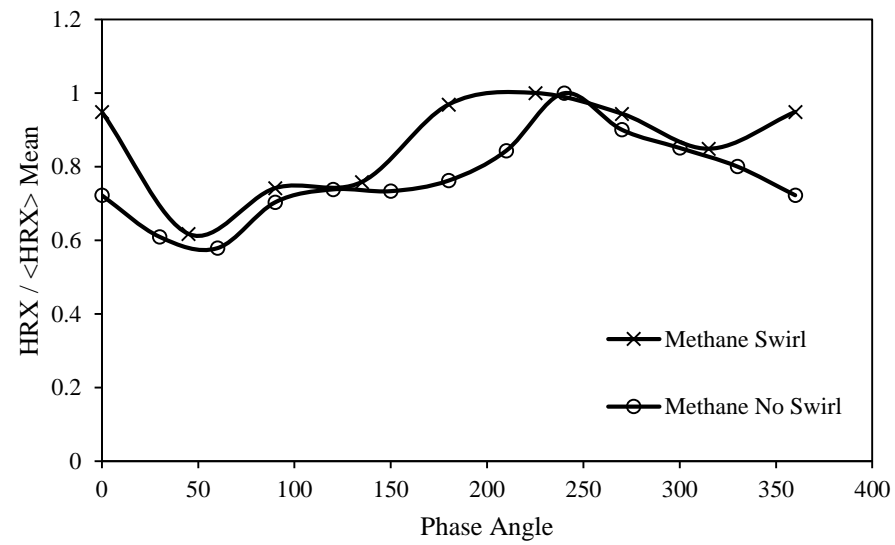


Figure 5-25: Comparison between Pure methane swirl and no swirl at the same forcing amplitude

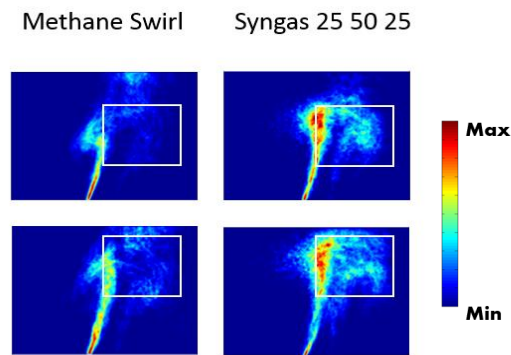


Figure 5-26: HRX Methane and Syngas (methane/carbon-monoxide/hydrogen) at Phased angle 90 & 135 degrees at the same forcing amplitude equivalence ratio of 0.7

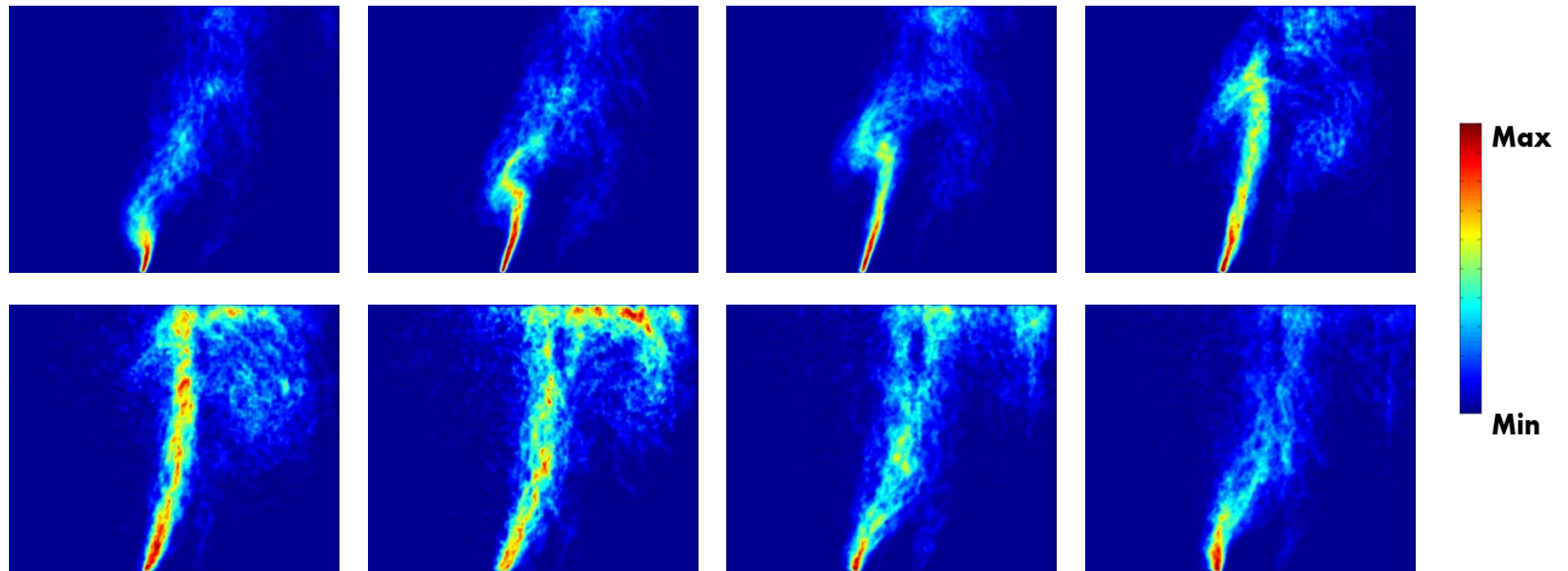


Figure 5-27: HRX Phased resolved swirl Pure Methane flames at 45 degrees phase intervals, at equivalence ratio of 0.7

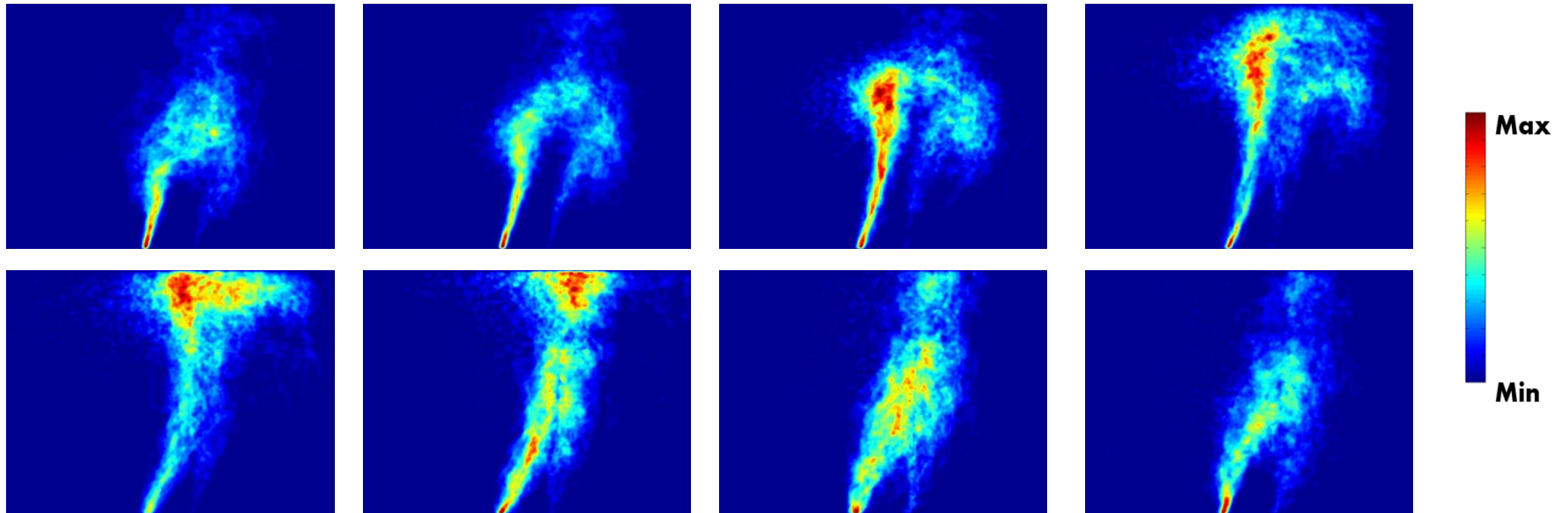


Figure 5-28: HRX Phased resolved Syngas 25:50:25 (methane/carbon-monoxide/hydrogen) at 45 degrees phase angle, at equivalence ratio of 0.7

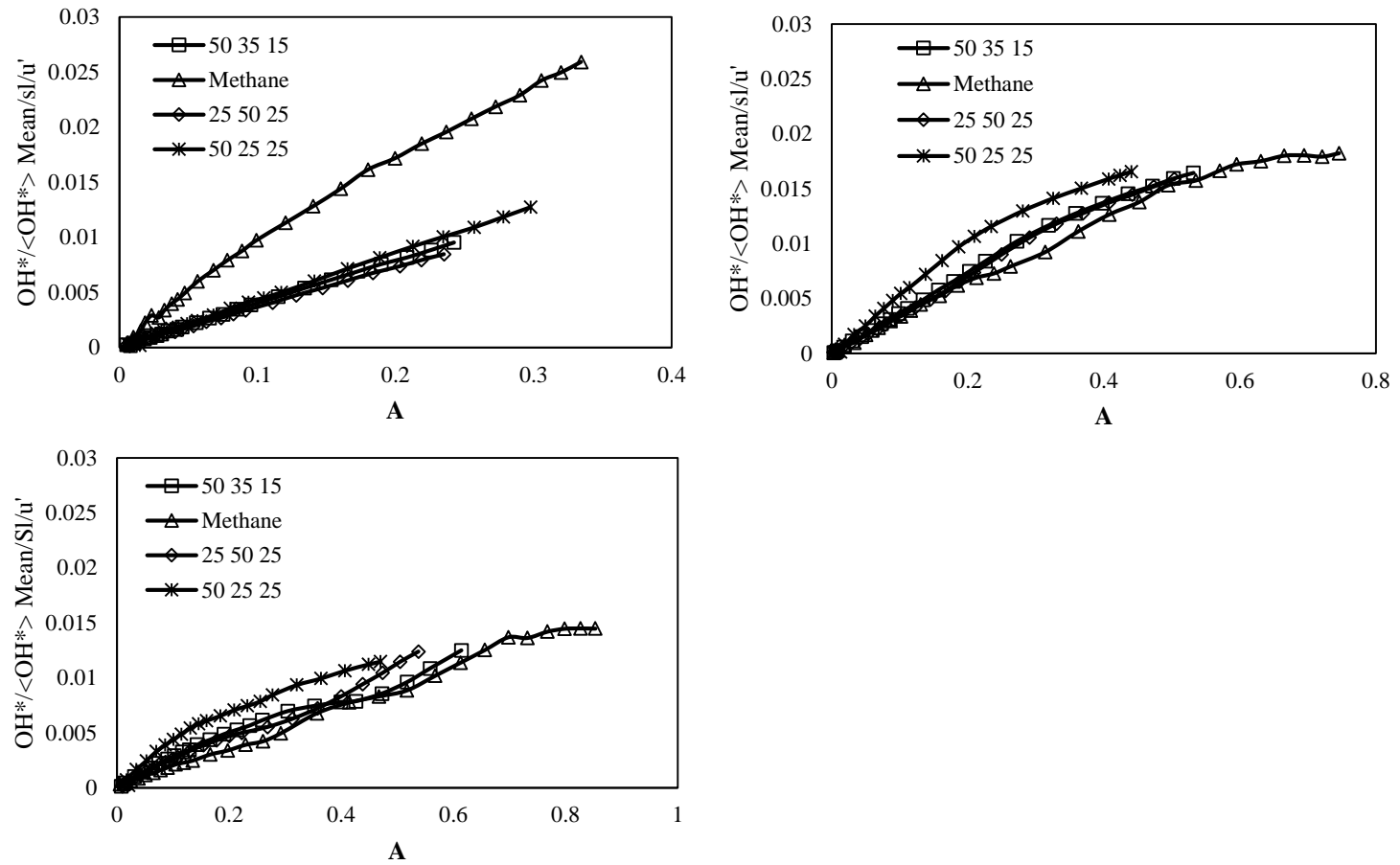


Figure 5-29: Normalised Syngas (methane/carbon-monoxide/hydrogen) mixtures with their respective laminar flame speed and the unforced vertical velocity fluctuation

Chapter 6

6. Conclusions & Suggestions for Further Research

One of the main objectives of this work was to develop and validate the laser-based heat release rate measurement techniques based on simultaneous OH and H₂CO PLIF for multi component fuels. Numerical simulation and previous studies have shown that this dual PLIF technique works well for hydrocarbon flames. This technique was applied to laminar and turbulent premixed flames of varying fuel compositions in this work. For that purpose, a laboratory scale impinged jet and bluff-body combustor were developed. In the bluff-body configuration, experimental investigation of the flame response with acoustic excitation was also studied. From this an effort was made to understand the influence of the laminar flame speed on the flame response of different air fuel/mixtures. Prior to performing any heat release measurements, the cold flow field characteristics were first established for both burners and in the case of the bluff-body the cold flow acoustic characteristics were also carried out. Finally, this chapter closes with suggestions of further research.

6.1. Summary of various conclusions

6.1.1. Development of the impinged jet burner, laminar flame speed and heat release rate measurements

The heat release rate measurement technique developed for this work was based on indirect measurements of the concentration of HCO, which has been found to correlate well with the heat release rate. As outlined in the work of Najm et al. (1998), HCO is the final step along the major pathways to the production of CO, and a large fraction of the reactions proceed along this chemical pathways. Due to the predissociative transitions and strongly quenched fluorescence signals of HCO, fluorescence is difficult to measure experimentally. However, an alternate approach uses the product of OH and H₂CO PLIF measurements to obtain a signal that correlates with the HCO production rate. Therefore a pixel-by-pixel multiplication product of the PLIF images of OH and H₂CO captured an image, which correlates well with heat release

rate. Previous numerical and experimental studies for hydrocarbon flames in both a laminar and turbulent flow fields have provided reasonable validation for the technique. Little information is available for multi-components fuels, especially when diluents are added. In order to be able to clarify whether the technique is applicable to multi-components fuel, it should be investigated on both laminar and turbulent flames. For the laminar flames, the impinging jet configuration was used, whilst in the turbulent flames the bluff-body stabilised flames were employed.

The impinged burner allowed for a steady one dimensional laminar flame to be stabilised in a well-defined stagnation flow-field. These types of flames allowed for easy implementation and study of different types of laser diagnostics techniques. Before the heat release rate measurements were carried out, the cold field was first characterised for both cold and hot flow. The cold flow measurements showed a uniform field, which suggests that there was a minimal exit boundary layer displacement. During the characterisation of the hot flow, the effect of the co-flow on the axial velocity profile was investigated. It was observed that the co-flow had no effect on the axial velocity provided it was kept below 19 lpm. As well as creating a steady one dimensional flame, the impinged jet burner can be used to calculate the laminar flame speed. Using the method proposed by Law et al. (1985), the laminar flame speed of methane, biogas and syngas of different compositions were calculated. The laminar flame speed calculated was later used in the analysis of the flame response to imposed acoustic excitation. Once the burner characterisation was carried out the OH and H₂CO dual PLIF technique was implemented for understanding 1) Effect of varying equivalence ratio in pure methane-air flames, 2) Effect of bulk strain rate in a pure methane-air flame, 3) Effect of varying CO₂ addition to a methane air flame.

The results were as expected in the case of varying equivalence ratio; the HRX increased with equivalence ratio to reach a maxima at about 1.1 and then started to decrease. The variation in strain rate does not appear to affect the thickness of CH₂O. Any change in strain rate was not high enough to show any significant change in the HRX values. In the case of CO₂ addition, the CH₂O thickness shows a mild increase as the CO₂ addition was increased from 0 to 40% of the methane flow rate. The heat release rate decreases mildly with an increase in the CO₂ concentration. While the proportion of CO₂ was increased, changes in flame structure were also observed; HRX shows slight decreasing trend and formaldehyde thickness showed a proportionally small increasing trend. A decrease in HRX with the addition of CO₂ can be

attributed to carbon dissociation and the associated heat capacity of CO₂. The results indicate that the HRX measuring technique can be extended to methane diluted with CO₂ and provide a correlation for heat release rate measurement.

6.1.2. Development of the bluff-body combustor and Heat Release Measurement in turbulent unforced flames

The burner developed for the turbulent flame measurement is a laboratory scale gas combustor with different modes of combustion. For the study carried out, the premixed mode was used where the fuel and oxidiser were mixed upstream of the flow and the flame was stabilised on a centrally bluff-body. The same configuration was later used in the study of the flame response to velocity perturbations. As in the case of the laminar condition, prior to performing the HRX measurements cold flow characterisation was performed.

Firstly a detailed acoustic characterisation was carried out and the results showed that the peak for the highest amplitude of forcing were at frequencies were around 30, 255 and 315 Hz. Secondly, PIV measurements were carried out to obtain the flow field for the conditions with and without velocity perturbations at one of the frequencies identified. From the unforced PIV measurements, the spatial length scales and strain rate measurements were extracted. It was observed, in region close to the bluff-body the length scales were notably smaller compared to region further downstream with the largest strain rate being recorded at a close proximity to the bluff-body. PIV measurements were carried out at a higher forcing frequency for flow visualisation. Previous studies have suggested at low a frequency of forcing, the shear layer modulation was by oscillatory motion and even at the highest amplitude there was no shear layer roll-up. Measurements were carried out at 255 Hz at an amplitude of $A = 80\%$ which showed shear layer roll-up with counter rotating vortices on either side of the bluff-body. The sizes of the vortices were dependent on the amplitude of forcing.

Once the flow field was characterised, unforced flame investigations were carried out for methane and methane diluted with CO₂ (biogas) flames. During the investigations two measuring techniques were predominantly employed. These techniques were 1) OH* chemiluminescence using photo-multiplier tubes (PMT) and for some cases an ICCD camera and 2) OH and H₂CO PLIF for HRX estimates. The results obtained from the reacting flow can be summarised as follows:

- For both methane and biogas, unforced flames the mean signal strength obtained using OH* chemiluminescence showed an increasing trend with an increase in equivalence ratio.
- While the laminar flame speed was kept constant and the overall bulk velocity was increased, OH* chemiluminescence signal variation showed a linear relationship with overall flow rate.
- Further experimental investigation using the flame surface extracted from OH PLIF measurements indicate increased wrinkling of the flame front at higher bulk velocities.
- During further investigation with matching laminar flame speed of methane and biogas flames, similar curvatures were calculated at the same overall flow velocity.
- When the HRX measurements for methane and biogas flames were compared to those of OH* chemiluminescence measured using an ICCD camera for varying equivalence ratios, a similar increasing trend was observed. This would suggest that the HRX measurement technique is suitable for turbulent applications as it is in the laminar flame case.
- When the HRX technique was applied to conditions near to blow-off, the HRX signal was observed at the boundary of the isolated flame pockets inside the inner recirculation. In some cases, regions were void of both OH and H₂CO indicating the entrainment of cold reactants.

6.1.3. Heat Release measurements for methane, biogas and syngas flames subjected to velocity perturbations

Important conclusions established from the detailed experimental investigations performed to measure the response of lean fully premixed turbulent flames of fuels with varying compositions subjected to inlet velocity perturbations are summarised here. The conclusions reached from the HRX measurements, were used to support the findings from the flame response measured using OH* (global heat release rate). The flame response was also studied for varying equivalence ratios and different bulk velocities.

The HRX and the flame response measurements can be summarised as follows:

- When the laminar flame speed of methane and biogas were matched, the same flame response was observed at all the forcing frequencies and the forcing amplitudes. Any

notable differences were only present at the amplitudes that corresponded to the appearance of a vortex close to the bluff-body.

- In the case of syngas of varying compositions when the laminar flame speed was matched, the difference in flame response between methane and syngas mixtures were not significant except at a forcing frequency of 30 Hz. This seems to indicate that there are other parameters such as the density of the fuel that needs to be taken into account.
- The phase difference obtained from the HRX measurements for both methane and biogas flames showed good agreement. This suggests that in the case of biogas flames even under high strain the HRX technique effectively captures the spatial heat release variation.
- The results show that the heat release measurement (HRX) is adequate for flame stability studies for multi-components fuels such as biogas and some syngas mixtures even for large amplitude of forcing. It has to be noted that in the case of syngas the carbon-monoxide and hydrogen proportions were not significantly high.

6.2. Future work

The data produced from the HRX and flame measurements on premixed methane, biogas and syngas mixtures can be used for validation of flame models and acoustic network models. The study of the flame response when the velocities are matched can be extended to longer chain hydrocarbon and fuels with a hydroxyl radical as well.

The current facilities set-up can be used to measure experimentally the laminar flame speed of longer chain hydrocarbons and with some modifications even the laminar flame speed of liquid fuels. These will help in the validation of computer-based models and enable assessment of experimental measurements for their adequacy. These advanced measurement techniques can give an insight not, only into the chemistry of the combustion, but also into the flow field and combustion interaction. The laminar set-up allows for easy implementation of laser diagnostic techniques and the current apparatus can help in the integration of various non-intrusive temperature measurements such as Rayleigh scattering and two line OH PLIF thermometry.

Information about the temperature in the turbulent flame can provide insightful information on the spatial distribution of temperature for different fuels or modes of combustion. This study can be used to further the understanding into the mechanism of flame blow-off. The accuracy

of the HRX measurements can also be compared with other approaches using two-species PLIF measurements such as H₂CO and atomic H PLIF (Mulla et al. 2015).

List of publications:

Hussain, T., Dowlut, A. & Balachandran, R. (2011), “Experimental Investigation of Response of Hydrogen Enriched Methane Flames to Acoustic Oscillations”, Fifth European Combustion Meeting, Cardiff, Great Britain.

Hussain, T., Dowlut, A. & Balachandran, R. (2012), “Investigation in to the effect of hydrogen enrichment on the response of turbulent premixed flames subjected to acoustic excitation”, 19th International Congress on Sound & Vibration, Vilnius, Lithuania.

Dowlut, A., Hussain, T. & Balachandran, R. (2012), “Experimental investigation of dynamic response of acoustically forced turbulent premixed CH₄/CO₂/air flames”, 19th International Congress on Sound & Vibration, Vilnius, Lithuania.

Yuan R, Kariuki J, Dowlut A, Balachandran R, Mastorakos E. Reaction zone visualisation in swirling spray n-heptane flames. *Proceedings of the Combustion Institute*. 2014.

Kariuki J, Dowlut A, Yuan R, Balachandran R, Mastorakos E. Heat release imaging in turbulent premixed methane-air flames close to blow-off. *Proceedings of the Combustion Institute*. 2014.

A. Mulla, A. Dowlut, T. Hussain, Z. M. Nikolaou, S. R. Chakravarthy, N. Swaminathan, R. Balachandran Heat release rate estimation in laminar premixed flames using laser-induced fluorescence of CH₂O and H-atom. *Combustion and Flame* 2016

Reference:

- Allison, P., Driscoll, J. & Ihme, M., 2012. Acoustic Behavior of a Partially-Premixed Gas Turbine Model Combustor. In *50th AIAA Aerospace Sciences Meeting including the New Horizons Forum and Aerospace Exposition*. Reston, Virginia: American Institute of Aeronautics and Astronautics.
- Altay, H.M. et al., 2009. Modeling the dynamic response of a laminar perforated-plate stabilized flame. *Proceedings of the Combustion Institute*, 32(1), pp.1359–1366.
- Armitage, C.A. et al., 2006. Investigation of the nonlinear response of turbulent premixed flames to imposed inlet velocity oscillations. *Combustion and Flame*, 146(3), pp.419–436.
- Ayoola, B.O. et al., 2006. Spatially resolved heat release rate measurements in turbulent premixed flames. *Combustion and Flame*, 144, pp.1–16.
- Balachandran, R., 2011. Dynamics of bluff-body stabilised flames subjected to equivalence ratio oscillations. *Proceeding of the ECM 2011*, (i), pp.1–6.
- Balachandran, R. et al., 2005. Experimental investigation of the non linear response of turbulent premixed flames to imposed inlet velocity oscillations. *Combustion and Flame*, 143, pp.37–55.
- Bellows, B.D. et al., 2007. Flame transfer function saturation mechanisms in a swirl-stabilized combustor. *Proceedings of the Combustion Institute*, 31(2), pp.3181–3188.
- Benim, A.C. & Syed, K.J., 2014. *Flashback Mechanisms in Lean Premixed Gas Turbine Combustion*, Elsevier Science.
- Bergthorson, J.M., Salusbury, S.D. & Dimotakis, P.E., 2011. Experiments and modelling of premixed laminar stagnation flame hydrodynamics. *Journal of Fluid Mechanics*.
- Bernier, D. et al., 2003. Transfer function measurements in a model combustor: Application to adaptive instability control. *Combustion Science and Technology*, 175(5), pp.993–1013.
- Bloxside, G.J., Dowling, A.P. & Langhorne, P.J., 2006. Reheat buzz: an acoustically coupled combustion instability. Part 2. Theory. *Journal of Fluid Mechanics*, 193(-1), p.445.
- Böckle, S. et al., 2000. Simultaneous single-shot laser-based imaging of formaldehyde, OH, and temperature in turbulent flames. *Proceedings of the Combustion Institute*, 28(1), pp.279–286.
- Borghi, R., 1988. Turbulent combustion modelling. *Progress in Energy and Combustion Science*, 14(4), pp.245–292.
- Bouvet, N. et al., 2011. Characterization of syngas laminar flames using the Bunsen burner configuration. *International Journal of Hydrogen Energy*, 36(1), pp.992–1005.

- Cala, C.E.C., Fernandes, E.C. & Heitor, M. V, Analysis of oscillating shear layer.
- Candel, S., 2002. Combustion dynamics and control: Progress and challenges. *Proceedings of the Combustion Institute*, 29(1), pp.1–28.
- Chao, B.. & Law, C., 1994. Laminar flame propagation with volumetric heat loss and chain branching-termination reactions. *International Journal of Heat and Mass Transfer*, 37(4), pp.673–680.
- Chao, B.H., Egolfopoulos, F.N. & Law, C.K., 1997. Structure and propagation of premixed flame in nozzle-generated counterflow. *Combustion and Flame*, 109(4), pp.620–638.
- Cho, P. et al., 1988. Structure and propagation of turbulent premixed flames astabilized in a stagnation flow. *Symposium (International) on Combustion*, 21(1), pp.1493–1499.
- Chong, C.T. & Hochgreb, S., 2011. Measurements of laminar flame speeds of liquid fuels: Jet-A1, diesel, palm methyl esters and blends using particle imaging velocimetry (PIV). *Proceedings of the Combustion Institute*, 33(1), pp.979–986.
- Chung, S.H. & Law, C.K., 1984. An invariant derivation of flame stretch. *Combustion and Flame*, 55(1), pp.123–125.
- Cohé, C. et al., 2009. CO₂ addition and pressure effects on laminar and turbulent lean premixed CH₄ air flames. *Proceedings of the Combustion Institute*, 32 II, pp.1803–1810.
- Coward, H.F. & Hartwell, F.J., 1932. 277. Studies in the mechanism of flame movement. Part I. The uniform movement of flame in mixtures of methane and air, in relation to tube diameter. *Journal of the Chemical Society (Resumed)*, p.1996.
- Das, A.K., Kumar, K. & Sung, C.-J., 2011. Laminar flame speeds of moist syngas mixtures. *Combustion and Flame*, 158(2), pp.345–353.
- Dawson, J.R. et al., 2011. Visualization of blow-off events in bluff-body stabilized turbulent premixed flames. *Proceedings of the Combustion Institute*, 33(1), pp.1559–1566.
- Devriendt, K. & Peeters, J., 1997. Direct Identification of the $C_2H(X^2\Sigma^+) + O(3P) \rightarrow CH(A^2\Delta) + CO$ Reaction as the Source of the $CH(A^2\Delta \rightarrow X^2\Pi)$ Chemiluminescence in $C_2H_2/O_2/H$ Atomic Flames. *The Journal of Physical Chemistry A*, 101(14), pp.2546–2551.
- Van Doorne, C.W.H. & Westerweel, J., 2006. Measurement of laminar, transitional and turbulent pipe flow using Stereoscopic-PIV. *Experiments in Fluids*, 42(2), pp.259–279.
- Dowling, a. P., 1995. The calculation of thermoacoustic oscillations. *Journal of Sound and Vibration*, 180, pp.557–581.
- Dowling, A.P. & Hubbard, S., 2000. Instability in lean premixed combustors. *Proceedings of the Institution of Mechanical Engineers, Part A: Journal of Power and Energy*, 214(4), pp.317–332.

- Driscoll, J.F. & Temme, J., 2011. Role of Swirl in Flame Stabilization. *49th AIAA Aerospace Sciences Meeting*, (January), pp.1–11.
- Eriksson, O.N., 2014. Biogas and natural gas.
- Fayoux, A. et al., 2005. Experimental and numerical determination of heat release in counterflow premixed laminar flames. *Proceedings of the Combustion Institute*, 30(1), pp.251–257.
- Ferguson, D., Richard, G.A. & Straub, D., 2008. Fuel Interchangeability for Lean Premixed Combustion in Gas Turbine Engines. In *Volume 3: Combustion, Fuels and Emissions, Parts A and B*. ASME, pp. 973–981.
- Figura, L. et al., 2007. The Effects of Fuel Composition on Flame Structure and Combustion Dynamics in a Lean Premixed Combustor. In *Volume 2: Turbo Expo 2007*. ASME, pp. 181–187.
- Gibbs, G.J. & Calcote, H.F., 1959. Effect of Molecular Structure on Burning Velocity. *Journal of Chemical & Engineering Data*, 4(3), pp.226–237. Available at: <http://dx.doi.org/10.1021/jc60003a011> [Accessed March 4, 2015].
- Gu, X. et al., 2009. Measurements of Laminar Burning Velocities and Markstein Lengths of n-Butanol–Air Premixed Mixtures at Elevated Temperatures and Pressures. *Energy & Fuels*, 23(10), pp.4900–4907.
- Günther, R., 1979. *Flames - Their Structure, Radiation and Temperature*. VonA. G. Gaydon undH. G. Wolfhard. Chapman and Hall Ltd., London 1979 4. Aulf., XIII, 449 S., zhalr. Abb. u. Tab., Ln., £ 18.00. *Chemie Ingenieur Technik*, 51(7), pp.765–765.
- Günther, R. & Janisch, G., 1972. Measurements of burning velocity in a flat flame front. *Combustion and Flame*, 19(1), pp.49–53.
- Haber, L.C., 2001. An investigation into the origin, measurement and application of chemiluminescent light emissions from premixed flames.
- Halter, F. et al., 2009. Analysis of flame surface density measurements in turbulent premixed combustion. *Combustion and Flame*, 156(3), pp.657–664.
- Haq, M. et al., 2002. Wrinkling and curvature of laminar and turbulent premixed flames. *Combustion and Flame*, 131(1-2), pp.1–15.
- Hardalupas, Y. & Orain, M., 2004. Local measurements of the time-dependent heat release rate and equivalence ratio using chemiluminescent emission from a flame. *Combustion and Flame*, 139(3), pp.188–207.
- Harrington, J.E. & Smyth, K.C., 1993. Laser-induced fluorescence measurements of formaldehyde in a methane/air diffusion flame. *Chemical Physics Letters*, 202(3-4), pp.196–202.

- Hassan, M.I., Aung, K.T. & Faeth, G.M., 1997. Properties of Laminar Premixed CO/H₂/Air Flames at Various Pressures. *Journal of Propulsion and Power*, 13(2), pp.239–245.
- Hemchandra, S. & Lieuwen, T., 2010. Premixed flame response to equivalence ratio perturbations. *Combustion Theory and Modelling*, 14(5), pp.681–714.
- Hendricks, A.G. & Vandsburger, U., 2007. The effect of fuel composition on flame dynamics. *Experimental Thermal and Fluid Science*, 32(1), pp.126–132.
- Hurle, I.R. et al., 1968a. Sound Emission from Open Turbulent Premixed Flames. *Proceedings of the Royal Society A: Mathematical, Physical and Engineering Sciences*, 303(1475), pp.409–427.
- Hurle, I.R. et al., 1968b. Sound Emission from Open Turbulent Premixed Flames. *Proceedings of the Royal Society A: Mathematical, Physical and Engineering Sciences*, 303(1475), pp.409–427.
- Ionut Porumbel, 2006. Large Eddy Simulation of bluff body stabilized premixed and partially premixed combustion Ionut , Porumbel Large Eddy Simulation of bluff body stabilized premixed and partially premixed combustion.
- Ishizuka, S. & Law, C.K., 1982. An experimental study on extinction and stability of stretched premixed flames. *Symposium (International) on Combustion*, 19(1), pp.327–335.
- Ishizuka, S., Miyasaka, K. & Law, C.K., 1982. Effects of heat loss, preferential diffusion, and flame stretch on flame-front instability and extinction of propane/air mixtures. *Combustion and Flame*, 45, pp.293–308.
- Ju, Y., Masuya, G. & Ronney, P.D., 1998. Effects of radiative emission and absorption on the propagation and extinction of premixed gas flames. *Symposium (International) on Combustion*, 27(2), pp.2619–2626.
- Kariuki, J. et al., 2014. Heat release imaging in turbulent premixed methane-air flames close to blow-off. *Proceedings of the Combustion Institute*.
- Kido, H. et al., 2002. Influence of local flame displacement velocity on turbulent burning velocity. *Proceedings of the Combustion Institute*, 29(2), pp.1855–1861.
- Kohse-Höinghaus, K. et al., 2005. Combustion at the focus: laser diagnostics and control. *Proceedings of the Combustion Institute*, 30(1), pp.89–123.
- Külsheimer, C. & Büchner, H., 2002. Combustion dynamics of turbulent swirling flames. *Combustion and Flame*, 131(1-2), pp.70–84.
- KUMAR, K. et al., 2008a. An experimental investigation of ethylene/O₂/diluent mixtures: Laminar flame speeds with preheat and ignition delays at high pressures. *Combustion and Flame*, 153(3), pp.343–354.

- Kumar, K. et al., 2008b. An experimental investigation of ethylene/O₂/diluent mixtures: Laminar flame speeds with preheat and ignition delays at high pressures. *Combustion and Flame*, 153(3), pp.343–354.
- Kumar, K., 2007. Global Combustion Responses of Practical Hydrocarbon Fuels: *n*-Heptane, *iso*-Octane, *n*-Decane, *n*-Dodecane and Ethylene.
- Kumar, K. et al., 2007. Laminar Flame Speeds of Preheated *iso*-Octane/O₂/N₂ and *n*-Heptane/O₂/N₂ Mixtures. *Journal of Propulsion and Power*, 23(2), pp.428–436.
- Kumar, K. & Sung, C.-J., 2007. Laminar flame speeds and extinction limits of preheated *n*-decane/O₂/N₂ and *n*-dodecane/O₂/N₂ mixtures. *Combustion and Flame*, 151(1-2), pp.209–224.
- Kuo, K.K., 1986. *Principles of combustion*, Wiley.
- Kutne, P. et al., 2011. Experimental analysis of the combustion behaviour of oxyfuel flames in a gas turbine model combustor. *Proceedings of the Combustion Institute*, 33(2), pp.3383–3390.
- Lawn, C.J., 2000. Distributions of instantaneous heat release by the cross-correlation of chemiluminescent emissions. *Combustion and Flame*, 123(1-2), pp.227–240.
- Lawn, C.J. & Polifke, W., 2004. A model for the thermoacoustic response of a premixed swirl burner, Part II: The flame response. *Combustion Science and Technology*, 176(8), pp.1359–1390.
- Lee, S.-Y. et al., 2000. An experimental estimation of mean reaction rate and flame structure during combustion instability in a lean premixed gas turbine combustor. *Proceedings of the Combustion Institute*, 28(1), pp.775–782.
- Lee, J.G. & Santavicca, D.A., 2003. Experimental Diagnostics for the Study of Combustion Instabilities in Lean Premixed Combustors. *Journal of Propulsion and Power*, 19(5), pp.735–750.
- Lieuwen, T. & Neumeier, Y., 2002. Nonlinear pressure-heat release transfer function measurements in a premixed combustor. *Proceedings of the Combustion Institute*, 29(1), pp.99–105.
- Lieuwen, T. & Richards, G., 2006. BURNING QUESTIONS. *Mechanical Engineering-CIME*.
- Lieuwen, T. & Zinn, B.T., 1998. The role of equivalence ratio oscillations in driving combustion instabilities in low NO_x gas turbines. *Symposium (International) on Combustion*, 27(x), pp.1809–1816.
- Liu, F., Guo, H. & Smallwood, G.J., 2003. The chemical effect of CO₂ replacement of N₂ in air on the burning velocity of CH₄ and H₂ premixed flames. *Combustion and Flame*, 133, pp.495–497.

- Najm, H.N. et al., 1998. A Study of Flame Observables in Premixed Methane - Air Flames. *Combustion Science and Technology*, 140(1-6), pp.369–403.
- Najm, H.N. et al., 1998a. On the Adequacy of Certain Experimental Observables as Measurements of Flame Burning Rate. *Combustion and Flame*, 113, pp.312–332.
- Najm, H.N. et al., 1998b. On the Adequacy of Certain Experimental Observables as Measurements of Flame Burning Rate. *Combustion and Flame*, 113(3), pp.312–332.
- Najm, H.N. & Wyckoff, P.S., 1996. Premixed Flame Response to Unsteady Strain-Rate and Curvature. *Wss/Ci96F-105*, 112, pp.92–112.
- Natarajan, J., Lieuwen, T. & Seitzman, J., 2007a. Laminar Flame Speeds and Strain Sensitivities of Mixtures of H. In *Volume 2: Turbo Expo 2007*. ASME, pp. 751–760.
- Natarajan, J., Lieuwen, T. & Seitzman, J., 2007b. Laminar flame speeds of H₂/CO mixtures: Effect of CO₂ dilution, preheat temperature, and pressure. *Combustion and Flame*, 151(1-2), pp.104–119.
- Nguyen, Q.-V. & Paul, P.H., 1996. The time evolution of a vortex-flame interaction observed via planar imaging of CH and OH. *Symposium (International) on Combustion*, 26(1), pp.357–364.
- Oleszek, M. et al., 2014. Comparison of biogas production from wild and cultivated varieties of reed canary grass. *Bioresource technology*, 156, pp.303–6.
- Paul, P.H. & Najm, H.N., 1998. Planar laser-induced fluorescence imaging of flame heat release rate. *Symposium (International) on Combustion*, 27(1), pp.43–50.
- Peters, N., 2000. *Turbulent Combustion*, Cambridge University Press.
- Poinsot, T.J. et al., 1987. Vortex-driven acoustically coupled combustion instabilities. *Journal of Fluid Mechanics*, 177, p.265.
- Price, R.B., Hurle, I.R. & Sugden, T.M., 1969. Optical studies of the generation of noise in turbulent flames. *Symposium (International) on Combustion*, 12(1), pp.1093–1102.
- Pun, W., Palm, S.L. & Culick, F.E.C., 2003. Combustion dynamics of an acoustically forced flame. *Combustion Science and Technology*, 175(3), pp.499–521.
- Putnam, B.A.A. & Dennis, W.R., 1952. Cellular flames and oscillatory combustion. , (1890), pp.566–575.
- Qin, X. & Ju, Y., 2005. Measurements of burning velocities of dimethyl ether and air premixed flames at elevated pressures. *Proceedings of the Combustion Institute*, 30(1), pp.233–240.
- Ren, J.-Y. et al., 2001. Strain-rate effects on hydrogen-enhanced lean premixed combustion. *Combustion and Flame*, 124(4), pp.717–720.

- Richards, G. et al., 2001. Issues for low-emission, fuel-flexible power systems. *Progress in Energy and Combustion Science*, 27(2), pp.141–169.
- Ruan, J. et al., 2001. Combined effects of nongray radiation and pressure on premixed CH₄/O₂/CO₂ flames. *Combustion and Flame*, 124(1-2), pp.225–230.
- Sadanandan, R. et al., 2012. Investigation of the syngas flame characteristics at elevated pressures using optical and laser diagnostic methods. *Flow, Turbulence and Combustion*, 89, pp.275–294.
- Samaniego, J.-M. & Mantel, T., 1999. Fundamental mechanisms in premixed turbulent flame propagation via flame–vortex interactions. *Combustion and Flame*, 118(4), pp.537–556.
- Schadow, K.C. & Gutmark, E., 1992. Combustion instability related to vortex shedding in dump combustors and their passive control. *Progress in Energy and Combustion Science*, 18(2), pp.117–132.
- Schimmer, H. & Vortmeyer, D., 1977. Acoustical oscillation in a combustion system with a flat flame. *Combustion and Flame*, 28, pp.17–24.
- Scholte, T.G. & Vaags, P.B., 1959. Burning velocities of mixtures of hydrogen, carbon monoxide and methane with air. *Combustion and Flame*, 3, pp.511–524.
- Schuller, T., 2003. Self-induced combustion oscillations of laminar premixed flames stabilized on annular burners. *Combustion and Flame*, 135(4), pp.525–537.
- Seybert, A.F. & Parrott, T.L., 1978. Impedance measurement using a two-microphone, random-excitation method.
- Shanbhogue, S.J., 2008. *Dynamics of Perturbed Exothermic Bluff-Body Flow-Fields*. Georgia Institute of Technology.
- Shy, S. et al., 2005. Turbulent burning velocities of premixed CH₄/diluent/air flames in intense isotropic turbulence with consideration of radiation losses. *Combustion and Flame*, 143(1-2), pp.106–118.
- Stevens, F.W., 1926. THE RATE OF FLAME PROPAGATION IN GASEOUS EXPLOSIVE REACTIONS 1. *Journal of the American Chemical Society*, 48(7), pp.1896–1906.
- Taylor, A.M.K.P., *Instrumentation for Flows with Combustion*: Amazon.co.uk: Alexander M.K.P. Taylor: 9780126839203: Books.
- Torres, H. et al., 1999. Experimental investigation of combustion instabilities in a gas turbine combustor simulator. *AIAA paper*, (99-0712).
- Vagelopoulos, C.M. & Egolfopoulos, F.N., 1998. Direct experimental determination of laminar flame speeds. *Symposium (International) on Combustion*, 27(1), pp.513–519.

- Vagelopoulos, C.M. & Egolfopoulos, F.N., 1994. Laminar flame speeds and extinction strain rates of mixtures of carbon monoxide with hydrogen, methane, and air. *Symposium (International) on Combustion*, 25(1), pp.1317–1323.
- Vagelopoulos, C.M., Egolfopoulos, F.N. & Law, C.K., 1994. Further considerations on the determination of laminar flame speeds with the counterflow twin-flame technique. *Symposium (International) on Combustion*, 25(1), pp.1341–1347.
- Venkataraman, K.K. et al., 1999. Mechanism of Combustion Instability in a Lean Premixed Dump Combustor. *Journal of Propulsion and Power*, 15(6), pp.909–918.
- Veynante, D., Duclos, J.M. & Piana, J., 1994. Experimental analysis of flamelet models for premixed turbulent combustion. *Symposium (International) on Combustion*, 25(1), pp.1249–1256.
- Wu, C. et al., 2009. Effects of CO addition on the characteristics of laminar premixed CH₄/air opposed-jet flames. *Combustion and Flame*, 156(2), pp.362–373.
- Wu, C.K. & Law, C.K., 1985a. On the determination of laminar flame speeds from stretched flames. *Symposium (International) on Combustion*, 20(1), pp.1941–1949.
- Wu, C.K. & Law, C.K., 1985b. On the determination of laminar flame speeds from stretched flames. *Symposium (International) on Combustion*, 20(1), pp.1941–1949.
- Wu, X. et al., 2003. Combustion instability due to the nonlinear interaction between sound and flame. *Journal of Fluid Mechanics*, 497(1984), pp.23–53.
- Wu, X. et al., 2012. Laminar burning characteristics of 2,5-dimethylfuran and iso-octane blend at elevated temperatures and pressures. *Fuel*, 95, pp.234–240.
- Yu, G., Law, C.K. & Wu, C.K., 1986. Laminar flame speeds of hydrocarbon + air mixtures with hydrogen addition. *Combustion and Flame*, 63(3), pp.339–347.
- Yuan, R. et al., 2014. Reaction zone visualisation in swirling spray n-heptane flames. *Proceedings of the Combustion Institute*.
- Zhao, Z. et al., 2004. The initial temperature and N₂ dilution effect on the laminar flame speed of propane/air. *Combustion Science and Technology*, 176(10), pp.1705–1723.
- Zhao, Z., Kazakov, A. & Dryer, F.L., 2004. Measurements of dimethyl ether/air mixture burning velocities by using particle image velocimetry. *Combustion and Flame*, 139(1-2), pp.52–60.
- Zukoski, E.E., 1954. Flame Stabilization on bluff bodies at low and intermediate Reynolds numbers. , p.96.